CORA Cork Open Research Archive
Cartlann Taighde Oscailte Chorcaí

Title	Nonlinear optics with cold Rb atoms using tapered optical nanofibres
Authors	Kumar, Ravi
Publication date	2015
Original Citation	Kumar, R. 2015. Nonlinear optics with cold Rb atoms using tapered optical nanofibres. PhD Thesis, University College Cork.
Type of publication	Doctoral thesis
Rights	© 2015, Ravi Kumar. - http://creativecommons.org/licenses/by-nc-nd/3.0/
Download date	2026-11-15 17:56:19
Item downloaded from	https://hdl.handle.net/10468/2885



Nonlinear Optics with Cold Rb Atoms Using Tapered Optical Nanofibres

Ravi Kumar
MSc
111220192

NATIONAL UNIVERSITY OF IRELAND, CORK

College of Science, Engineering and Food Science

Department of Physics

Thesis submitted for the degree of Doctor of Philosophy

November 2015

Head of Department: Professor John McInerney

Supervisors: Professor Síle Nic Chormaic
Professor Paul Callanan

Research supported by the Okinawa Institute of Science and Technology Graduate University, Okinawa, Japan

Contents

List of Figures . . . iv
List of Tables . . . vii
Acknowledgements . . . x
Abstract . . . xii
List of Publications . . . xiii
List of Presentations . . . xiv
List of Symbols . . . xv
List of Abbreviations . . . xix

1 Introduction **1**
1.1 Optical Nanofibres and Atoms . . . 2
1.2 Thesis Outline . . . 4

2 Optical Nanofibres: Light Propagation and Fabrication **6**
2.1 Propagation of Light in Optical Fibres . . . 6
2.2 Modes of an Optical Nanofibre . . . 14
2.2.1 Fundamental mode . . . 15
2.2.2 First higher order fibre modes . . . 17
2.3 Energy Flow . . . 19
2.4 Fabrication of Optical nanofibres . . . 21
2.4.1 Adiabatic criterion . . . 21
2.4.2 Fibre pulling rig . . . 23
2.4.3 Single-mode optical nanofibre (SM-ONF) . . . 24
2.4.4 Few-mode optical nanofibre (FM-ONF) . . . 25
2.5 Conclusion . . . 26

3 Light-Atom Interactions **27**
3.1 Two-level Atoms . . . 27
3.1.1 Interaction with monochromatic radiation . . . 29
3.1.2 Optical Bloch equations . . . 31
3.1.3 Steady state solutions . . . 32
3.1.4 Saturation and power broadening . . . 33
3.1.5 The light shift . . . 34
3.2 Three-Level Atoms . . . 35
3.2.1 Aulter-Townes splitting . . . 38
3.2.2 Electromagnetically induced transparency . . . 39
3.3 Conclusion . . . 40

4 Magneto-Optical Trapping of Rubidium **43**
4.1 Radiative Optical Forces . . . 43
4.2 Optical Molasses . . . 44
4.3 Magneto-Optical Trap . . . 46
4.4 Cooling and Trapping Rubidium Atoms . . . 49
4.4.1 Rubidium atoms . . . 50
4.4.2 Optical setup . . . 51

4.4.3 Magnetic field . . . 53
4.4.4 Ultra-high vacuum system . . . 55
4.5 Conclusion . . . 58

5 Temperature Measurement of Cold Atoms Using an Optical Nanofibre 59
5.1 Fluorescence Measurements Using an Optical Nanofibre . . . 59
5.1.1 MOT loading and effective number of atoms . . . 59
5.1.2 Temperature measurement by the release-recapture technique . . . 62
5.2 Absorption Measurements Using an Optical Nanofibre . . . 63
5.2.1 Measurement of linewidth . . . 64
5.2.2 Temperature measurement using transient absorption . . . 65
5.3 Conclusion . . . 68

6 Autler-Townes Splitting at Ultra-Low Power 69
6.1 Introduction . . . 71
6.2 Experimental Details . . . 71
6.3 Results and Discussion . . . 73
6.4 Conclusion . . . 80

7 Electromagnetically Induced Transparency with Optical Nanofibres 81
7.1 Introduction . . . 83
7.2 Experimental Methods . . . 84
7.2.1 Optical nanofibre fabrication . . . 84
7.2.2 Cold atoms . . . 84
7.2.3 Ladder type electromagnetically induced transparency system . . . 85
7.3 Results and Discussions . . . 86
7.3.1 Multilevel electromagnetically induced transparency . . . 87
7.3.2 All-fibred-all-optical-switching . . . 90
7.4 Conclusion . . . 91

8 Atom Interaction with Higher Order Modes of an Optical Nanofibre 93
8.1 Introduction . . . 96
8.2 Experiment . . . 98
8.2.1 Higher order mode optical nanofibre . . . 98
8.2.2 Magneto-optical trapping of atoms . . . 101
8.3 Measurements and Results . . . 103
8.3.1 Coupling of MOT beams to the nanofibre . . . 103
8.3.2 Fluorescence measurements . . . 103
8.3.3 Absorption measurements . . . 105
8.4 Conclusion . . . 107

9 Conclusions 108

A Other Published Works **110**
A.1 Release-Recapture Temperature Measurement 110
A.2 Probing a Dark-Magneto Optical Trap with an Optical Nanofibre 116
A.3 Optical Nanofibre Facilitated Nonlinear Optics Effects 125
A.4 Spectroscopy, Manipulation and Trapping Using Optical Nanofibres 134

List of Figures

2.1 Illustration of an optical fibre 7
2.2 Plot of Bessel functions 11
2.3 Effective refractive index with respect to the V-number 15
2.4 Intensity profile for a quasi-linearly polarised light propagating through an ONF 17
2.5 Intensity profile for a quasi-circularly polarised light propagating through an ONF 18
2.6 Intensity distribution for the first four modes (HE_{11}, TE_{01}, TM_{01}, and HE_{21}) of an ONF 19
2.7 Mode power flux in the core of an ONF as a function of its diameter 20
2.8 Illustration of an ONF 21
2.9 Illustration of a fibre taper showing the local taper parameters . 22
2.10 Illustration of the fibre pulling rig 24
2.11 Transmission during nanofibre pulling for light coupled to the LP_{11} mode 26

3.1 Two-level atom with a coupling laser of angular frequency ω . . 28
3.2 Scattering rate for the 5 $S_{1/2}$ F=2 $\rightarrow$ 5 $P_{3/2}$ F′=3 transition of ^{87}Rb ($\Gamma/2\pi = 6$ MHz) as a function of δ/Γ. 34
3.3 Three-level atom coupled to two lasers 36
3.4 Calculated absorption spectra showing Aulter-Townes splitting . 41
3.5 Calculated EIT spectra 42

4.1 One-dimensional Doppler cooling 45
4.2 Velocity dependence of the damping force in one-dimension . . . 46
4.3 One-dimensional MOT scheme 47
4.4 Three-dimensional MOT scheme arrangement 48
4.5 Energy level diagram for ^{87}Rb showing the hyperfine transitions 49
4.6 Schematic of the optical setup for the MOT 52
4.7 Schematic of a typical AOM double-pass setup 53
4.8 Saturable absorption spectrum of rubidium 54
4.9 A picture of the vacuum chamber with the magnetic coils used for creating the MOT. 55
4.10 Illustration of vacuum components of the experimental setup . . 56

5.1 (a) Illustration of a basic setup with an ONF, (b) An image of the cold atom cloud with the ONF taken using a CMOS camera . . 60
5.2 Photon counts registered by the SPCM during the loading of atoms in the MOT 61
5.3 Fraction of atoms remaining in the trap for different release times with their theoretical fittings 63
5.4 Absorption spectrum of cold ^{87}Rb atoms in a MOT for a probe sent through an ONF 64
5.5 Transient absorption for different input probe powers through an ONF 66

5.6 Transient absorption with theoretical fits for various probe powers 67
5.7 Temperature measured by the transient absorption technique with a probe propagating through the ONF 67

6.1 Energy level diagram for ^{87}Rb atoms showing the 780 nm coupling and 776 nm probe beams 73
6.2 Schematic of the experimental setup 74
6.3 Transmission of 780 nm light passing through the ONF with cold ^{87}Rb atoms around the waist 75
6.4 (a) 420 nm photon count rate as ω_2 is scanned across the $5P_{3/2}$ to $5D_{5/2}$ transition, (b) Maximum blue photon count for different powers of ω_2 76
6.5 Blue fluorescence from the atoms collected via the ONF for different powers in ω_1, which is 14 MHz red-detuned from the $5S_{1/2}$ F=2 to $5P_{3/2}$ F′=3 transition, while ω_2 is scanned across the $5P_{3/2}$ F′=3 to $5D_{5/2}$ hyperfine levels 77
6.6 Measured A-T splitting as a function of the square-root of the power in the 780 nm coupling beam 78
6.7 Variation of γ_{23} and γ_{13} as a function of coupling power, P_{ω_1} . . 79

7.1 Energy level diagram for ^{87}Rb. The relevant levels for the EIT experiment are marked as $|1\rangle$, $|2\rangle$, $|3\rangle$ and $|4\rangle$ 85
7.2 Schematic of the experimental setup 85
7.3 Transmission through the fibre as the frequency of the probe beam is scanned 88
7.4 Multiple EIT peaks for coupling beam powers from 0-800 nW as indicated on the graphs 89
7.5 (a) Rabi frequency as a function of the square root of power in the coupling beam for the strong coupling beam condition, (b) Linewidth of the two transparency peaks as a function of coupling power 89
7.6 Transmission through nanofibre as a function of time to demonstrate all-optical-switching 91

8.1 (a) Intensity distribution of the first four fibre modes (HE_{11}, TE_{01}, TM_{01}, and HE_{21}) of a nanofibre (radius 350 nm) for 780 nm light, (b) Corresponding intensity profiles in one-dimension 97
8.2 (a) V-number plot for different modes of the nanofibre with the V-parameter on the x-axis, (b) Simulated profile for the LP_{11} mode exiting from a nanofibre pigtail, (c) Observed experimental profile for (b) 100
8.3 Transmission for light coupled to the LP_{11} mode of the fibre during tapering 100
8.4 Schematic of the experimental setup for the absorption and fluorescence measurements with FM-ONF 102

8.5 Intensity of the light collected by a CCD camera at one output of the nanofibre when only the MOT beams are on with horizontal and vertical profiles fitted using a combination of LG_{01} and the fundamental mode 104
8.6 (a) Schematic of the experimental setup for the mode filtering experiment, (b) Cold atom cloud loading curve when light is coupled to the guided modes of the FM-ONF, (c) the same as (b) but only for the fundamental mode, (d) Comparison of fluorescence counts based on the exponential fits to the loading curves in (b) and (c) 104
8.7 Timing sequence for the MOT beams and the SPCM during absorption experiments 106
8.8 Absorption spectra obtained when either higher order modes or a fundamental mode probe beam was coupled into the FM-ONF . 106

List of Tables

4.1 Physical properties of ^{87}Rb 49
4.2 Optical properties of ^{87}Rb D_2 transition ($5^2S_{1/2} \rightarrow 5^2P_{3/2}$) . . . 50

I, Ravi Kumar, certify that this thesis is my own work and I have not obtained a degree in this university or elsewhere on the basis of the work submitted in this thesis.

Ravi Kumar

To Vedmurthy Taponishtha Pt. Sriram Sharma Acharya and Mata Bhagwati Devi Sharma

Acknowledgements

Foremost, I would like to express my sincere gratitude to my supervisor Prof. Síle Nic Chormaic for the continuous support, encouragement and motivation during my PhD study and research. Her guidance helped me a lot in all the time of research and writing of this thesis. I thank a lot to Prof. Paul Callanan for being my co-supervisor, supporting throughout my PhD years and offering the teaching assignment as a lab demonstrator which was a memorable experience for me. I wish to thank the Physics Department, University College Cork (UCC) for admitting me in the PhD program and the Okinawa Institute of Science and Technology Graduate University (OIST) for providing the financial support for my PhD study and research. I would like to thank post-doctoral research scholars, Dr. Vandna Gokhroo, Dr. Vibhuti Bhushan Tiwari and Dr. Kieran Deasy, who closely worked on the cold atom project with me and shared their knowledge and skills with me. I joined the Quantum Optics Group at the Tyndall National Institute, UCC in 2011 and started working with another PhD student, (Dr.) Laura Russell. I would like to thank her for introducing me to the experimental setup, providing the techniques required for handling and operation of the system and for her patience in satiating my ardent curiosity as an early stage research student in my first year of PhD study. I thank Dr. V. B. Tiwari for guiding me through the sail in the sea of knowledge in cold atoms and for sharing his vast experience during his stay at UCC. In 2012, our group moved to the Okinawa Institute of Science and Technology Graduate University (OIST) and experiments were required to be rebuilt. It would not have been possible to get a quick start and run the experiment so fruitfully for years without Dr. Vandna Gokhroo who worked along with me on all aspects of research. I wish to thank Dr. Kieran Deasy for incorporating his technical expertise in the experiments and holding a lot of organisational responsibilities. I would like to thank Aili Maimaiti and Dr. Ciarán Phelan for working together on the higher-order mode experiment. I am thankful to Dr. Jonathan Ward and Vu Hong Le for designing the fibre pulling rig which allowed us to make suitable nanofibres for the experiments. I would like to thank Emi Nakamura-san and Momoko Zamami-san who helped with various administrative processes during their appointments as research administrators of the Light-Matter Interactions Unit at OIST. It is always a privilege to work in a pleasant and friendly environment such as the one which I got during my PhD study. It has been so much fun in the lab and outside due to the presence of Ramgopal Madugani, Aili Maimaiti, Eugen Prel, Mark Daly, (Dr.) Laura Russell, (Dr.) Mary Frawley, Alex Petcu-Colan, (Dr.) Amy Watkins, Dr. V. B. Tiwari, Dr. Vandna Gokhroo, Dr. Kieran Deasy, Dr. Giang Truong, Dr. Yong Yang, Dr. Jonathan Ward, Vu Hong Le, Alan Curtis, Bishwajeet Singh, Sunny Saurabh, Nitesh Dhasmana, Krishnapriya Subramonian Rajasree, Elaine Wong, Dr. Ivan Gusachenko, Dr. Ciarán Phelan, Dr. Marios Sergides, Thomas Nieddu, Simon Peter Mekhail, Dr. Tridib Ray, Dr. Jinjin Du, Dr. Xue Han, Vikraman Karunanidhi, Christiane Ebongue, Tushar Kanti Saha, Sanele Dlamini, Sahar Hejazy and several project/rotation students during the common time period I

shared with them in Cork/Okinawa. I would like to thank Prof. Thomas Busch for his time to time interactions and motivation. In 2013 and 2014, I visited Prof. Kozue Hakuta's lab at the University of Electro-Communications, Tokyo, Japan and Prof. Arno Rauschenbeutel's lab at the Institute of Atomic and Subatomic Physics, Vienna University of Technology, Austria, respectively, for one week each. I would like to express my gratitude to Prof. Hakuta and Prof. Rauschenbeutel for providing me with such opportunities and their group members for making the stay enjoyable and fruitful. I thank many times my friends in Cork and Okinawa for all the outdoor activities and enjoyable sightseeing trips. Last but not least, I wish to thank a lot to my parents, siblings and cousins for continuous support and encouragements throughout my life and research carrier, and to my wife for her patience, care and moral support during the writing of this thesis.

Abstract

Optical nanofibres (ONFs) are very thin optical waveguides with sub-wavelength diameters. ONFs have very high evanescent fields and the guided light is confined strongly in the transverse direction. These fibres can be used to achieve strong light-matter interactions. Atoms around the waist of an ONF can be probed by collecting the atomic fluorescence coupling or by measuring the transmission (or the polarisation) of the probe beam sent through it. This thesis presents experiments using ONFs for probing and manipulating laser-cooled ^{87}Rb atoms. As an initial experiment, a single mode ONF was integrated into a magneto-optical trap (MOT) and used for measuring the characteristics of the MOT, such as the loading time and the average temperature of the atom cloud. The effect of a near-resonant probe beam on the local temperature of the cold atoms has been studied. Next, the ONF was used for manipulating the atoms in the evanescent fields region in order to generate nonlinear optical effects. Four-wave mixing, ac Stark effect (Autler-Townes splitting) and electromagnetically induced transparency have been observed at unprecedented ultralow power levels. In another experiment, a few-mode ONF, supporting only the fundamental mode and the first higher order mode group, has been used for studying cold atoms. A higher pumping rate of the atomic fluorescence into the higher order fibre-guided modes and more interactions with the surrounding atoms for higher order mode evanescent light, when compared to signals for the fundamental mode, have been identified. The results obtained in the thesis are particularly for a fundamental understanding of light-atom interactions when atoms are near a dielectric surface and also for the development of fibre-based quantum information technologies. Atoms coupled to ONFs could be used for preparing intrinsically fibre-coupled quantum nodes for quantum computing and the studies presented here are significant for a detailed understanding of such a system.

List of Publications

1. Multi-level cascaded electromagnetically induced transparency in cold atoms using an optical nanofibre interface; R. Kumar, V. Gokhroo and S. Nic Chormaic, *New Journal of Physics* 17, 123012 (2015)

2. Optical nanofiber facilitated nonlinear optics effects in cold atoms; V. Gokhroo, R. Kumar and S. Nic Chormaic, *Proc. SPIE 9503, Nonlinear Optics and Applications IX*, 95030D (2015)

3. Autler-Townes splitting via frequency up-conversion at ultralow-power levels in cold ^{87}Rb atoms using an optical nanofiber; R. Kumar, V. Gokhroo, K. Deasy and S. Nic Chormaic, *Physical Review A* 91 (5), 053842 (2015)

4. Interaction of laser-cooled ^{87}Rb atoms with higher order modes of an optical nanofibre; R. Kumar, V. Gokhroo, K. Deasy, A. Maimaiti, M. Frawley, C. Phelan and S. Nic Chormaic, *New Journal of Physics* 17 (1), 013026 (2015)

5. Investigation of a ^{85}Rb dark magneto-optical trap using an optical nanofibre; L. Russell, R. Kumar, V. B. Tiwari, S. Nic Chormaic, *Measurement Science and Technology* 25, 055203 (2014)

6. Measurements on release-recapture of cold ^{85}Rb atoms using an optical nanofibre in a magneto-optical trap; L. Russell, R. Kumar, V. B. Tiwari and S. Nic Chormaic, *Optics Communications* 309, 313–317 (2013)

7. Spectroscopy, manipulation and trapping of neutral atoms, molecules, and other particles using optical nanofibers: A review; M. J. Morrissey, K. Deasy, M. Frawley, R. Kumar, E. Prel, L. Russell, V. G. Truong and S. Nic Chormaic, *Sensors* 13 (8), 10449-10481 (2013)

List of Presentations

Oral

1. Studies of cold atoms using optical nanofibres; R. Kumar, V. Gokhroo and S. Nic Chormaic, *Okinawa School in Physics: Coherent Quantum Dynamics*, Okinawa, Japan, October 2015

2. Nanofibre mediated frequency up-conversion in cold Rb atoms; R. Kumar, V. Gokhroo, K. Deasy and S. Nic Chormaic, *Asian Student Photonic Conference*, Kolkata, India, July 2014

3. Optical nanofibres integrated into a MOT; R. Kumar, V. Gokhroo, K. Deasy and S. Nic Chormaic, *Optical Nanofibre Applications Workshop*, Okinawa, Japan, June 2013

Poster

1. All optical switching with cold Rb atoms using an optical nanofibre; R. Kumar, V. Gokhroo, T. Ray and S. Nic Chormaic, *Optical Nanofibre Applications Workshop*, Okinawa, Japan, May 2015

2. Autler-Townes splitting in cold Rb atoms at ultra-low power using an optical nanofibre; R. Kumar, V. Gokhroo, K. Deasy and S. Nic Chormaic, *Topical Research Meeting on Hybrid Quantum Systems*, Nottingham, UK, December 2014

3. Release-recapture experiment on cold ^{85}Rb atoms with an optical nanofibre probe; R. Kumar, L. Russell, V. B. Tiwari and S. Nic Chormaic, *Conference on Lasers and Electro-Optics Pacific Rim (CLEO-PR)*, Kyoto, Japan, July 2013

4. Probing cold atoms with a hot sensor; R. Kumar, V. Gokhroo, K. Deasy and S. Nic Chormaic, *International Conference in Lasers and Spectroscopy - ICOLS*, Berkeley, USA, June 2013

5. Temperature measurement of cold atoms using transient absorption from an optical nanofibre; R. Kumar, L. Russell, M. Daly, V. B. Tiwari and S. Nic Chormaic, *Coherent Control of Complex Quantum Systems (C3QS) Workshop*, Okinawa, May 2013

6. Probing laser cooled atoms through a nanofibre; V. Gokhroo, R. Kumar, K. Deasy and S. Nic Chormaic, *Optical Nanofibre Applications Workshop*, Okinawa, Japan, June 2013

List of Symbols [1]

Symbol	Description
n_1	refractive index of the core
n_2	refractive index of the cladding
a	radius of the core of the fibre
$\mathbf{H}$	magnetic field intensity vector
$\mathbf{D}$	electric displacement vector
$\mathbf{E}$	electric field intensity vector
$\mathbf{B}$	magnetic flux density vector
∇	differential operator
i	$\sqrt{-1}$
ε	dielectric permittivity
μ	magnetic permeability
v_c	velocity of light
ω	angular frequency
β	propagation constant
J_l	Bessel function of the first kind
Y_l	Bessel function of the second kind
I_l	modified Bessel function of the first kind
K_l	modified Bessel function of the second kind
A, B, C, D, P, Q	constants
ε_1, ε_2	dielectric constants
k	wavenumber
λ	wavelength
k_0	free space wavenumber
k_1	wavenumber in the core
k_2	wavenumber in the cladding
λ_0	wavelength in free space
κ	$\sqrt{k^2 - \beta^2}$
d	diameter of the ONF
Ω_z	local taper angle
$r(z)$	local radius of the taper transition
z_b	beat length
z_t	local taper length

[1] A few symbols represent different quantities; however, the intended meaning should be obvious from the context.

β_1 , β_2	propagation constants
h	$\sqrt{k_1^2 - \beta^2}$
q	$\sqrt{\beta^2 - k_2^2}$
$\mathbf{S}$	Poynting vector; spin angular momentum
$\overline{\mathbf{S}}$	time averaged Poynting vector
r_0	initial untapered fibre diameter
H	Hamiltonian of an atom
H_0	Hamiltonian of the unperturbed atom
H_I	interaction Hamiltonian
E_n	energy of an atom
Ψ_n	wavefunction for an atom
c_n	amplitude coefficient
ρ	density operator
ρ_{ij}	density matrix element
Z	atomic number
$-e$	charge of an electron
$\mathbf{e}$	unit vector
$\mathbf{D}$	atomic dipole moment
Ω	Rabi frequency
ψ_1, ψ_2	real wavefunctions
δ	detuning of the radiation
Γ_s	scattering rate
Γ	natural linewidth
Γ'	power broadened linewidth
τ_R	radiative lifetime
s	saturation parameter
w	population difference parameter
I	laser field intensity; current; total nuclear angular momentum
I_s	the saturation intensity
λ_0	resonance transition wavelength
n	number density of atoms
$\boldsymbol{\mu}_{\mathrm{mn}}$	atomic dipole matrix element
H_{int}	Hamiltonian in the interaction picture
$\mathcal{U}$	unitary operator
$\mathcal{L}$	Liouville operator
σ_{ij}	density matrix element in the interaction picture
Γ_2, Γ_3	decays rates

Γ_{21}, Γ_{32}	natural linewidths
γ_2, γ_3	dephasing rates
σ_{jj}	population of the state $\|j\rangle$
$\sigma_{jj'}$	coherence between the sates $\|j\rangle$ and $\|j'\rangle$
$\langle E_z \rangle$	average kinetic energy
k_B	Boltzmann's constant
T	temperature of atoms
M	atomic mass
α	damping or friction coefficient
Γ_{MOT}	damping rate
ω_{MOT}	oscillation frequency
g_S	electron spin quantum number
g_L	electron orbital quantum number
g_I	nuclear "g-factors"
g_F	hyperfine Landé g-factor
$\mathbf{L}$	orbital angular momentum
$\mathbf{J}$	total electron angular momentum
$\mathbf{F}$	atomic angular momentum
a_c	radius of the MOT coils
d_c	separation between the MOT coils
μ_0	permeability of the vacuum
N_{coil}	number of turns
β_g	Zeeman shift gradient
$\mathbf{v}$	velocity of atom
$\mathbf{F}$	force
r	radial coordinate
z	axial coordinate
σ_r	radius of the cloud
N	total number of atoms
$g(r)$	modification factor due to the presence of the ONF
N_{eff}	effective number of atoms
η_{ONF}	coupling efficiency of spontaneous emission
Γ_s	atomic scattering rate
T_r	transmission of the ONF from the waist to one end
η_D	detector quantum efficiency
v_T	thermal velocity
r	radial coordinate

w_0	initial Gaussian waist of the cloud
$\bar{v}$	average thermal velocity
$A(t)$	peak density at time t
σ_a	atom-light absorption cross-section
$I(r)$	evanescent field intensity at a radial distance r
γ_{12}, γ_{13}, γ_{23}	dephasings
δ_c	coupling detuning
δ_p	probe detuning
Ω_c	Rabi frequency of the coupling transition
ω_p	frequency of the probe beam
Ω_c	Rabi frequency of the coupling beam
λ	wavelength of the light propagating in the fibre
V	V-number

List of Abbreviations

ONF	Optical nanofibre
TOF	Tapered optical fibre
MOT	Magneto-optical trap
SM-ONF	Single-mode optical nanofibre
FM-ONF	Few-mode optical nanofibre
SPCM	Single photon counting module
ECDL	Extended cavity diode laser
EIT	Electromagnetically-induced transparency
PBS	polarisation beam splitter
HWP	Half waveplate
QWP	Quarter waveplate
AOM	Acousto-optic modulator
SLM	Spatial light modulator
FWHM	Full-width-at-half-maximum
UHV	Ultra-high vacuum
TPS	Turbo-molecular pump
CF	Conflate flange
TPS	TPS Compact pump
6X	Six-way cross
4X	Four-way cross
RR	Release-recapture
PMT	Photo-multiplier tube
A-T	Autler-Townes
CCD	Charge-coupled device
CMOS	Complementary metal-oxide semiconductor
OAM	Orbital angular momentum
HOM	Higher order mode
IR	Infra-red
DMOT	Dark-MOT
BMOT	Bright-MOT
SMF	Single-mode fibre

Chapter 1

Introduction

Light has always been a matter of curiosity for mankind. Much effort has been placed on the understanding of the generation of light and its effect on various objects. Light-matter interactions are as much of interest for fundamental research as for technological advancement. Manipulation of matter at the atomic scale, while keeping the power used extremely small, has been one of the highly ambitious goals for scientists for ages. Significant efforts have focused on achieving strong coupling between photons and atoms [1–4]. The 21st Century has seen evidence of controlling single atoms with single photons [4–6]. Atoms in cavities are highly investigated due to the small mode volume of the cavities leading to a strong interaction of atoms with the photons in the cavity mode [3, 7–10]. Optical nanofibres (ONFs) [11], also known as subwavelength-diameter optical fibres or tapered optical fibres (TOFs) [12], are one of the alternative systems which can achieve strong atom-photon interaction with additional advantages, such as the intrinsic fibre coupling of the interacting photons [13]. ONFs are ultra-thin optical waveguides which have a high evanescent field region and strong confinement of light in the transverse direction [14, 15] and allow for propagation of light with extremely good transmission. In addition to these, they have excellent mechanical properties which allows them to be bent and manipulated without damage, thereby facilitating the fabrication of highly compact devices [16–19].

TOFs with submicron diameters are usually refered to as ONFs, which most of the works in this thesis are based on. ONFs have proven to be efficient tools for probing and manipulating cold atoms, and have gained signification attention for quantum optics applications as described in the next section.

1.1 Optical Nanofibres and Atoms

Until recently, the field of optical nanofibres and cold atoms was dominated by several key groups based in Tokyo, Moscow, Cork/ Okinawa and Bonn/Vienna, with several other groups making important contributions. ONFs have been investigated widely for sensing and manipulating atomic samples in the surroundings. The combined system of ONFs and cold atoms can be viewed as a good candidate for developing quantum networks and other quantum technologies. This section presents a brief review of some of the important developments in this area to date.

Theoretical studies with the "atom-ONF" system is so prolific that it is only possible to cover some of the works here. In 2002, Patnaik *et al.* [20] proposed a configuration that utilises electromagnetically-induced transparency (EIT) in surrounding atoms or molecules to tailor a fibre mode propagating inside an ONF and coherently control its dispersion properties to drastically reduce the group velocity of the fibre mode. They calculated the group velocity of the modified fibre mode to be ≈ 44 m/sec using a specific EIT medium. In 2004, atom trapping and guiding with a subwavelength-diameter ONF was proposed by Balykin *et al.* [21] utilising the gradient force of a red-detuned evanescent field in the fundamental mode to balance the centrifugal force of an atom and, subsequently, a more robust two-colour evanescent light trap was proposed [22]. In 2005, Le Kien *et al.* calculated that up to 28% of the spontaneous emission from a caesium atom can be channelled through an ONF of diameter 400 nm [23]. In 2006, the scattering of an evanescent light field by a single caesium atom outside a nanofibre was investigated [24] and it was found that the transmittance of the field in the stationary regime can be reduced by up to 48%. It was identified that circularly polarised light confined in the fundamental mode of an ONF has a finite angular momentum, with both spin and orbital components, [25] which forces an atom outside the ONF to rotate around it with increasing angular momentum with time [26]. In 2008, the possibility of fibre-mediated superfluorescence was identified based on the calculations of the correlation functions of fluorescence from a multi-atom system into the guided modes of an ONF [27]. In the same year, evanescent field traps for atoms based on mode interference in ONFs were proposed [28, 29]. In 2009, the possibility of slowing down the guided light field along a nanofibre in a cold atomic sample via the process of EIT was investigated [30].

Following a different direction, Minogin and Nic Chormaic [31] studied the asymmetry in the frequency dependence of the spontaneous emission coupled into the guided mode of an ONF due to the influence of the van der Walls interaction between the atoms and the ONF surface. For 100-1000 nm diameter ONFs, the van der Waals red shift was shown to increase the red half-width of the spontaneous emission line by 10–30% while keeping the blue half-width of the spectral line unchanged. Russell *et al.* included the effect of Casimir–Polder into the model and found that this leads to a slight reduction in the red-shift of the peak position [32]. The asymmetry in the lineshape is more evident for atomic ensembles that are tightly confined around the ONF. The curvature of the surface has also a significant effect on the van der Waals interaction of a neutral atom [33, 34].

Le Kien and Hakuta studied the motion of an atom in a weakly driven fibre-Bragg-grating cavity formed on an ONF in 2010 [35] and investigated the controlled production of entangled guided photons with a single atom in a nanofibre cavity in 2011 [36]. In 2013, Le Kien *et al.* [37] studied the quantum dynamics of an atom orbiting around an ONF and showed that the atomic centre-of-mass motion exhibits genuine quantum effects like collapse and revival of the atomic wave packet. Also, Masalov and Minogin [38] analysed the pumping efficiency of the higher-order modes of an ONF by laser-excited atoms. In 2014, the anisotropy in scattering of light from an atom into the guided modes of a ONF was studied [39]. It was found that the rate of scattering of guided light from the atom in the steady-state regime into the guided modes is asymmetric with respect to the forward and backward directions and depends on the polarisation of the probe field. Later, an ONF based atom trap for cold neutral atoms created by combining fictitious and real magnetic fields was proposed [40].

Experimental investigations with laser-cooled atoms and ONF systems in the early stage were conducted by the Tokyo, Cork/Okinawa and Bonn/Vienna groups. In 2007, Nayak *et al.* [41] experimentally demonstrated efficient coupling of atomic fluorescence to the guided mode of an ONF by overlapping a cold atom cloud of Cs-atoms with the ONF. Light-induced dipole forces and the van der Waals interaction in a similar system were observed by Sagué *et al.* [42] using high resolution spectroscopy. In 2008, a Hanbury-Brown and Twiss experiment was performed by the Tokyo team [13] with the fluorescence light being collected through an ONF. The effective number of atoms in the vicinity of the ONF was much less than one and the splitting of the excitation spectrum into two peaks was observed. The separation was smaller than the natural linewidth. In 2009, the group in Cork used an ONF to measure characteristics of a magneto-optical

trap (MOT) for cold Rb atoms by monitoring the fluorescence coupling to the ONF [43]. The shape and size of the atom cloud was determined by translating the cold atom cloud across the ONF. In 2010, Das *et al.* [44] measured the fluorescence emission spectrum of a few atoms using an ONF combined with optical heterodyne and photon correlation spectroscopy and observed the Mollow triplet spectrum of atoms at high excitation intensity. In the same year, a major advance was made when a fibre-based atom trap was realised by the Vienna team [45]. This created a one-dimensional optical lattice of atoms about 200 nm above the nanofibre surface. In 2012, sub-Doppler temperatures of laser-cooled atoms were measured by Russell *et al.* [46] utilising a forced oscillations technique with fluorescence detection through an ONF. Further, the group also implemented a release-recapture technique for the temperature measurement of cold atoms using an ONF [47]. The backscattering properties of an array of atoms coupled to an ONF in the strongly nonparaxial regime was investigated by Reitz *et al.* [48]. The authors observed that the power and the polarisation of the backscattered light may depend on the nanofibre-guided excitation field. More recently, the interaction of higher-order modes of an ONF with cold atoms was investigated, which is a part of this thesis. Atomic fluorescence coupling through the waist and the absorption of a probe beam through a few-mode ONF were studied to demonstrate more interactions for the light propagating in the higher-order modes than in the fundamental mode for the few-mode ONF [49]. Four-wave mixing phenomena and the ac-Stark effect have been observed in cold atoms at ultra-low power level ($\sim$ nW) using an ONF as an excitation and detection tool simultaneously [50], which is again part of this thesis work. Sayrin *et al.* [51] and Gouraud *et al.* [52] observed the EIT phenomenon in a Λ-type system with laser-cooled caesium atoms and slowed down the light propagating in the guided mode of ONFs demonstrating the potential of an ONF-cold atom based system. We also observed a multi-peak EIT phenomenon in a ladder type system with laser-cooled rubidium atoms and demonstrated all-optical-switching, as described later in the thesis.

Other groups have focussed on integration of ONFs in atomic vapours [53–60].

1.2 Thesis Outline

The aim of the work in this thesis was to investigate some of the nonlinear optics phenomena with ONFs. In particular, the ac-Stark effect (Autler-Townes splitting

[61]) and electromagnetically-induced transparency (EIT) [62] were investigated. These can be generated in the medium surrounding the ONF by sending light though it. The required power for the observation of these effects with an ONF is a few orders of magnitude lower than that in free space experiments due to strong confinement of the guided field in the transverse direction. The interaction of atoms with the different modes of the ONF is also investigated.

Chapter 2 describes the propagation of light through an ONF using the electromagnetic theory of light and presents the method we use for fabricating ONFs. Chapter 3 provides an introduction to light-matter interactions starting with the two level approximation of an atom, followed by a discussion for three-level systems, mainly focussing on the Autler-Townes splitting of an energy level and EIT. The experiments are done with cold ^{87}Rb atoms and Chapter 4 presents the theory of laser cooling of atoms in a magneto-optical trap and describes the details of the experimental setup for the formation of a cold atom cloud around the waist of an ONF. Preliminary experiments with the system, which include the measurement of the temperature of the cloud via two different methods based on fluorescence and absorption detection through an ONF, are presented in Chapter 5. Chapter 6 describes frequency up-conversion in cold atoms by a four-wave mixing process at ultra-low powers and the observation of Autler-Townes splitting of an optical transition in ^{87}Rb atoms. In Chapter 7, the observation of EIT is presented and all-optical switching with both the control and probe beams passing through an ONF overlapping on a cold atom ensemble is shown. Chapter 8 presents experiments with an ONF supporting the first higher-order mode group and reports on the first integration of higher-order modes of an ONF with cold atoms. A conclusion to the work and future prospects are given in Chapter 9. An appendix presents some related works, such as, the temperature measurements of cold atoms and sensing a dark-MOT with an ONF.

Chapter 2

Optical Nanofibres: Light Propagation and Fabrication

In order to discuss light propagation in optical nanofibres (ONFs), one should first consider the more general case of standard optical fibres. Optical fibres are one of the most common types of optical waveguides. They are widely used in communications for transferring data using light. For example, a transatlantic telecommunications cable connects one side of the Atlantic Ocean to the other. These cables consist of bundles of optical fibres carrying digital data, which includes telephone and internet data traffic. Optical fibres are made of extremely pure glass (or plastic), which is transparent over a wide range of wavelengths, offering a high bandwidth of data transfer encoded in light. Usually, these optical fibres are comparable in diameter to a human hair ($\sim$100 μm) and offer light transmission at different wavelengths simultaneously. The light is guided down the centre of the fibre, called the "core", which is surrounded by a "cladding" region, as illustrated in Fig. 2.1. The refractive index of the cladding is kept lower than that of the core in order to facilitate total internal reflection of the light being guided in the core.

2.1 Propagation of Light in Optical Fibres

Light is an electromagnetic wave and, hence, the propagation of light can be described using Maxwell's equations [63] given as

$$\nabla \times \mathbf{H} = \frac{\partial \mathbf{D}}{\partial t} \tag{2.1}$$

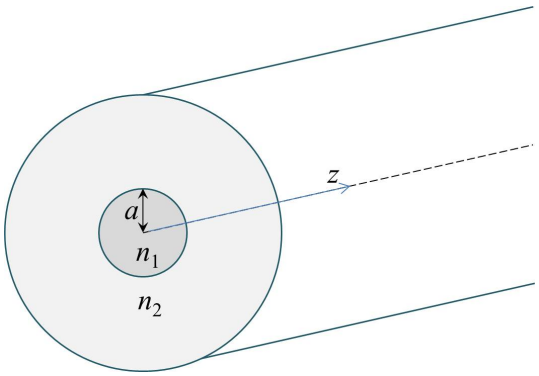


Figure 2.1: Illustration of an optical fibre. The central region is the 'core' of the fibre with a refractive index n_1 and radius a. This is surrounded by the 'cladding' with a refractive index n_2, with $n_1 > n_2$. The cladding region is assumed to extend to infinity for the derivation of the equations describing light propagation in an optical fibre.

and

$$\nabla \times \mathbf{E} = -\frac{\partial \mathbf{B}}{\partial t}, \tag{2.2}$$

where $\mathbf{H}$ is the magnetic field intensity vector, $\mathbf{D}$ is the electric displacement vector, $\mathbf{E}$ is the electric field intensity vector and $\mathbf{B}$ is the magnetic flux density vector. The current term is neglected in Eq. 2.1 which means the generation of light by current is neglected, as is generally the case.

For a linear, isotropic medium

$$\mathbf{D} = \varepsilon \mathbf{E}, \tag{2.3}$$

where ε is the dielectric permittivity. For a nonmagnetic material

$$\mathbf{B} = \mu \mathbf{H}, \tag{2.4}$$

where μ is the magnetic permeability.

In the absence of electric charge, we have that

$$\nabla \cdot \mathbf{D} = 0 \tag{2.5}$$

and, the magnetic induction vector always obeys the relation

$$\nabla \cdot \mathbf{B} = 0. \tag{2.6}$$

Thus, in the absence of currents and charges, an electromagnetic field in a linear, isotropic medium is completely described by Eqs. 2.1 - 2.6. Substituting Eq. 2.4

into Eq. 2.2 and taking the curl we get

$$\nabla \times (\nabla \times \mathbf{E}) = -\mu \frac{\partial}{\partial t}(\nabla \times \ \mathbf{H}). \tag{2.7}$$

Substituting Eqs. 2.1 and 2.3 into Eq. 2.7 gives

$$\nabla \times (\nabla \times \mathbf{E}) + \varepsilon\mu \frac{\partial^2 \mathbf{E}}{\partial t^2} = 0. \tag{2.8}$$

Using Eqs. 2.2 and 2.3 and the vector identity, $\nabla \times (\nabla \times \mathbf{E}) = \nabla(\nabla \cdot \mathbf{E}) - \nabla^2\mathbf{E}$, Eq. 2.8 can be rewritten as

$$\nabla^2 \mathbf{E} + \nabla[\mathbf{E} \cdot \frac{\nabla \varepsilon}{\varepsilon}] = \varepsilon\mu \frac{\partial^2 \mathbf{E}}{\partial t^2}. \tag{2.9}$$

For a medium with a constant ε, the gradient of ε vanishes and Eq. 2.9 assumes the form of the wave equation where

$$\nabla^2 \mathbf{E} = \varepsilon\mu \frac{\partial^2 \mathbf{E}}{\partial t^2}. \tag{2.10}$$

This satisfies the scalar wave function for each component of the electric field such that

$$\nabla^2 E_i = \frac{1}{v_c^2} \frac{\partial^2 E_i}{\partial t^2}, \tag{2.11}$$

where $v_c = 1/\sqrt{\varepsilon\mu}$ is the velocity of light in the medium.

Similarly, using Eq. 2.1, we can obtain an equation similar to Eq. 2.10 for the magnetic field such that

$$\nabla^2 \mathbf{H} = \varepsilon\mu \frac{\partial^2 \mathbf{H}}{\partial t^2}. \tag{2.12}$$

We shall always assume μ to be a constant; however, for a real waveguide, ε may depend on the space coordinates. Let us assume a cylindrical waveguide, i.e. an optical fibre, with its main axis along the z-direction and cross-section on the x-y plane. In this case, the dielectric constant, ε, does not depend on z and can be taken as a constant in this direction. Mode propagation along the fibre is described by

$$\mathbf{E} = \mathbf{E}_0(x, y)e^{i(\omega t - \beta z)} \tag{2.13}$$

$$\text{and } \mathbf{H} = \mathbf{H}_0(x, y)e^{i(\omega t - \beta z)}, \tag{2.14}$$

where ω is the angular frequency and β is the propagation constant.

Substituting these equations in to Eqs. 2.1 and 2.2 and using Eqs. 2.3 and 2.4,

we get the following set of equations [63]:

$$\frac{\partial H_z}{\partial y} + i\beta H_y = i\omega\varepsilon E_x, \tag{2.15}$$

$$-i\beta H_x - \frac{\partial H_z}{\partial x} = i\omega, \varepsilon E_y \tag{2.16}$$

$$\frac{\partial H_y}{\partial y} - \frac{\partial H_x}{\partial y} = i\omega\varepsilon E_z, \tag{2.17}$$

$$\frac{\partial E_z}{\partial y} + i\beta E_y = -i\omega\mu H_x, \tag{2.18}$$

$$i\beta E_x + \frac{\partial E_z}{\partial x} = i\omega\mu H_y, \tag{2.19}$$

$$\frac{\partial E_y}{\partial x} - \frac{\partial E_x}{\partial y} = -i\omega\mu H_z. \tag{2.20}$$

The transverse field components can be expressed in terms of E_z and H_z, with the help of Eqs. 2.15, 2.16, 2.18 and 2.19, as

$$E_x = -\left(\frac{i}{\kappa}\right)\left(\beta\frac{\partial E_z}{\partial x} + \omega\mu\frac{\partial H_z}{\partial y}\right), \tag{2.21}$$

$$E_y = -\left(\frac{i}{\kappa^2}\right)\left(\beta\frac{\partial E_z}{\partial y} - \omega\mu\frac{\partial H_z}{\partial x}\right), \tag{2.22}$$

$$H_x = -\left(\frac{i}{\kappa^2}\right)\left(\beta\frac{\partial H_z}{\partial x} - \omega\varepsilon\frac{\partial E_z}{\partial y}\right), \tag{2.23}$$

$$H_y = -\left(\frac{i}{\kappa^2}\right)\left(\beta\frac{\partial H_z}{\partial y} + \omega\varepsilon\frac{\partial E_z}{\partial x}\right), \tag{2.24}$$

where $\kappa^2 = k^2 - \beta^2$ and $k^2 = \omega^2\varepsilon\mu$. Replacing H_y, H_x, E_y and E_x in Eqs. 2.17 and 2.20, the wave equations for the z-components are

$$\frac{\partial^2 E_z}{\partial x^2} + \frac{\partial^2 E_z}{\partial y^2} + \kappa^2 E_z = 0 \tag{2.25}$$

and

$$\frac{\partial^2 H_z}{\partial x^2} + \frac{\partial^2 H_z}{\partial y^2} + \kappa^2 H_z = 0. \tag{2.26}$$

Eqs. 2.21−2.24 are exact, but Eqs. 2.25 and 2.26 are exact only for a constant value of ε. However, these are correct in the present situation as they are only applied in regions of the fibre with homogeneous refractive indices.

Eqs. 2.21−2.26 can be rewritten in cylindrical coordinates (r, ϕ, z) as [63]

$$E_r = -\left(\frac{i}{\kappa}\right)\left(\beta\frac{\partial E_z}{\partial r} + \omega\mu\frac{1}{r}\frac{\partial H_z}{\partial \phi}\right), \tag{2.27}$$

$$E_\phi = -\left(\frac{i}{\kappa^2}\right)\left(\beta\frac{1}{r}\frac{\partial E_z}{\partial \phi} - \omega\mu\frac{\partial H_z}{\partial r}\right), \tag{2.28}$$

$$H_r = -\left(\frac{i}{\kappa^2}\right)\left(\beta\frac{\partial H_z}{\partial r} - \omega\varepsilon\frac{1}{r}\frac{\partial E_z}{\partial \phi}\right), \tag{2.29}$$

$$H_\phi = -\left(\frac{i}{\kappa^2}\right)\left(\beta\frac{1}{r}\frac{\partial H_z}{\partial \phi} + \omega\varepsilon\frac{\partial E_z}{\partial r}\right), \tag{2.30}$$

$$\frac{\partial^2 E_z}{\partial r^2} + \frac{1}{r}\frac{\partial E_z}{\partial r} + \frac{1}{r^2}\frac{\partial^2 E_z}{\partial \phi^2} + \kappa^2 E_z = 0, \tag{2.31}$$

$$\frac{\partial^2 H_z}{\partial r^2} + \frac{1}{r}\frac{\partial H_z}{\partial r} + \frac{1}{r^2}\frac{\partial^2 H_z}{\partial \phi^2} + \kappa^2 H_z = 0, \tag{2.32}$$

with the axial components of the fields given by

$$E_z(r, \phi, z, t) = E_z(r, \phi)e^{i(\omega t - \beta z)} \tag{2.33}$$

$$H_z(r, \phi, z, t) = H_z(r, \phi)e^{i(\omega t - \beta z)}. \tag{2.34}$$

Equation 2.31 is separable with a solution of the form

$$E_z(r, \phi) = R(r)e^{il\phi}, \tag{2.35}$$

where l must be a positive or negative integer or zero to ensure that the field is periodic in ϕ with a period of 2π. Substituting Eq. 2.35 into Eq. 2.31 yields

$$\left(\frac{\partial^2}{\partial r^2} + \frac{1}{r}\frac{\partial}{\partial r} + \frac{1}{r^2}\frac{\partial^2}{\partial \phi^2} + \kappa^2 - \frac{l^2}{r^2}\right)R(r) = 0, \tag{2.36}$$

which is a differential equation for Bessel functions with a general solution depending on the sign of κ^2. If $\kappa^2 > 0$, the general solution of Eq. 2.36 is [64]

$$R(r) = CJ_l(\kappa r) + DY_l(\kappa r), \tag{2.37}$$

where $J_l(\kappa r)$ and $Y_l(\kappa r)$ are Bessel functions of the first and second kind, respectively, and, C and D are constants. The Bessel functions are oscillatory functions

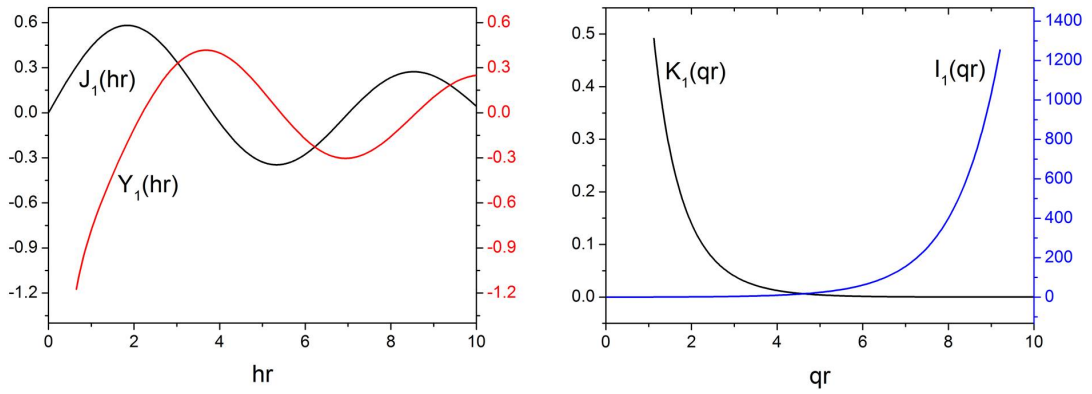


Figure 2.2: Left: Plot of the first order Bessel functions of the first and second kind. Right: Plot of the first order modified Bessel functions of the first and second kind.

of r as shown in Fig. 2.2 (left). If $\kappa^2 < 0$, the general solution of Eq. 2.36 is

$$R(r) = QI_l(|\kappa|r) + PK_l(|\kappa|r), \tag{2.38}$$

where $I_l(|\kappa|r)$ and $K_l(|\kappa|r)$ are the modified Bessel functions of the first and the second kind, respectively, and Q and P are constants. These are monotonically increasing and decreasing functions of r as shown in Fig. 2.2 (right). Since Y_l is singular at $r = 0$ and I_l diverges as $r \to \infty$, we reject these two as physically unreasonable. Thus, Eqs. 2.37 and 2.38 become

$$R(r) = CJ_l(\kappa r), \text{ for } \kappa^2 > 0 \tag{2.39}$$

$$R(r) = PK_l(|\kappa|r), \text{ for } \kappa^2 < 0, \tag{2.40}$$

for an optical fibre guiding energy with the refractive indices of the core and the cladding being n_1 and n_2, respectively, with $n_1 > n_2$. If k_0 is the free space wavenumber, the wavenumber in the core $k_1 = n_1 k_0$ and in the cladding $k_2 = n_2 k_0$. For bound rays, i.e. lossless modes confined to the core [65],

$$k_2 < \beta < k_1. \tag{2.41}$$

The closer β approaches k_1 the more confined are the fields to the core of the fibre, while for β approaching k_2 they penetrate far into the cladding. In the core, $k^2 > \beta^2$, i.e. $\kappa^2 > 0$, and we define

$$\kappa = h = \sqrt{k_1^2 - \beta^2} = \sqrt{n_1^2 k_0^2 - \beta^2} \tag{2.42}$$

and in the cladding, $k^2 > \beta^2$, i.e. $\kappa^2 > 0$, with

$$|\kappa| = q = \sqrt{\beta^2 - k_2^2} = \sqrt{\beta^2 - n_2^2 k_0^2}. \tag{2.43}$$

Now, using Eqs. 2.33, 2.35, 2.39 and 2.42, we can write the electric field component of the field inside the core as

$$E_z(r, \phi, z, t) = CJ_l(hr)e^{i(\omega t - \beta z + l\phi)} \tag{2.44}$$

and, using Eqs. 2.33, 2.35, 2.40 and 2.43, we can write the electric field component of the field outside the core as

$$E_z(r, \phi, z, t) = PK_l(qr)e^{i(\omega t - \beta z + l\phi)}. \tag{2.45}$$

Similarly, the magnetic field component of the field inside the core can be written as

$$H_z(r, \phi, z, t) = AJ_l(hr)e^{i(\omega t - \beta z + l\phi)} \tag{2.46}$$

and outside the core as

$$H_z(r, \phi, z, t) = BK_l(qr)e^{i(\omega t - \beta z + l\phi)}. \tag{2.47}$$

Thus, we are now able to write the field inside and outside the core using Eqs. 2.27−2.30 and 2.44−2.47. Considering the radius of the fibre to be a we have [63],

for $r < a$,

$$\begin{aligned}
E_r(r, \phi, z, t) &= -\frac{i}{h^2}[\beta h C J_l'(hr) + i\omega\mu_0 \frac{l}{r} A J_l(hr)]e^{i(\omega t - \beta z + l\phi)} \\
E_\phi(r, \phi, z, t) &= -\frac{i}{h^2}[i\beta \frac{l}{r} C J_l(hr) - h\omega\mu_0 A J_l'(hr)]e^{i(\omega t - \beta z + l\phi)} \\
E_z(r, \phi, z, t) &= CJ_l(hr)e^{i(\omega t - \beta z + l\phi)} \\
H_r(r, \phi, z, t) &= -\frac{i}{h^2}[-i\omega\varepsilon_1 \frac{l}{r} C J_l(hr) + h\beta A J_l'(hr)]e^{i(\omega t - \beta z + l\phi)} \\
H_\phi(r, \phi, z, t) &= -\frac{i}{h^2}[h\omega\varepsilon_1 C J_l'(hr) + i\beta \frac{l}{r} A J_l(hr)]e^{i(\omega t - \beta z + l\phi)} \\
H_z(r, \phi, z, t) &= AJ_l(hr)e^{i(\omega t - \beta z + l\phi)}
\end{aligned} \tag{2.48}$$

where $J_l'(hr) = J_l(hr)/hr$ and $\varepsilon_1 = n_1^2\varepsilon_0$ is the dielectric constant of the core,

and

for $r > a$,

$$\begin{aligned}
E_r(r,\phi,z,t) &= \frac{i}{q^2}[\beta q P K_l'(qr) + i\omega\mu_0 \frac{l}{r} B K_l(qr)] e^{i(\omega t - \beta z + l\phi)} \\
E_\phi(r,\phi,z,t) &= \frac{i}{q^2}[i\beta \frac{l}{r} P K_l(qr) - q\omega\mu_0 B K_l'(qr)] e^{i(\omega t - \beta z + l\phi)} \\
E_z(r,\phi,z,t) &= P K_l(qr) e^{i(\omega t - \beta z + l\phi)} \\
H_r(r,\phi,z,t) &= \frac{i}{q^2}[-i\omega\varepsilon_2 \frac{l}{r} P K_l(qr) + q\beta B K_l'(qr)] e^{i(\omega t - \beta z + l\phi)} \\
H_\phi(r,\phi,z,t) &= \frac{i}{q^2}[q\omega\varepsilon_2 P K_l'(qr) + i\beta \frac{l}{r} B K_l(qr)] e^{i(\omega t - \beta z + l\phi)} \\
H_z(r,\phi,z,t) &= B K_l(qr) e^{i(\omega t - \beta z + l\phi)}
\end{aligned} \tag{2.49}$$

where $K_l'(qr) = \dfrac{K_l(qr)}{qr}$ and $\varepsilon_2 = n_2^2\varepsilon_0$ is the dielectric constant of the medium surrounding the core. The constants C, P, A and B can be determined by the boundary conditions. Eqs. 2.48 and 2.49 are solutions of Maxwell's equations, but in order to describe the modes of a fibre they must satisfy boundary conditions at the core-cladding interface, i.e. at $r = a$. Equating the tangential components, E_z, E_ϕ, H_z and H_ϕ at $r = a$, yields a set of four equations,

$$\begin{aligned}
J_l(ha)C - K_l(qa)P &= 0 \\
\frac{i\beta l}{h^2 a} J_l(ha)C - \frac{\omega\mu_0}{h} J_l'(ha)A + \frac{i\beta l}{q^2 a} K_l(qa)P - \frac{\omega\mu_0}{q} K_l'(qa)B &= 0 \\
A J_l(ha) - K_l(qa)B &= 0 \\
\frac{\omega\varepsilon_1}{h} J_l'(ha)C + \frac{i\beta l}{h^2 a} J_l(ha)A + \frac{\omega\varepsilon_2}{q} K_l'(qa)P + \frac{i\beta l}{q^2 a} K_l(qa)B &= 0.
\end{aligned} \tag{2.50}$$

The set of homogeneous equations described by Eq. 2.50 can have solutions only if the determinant of the equation system vanishes. The condition for the determinant to be zero is called the eigenvalue equation and is given by [66]

$$\begin{aligned}
\left(\frac{J_l'(ha)}{haJ_l(ha)} + \frac{K_l'(qa)}{qaK_l(qa)}\right)\left(\frac{J_l'(ha)}{haJ_l(ha)} + \frac{n_2^2 K_l'(qa)}{n_1^2 qaK_l(qa)}\right) = \\
l^2\left(\frac{\beta}{kn_1}\right)^2\left[\left(\frac{1}{ha}\right)^2 + \left(\frac{1}{qa}\right)^2\right]^2
\end{aligned} \tag{2.51}$$

for the HE_{lm} and EH_{lm} hybrid modes. Each of the eigenvalues, β, obtained from this equation describes a propagation mode of the fibre. Taking appropriate components of the fields to be zero (e.g. $H_z = 0$ for the TM modes) and using

the identities $J_0'(ha) = -J_1(ha)$ and $K_0'(qa) = -K_1(qa)$, Eq. 2.51 yields

$$\frac{J_1(ha)}{haJ_0(ha)} + \frac{K_1(qa)}{qaK_0(qa)} = 0 \tag{2.52}$$

for the TE_{0m} modes, and

$$\frac{J_1(ha)}{haJ_0(ha)} + \frac{n_2^2}{n_1^2}\frac{K_1(qa)}{qaK_0(qa)} = 0 \tag{2.53}$$

for the TM_{0m} modes.

Usually, for optical fibres used for light transmission, the core and cladding refractive indices are very close to each other (around less than 1% difference) such that $n_1 - n_2 \ll 1$. Hence, for such fibres a weakly guiding approximation can be used [67]. However, we shall refrain from using this approximation as it is not valid for an optical nanofibre, one of the main considerations in this thesis.

2.2 Modes of an Optical Nanofibre

Optical nanofibres (ONFs) [68] are sub-wavelength diameter optical fibres, i.e the core diameter of an ONF is usually less than the wavelength of light. For the preparation of an ONF, usually a silica (SiO_2) optical fibre is tapered down to submicron diameter. In this condition, the core of the fibre becomes negligibly small and the material of the ONF can be taken as the cladding material of the optical fibre. Thus, for an ONF in air/vacuum the core has the refractive index of glass (i.e. $n_1 \approx 1.46$), whereas the cladding has the refractive index of air/vacuum, $n_2 = 1$. All the equations described in the previous section are valid for ONFs as well. The V-parameter, often called the V-number, describes the number of modes an optical fibre can support. The V-number is given by

$$V = k_0 a\sqrt{n_1^2 - n_2^2}, \tag{2.54}$$

where $k_0 (= 2\pi/\lambda_0)$ is the free space wavenumber, λ_0 is the wavelength and a is the radius of the core. For an ONF in vacuum Eq. 2.54 becomes

$$V = \frac{\pi}{\lambda_0} d\sqrt{n_1^2 - 1}, \tag{2.55}$$

where n_1 is the refractive of the nanofibre material (SiO_2) and d is the diameter of the ONF. Using this relation we can find the cut-off diameter for ONFs for

various modes at a specified wavelength.

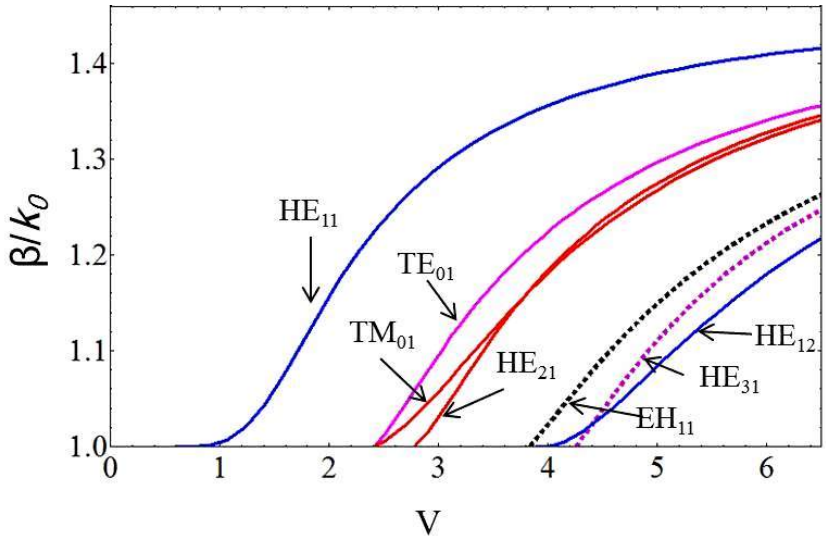


Figure 2.3: The propagation constant, β, normalised over the free space wavenumber, k_0, with respect to the V-number for a vacuum silica ONF. β/k_0 is also known as the effective refractive index. This graph can be used to identify which modes are supported at any specific V-number. The LP_{01} fibre mode corresponds to the HE_{11} true mode and the LP_{11} mode corresponds to the TE_{01}, TM_{01} and $HE_{21e,o}$ modes in an ONF. The decomposition of the LP_{11} mode into the three true modes is clearly evident in case of an ONF due to high difference in the core and cladding refractive indices. [This graph is prepared by Aili Maimati.]

The ratio of the propagation constant, β, of the guided modes to the free space wavenumber, k_0, can be plotted as a function of the V-number using Eq. 2.51 (see Fig. 2.3). For $V < 2.405$, only the HE_{11} mode, called the fundamental mode, can propagate. Such fibres are known as single-mode fibres. The single mode cut-off diameter of a silica ONF for 780 nm light is ~564 nm (calculated for $n_1 = 1.456$), which means that an ONF with a diameter less than this should only permit the fundamental mode to propagate.

2.2.1 Fundamental mode

The eigenvalue equation (Eq. 2.51) for the fundamental mode, HE_{11}, leads to [68]

$$\frac{J_0(ha)}{haJ_1(ha)} = -\left(\frac{n_1^2+n_2^2}{2n_1^2}\right)\frac{K_1'(qa)}{qaK_1(qa)} + \frac{1}{h^2a^2} - \left[\left(\frac{n_1^2-n_2^2}{2n_1^2}\right)^2\left(\frac{K_1'(qa)}{qaK_1(qa)}\right)^2 + \left(\frac{\beta}{n_1k}\right)^2\left(\frac{1}{h^2a^2}+\frac{1}{q^2a^2}\right)^2\right]^{1/2}, \tag{2.56}$$

which should be used to find the propagation constant. Assuming a silica core ($n_1 = 1.456$) and a vacuum clad ($n_2 = 1$) ONF with a diameter of 350 nm ($a = 175$ nm) and a wavelength of 780 nm, we get $ha = 1.41034$, $qa = 0.486324$ and $\beta a = 1.49122$. 780 nm wavelength is chosen as it corresponds to the 5 $S_{1/2} \rightarrow$ 5 P $_{3/2}$ transition lines of Rb. The V-number in this case is 1.492.

The components of the electric field, **E**, for the fundamental mode are given by [15]

$$\left.\begin{aligned} E_x &= -iS\frac{\beta}{2h}\left[(1-s)J_0(hr)\cos\phi_0 - (1+s)J_2(hr)\cos(2\phi-\phi_0)\right]e^{i(\omega t-\beta z)} \\ E_y &= -iS\frac{\beta}{2h}\left[(1-s)J_0(hr)\sin\phi_0 - (1+s)J_2(hr)\sin(2\phi-\phi_0)\right]e^{i(\omega t-\beta z)} \\ E_z &= SJ_1(hr)\cos(\phi-\phi_0)e^{i(\omega t-\beta z)}, \end{aligned}\right\} \tag{2.57}$$

for $r < a$ and by

$$\left.\begin{aligned} E_x &= -iS\frac{\beta}{2q}\frac{J_1(ha)}{K_1(qa)}\left[(1-s)K_0(hr)\cos\phi_0 - (1+s)K_2(hr)\cos(2\phi-\phi_0)\right]e^{i(\omega t-\beta z)} \\ E_y &= -iS\frac{\beta}{2q}\frac{J_1(ha)}{K_1(qa)}\left[(1-s)K_0(hr)\sin\phi_0 - (1+s)K_2(hr)\sin(2\phi-\phi_0)\right]e^{i(\omega t-\beta z)} \\ E_z &= S\frac{J_1(ha)}{K_1(qa)}K_1(qr)\cos(\phi-\phi_0)e^{i(\omega t-\beta z)}, \end{aligned}\right\} \tag{2.58}$$

for $r > a$, where S is a normalisation constant, ϕ_0 determines the orientation of the polarisation of the field and $s = \left(\frac{1}{h^2a^2} + \frac{1}{q^2a^2}\right) / \left(\frac{J_1'(ha)}{haJ_1(ha)} + \frac{K_1'(qa)}{qaK_1(qa)}\right)$.

From Eq. 2.57, the intensity is given by [15]

$$\begin{aligned} |\boldsymbol{E}|^2 = g_{in}\{&J_0^2(hr) + uJ_1^2(hr) + fJ_2^2(hr) + \\ &[uJ_1^2(hr) - f_pJ_0(hr)J_2(hr)]\cos[2(\phi-\phi_0)]\}, \text{ for } r < a \end{aligned} \tag{2.59}$$

$$\begin{aligned} |\boldsymbol{E}|^2 = g_{out}\{&K_0^2(qr) + wK_1^2(qr) + fK_2^2(qr) + \\ &[wK_1^2(qr) + f_pK_0(qr)K_2(qr)]\cos[2(\phi-\phi_0)]\}, \text{ for } r > a \end{aligned} \tag{2.60}$$

where $u = \frac{2h^2}{\beta^2(1-s)^2}, w = \frac{2q^2}{\beta^2(1-s)^2}, f = \frac{(1+s)^2}{(1-s)^2}$ and $f_p = \frac{2(1+s)}{(1-s)}$.

For an ONF, the HE_{11} mode profile could be significantly different than the LP_{01} mode. Fig. 2.4 shows the intensity profile of this mode for quasi-linearly polarised light (it is said to be 'quasi'-linear as the light at the ONF waist is not completely linear). It can be seen that the mode profile is not cylindrically symmetric, unlike

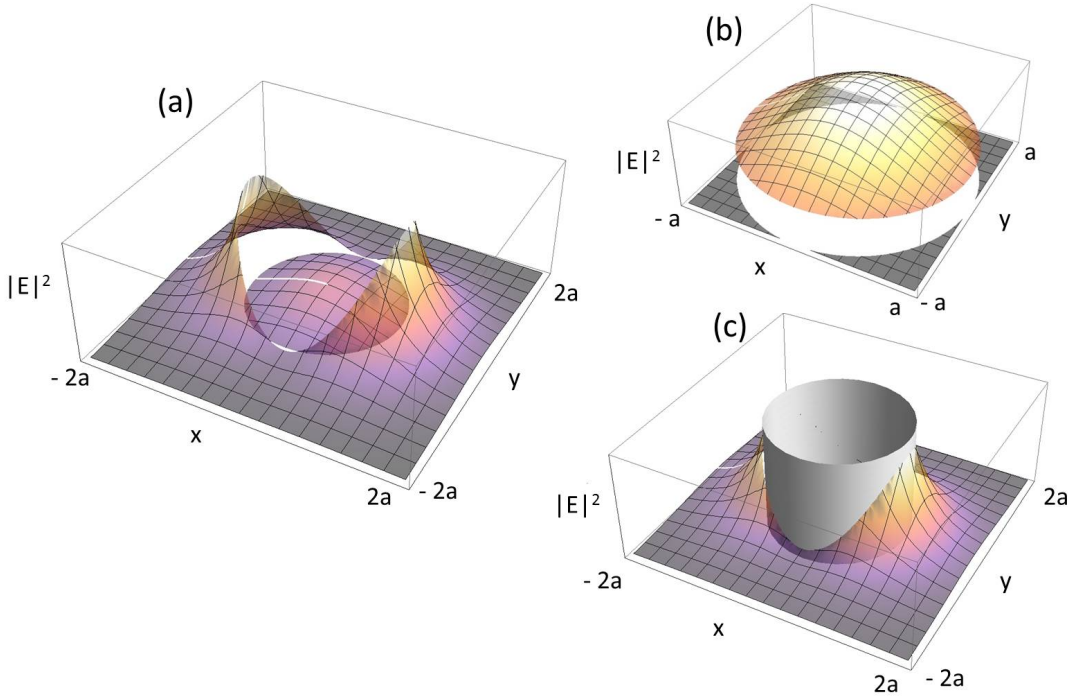


Figure 2.4: (a) Intensity profile at a nanofibre cross-section for quasi-linearly polarised 780 nm light passing through an ONF with diameter 350 nm. (b) Intensity profile in the ONF core. (c) Intensity profile outside the ONF core. The gray cylinder represents the ONF.

the case with the LP_{01} mode. However, for quasi-circularly polarised light, the pattern is almost cylindrically symmetric (see Fig. 2.5). The discontinuity of the field at the boundary is very evident due to the sudden large change in the refractive index at the ONF boundary. The evanescent field at the surface is very high and decays exponentially. This transversal confinement of the light around an ONF is one of its most important properties for the studies reported in this thesis.

2.2.2 First higher order fibre modes

By changing the diameter of an ONF, it is possible to have a desired number of modes propagating. For example, looking at Fig. 2.3, we can see that an ONF with V-number around 3 can support the TE_{01}, TM_{01} and $HE_{21}^{e,o}$ modes along with the fundamental mode. For 780 nm light, the diameter of the ONF corresponding to this V-number is ∼700 nm (using Eq. 2.55). The family of modes, TE_{01}, TM_{01} and $HE_{21}^{e,o}$, are referred to as the first group of higher order modes. In the LP mode approximation for a weakly guiding fibre these modes

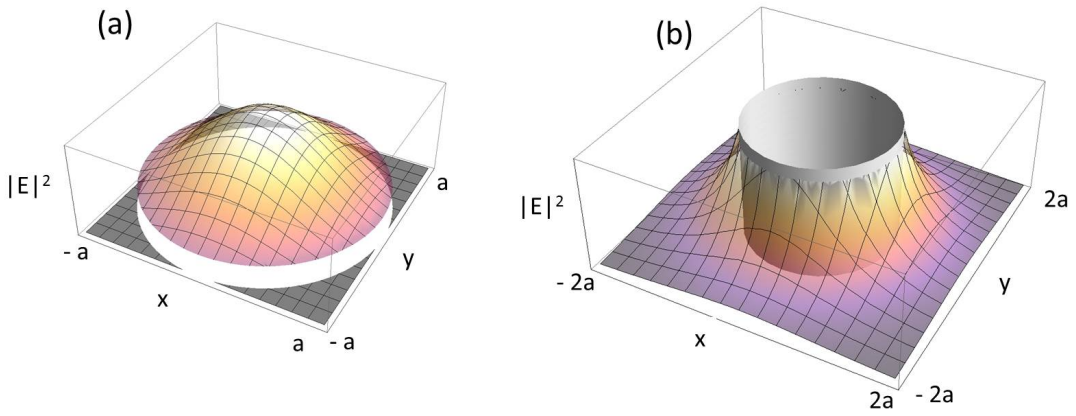


Figure 2.5: Intensity profile at a nanofibre cross-section for quasi-circularly polarised light: (a) inside the ONF core and (b) outside. All parameters are the same as in Fig. 2.4.

are not easily separable and are collectively referred to as LP_{11}. Propagation constants of the modes are defined by the eigenvalue equations, as usual, which are [38]

$$\frac{J_1(ha)}{haJ_0(ha)} = -\frac{K_1(qa)}{qaK_0(qa)} \text{ for the } TE_{01} \text{ mode,} \tag{2.61}$$

$$\frac{J_1(ha)}{haJ_0(ha)} = -\frac{n_2^2}{n_1^2}\frac{K_1(qa)}{qaK_0(qa)} \text{ for the } TM_{01} \text{ mode} \tag{2.62}$$

$$\text{and } \frac{J_1(ha)}{haJ_2(ha)} = -\left(\frac{n_1^2+n_2^2}{2n_1^2}\right)\frac{K_2'(qa)}{qaK_2(qa)} + \frac{2}{h^2a^2} - \left(\frac{n_1^2-n_2^2}{n_1^2}\right)\left[\left(\frac{K_2'(qa)}{2qaK_2(qa)}\right)^2 + \left(\frac{2n_1k\beta}{h^2q^2a^2}\right)^2\right]^{1/2} \tag{2.63}$$

for the HE_{21} mode.

The spatial distribution of intensities for these modes are shown in Fig. 2.6. Th peak light intensity for the fundamental mode in this case is higher in the core than outside, unlike in Fig. 2.4, as the diameter of the ONF in this case is double that of the previous case. However, the light propagating in the HE_{21} mode provides a higher intensity outside the core than inside. Effectively, for higher mode propagation, larger diameter ONFs are required compared to for single mode. We term such fibres few-mode ONFs (FM-ONFs) compared to the usual single-mode ONFs (SM-ONFs). Light in higher modes has some advantages over the fundamental mode, such as a larger spatial extension, higher intensity,

and the possibility of carrying orbital angular momentum [69], to name just a few.

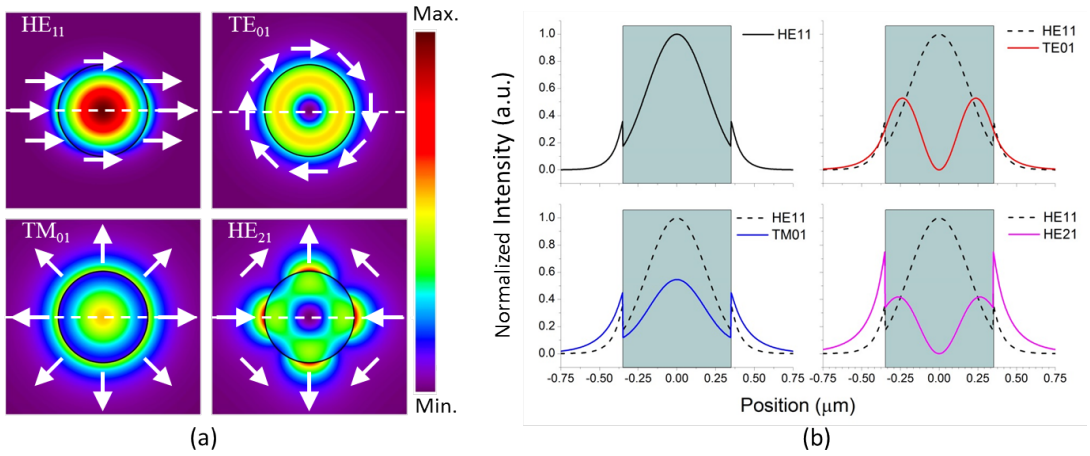


Figure 2.6: (a) Intensity distribution of 780 nm light for the first four modes (HE_{11}, TE_{01}, TM_{01}, and HE_{21}) of an ONF with diameter 700 nm. Refractive indices of the nanofibre material and the surrounding medium are taken as 1.456 and 1, respectively. Black circles denote the nanofibre boundary. Arrows denote the polarisation of the light fields. The amount of power in each mode is identical and the four plots are normalised to the maximum intensity in the HE_{11} mode. (b) Intensity profile along the white dashed line in (a) with the zero position at the fibre axis. The shaded region denotes the fibre. The intensities are normalised to the maximum intensity in the HE_{11} mode. The profile of the HE_{11} mode is plotted along with the other modes for ease of comparison. [These graphs are prepared by Kieran Deasy.]

2.3 Energy Flow

An important parameter to describe the flow of electromagnetic radiation in space is the power flow density vector, also known as the Poynting vector and given by

$$\mathbf{S} = \mathbf{E} \times \mathbf{H}. \tag{2.64}$$

The time averaged Poynting vector can be written as [64]

$$\overline{\mathbf{S}} = \frac{1}{2} [\mathbf{E} \times \mathbf{H}^*] \tag{2.65}$$

where $\mathbf{H}^*$ denotes the complex conjugate of $\mathbf{H}$. The factor 1/2 appears due to time averaging of the oscillating field. The real part of the function gives the physical time average power flow vector. Considering the components of the real part of the time averaged power flow vector in cylindrical coordinates as S_z, S_ϕ

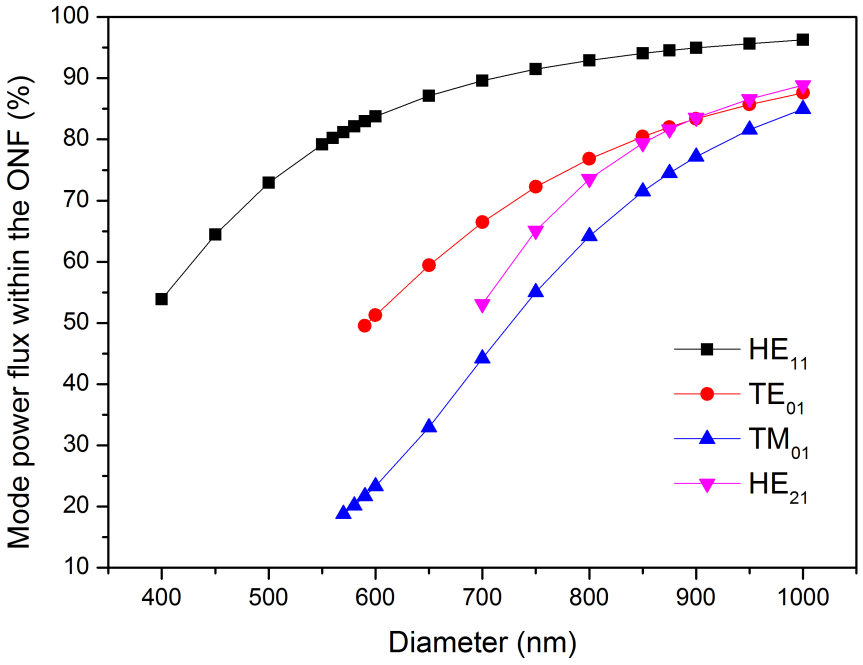


Figure 2.7: Mode power flux in the core of an ONF as a function of its diameter calculated using FIMMWAVE software for first four ONF modes and 780 nm light. [This graph is prepared by Kieran Deasy.]

and S_r, the guided mode S_r should always be zero. S_ϕ describes the energy flow that circulates around the fibre which could be substantial for nanofibres due to the non-zero longitudinal component of the field. The propagating power, P_z, is determined by the integral of S_z over the transverse plane of the fibre where

$$P_z = \int_0^{2\pi} d\phi \int_0^{\infty} r S_z dr. \tag{2.66}$$

The mode power flux in the core of an ONF can be calculated using Eq. 2.66 taking the integral limits for r from 0 to a. Fig. 2.7 shows the dependence of the power flux in the core on the diameter of the ONF. The percentage of the total flux inside the core is higher for larger diameters, i.e. the fraction of power flowing at the fibre surface outside its physical boundary is higher for smaller diameters. Hence, it is advantageous to keep the diameter small when a high intensity in the evanescent field is required.

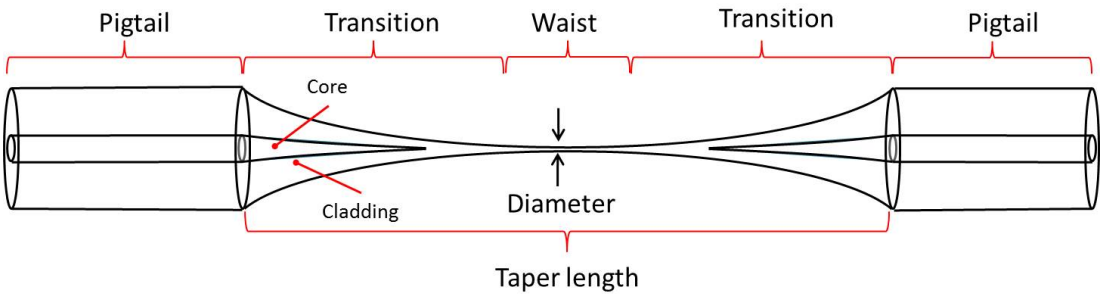


Figure 2.8: Illustration of an ONF. The taper length is typically around 5 - 8 cm which covers both the transition regions. In the transition region, the core and the cladding of the optical fibre get smaller and smaller to reach the waist diameter.

2.4 Fabrication of Optical nanofibres

There are various ways of fabricating ONFs including CO_2 laser [70], acid flow etching, [71], flame-brushing [72], direct drawing from bulk material [73], self-modulated taper-drawing [74] and electrospining [75]. ONFs used for the works described in this thesis are prepared by a "heat-and-pull" technique [76]. Unjacketed, standard optical fibre is heated to a temperature between 1200°C - 1500°C, to be above the annealing temperature of silica so that its viscosity is lowered sufficiently to allow deformation, while remaining below the softening temperature so that the glass does not sag under its own weight, and pulled simultaneously at each end using computer controlled motors. This pulling results in tapering of the original fibre (with typical diameters of the core and cladding being in the range of 125-250 μm and 4-10 μm, respectively) and provides an ONF with a waist region of sub-micron diameter (Fig. 2.8). At the waist of the ONF, the core of the original fibre almost vanishes and, hence, the waist of an ONF is considered to be made from the cladding material of the non-tapered optical fibre used to prepare it. In the experiments reported here, we typically used ONFs with waists in the 350-700 nm range.

2.4.1 Adiabatic criterion

ONFs should be prepared in a manner that will ensure that they have high transmission of light from one end to the other. This requires the tapering process to be adiabatic [77], which means that there should be no coupling from the guided mode in consideration to other fibre (or cladding) modes. In case of deviation from adiabaticity, it is most likely that there will be coupling between modes

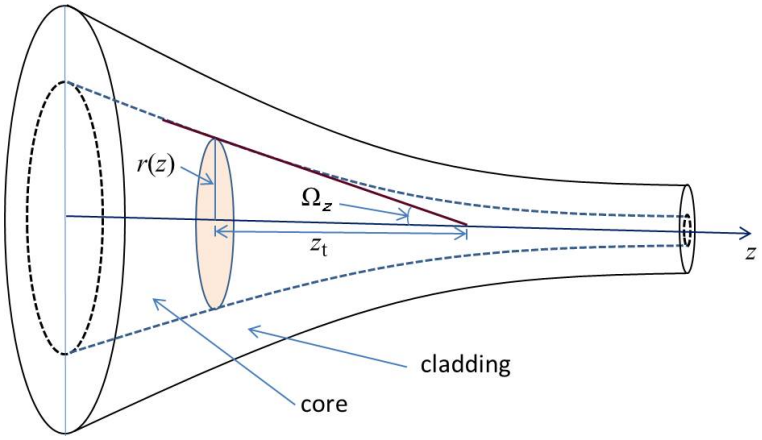


Figure 2.9: Illustration of a fibre taper showing local taper parameters, $\Omega_z, r(z)$ and z_t.

with nearby propagation constants. The taper angle, Ω_z, (see Fig. 2.9) has to be shallow enough to prevent this mode coupling from occurring. The maximum taper angle, $\Omega_{z_{max}}$, which allows for adiabatic transmission is given by [78],

$$\Omega_{z_{max}} = \frac{r(z)}{z_b}, \tag{2.67}$$

where $r(z)$ is the local radius of the taper transition and z_b is the beat length defined as $2\pi/(\beta_1 - \beta_2)$ with β_1 and β_2 being the local propagation constants of the propagating mode and the nearest symmetric mode. For adiabatic tapering, the local taper length $z_t \gg z_b$, where $z_t \approx r(z)/\Omega_z$. For an ideal adiabatic taper, light propagating as core modes in the non-tapered region can be considered unperturbed as they evolve from being core-guided to cladding-guided, whereas, in the case of non-adiabatic tapering, the core modes couple to higher-order cladding modes of the same cylindrical symmetry.

For a SM-ONF, which supports only the fundamental, HE_{11}, mode the taper angle can be relatively large due to the large propagation constant difference between two neighbouring modes. However, for ONFs which support higher order modes (FM-ONF) the required angle for an adiabatic taper is smaller due to the small separation of the propagation constants between the neighbouring modes [79]. For a fixed length of fibre, L_0, uniformly heated and stretched, the taper transitions remain always exponential in shape and the radius of the fibre along the z-axis is given by [80]

$$r(z) = r_0 \exp[-z/L_0] \tag{2.68}$$

where r_0 is the initial untapered fibre diameter. A change in the hot-zone length during the ONF fabrication may lead to various different taper profiles. Solving

"the reverse problem [12]", parameters for a desired taper shape can be calculated. It has been shown that utilization of linear taper profiles instead of exponential, with smaller fibre diameters, could result in better transmission for higher-order mode propagation for a relatively shorter taper length [79]. For the works described in this thesis, fibre shapes are exponential only, though linear profiles are used for other work in the research unit.

2.4.2 Fibre pulling rig

We use a flame-brushing technique, which is one of most common due to its ease of design, high degree of accuracy and versatility of the possible taper profiles. Also, this technique provides a nanofibre with pigtails on both sides, thereby making it very easy to couple light into the nanofibre or collect any light being coupled to it at the waist. The pulling rig is built in house and has been designed and improved upon by many unit members over the years. The rig employs an oxy-hydrogen torch, microcontrollers and stepper motors as shown in Fig. 2.10. An oxy-butane torch could also be used; however, if the oxygen:butane ratio is not correct it could lead to carbon soot on the fibre that could affect the performance of the ONF significantly. Also, the required temperature (up to 1500°C) can be achieved with an oxy-hydrogen flame with relatively low gas flow rates. This reduces the flame pressure on the fibre during the fabrication process. The flame can either be stationary or brushed depending on the taper profiles required. The flame nozzle is 1 mm^2 with 9 holes of 200 μm diameter arranged in a 3×3 matrix. Oxygen and hydrogen gases are premixed before reaching the nozzle in a volumetric ratio of 2:1 in order to ensure complete combustion. The gas flow rates are controlled using mass-flow controllers. The fibre is kept in the flame at an appropriate height depending on the gas flow rates. The two pigtails are clamped on motorised translation stages (1D stepper motors). The two translation stages have to be aligned linearly with good precision so that, while the two stages move apart in order to stretch the fibre in the flame, the centre of the fibre does not deviate from its position with respect to the initial position of the flame. The flame nozzle is also mounted on a 2D translational stage with one axis perpendicular to the fibre and one parallel, so that the flame can be brought to the fibre and removed as per need and brushed along the fibre when required. Movements of all the translation stages are controlled using an XPS-Q4 controller, which receives velocity, acceleration and position commands from a LabVIEW program. As the LabVIEW program is initialised, the flame is

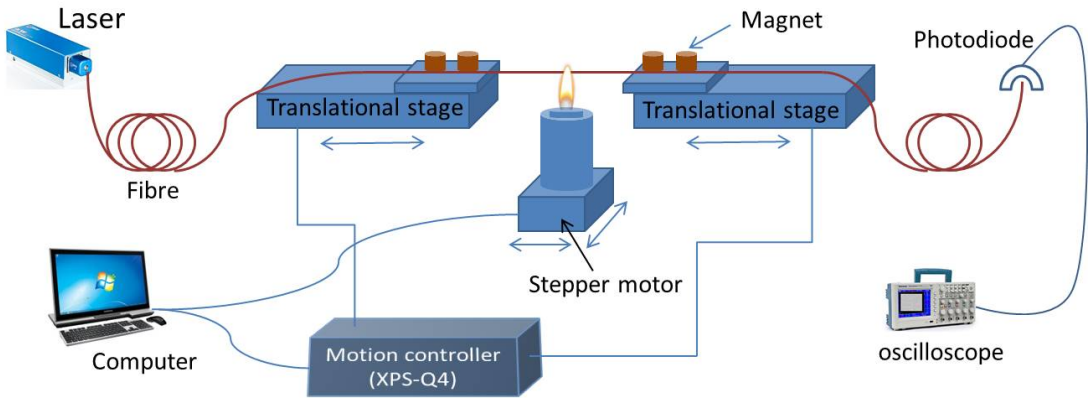


Figure 2.10: Illustration of the fibre pulling rig

brought under the clamped fibre and it stays there for two seconds, then starts oscillating along the fibre axis over a desired length, called the 'hot zone', and the two ends of the fibre are pulled in opposite directions by the two linear stages. When the pulling process is complete, the flame returns to its home position away from the fibre. The required taper profile is obtained by setting pre-calculated values of hotzone, pull speed and pull length.

The transmission through the fibre is monitored throughout the pulling process. For this, a laser beam is coupled to one end of the fibre before starting the LabVIEW program and the other end is connected to a photodiode whose voltage output signal is recorded on a digital oscilloscope.

2.4.3 Single-mode optical nanofibre (SM-ONF)

A commercially available optical fibre (780HP, Thorlabs) is used to prepare a SM-ONF. This fibre has core and cladding diameters of 125 μm and 4.4 μm, respectively. The second mode cut-off for this fibre is 730$\pm$30 nm ensuring single mode operation at 780 nm. Around 5 cm length of this fibre is unjacketed using a fibre stripper. A sufficient length of pigtails ($\sim$1.5 m) are kept on both sides. The unjacketed part is wiped with acetone to ensure no residual acrylic coating and the ends are clamped on the translation stages. 780 nm laser light is coupled to one end for monitoring the transmission during the pulling. LabVIEW parameters are set to obtain an exponential profile nanofibre of $\sim$350 nm diameter. A hot zone of 3 cm is used. This means the obtained nanofibre should have a waist length of 3 cm with a uniform radius. Further details of the fabricated fibres for specific experiments are given in the relevant chapters. Note that the prior estimation of the diameter is based on pre-calibration of the pulling rig and

the actual diameter can be verified, after completing the experiments, using a scanning electron microscope.

2.4.4 Few-mode optical nanofibre (FM-ONF)

For the fabrication of an FM-ONF, we use a few-mode (at 780 nm) fibre (SM1250G80, Thorlabs). This fibre supports four families of modes (LP_{01}, LP_{11}, LP_{21} and LP_{02}) at 780 nm. The cladding diameter of this fibre is 80 μm (rather than 125 μm). The smaller cladding diameter allows us to obtain a better transmission for higher-order modes [79, 81]. This also reduces the taper length, which is a benefit when mounting on a small length fibre holder.

For higher-order mode work, we require a nanofibre which only supports the LP_{01} (i.e HE_{11}) mode and LP_{11} mode (i.e. TE_{01}, TM_{01} and HE_{21} true modes) at the waist for 780 nm. The process of fabrication is the same as for an SM-ONF, but, in this case, the pulling parameters become more crucial. For the SM-ONF, a slight deviation in the pull length would only cause a change in the diameter of the nanofibre and, thence, the percentage of field propagating through the nanofibre. The propagation would still be in the single mode regime as the next mode cut-off is far away (Fig. 2.3). However, the mode cut-off values are close to each other in the case of higher modes (TE_{01}, TM_{01} and HE_{21}) and a slight change in pull length may result in the loss of a mode if the fibre diameter is close to the mode cut-off. We prepare a fibre which can support the first four modes (HE_{11}, TE_{01}, TM_{01} and HE_{21}) and try to keep the diameter small, i.e. close to the cut-off of the HE_{21} mode to increase the intensity in the evanescent field. We determine the pulling length experimentally as we find this is more reliable than calculated values. For this, we first pull a test fibre to a length where all the mode cut-offs can be identified. Then, after finding the mode cut-off for the required modes, the actual fibre for the experiment is pulled. However, to determine the mode cut-offs we need to measure the transmission for higher order modes while pulling. Hence, a doughnut shape beam (i.e. an LG_{01} free space mode) is coupled to the fibre to excite the LP_{11} mode group. The LG_{01} mode is generated using a spatial light modulator (SLM) [82]. More details are given in Chapter 8.

Fig. 2.11(a) shows the transmission of a test fibre which provides the information that a pull length of 70 mm would result in an ONF which supports the fundamental and first higher order mode group (LP_{11}). This pulling length corresponds to a waist diameter of 700 nm with an exponential taper profile. Fig. 2.11(b)

shows the transmission curve for a fibre supporting the fundamental and first higher order mode group at the waist. The oscillations in the transmission are due to mode beating caused by the interference between the core mode (LP_{11}) and the higher order cladding modes (LP_{1n}), which are excited when a portion of the transition region becomes non-adiabatic for that mode [83].

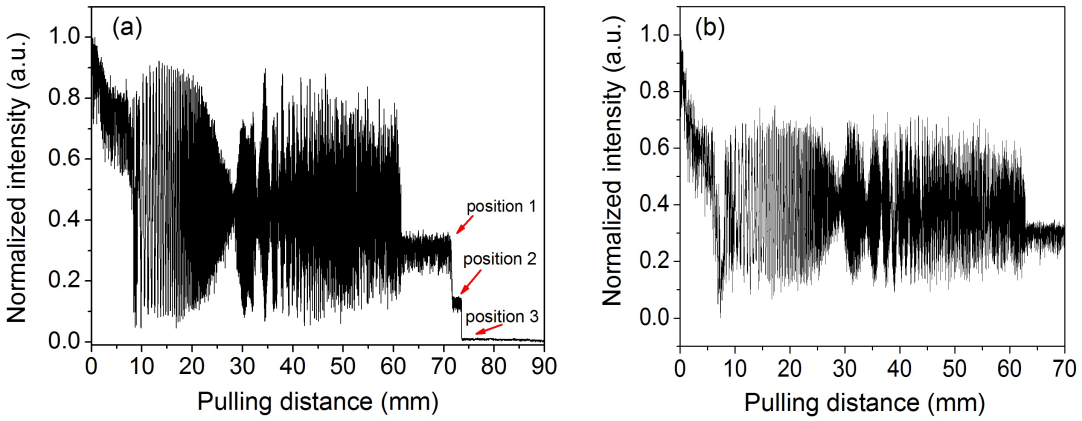


Figure 2.11: Transmission during pulling for light coupled to the LP_{11} mode. (a) Pulling a test fibre for a pull length of 90 mm to cut-off all the higher modes, and (b) pulling a fibre for a 70 mm pulling length to ensure that the nanofibre supports only the HE_{11}, TE_{01}, TM_{01} and HE_{21} modes. In (a) Position 1 is the cut-off point for the coupled HE_{21} mode, Position 2 is the cut-off for the TE_{01} and TM_{01} modes (the mode cut-offs for the two modes are so close to each other that they are unresolved in the transmission graph at this resolution) and Position 3 is the portion of the residual fundamental mode guided by the nanofibre.

2.5 Conclusion

This chapter provided a theoretical description of light propagation in an ONF and the method of fabrication for an ONF. At first, the propagation of light through an optical fibre is described using Maxwell's equations in order to get the general understanding of light propagation through a cylindrical waveguide and, based on this, the propagation of the fundamental and the first higher order mode of an ONF is described. Intensity profiles of the different modes are presented which show the high extent of the evanescent field of an ONF. This is one of the most crucial requirements for the experiments presented in this thesis. Energy flow through an ONF and adiabatic criteria for the fabrication of an ONF are discussed followed by the description of the fibre pulling rig. Methods of the fabrication of the ONFs of different kinds used in the experiments are presented at the end of the chapter.

Chapter 3

Light-Atom Interactions

Since the focus of this thesis is the interaction of laser-cooled atoms with light an introduction to related phenomena is desirable at this point. We shall use a simple two-level atom model for a basic understanding, and then will proceed to explore three-level systems to provide more clarity for some of the experiments conducted, e.g. electromagnetically induced transparency (EIT). A theoretical model for systems with more than three levels is beyond the scope of this thesis, though would be required to fully explain some of the observed phenomena.

We shall use a semi-classical treatment to describe light-atom interactions in a two-level atomic system. Here, an atom interacts with monochromatic, near-resonant light, which is considered as a classical electromagnetic field, whereas the atom is treated using quantum mechanics.

3.1 Two-level Atoms

Let us start by considering $\Psi(\mathbf{r}, t)$ as the atomic wavefunction. The time-dependent Schrödinger equation can be written as [84]

$$i\hbar \frac{\partial \Psi(\mathbf{r}, t)}{\partial t} = H\Psi(\mathbf{r}, t), \tag{3.1}$$

where $H = H_0 + H_I(t)$, H_0 is the Hamiltonian of the unperturbed atom and $H_I(t)$ describes the interaction of the atom with the oscillating electric field.

The wavefunction for an atom with energy E_n can be written as

$$\Psi_n(\mathbf{r},t) = \psi_n(\mathbf{r})e^{-iE_nt/\hbar} \tag{3.2}$$

and the eigenvalue equation can be written as

$$H_0\psi_n(\mathbf{r}) = E_n\psi_n(\mathbf{r}). \tag{3.3}$$

For a two-level atom (Fig. 3.1) with energy levels E_1 and E_2 (described by states $|1\rangle$ and $|2\rangle$, respectively), the wavefunction is given by

$$\Psi(\mathbf{r},t) = c_1(t)\Psi_1(\mathbf{r},t) + c_2(t)\Psi_2(\mathbf{r},t), \tag{3.4}$$

with the time-dependent coefficients, c_1 and c_2, satisfying the normalisation condition

$$\int |\Psi(\mathbf{r},t)|^2 dV = |c_1(t)|^2 + |c_2(t)|^2 = 1. \tag{3.5}$$

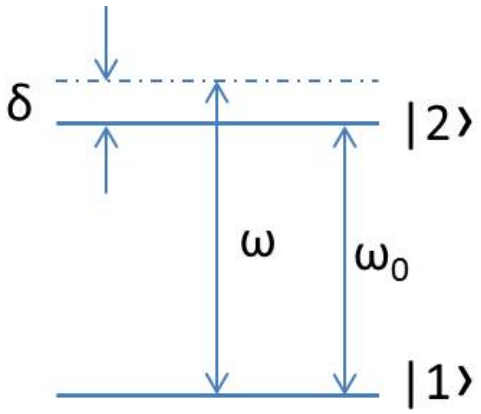


Figure 3.1: Two-level atom with a coupling laser of angular frequency ω. δ is the laser detuning from the atom's resonance frequency, ω_0, such that $\omega = \omega_0 - \delta$.

In Dirac ket notation, $\psi_n(\mathbf{r}) \to |n\rangle$ and $E_n/\hbar \to \omega_n$. Also, we can take $c_n(t) \to c_n$ assuming implicit time dependence. Thus, Eq. 3.4 can be rewritten as

$$\Psi(\mathbf{r},t) = c_1|1\rangle e^{-i\omega_1 t} + c_2|2\rangle e^{-i\omega_2 t}. \tag{3.6}$$

Inserting $\Psi(\mathbf{r},t)$ from Eq. 3.4 into Eq. 3.1, multiplying from the left by $\Psi_1^*(\mathbf{r},t)$ and integrating over all space, the dynamic evolution of the wavefunction in terms

of the amplitude coefficient, $c_1(t)$, is

$$i\dot{c_1} = c_1\langle 1|H_I|1\rangle + c_2 e^{-i\omega_0 t}\langle 1|H_I|2\rangle, \tag{3.7}$$

where $\omega_0 = (E_2 - E_1)/\hbar$ and $\langle 1|H_I|2\rangle = \int \psi_1^* H_I \psi_2 dV$ denotes the matrix elements of the interaction Hamiltonian H_I. Similarly, for $c_2(t)$, the dynamic evolution is

$$i\dot{c_2} = c_1 e^{i\omega_0 t}\langle 2|H_I|1\rangle + c_2\langle 2|H_I|2\rangle. \tag{3.8}$$

The oscillating electric field, $\mathbf{E}$, of the electromagnetic radiation interacting with the atom can be written as $\mathbf{E} = \mathbf{E}_0 \cos(\omega t)$. Considering an atom with nucleus of charge Ze located at the centre of the coordinate system and the vector $\mathbf{r}_i(t)$ describing the position of the ith electron with charge $-e$, the total electric dipole moment of the atom is given as $-e\mathbf{D}$ where

$$\mathbf{D} = \sum_{j=1}^{z} \mathbf{r}_j. \tag{3.9}$$

3.1.1 Interaction with monochromatic radiation

The potential energy due to the electric dipole is the main contributor to the interaction Hamiltonian, as the higher multipole contribution is negligible. Thus, we can write the interaction Hamiltonian for the electric dipole moment, $\boldsymbol{\mu}$, as [85]

$$H_I = -\boldsymbol{\mu} \cdot \mathbf{E} = e\mathbf{D} \cdot \mathbf{E}_0 \cos(\omega t). \tag{3.10}$$

H_I is real and changes sign under inversion in the nucleus, i.e. when $\mathbf{r}_j$ is replaced by $-\mathbf{r}_j$. Thus, the diagonal matrix elements vanish, i.e.

$$\langle 1|H_I|1\rangle = \langle 2|H_I|2\rangle = 0 \tag{3.11}$$

and the off-diagonal elements are related through

$$\langle 2|H_I|1\rangle = \langle 1|H_I|2\rangle^*. \tag{3.12}$$

Taking the orientation of $\mathbf{E}_0$ along the x-direction, we can write

$$\langle 1|H_I|2\rangle = e|\mathbf{E}_0|X_{12}\cos(\omega t), \tag{3.13}$$

where $X_{12} = \langle 1|x|2\rangle = \int \psi_1^* x \psi_2 dV$, with x as the x-component of the atomic dipole moment, $\mathbf{D}$. X_{12} can also be expressed as

$$X_{12} = \int \psi_1^* \mathbf{e} \cdot \mathbf{D} \psi_2 dV = \mathbf{e} \cdot \mathbf{D}_{12}, \tag{3.14}$$

where $\mathbf{e}$ is the unit vector in the direction of the electric field of the interacting light and $\mathbf{D}_{12}$ is the dipole moment for the respective transition between $|1\rangle$ and $|2\rangle$, known as the transition dipole moment. A quantity Ω, given by the expression

$$\Omega = \frac{e|\mathbf{E}_0|X_{12}}{\hbar} = \frac{e|\mathbf{E}_0|(\mathbf{e} \cdot \mathbf{D}_{12})}{\hbar} \tag{3.15}$$

is known as the Rabi frequency. This is a complex quantity in general, but it is real for transitions between bound states, where ψ_1 and ψ_2 are real wavefunctions [86]. Using Eqs. 3.7, 3.11, 3.13 and 3.15, we get

$$\begin{aligned} i\dot{c_1} =& c_2 e^{-i\omega_0 t} \Omega \cos(\omega t) \\ =& c_2 \left\{ e^{i(\omega-\omega_0)t} + e^{-i(\omega+\omega_0)t} \right\} \frac{\Omega}{2}. \end{aligned} \tag{3.16}$$

Now, for $|\omega - \omega_0| \ll \omega$ using the rotating-wave approximation indicates that the term with $(\omega + \omega_0)t$ oscillates very quickly and, therefore, averages to zero over any reasonable interaction time. Hence, Eq. 3.16 can be rewritten as

$$i\dot{c_1} = c_2 e^{i(\omega-\omega_0)t} \frac{\Omega}{2}. \tag{3.17}$$

Similarly, we get

$$i\dot{c_2} = c_1 e^{-i(\omega-\omega_0)t} \frac{\Omega}{2}. \tag{3.18}$$

For zero laser detuning ($\omega = \omega_0$), and initial population in the ground state ($|c_1|^2 = 1$ and $|c_2|^2 = 0$ at $t = 0$), we get the solution for Eqs. 3.17 and 3.18 as

$$|c_1(t)|^2 = \cos^2(\Omega t/2); |c_2(t)|^2 = \sin^2(\Omega t/2). \tag{3.19}$$

This indicates that the electron oscillates back and forth between the upper and the lower levels at a frequency of $\Omega/2\pi$. This effect is known as Rabi oscillation or Rabi flopping [87].

3.1.2 Optical Bloch equations

The density operator, ρ, can be expressed in terms of $c_1(t)$ and $c_2(t)$ as

$$\rho = |\Psi\rangle\langle\Psi| = \begin{pmatrix} c_1 & c_2 \end{pmatrix} \begin{pmatrix} c_1^* \\ c_1^* \end{pmatrix}$$

$$\Rightarrow \begin{pmatrix} \rho_{11} & \rho_{12} \\ \rho_{21} & \rho_{22} \end{pmatrix} = \begin{pmatrix} |c_1|^2 & c_1 c_2^* \\ c_2 c_1^* & |c_2|^2 \end{pmatrix}. \tag{3.20}$$

The diagonal elements of the matrix are populations and the off-diagonal matrix elements are called coherences, with the relationships $\rho_{11} + \rho_{22} = 1$ and $\rho_{21} = \rho_{12}^*$. As $\rho_{ij} = c_i c_j^*$, the equation of motion for the density matrix can be written as

$$\dot{\rho_{ij}} = c_i \dot{c_j^*} + \dot{c_i} c_j^*. \tag{3.21}$$

Substituting from Eqs. 3.17 and 3.18, we get the equations of motion

$$\begin{aligned} \dot{\rho_{22}} = -\dot{\rho_{11}} &= -\frac{1}{2} i\Omega \left(e^{i(\omega_0 - \omega)t} \rho_{12} - e^{-i(\omega_0 - \omega)t} \rho_{21} \right) \\ \text{and } \dot{\rho_{12}} = \dot{\rho_{21}^*} &= \frac{1}{2} i\Omega e^{i(\omega_0 - \omega)t} \left(\rho_{11} - \rho_{22} \right). \end{aligned} \tag{3.22}$$

These are known as the optical Bloch equations [86]. Oscillating factors can be removed from these equations for convenience by substituting

$$\begin{aligned} \tilde{\rho_{12}} &= e^{-i\delta t} \rho_{12}, \\ \tilde{\rho_{21}} &= e^{i\delta t} \rho_{21} = \tilde{\rho_{12}}^*, \\ \tilde{\rho_{11}} &= \rho_{11} \text{ and } \tilde{\rho_{22}} = \rho_{22}, \end{aligned} \tag{3.23}$$

where $\delta = \omega - \omega_0$ is the detuning of the radiation from the atomic resonance, as already defined. Thus, Eq. 3.22 can be expressed as

$$\begin{aligned} \dot{\tilde{\rho_{22}}} = -\dot{\tilde{\rho_{11}}} &= -\frac{1}{2} i\Omega \left(\tilde{\rho_{12}} - \tilde{\rho_{21}} \right) \\ \text{and } \dot{\tilde{\rho_{12}}} = \dot{\tilde{\rho_{21}}}^* &= \frac{1}{2} i\Omega \left(\tilde{\rho_{11}} - \tilde{\rho_{22}} \right) - i\delta \tilde{\rho_{12}}. \end{aligned} \tag{3.24}$$

To include spontaneous emission in the treatment, it is necessary to take into account the radiative decay (neglecting other decay mechanism) for the number of atoms in the excited state as

$$\rho_{22}(t) = \rho_{22}(0) e^{-\Gamma t}, \tag{3.25}$$

where the radiative decay rate, Γ, is given by Einstein's A coefficient and is related to the radiative lifetime, τ_R, as

$$\Gamma = A_{21} = \frac{1}{\tau_R} = \frac{e^2\omega_0^3 D_{12}^2}{3\pi\epsilon_0\hbar c^3}. \tag{3.26}$$

This modifies Eq. 3.24 to include the decay rate and provides the optical Bloch equations for a two-level atom for pure radiative damping as [86]

$$\begin{aligned}
\dot{\tilde{\rho_{11}}} =& \frac{1}{2}i\Omega\left(\tilde{\rho_{12}} - \tilde{\rho_{21}}\right) + \Gamma\tilde{\rho_{22}},\\
\dot{\tilde{\rho_{12}}} =& \frac{1}{2}i\Omega\left(\tilde{\rho_{11}} - \tilde{\rho_{22}}\right) - \left\{i\delta + \Gamma/2\right\}\tilde{\rho_{12}},\\
\dot{\tilde{\rho_{21}}} =& \frac{1}{2}i\Omega\left(\tilde{\rho_{22}} - \tilde{\rho_{11}}\right) - \left\{-i\delta + \Gamma/2\right\}\tilde{\rho_{12}},\\
\dot{\tilde{\rho_{22}}} =& \frac{1}{2}i\Omega\left(\tilde{\rho_{21}} - \tilde{\rho_{12}}\right) - \Gamma\tilde{\rho_{22}}.
\end{aligned} \tag{3.27}$$

3.1.3 Steady state solutions

We now introduce the terms $u = \tilde{\rho_{12}} + \tilde{\rho_{21}}, v = -i\left(\tilde{\rho_{12}} - \tilde{\rho_{21}}\right)$ and $w = \tilde{\rho_{11}} - \tilde{\rho_{22}}$. In this notation, the optical Bloch equations (Eq. 3.27) can be expressed as [88]

$$\begin{aligned}
\dot{u} =& \delta v - \frac{\Gamma}{2}u,\\
\dot{v} =& -\delta u + \Omega w - \frac{\Gamma}{2}u,\\
\dot{w} =& -\Omega v - \Gamma\left(w - 1\right).
\end{aligned} \tag{3.28}$$

For a sufficiently long time compared to the lifetime of the upper state ($t \gg \tau_R$), the system settles down into a steady-state. The steady-state solution of the system of Eq. 3.28 is given by

$$\begin{pmatrix} u \\ v \\ w \end{pmatrix} = \frac{1}{\delta^2 + \Omega^2/2 + \Gamma^2/4}\begin{pmatrix} \Omega\delta \\ \Omega\Gamma/2 \\ \delta^2 + \Gamma^2/4 \end{pmatrix}. \tag{3.29}$$

Now, as we have $\tilde{\rho_{11}} - \tilde{\rho_{22}} = w$ and $\tilde{\rho_{11}} + \tilde{\rho_{22}} = 1$, the upper-level steady-state population is

$$\tilde{\rho_{22}}(\infty) = \frac{1 - w}{2} = \frac{\Omega^2/4}{\delta^2 + \Omega^2/2 + \Gamma^2/4}. \tag{3.30}$$

The optical coherence term at steady-state is given by

$$\tilde{\rho_{12}}(\infty) = \frac{u+iv}{2} = \frac{(\Omega/2)(\delta + i\Gamma/2)}{\delta^2 + \Omega^2/2 + \Gamma^2/4}. \tag{3.31}$$

Eq. 3.30 indicates that, for a strong driving field ($\Omega \to \infty$), the population in the ground and the excited state equalises at the steady-state ($\tilde{\rho_{12}}(\infty) \to 1/2$) independent of the initial conditions.

3.1.4 Saturation and power broadening

The population difference parameter, w, is given by Eq. 3.29 as

$$w = \frac{(\delta^2 + \Gamma^2/2)}{\delta^2 + \Omega^2/2 + \Gamma^2/4} = \frac{1}{1+s}, \tag{3.32}$$

where $s = \dfrac{\Omega^2/2}{\delta^2 + \Gamma^2/4}$ is called the saturation parameter. It is evident that, for $s \ll 1, w \to 1$ which means that the atoms are in the ground state, and for $s \gg 1, w \to 0$ which means that the population is equally distributed between the ground and the excited state. The on-resonance saturation parameter is defined for $\delta = 0$ by

$$s_0 = \frac{2\Omega^2}{\Gamma^2} = \frac{I}{I_s}, \tag{3.33}$$

where I is the laser field intensity and the saturation intensity, I_s, is given by

$$I_s = \frac{\pi hc}{3\lambda_0^3 \tau_R}, \tag{3.34}$$

where λ_0 is the resonance transition wavelength. Eq. 3.30 can be expressed in terms of s_0 as

$$\tilde{\rho_{22}}(\infty) = \frac{s_0/2}{1 + s_0 + (2\delta/\Gamma)^2}. \tag{3.35}$$

At steady-state, the excitation rate and the decay rate are equal; the total scattering rate of the excitation light beam is given by [89]

$$\begin{aligned} \Gamma_s = \Gamma\tilde{\rho_{22}}(\infty) =& \frac{s_0\Gamma/2}{1 + s_0 + (2\delta/\Gamma)^2} \\ =& \frac{s_0 \left(\Gamma/2\right)^3}{(\omega - \omega_0)^2 + (\Gamma/2)^2(1+s_0)} \end{aligned} \tag{3.36}$$

using the relation $\delta = \omega - \omega_0$. This is a Lorentzian function of ω centred at ω_0

and with a full-width-at-half-maximum (FWHM) value of

$$\Gamma' = \Gamma(1 + s_0). \tag{3.37}$$

The width, Γ', is called the power broadened linewidth of the transition. It increases with an increase in power and has a minimum value of Γ, the natural linewidth. The saturation behaviour and the power broadening can be seen by plotting the scattering rate, Γ_s, for various s_0 values (see Fig. 3.2). A near-

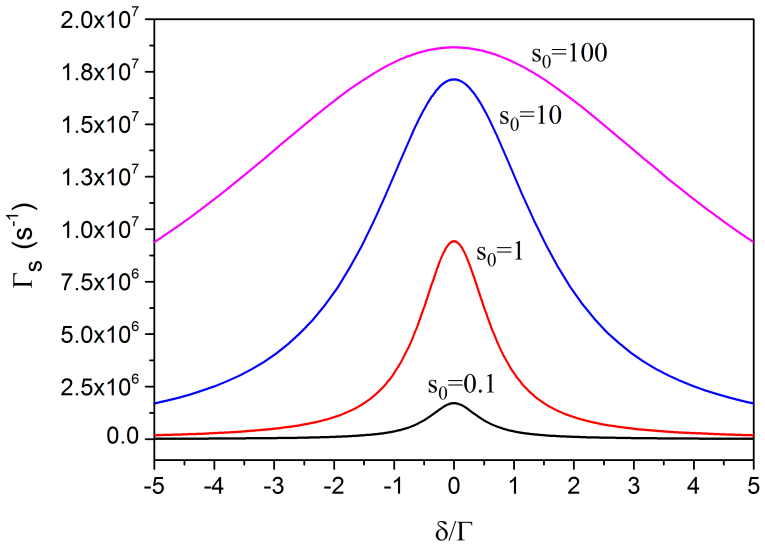


Figure 3.2: Scattering rate for the 5 $S_{1/2}$ F=2 $\rightarrow$ 5 $P_{3/2}$ F′=3 transition of ^{87}Rb ($\Gamma/2\pi = 6$ MHz) as a function of δ/Γ.

resonant beam travelling through an atomic sample gets attenuated as a result of scattering. The amount of power scattered per unit volume is given by $\hbar\omega\Gamma_s n$, where n is the number density of atoms in the sample [89].

3.1.5 The light shift

The perturbing radiation does not only affect the populations, but also the energy levels of the atom are shifted - this effect is known as the light shift. In order to calculate this shift, we introduce two parameters

$$\tilde{c_2} = c_2 e^{i\delta t/2} \quad \text{and} \quad \tilde{c_1} = c_1 e^{-i\delta t/2}. \tag{3.38}$$

The time derivative of Eq. 3.38 multiplied by i is

$$i\dot{\tilde{c}_1} = (\delta\tilde{c_1} + \Omega\tilde{c_2})/2 \quad \text{and} \quad i\dot{\tilde{c}_2} = \quad (\Omega\tilde{c_1} - \delta\tilde{c_2})/2 \tag{3.39}$$

using Eqs. 3.17 and 3.18 with $\delta = \omega - \omega_0$. Eq. 3.39 can be written in matrix form as

$$i\frac{d}{dt}\begin{pmatrix}\tilde{c_1}\\ \tilde{c_2}\end{pmatrix} = \frac{1}{2}\begin{pmatrix}\delta & \Omega\\ \Omega & -\delta\end{pmatrix}\begin{pmatrix}\tilde{c_1}\\ \tilde{c_2}\end{pmatrix}. \tag{3.40}$$

This is equivalent to the Schrödinger equation, $i\hbar\dfrac{\partial\Psi}{\partial t} = H\Psi$, with the Hamiltonian, H, given by

$$H = \frac{\hbar}{2}\begin{pmatrix}\delta & \Omega\\ \Omega & -\delta\end{pmatrix}, \tag{3.41}$$

which has a solution for the energies given by

$$E_{1,2} = \pm\frac{\hbar}{2}\sqrt{\delta^2 + \Omega^2}. \tag{3.42}$$

When the detuning $|\delta| \gg \Omega$,

$$E_{1,2} \simeq \pm\frac{\hbar}{2}\left(\delta + \frac{\Omega^2}{2\delta}\right). \tag{3.43}$$

This indicates that, in the presence of a far-detuned light field, the energy levels of the atoms are shifted by an amount

$$\Delta E_{1,2} = \pm\frac{\hbar\Omega^2}{4\delta}. \tag{3.44}$$

However, for the case $\Omega \gg |\delta|$,

$$\Delta E_{1,2} = \pm\frac{\delta}{|\delta|}\frac{\hbar\Omega}{2}. \tag{3.45}$$

This combined system of an atom with a light field is called "the dressed state of the atom". The atom is said to be "dressed by photons".

3.2 Three-Level Atoms

We now introduce one more level to the system as necessary for a discussion of three level processes. This three-level atom, if coupled to two light fields sharing a common energy level, may give rise to some more interesting physics. Let

us consider the case where the transition $|1\rangle \rightarrow |2\rangle$ is coupled to a laser field, $\mathbf{E}_1 \cos(\omega_1 t)$, with intensity corresponding to the Rabi frequency of Ω_1, and the laser field coupling to transition $|2\rangle \rightarrow |3\rangle$ is $\mathbf{E}_2 \cos(\omega_2 t)$ with the Rabi frequency of Ω_2. Let us assume that the transition $|1\rangle \rightarrow |3\rangle$ is dipole forbidden and each laser field only couples the designated transitions.

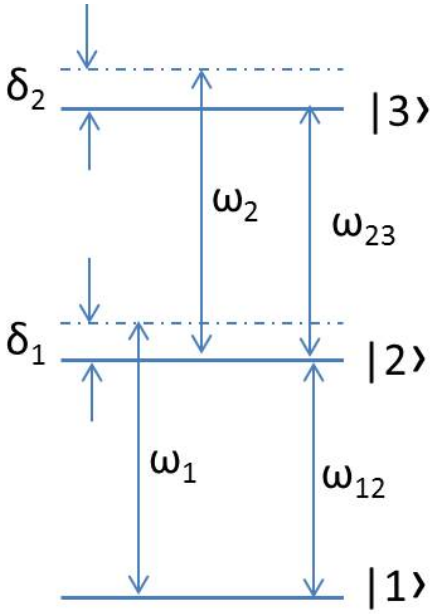


Figure 3.3: Three-level atom coupled to two lasers showing detunings $\delta_{1,2}$, laser frequencies $\omega_{1,2}$ and transitions $\omega_{12,23}$.

As before, the Hamiltonian of the system, H, is given by $H = H_0 + H_I$. H_I is now the interaction Hamiltonian describing the perturbation due to the two applied fields. The evolution of the density matrix, $\sigma(t)$, of the system is governed by the equation of motion

$$\dot{\rho} = \frac{1}{i\hbar}[H, \rho] + \mathbf{\Gamma_d}, \tag{3.46}$$

where $\mathbf{\Gamma_d}$ accounts for the phenomenological relaxation due to spontaneous emission, collisions, etc. [90].

Taking the energy of the ground level, $|1\rangle$, to be zero and other levels to be arranged in a cascaded system with the energy difference between $|1\rangle$ and $|2\rangle$ being $\hbar\omega_{12}$ and between $|2\rangle$ and $|3\rangle$ being $\hbar\omega_{23}$, H_0 can be written as [84]

$$\begin{aligned} H_0 =& \sum_{j=1}^{3} E_j |j\rangle\langle j| = \hbar\omega_{12}|2\rangle\langle 2| + \hbar(\omega_{12} + \omega_{23})|3\rangle\langle 3| \\ \Rightarrow H_0 =& \hbar(\omega_1 - \delta_1)|2\rangle\langle 2| + \hbar(\omega_1 + \omega_2 - \delta_1 - \delta_2)|3\rangle\langle 3| = H_l + H_d, \end{aligned} \tag{3.47}$$

where $\delta_1 = \omega_1 - \omega_{12}$, $\delta_2 = \omega_2 - \omega_{23}$, $H_l = \hbar\omega_1|2\rangle\langle 2| + \hbar(\omega_1 + \omega_2)|3\rangle\langle 3|$ and $H_d = -\hbar\delta_1|2\rangle\langle 2| - \hbar(\delta_1 + \delta_2)|3\rangle\langle 3|$. δ_1 and δ_2 are the detunings of the two lasers with respect to the atomic transition frequencies, as indicated in Fig. 3.3.

The interaction Hamiltonian, H_I, can be expressed as the sum of the perturbations created by the two lasers

$$H_I = -\boldsymbol{\mu} \cdot (\mathbf{E}_1 \cos(\omega_1 t) + \mathbf{E}_2 \cos(\omega_2 t)), \tag{3.48}$$

where $\boldsymbol{\mu} = \boldsymbol{\mu}_{\mathrm{mn}}(|n\rangle\langle m| + |m\rangle\langle n|)$ and $\boldsymbol{\mu}_{\mathrm{mn}}$ is the atomic dipole matrix element for the transition between the states $|m\rangle$ and $|n\rangle$ given as $\boldsymbol{\mu}_{\mathrm{mn}} = \langle m|\boldsymbol{\mu}|n\rangle = \langle n|\boldsymbol{\mu}|m\rangle$. Thus, we have that

$$H_I = \frac{\hbar\Omega_1}{2}(|2\rangle\langle 1| + |1\rangle\langle 2|)(e^{i\omega_1 t} + e^{-i\omega_1 t}) + \frac{\hbar\Omega_2}{2}(|3\rangle\langle 2| + |2\rangle\langle 3|)(e^{i\omega_1 t} + e^{-i\omega_2 t}) \tag{3.49}$$

using the electric-dipole approximation.

We can write the system in the interaction picture using a unitary transformation such that $\mathcal{U}^\dagger \rho \mathcal{U} = \sigma$, with $\mathcal{U} = \exp(-iH_l t/\hbar)$. This transforms Eq. 3.46 so that

$$\dot{\sigma} = \frac{1}{i\hbar}[H_{int}, \sigma] + \mathcal{L}, \tag{3.50}$$

where H_{int} is the Hamiltonian in the interaction picture which is given by

$$H_{int} = \mathcal{U}^\dagger (H_d + H_I)\mathcal{U} \tag{3.51}$$

and $\mathcal{L}$ is the Liouville operator which accounts for dissipation and dephasing of the three-level atom and is given by [91]

$$\mathcal{L} = \begin{pmatrix} \Gamma_{21}\sigma_{22} & -\frac{1}{2}\Gamma_2\sigma_{12} & -\frac{1}{2}\Gamma_3\sigma_{13} \\ -\frac{1}{2}\Gamma_2\sigma_{21} & -\Gamma_{21}\sigma_{22} + \Gamma_{32}\sigma_{33} & -\frac{1}{2}(\Gamma_2 + \Gamma_3)\sigma_{23} \\ -\frac{1}{2}\Gamma_3\sigma_{31} & -\frac{1}{2}(\Gamma_2 + \Gamma_3)\sigma_{32} & -\Gamma_{32}\sigma_{33} \end{pmatrix}, \tag{3.52}$$

where $\Gamma_2 = \gamma_2 + \Gamma_{21}$ and $\Gamma_3 = \gamma_3 + \Gamma_{32}$ are the decays rates, Γ_{21} and Γ_{32} are the natural linewidths, and γ_2 and γ_3 are the dephasing rates of $|2\rangle$ and $|3\rangle$, respectively. The term σ_{jj} denotes the population of the state $|j\rangle$, whereas the term $\sigma_{jj'}$ denotes the coherence between the states $|j\rangle$ and $|j'\rangle$.

Applying the rotating wave approximation to eliminate the high frequency oscil-

lating terms, H_{int} can be written in matrix form as [92]

$$H_{int} = \frac{\hbar}{2}\begin{pmatrix} 0 & \Omega_1 & 0 \\ \Omega_1 & -2\delta_1 & \Omega_2 \\ 0 & \Omega_2 & -2(\delta_1+\delta_2) \end{pmatrix}. \tag{3.53}$$

Eq. 3.50 yields the set of density matrix equations of motion

$$\begin{aligned}
\dot{\sigma_{11}} =& \frac{1}{2}\left[2\Gamma_{21}\sigma_{22} + i(\sigma_{12}-\sigma_{21})\Omega_1\right] \\
\dot{\sigma_{22}} =& \frac{1}{2}\left[-2\Gamma_{21}\sigma_{22} + 2\Gamma_{32}\sigma_{33} - i(\sigma_{12}\Omega_1 - \sigma_{21}\Omega_1 - \sigma_{23}\Omega_2 + \sigma_{32}\Omega_2)\right] \\
\dot{\sigma_{33}} =& \frac{1}{2}\left[-2\Gamma_{32}\sigma_{33} - i(\sigma_{23}-\sigma_{32})\Omega_2\right] \\
\dot{\sigma_{21}} =& \frac{1}{2}\left[-\Gamma_2\sigma_{21} + i(2\delta_1\sigma_{21} - \sigma_{11}\Omega_1 + \sigma_{22}\ \Omega_1 - \sigma_{31}\Omega_2)\right] \\
\dot{\sigma_{32}} =& \frac{1}{2}\left[-\Gamma_2\sigma_{32} - \Gamma_3\sigma_{32} + i(2\delta_2\sigma_{32} + \sigma_{31}\Omega_1 - \sigma_{22}\Omega_2 + \sigma_{33}\Omega_2)\right] \\
\dot{\sigma_{31}} =& \frac{1}{2}\left[-\Gamma_3\sigma_{31} + i(2\delta_1\sigma_{31} + 2\delta_2\sigma_{31} + \sigma_{32}\Omega_1 - \sigma_{22}\Omega_2\right].
\end{aligned} \tag{3.54}$$

The three-level atom can be studied in two different ways: (i) using a high intensity laser, ω_1, to drive the $|1\rangle \rightarrow |2\rangle$ transition and probing using a low intensity ω_2 beam or (ii) using a high intensity ω_2 to drive the $|2\rangle \rightarrow |3\rangle$ transition and probing using a low intensity ω_1 beam. Depending on which laser (ω_1 or ω_2) is intense, the obtained results are dramatically different [93]. In the following we consider these two situations.

3.2.1 Aulter-Townes splitting

In the presence of a high intensity ω_1 beam, under the near-resonance condition, the $|1\rangle \rightarrow |2\rangle$ transition splits into two due to the dressing of the atom. This splitting is a result of the AC Stark effect and is known as the Aulter-Townes splitting [61]. The splitting of the level can be probed using the ω_2 beam scanning the $|2\rangle \rightarrow |3\rangle$ resonance (see Fig. 3.3). The absorption of the probe is proportional to the negative of the imaginary part of the corresponding matrix element, σ_{32}, [94] which can be derived from the optical Bloch equations, i.e. Eq. 3.54. Numerical simulations for positive, zero and negative detunings of the dressing laser (ω_1) are shown in Fig. 3.4. The populations in the ground ($|1\rangle$) and the intermediate levels ($|3\rangle$) are taken as 1/2 each, with no population in the upper

level ($|3\rangle$) in order to prepare a model for a small probe intensity and high coupling intensity. We consider a fixed probe intensity with a Rabi frequency (Ω_2) of $2\pi\times200$ kHz and calculate the absorption spectra for various Rabi frequencies of the coupling beam (Ω_1) (Fig. 3.4). It can be seen from Fig. 3.4(b) that with the coupling beam at resonance, i.e. $\omega_1 = \omega_{12}$, the absorption at zero detuning of the probe reduces with an increase in Ω_1 from 0 and finally it splits into two peaks symmetrically spaced around the zero resonance position, indicated by the vertical line. However, for the red-detuned ($\delta_1 < 0$) coupling light (Fig. 3.4(a)), the absorption peak on the negative detuning side ($\delta_2 < 0$) is stronger than the peak in the positive detuning side ($\delta_2 > 0$) when two separate peaks are observed. For the blue-detuned ($\delta_1 > 0$) coupling field (Fig. 3.4(c)), the strength of the absorption peak in the positive detuning side is strong than that of the negative detuning side .

3.2.2 Electromagnetically induced transparency

In contrast to what we presented in Section 3.2.1, reversing the strength of the two fields coupling to the three level system, i.e., taking ω_2 as a strong coupling field and ω_1 as a weak probe field, an interesting phenomenon knows as "electromagnetically induced transparency" comes into effect which involves interference between the excitation pathways. The transition probabilities for the different path ways interfere and this can potentially reduce the absorption of the probe beam when a resonance condition is met. Quantum mechanics states that transitions having the same final level must interfere [95]. In a ladder type system (Fig. 3.1), the interference is produced between the two path ways : (i) the transition from $|1\rangle \rightarrow |2\rangle$ and (ii) another path following $|1\rangle \rightarrow |2\rangle \rightarrow |3\rangle \rightarrow |2\rangle$, with both ultimately having the same final state, $|2\rangle$.

The reduction in the probe absorption can be examined with a semi-classical approach utilising the optical Bloch equations (Eq. 3.54). The probe beam is scanned across the transition $|1\rangle \rightarrow |2\rangle$ and its absorption is proportional to the negative of the imaginary part of the matrix element, σ_{21}. Fig. 3.5 show numerical simulations of the probe absorption for a zero, red-, and blue-detuned coupling beam, respectively. It is assumed in all three cases that the total initial population is in the ground state ($|1\rangle$) only.

3.3 Conclusion

The two-level model of an atom is described in the beginning of the chapter and this provides the foundation for the basic understanding of light-matter interactions. The optical Bloch equations were derived for monochromatic light interacting with a two-level atom and have been used to obtain steady state solutions for the population in the ground and the excited states, followed by the description of intensity saturation of an atom, power broadening of the transition linewidth and the light-shift due to the dressing of atoms by the light field. Furthermore, a three-level atom model has been considered to describe Autler-Townes splitting and EIT; this is particularly important for understanding some of the primary experimental results presented in the thesis.

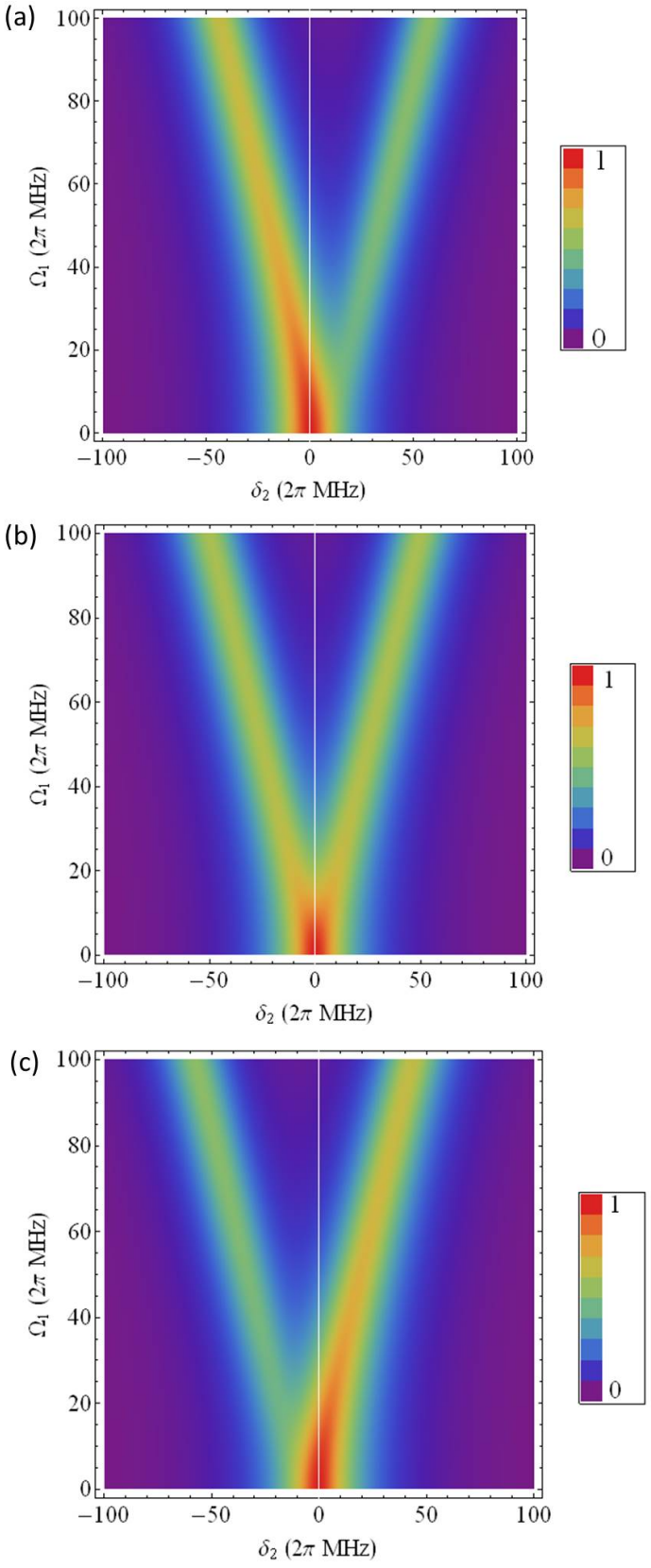


Figure 3.4: Calculated absorption spectra showing Aulter-Townes splitting with $\Omega_2 = 2\pi \times 200$ kHz, $\Gamma_2 = 2\pi\times$ 10 MHz and $\Gamma_3 = 2\pi\times$ 20 MHz for the coupling beam (ω_1): (a) 14 MHz red-detuned from the resonance (δ_1 = -14 MHz), (b) at resonance ($\delta_1 = 0$), and (c) the coupling beam 14 MHz blue-detuned from the resonance ($\delta_1 = +14$ MHz).

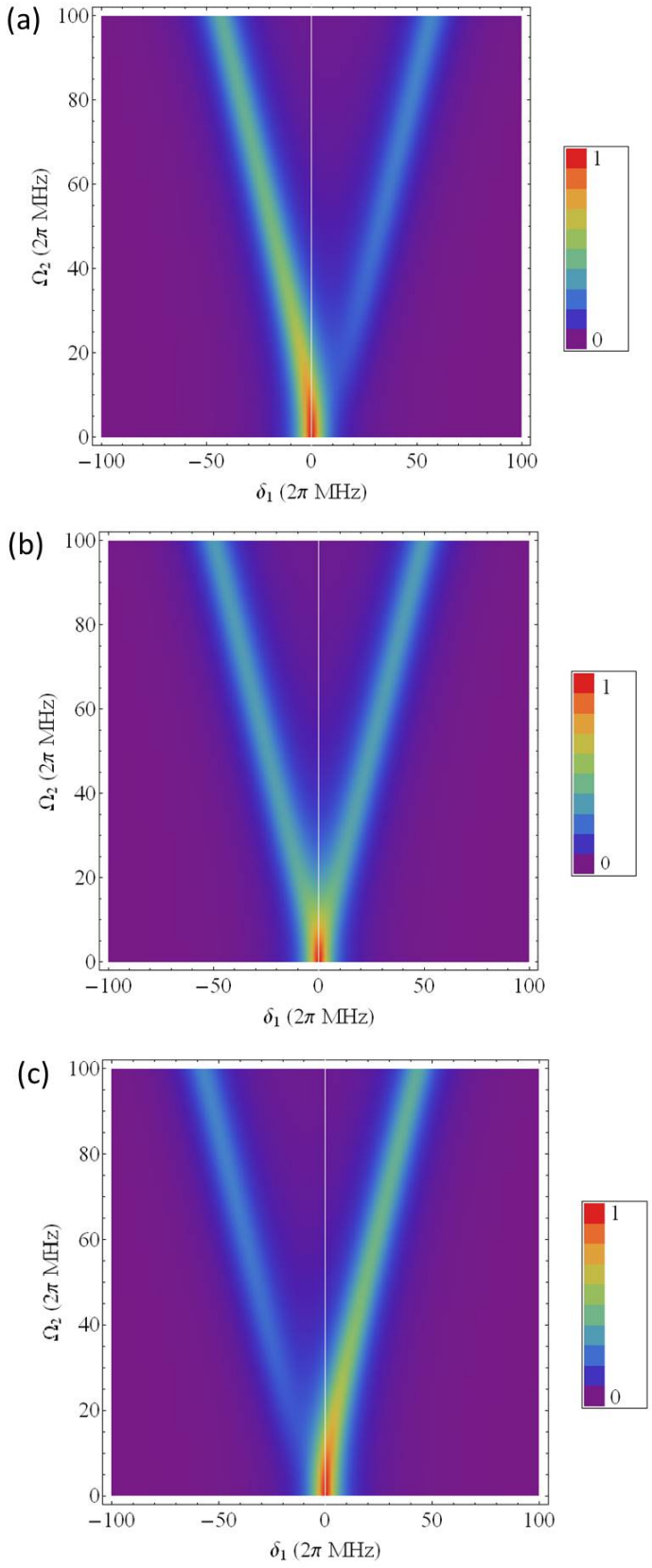


Figure 3.5: Calculated EIT spectra with $\Omega_1 = 2\pi \times 200$ kHz, $\Gamma_2 = 2\pi\times$ 10 MHz and $\Gamma_3 = 2\pi\times$ 20 MHz for the coupling beam (ω_2): (a) 14 MHz red-detuned, (b) at resonance, and (c) 14 MHz blue-detuned.

Chapter 4

Magneto-Optical Trapping of Rubidium

Atoms interacting with light may experience a mechanical force due to the light field. The deflection of atoms by light resonant with an atomic transition was first observed by Frisch in 1933 and was further explained by Ashkin in 1970 [96]. This led to the foundation of cooling and trapping neutral atoms using light beams. Cooling of atoms basically means a reduction in their average translational kinetic energy. The average kinetic energy, in one dimension, z, of a sample of atoms with a Maxwell–Boltzmann velocity distribution is given by $\langle E_z \rangle = k_B T/2$, where k_B is Boltzmann's constant and T is the temperature. Thus, the r.m.s velocity is given by [87]

$$v^{rms} = \sqrt{\frac{3k_B T}{M}}, \tag{4.1}$$

where M is the atomic mass. This chapter will cover an introduction to laser cooling and a description of the experimental setup used in our laboratory.

4.1 Radiative Optical Forces

A photon with energy $\hbar\omega$ has a momentum of $\mathbf{p} = \hbar\mathbf{k}$ with magnitude $p = \hbar\omega/c$. Absorption or emission of photons changes the momentum of atoms leading to a force, $\mathbf{F}$, on the atom such that

$$\mathbf{F} = d\mathbf{p}/dt. \tag{4.2}$$

When an on-resonance photon is absorbed by an atom, the atom makes a transition to the excited state; the atom then returns to the ground state either by spontaneous or stimulated emission. If the light intensity is low enough the atom is much more likely to return to the ground state by spontaneous emission than by stimulated emission. The fluorescent light is emitted in a random direction making the average momentum change of the atom zero. However, if the absorption photons have a certain direction then there is a net force on the atom in the direction of the laser beam. This force is directly proportional to the scattering rate, Γ_s, and is given as

$$\mathbf{F} = \hbar \mathbf{k} \Gamma_s, \tag{4.3}$$

where Γ_s is given by Eq. 3.36 for a stationary two-level atom.

An atom moving with a velocity, $\mathbf{v}$, observes a Doppler shift of $\omega_D = -\mathbf{k} \cdot \mathbf{v}$ in the frequency of the interacting photon. Thus, the scattering force can be written as

$$\mathbf{F} = \hbar \mathbf{k} \frac{\Gamma}{2} \left[\frac{s_0}{1 + s_0 + (2(\delta + \omega_D)/\Gamma)^2} \right] \tag{4.4}$$

using equation Eqs. 3.36 and 3.33.

The maximum deceleration is given as $\mathbf{a}_{max} = \mathbf{F}_{max}/M = \hbar \mathbf{k} \Gamma/(2M)$ which is fixed by atomic parameters. Maximum deceleration requires $s_0 \gg 1$ and $(\delta + \omega_D) \ll \Gamma$, i.e. the intensity should be high and the light should be nearly resonant with the atoms in their rest frame. If the light source is nearly monochromatic then, as the atoms slow down in the beam, their Doppler shift changes which brings them out of resonance. Hence, to have an effective cooling mechanism we must have $(\delta + \omega_D) \ll \Gamma$ either by changing $\omega_D (= -\mathbf{k} \cdot \mathbf{v})$ or $\delta (= \omega - \omega_0)$ for the decelerating atoms. The most common way to do this is to change ω_0, the atomic resonance frequency, by using a spatially inhomogeneous DC magnetic field which will be described later in this chapter.

4.2 Optical Molasses

In 1975, Hänsch and Schawlow proposed laser cooling of atoms by introducing the idea of illuminating atoms from all directions with a laser beam tuned slightly below the atomic absorption line [97]. Let us consider the case where an atom is illuminated by two counter-propagating beams with red-detuning ($\delta < 0$) as shown in Fig. 4.1. An atom moving towards a beam sees the frequency of

the beam shifted closer to the resonance, whereas for the beam in the opposite direction it sees the frequency to be shifted away from the resonance. Thus, the atom predominately scatters photons from the beam it is moving towards and slows down. The total force on the atom can be given by the addition of the

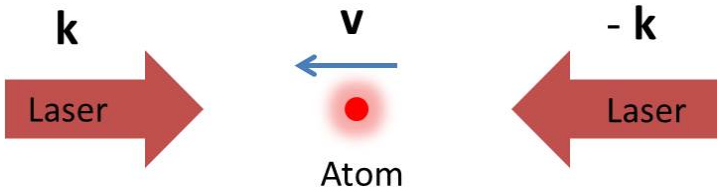


Figure 4.1: One-dimensional Doppler cooling. **v** is the velocity of atom and **k** is the wavevector of the light moving in the opposite direction to it.

forces due to the two beams, $\mathbf{F}_{1D} = \mathbf{F}_+ + \mathbf{F}_-$ where

$$\mathbf{F}_\pm = \pm\hbar\mathbf{k}\frac{\Gamma}{2}\left[\frac{s_0}{1+s_0+(2(\delta\mp|\omega_D|)/\Gamma)^2}\right]. \tag{4.5}$$

$$\Rightarrow \mathbf{F}_{1D} \simeq \frac{8\hbar\mathrm{k}^2\delta s_0\mathbf{v}}{\Gamma(1+s_0+(2\delta/\Gamma)^2)^2}, \tag{4.6}$$

where terms of the order of $(\mathrm{kv}/\Gamma)^4$ and higher are neglected [89]. Velocity dependence of this function is shown in Fig. 4.2.

Irrespective of the direction of **v**, the force is of the form

$$\mathbf{F}_{1D} = -\alpha\mathbf{v}, \tag{4.7}$$

where α is the damping or friction coefficient given by

$$\alpha = \frac{8\hbar\mathrm{k}^2(-\delta)s_0}{\Gamma(1+s_0+(2\delta/\Gamma)^2)^2}. \tag{4.8}$$

Eq. 4.7 describes the motion of a particle in a viscous medium where the motion is damped in both directions. Thus, the velocity of the atoms is damped towards v = 0 (with a spread around zero due to the stochastic nature of the absorption and spontaneous emission processes). This is why this arrangement of counter-propagating beams is called an "*optical molasses*". This one dimensional arrangement can be extended to three-dimensions with six beams instead of two in order to get damping of all the velocity components. However, it is to be noted that optical molasses is not a trap for neutral atoms since there is no

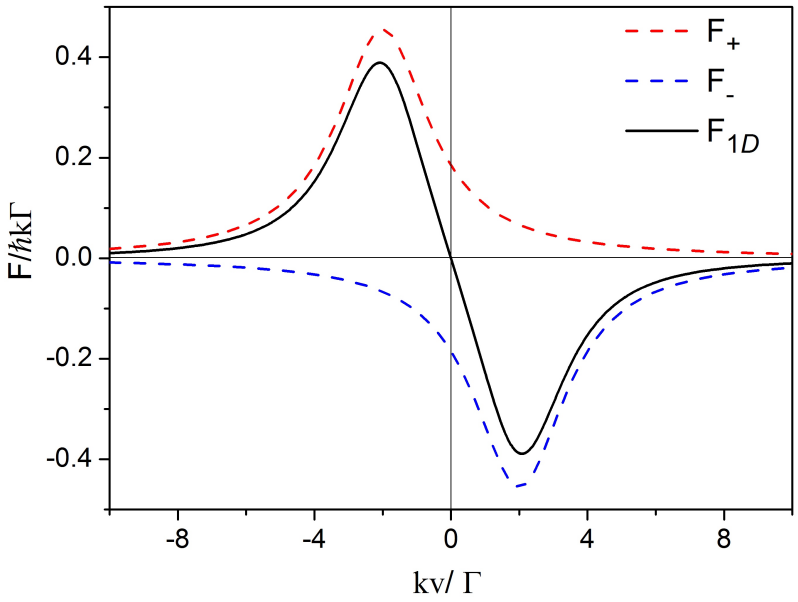


Figure 4.2: Velocity dependence of the damping force in one-dimension for $\delta = -2\Gamma$ and $s_0 = 10$. Near v = 0 m/s, the total force on the atom varies linearly with the velocity.

restoring force on them when they have moved away from the centre, but it is possible to confine atoms in a small region for times of the order of 0.1 s [98]. The confinement of atoms together with the damping of the velocity can be achieved using a magneto-optical trap (MOT), which was first realised in 1987 [99].

4.3 Magneto-Optical Trap

The position dependent force mentioned earlier is created using an inhomogeneous magnetic field to create a trapping region with appropriate polarisations of the laser beams. Let us consider a simplified one-dimensional model for an atom with a transition from a ground to an excited state, $J_g = 0 \rightarrow J_e = 1$, illuminated by two counter-propagating circularly polarised beams of same helicity, red-detuned by δ from the atomic transition. Assume the Zeeman shift due to the applied magnetic field is of the form $\beta_g z$, where z is the coordinate with respect to the centre and β_g is the Zeeman shift gradient. This provides an up shift of the $m'_J = +1$ energy level and a down shift of $m'_J = -1$ for $z > 0$, and a reverse for $z < 0$ (Fig. 4.3). Also, we know that σ^+ excites $\Delta m_J = +1$ and σ^- excites $\Delta m_J = -1$. An atom located at $z < 0$ would have the $m_J = 0 \rightarrow m'_J = +1$ transition closer to the laser frequency and if the atom is moving towards $-z$ then it would scatter σ^+ more efficiently and would be pushed towards the centre.

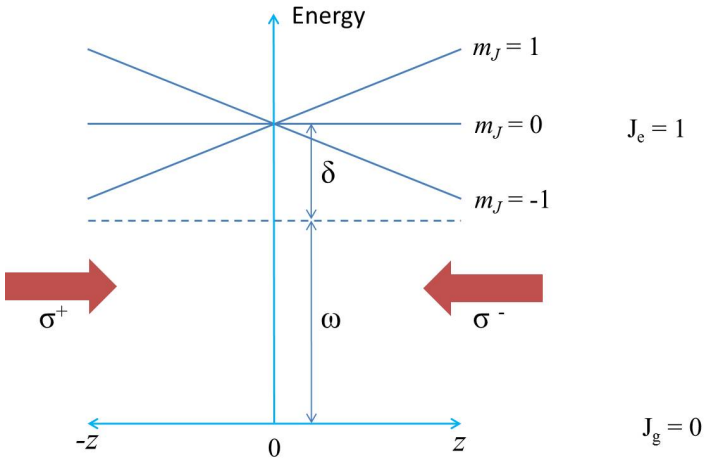


Figure 4.3: One-dimensional MOT scheme.

Similarly, an atom at $z > 0$ would scatter the σ^- beam more efficiently if it is moving away from the centre and would be pushed back again towards the centre. The force on the atom in an 1-D molasses is

$$\mathbf{F}_{MOT} = \hbar\mathbf{k}\frac{\Gamma}{2}\left[\frac{s_0}{1+s_0+(2(\delta-\eta)/\Gamma)^2} - \frac{s_0}{1+s_0+(2(\delta+\eta)/\Gamma)^2}\right], \tag{4.9}$$

where $\eta = \mathrm{kv} + \beta_g z$, which depends on both the velocity and the position of the atom. This can be further simplified similar to Eq. 4.6 such that

$$\mathbf{F}_{MOT}(\mathrm{v}, z) \simeq \frac{8\hbar\mathrm{k}s_0\delta(\mathrm{kv}+\beta_g z)}{\Gamma\left[(1+s_0+(2\delta/\Gamma)^2\right]^2}, \tag{4.10}$$

which, in the low-velocity limit, leads to damped harmonic oscillation of atoms governed by the equation

$$\ddot{z} + \Gamma_{MOT}\dot{z} + \omega_{MOT}^2 z = 0, \tag{4.11}$$

where $\Gamma_{MOT} = \alpha/M$ is the damping rate (α is given by Eq. 4.8) and $\omega_{MOT} = \sqrt{\beta_g\alpha/\mathrm{kM}}$ is the oscillation frequency. This scheme can be extended to three -dimensions with six beams crossing at the centre of the trapping region. Three pairs of σ^+ and σ^- beams are arranged in three orthogonal directions. A suitable magnetic field can be generated using two coils arranged in anti-Helmholtz configuration, each carrying a current, I, in opposite directions. Which beams should be σ^+ is determined by the direction of the flow of currents in the coils. Fig. 4.4 shows an example of the set up.

A MOT can be formed using three retro-reflected beams instead of six inde-

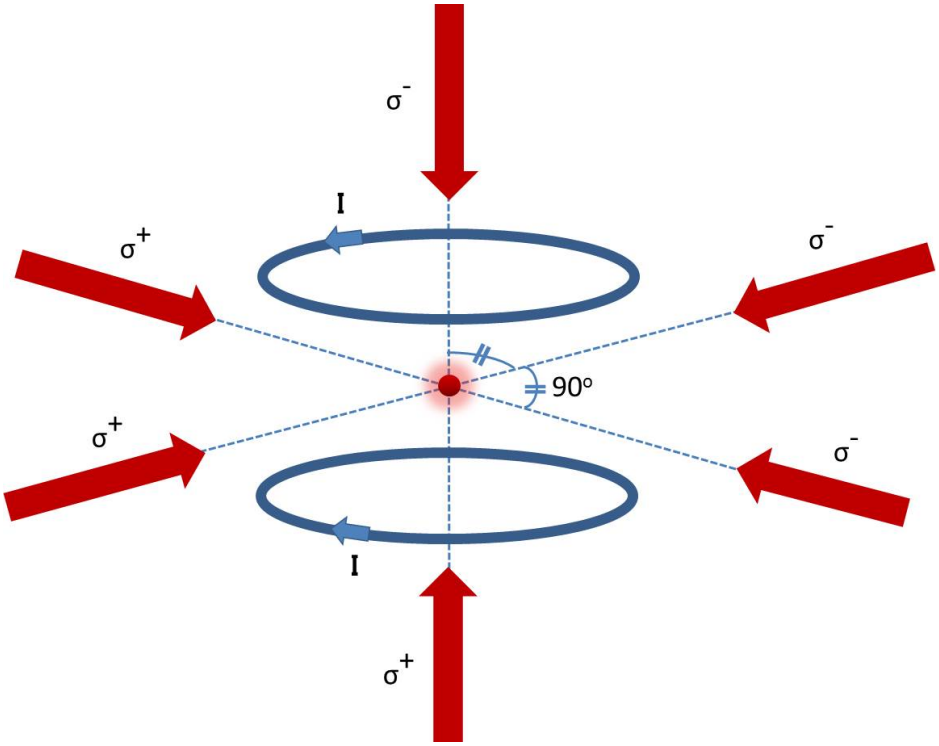


Figure 4.4: Three-dimensional MOT scheme arrangement.

pendent beams. During reflection a mirror reverses the helicity of a circularly polarised beam, hence a quarter-waveplate (QWP) must be placed in the beam path just before the reflecting mirror in order to get the original helicity of the beam back. For example, if a σ^+ beam is sent to the MOT from the left then, after passing the MOT centre, it should pass through a QWP and next reflect from a mirror and pass back through the QWP again before reaching the MOT centre in order to get σ^- polarisation of the beam.

A MOT requires an ultra-high vacuum (typically better than 10^{-8} mbar) in order to reduce collisions of the atoms in the molasses, otherwise the atoms being cooled would be hit by hot, high velocity atoms and could be lost. The detuning of the cooling beams is typically twice the natural linewidth of the transition with an intensity a few times the saturation intensity. The cooling beams address a closed cycle transition so that the atoms scatter the light continuously without being lost to any other state. The energy level diagram for ^{87}Rb is shown in Fig. 4.5. The ground state has two levels, with the upper being used for cooling. However, any cycling transition is never ideal and, hence, a repump beam is used to bring the atoms lost to the lower ground state back to the upper ground state addressed by the cooling beams.

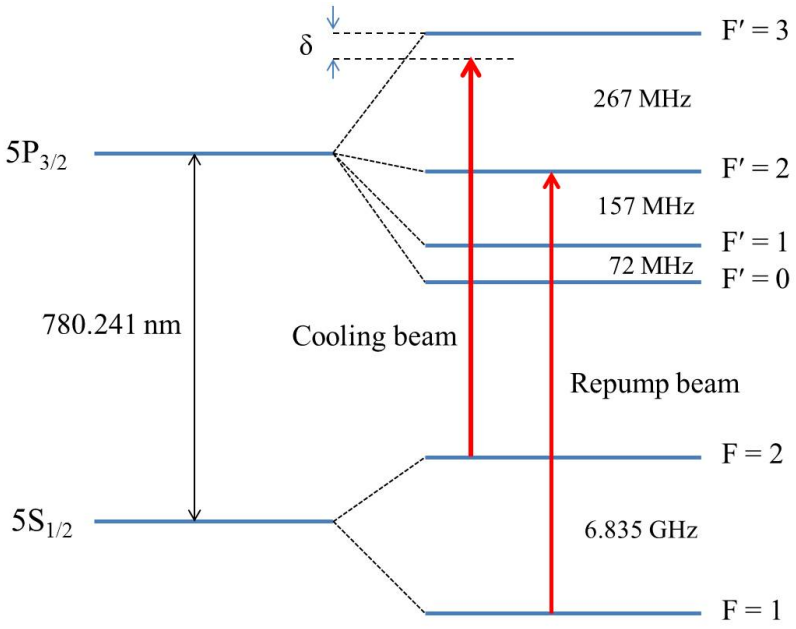


Figure 4.5: Energy level diagram for ^{87}Rb showing the hyperfine transitions. δ is the detuning of the cooling beams.

4.4 Cooling and Trapping Rubidium Atoms

It is most common to use the magneto-optical trapping technique to trap alkali atoms due to their simple atomic structure with only one free electron and offering the possibility of a cycling transition ($5^2S_{1/2} \rightarrow 5^2P_{3/2}$). Some relevant physical properties of ^{87}Rb is given in Table 4.1, and the optical properties of the cycling transition is given in Table 4.2.

Table 4.1: Physical properties of ^{87}Rb

Atomic number	37
Total nucleons	87
Relative Natural Abundance	27.83 %
Nuclear Lifetime	4.88 $\times 10^{10}$ yr
Atomic mass	1.44316065 $\times 10^{-25}$ kg
Vapour Pressure at 25°C	3.92 $\times 10^{-7}$ torr
Nuclear spin	3/2

Table 4.2: Optical properties of ^{87}Rb D_2 transition ($5^2S_{1/2} \rightarrow 5^2P_{3/2}$)

Frequency	$2\pi\times$384.2305 THz
Wavelength (Vacuum)	780.2412 nm
Wavelength (Air)	780.0333 nm
Lifetime	26.235 ns
Natural Line Width (FWHM)	$2\pi\times$6.067 MHz
Recoil Velocity	5.8845 mm/s
Recoil Temperature	180 nK
Doppler Temperature	145.57 μK
Saturation Intensity ($\sigma^{\pm}$ light)	1.669 mW/cm^2
Resonant Cross Section ($\sigma^{\pm}$ light)	2.9067×10^{-9} cm^2

4.4.1 Rubidium atoms

We use Rb due to its high scattering cross-section and availability of suitable commercial diode lasers to address the required transitions, as shown in Fig 4.5. ^{87}Rb is an isotope of rubidium with a relative natural abundance of 27.83 %; it is not a stable isotope, but has an extremely slow decay rate making it effectively stable (Table 4.1). The fine structure of ^{87}Rb has two transitions, $5^2S_{1/2} \rightarrow 5^2P_{3/2}$ (the D_2 line) and $5^2S_{1/2} \rightarrow 5^2P_{1/2}$ (the D_1 line), which, additionally, have hyperfine structures (see Fig 4.5 for the D_2 line). The fine structure is a result of the coupling between the orbital angular momentum, **L**, of the outer electron and its spin angular momentum, **S**, and the hyperfine structure is a result of the coupling of the total electron angular momentum, **J**, with the total nuclear angular momentum, **I**. The total electron angular momentum is given by **J** =**L**+**S**, with the condition that the corresponding quantum number must lie in the range $|L - S| \leq J \leq L + S$. For the ground state of ^{87}Rb, L=0 and S=1/2 so J=1/2, whereas for the first excited state L=1, so J=1/2 or 3/2. The atomic angular momentum, **F**, is given by **F** = **J**+**I**, with the condition that $|J - I| \leq F \leq J + I$. For ^{87}Rb, I=3/2. Thus, for the ground state, F =1 or 2, and for the excited state of the D_2 line, which is of interest to us due to the presence of the cycling transition as already mentioned, F = 0, 1, 2 or 3. Each of the hyperfine (F) energy levels contains 2F + 1 magnetic sublevels, m_F, which are degenerate in the absence of any external magnetic field; however, the degeneracy is broken when an external magnetic field is applied. The sublevels determine the angular distribution of the electronic wavefunction and the atomic interaction with the

magnetic field (**B**) is described by the Hamiltonian

$$H_B = \frac{\mu_B}{\hbar}(g_S\mathbf{S} + g_L\mathbf{L} + g_I\mathbf{I}) \cdot \mathbf{B}, \tag{4.12}$$

where g_S, g_L and g_I are the electron spin, electron orbital and the nuclear "g-factors", respectively, and account for the corresponding modifications to the dipole moment. For a magnetic field along the z-direction with magnitude B_z, Eq. 4.12 can be written as

$$H_B = \frac{\mu_B}{\hbar}(g_S\mathrm{S}_z + g_L\mathrm{L}_z + g_I\mathrm{I}_z)\mathrm{B}_z. \tag{4.13}$$

If the energy shift due to the magnetic field is small compared to the hyperfine splittings H_B can be expressed as [100]

$$\begin{aligned} H_B &= \frac{\mu_B}{\hbar}(g_J\mathrm{J}_z + g_I\mathrm{I}_z)\mathrm{B}_z \\ \Rightarrow H_B &= \frac{\mu_B}{\hbar}g_F\mathrm{F}_z\mathrm{B}_z, \end{aligned} \tag{4.14}$$

where g_F is the hyperfine Landé g-factor.

For weak magnetic fields, the interaction Hamiltonian, H_B, perturbs the zero-field eigenstates giving rise to the splittings between adjacent magnetic sublevels

$$\Delta E_{|F,m_F\rangle} = \mu_B g_F m_F \mathrm{B}_z. \tag{4.15}$$

The splitting is linear in this regime and is called the Zeeman effect.

4.4.2 Optical setup

For ^{87}Rb atoms the cycling transition is $5\mathrm{S}_{1/2}$ F=2 $\rightarrow$ $5\mathrm{P}_{3/2}$ F′=3 and the red-detuned cooling beams address this transition. With a probability of around 1:1000, an atom undergoing this cycle may decay to the $5\mathrm{S}_{1/2}$ F=1 state and will no longer be cooled, hence, a repump beam tuned to $5\mathrm{S}_{1/2}$ F=1 $\rightarrow$ $5\mathrm{P}_{3/2}$ F′=2 is needed to bring the atom back into the cooling cycle. The two lasers we use (Toptica, DL100 pro) are extended cavity diode lasers (ECDLs) with a central wavelength of 780.2 nm. These are narrow linewidth (<1 MHz) tunable lasers which can be locked to any hyperfine transition of Rb using a saturable absorption spectroscopy system (CoSy, Toptica).

A schematic of the experimental setup for the MOT is shown in Fig. 4.6. The

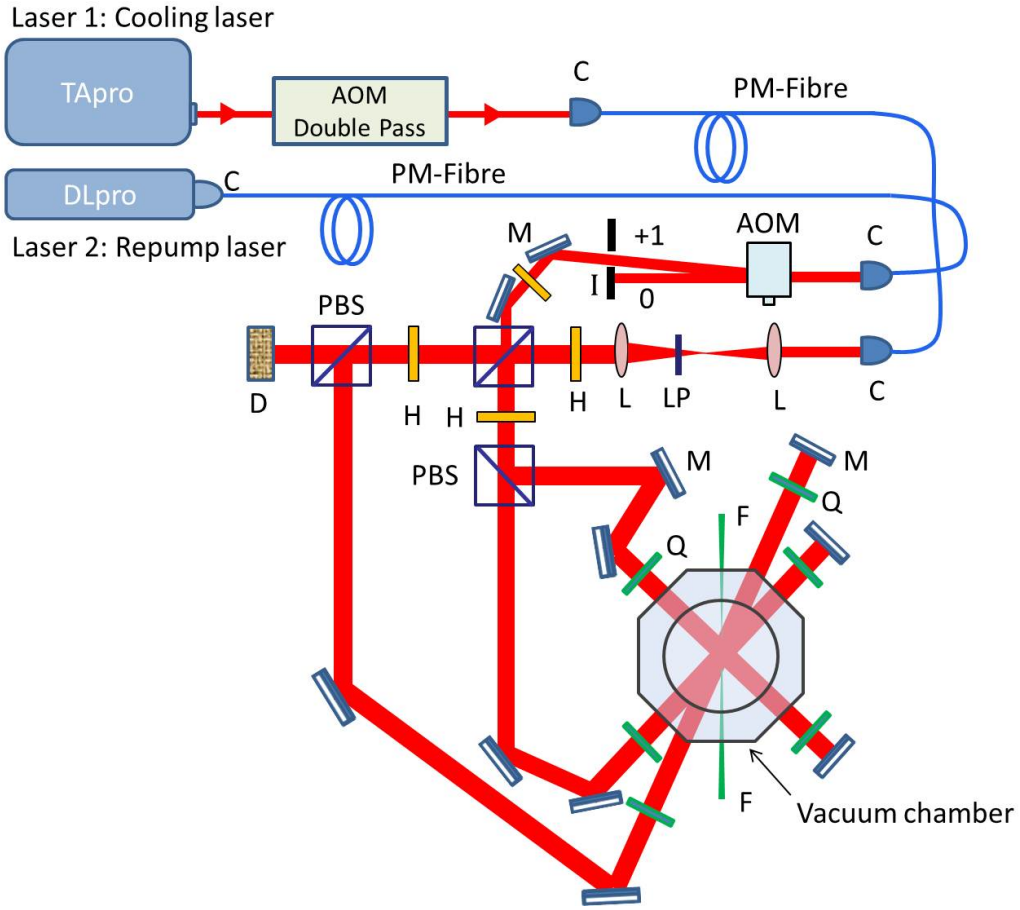


Figure 4.6: Schematic of the optical setup for the MOT. C: Fibre coupler, L: Convex Lens, LP: Linear polariser, M: Mirror, H: Half Waveplate, Q: Quarter Waveplate, PBS: Polarisation beam splitter, PM-Fibre : Polarisation maintaining fibre, I: Iris, +1: First order beam, 0: Zeroth order beam, D: Beam dump, F: ONF pigtail.

cooling beam is derived from a laser (say, Laser1) locked at the $5S_{1/2}F{=}2 \rightarrow 5P_{3/2}F'{=}(2,3)_{co}$ crossover peak of ^{87}Rb, and a beam derived from this laser is passed through a double-pass AOM (ATM-602DA2B, IntraAction Corp., central frequency: 60 MHz)(see Fig. 4.7) which brings the frequency of the beam to 14 MHz red-detuned from the cycling transition. This beam is coupled to a polarisation maintaining single mode fibre and brought near to the cold atom setup where it is out-coupled and passed through a telescope setup to get a collimated beam of 18 mm diameter. The beam is then split into three equal intensity beams using polarisation beam spliters (PBSs) and half-waveplate (HWPs) combinations. These three beams are made circular by passing through quarter-waveplates (QWPs) and passed through the vacuum chamber along three axes, which intersect at the centre of the vacuum chamber, using two mirrors per beam. After passing through the chamber, each beam is again passed through a QWP

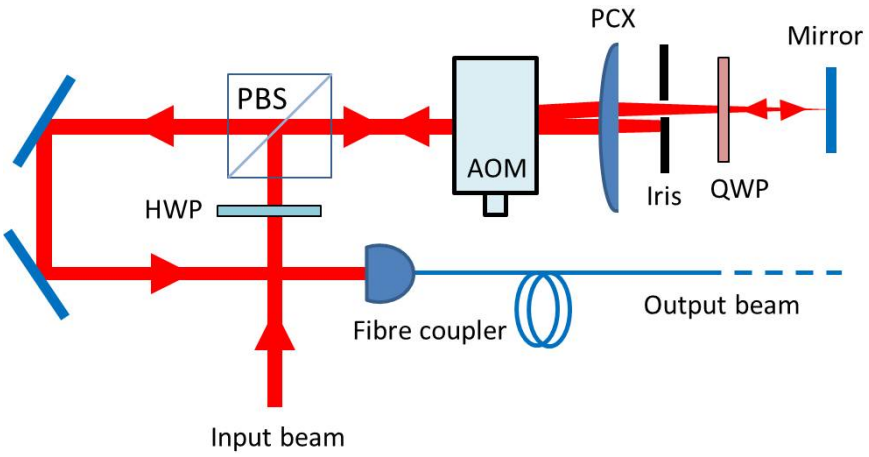


Figure 4.7: Schematic of a typical AOM double-pass setup. The incoming beam is linearly polarised and reflected completely at the PBS to pass through the AOM and a plano-convex lens (PCX). The first order beam is allowed to pass through the aperture in the pathway and the zeroth order beam is blocked. A mirror kept at the focal point of the PCX back-reflects the beam on the same path through the AOM. The beam passes through a QWP twice which rotates the polarisation of the beam by 90° to ensure that the beam coming to the PBS does not go to the input side but passes straight which is then coupled to a fibre coupler to transport. The advantage of using a double-pass AOM is that the position of the final beam is invariant with the amount of frequency shift introduced by the AOM and the coupling remains consistent for different frequency shifts.

and back reflected by a mirror. All the back reflected beams are aligned to overlap with the corresponding incoming beams. The polarisations of the beams are set, as depicted in Fig. 4.4, using QWPs in the beam paths. The intensity of each of the cooling beams is ∼6 mW/cm^2. A repump beam derived from a laser, say 'laser 2', locked to $5S_{1/2}F{=}1 \rightarrow 5P_{3/2}F'{=}(0,2)_{co}$ is passed through an AOM (ATM-1102DA2B, IntraAction Corp., central frequency: 110 MHz) to bring it close to the transition $5S_{1/2}F{=}2 \rightarrow 5P_{3/2}F'{=}2$. This allows us to have fast switching of the beam as required. The repump beam after passing through the AOM is overlapped to the cooling beams (see Fig. 4.6). The intensity of the repump beam is ∼4 mW/cm^2.

4.4.3 Magnetic field

The magnetic field required for trapping is created using two magnetic coils placed in a roughly anti-Helmholtz configuration at the two sides of the vacuum chamber with the axis of the coils aligned along a pair of the counter-propagating cooling beams (Fig. 4.9). The radius of each coil is 75 mm and the separation between the

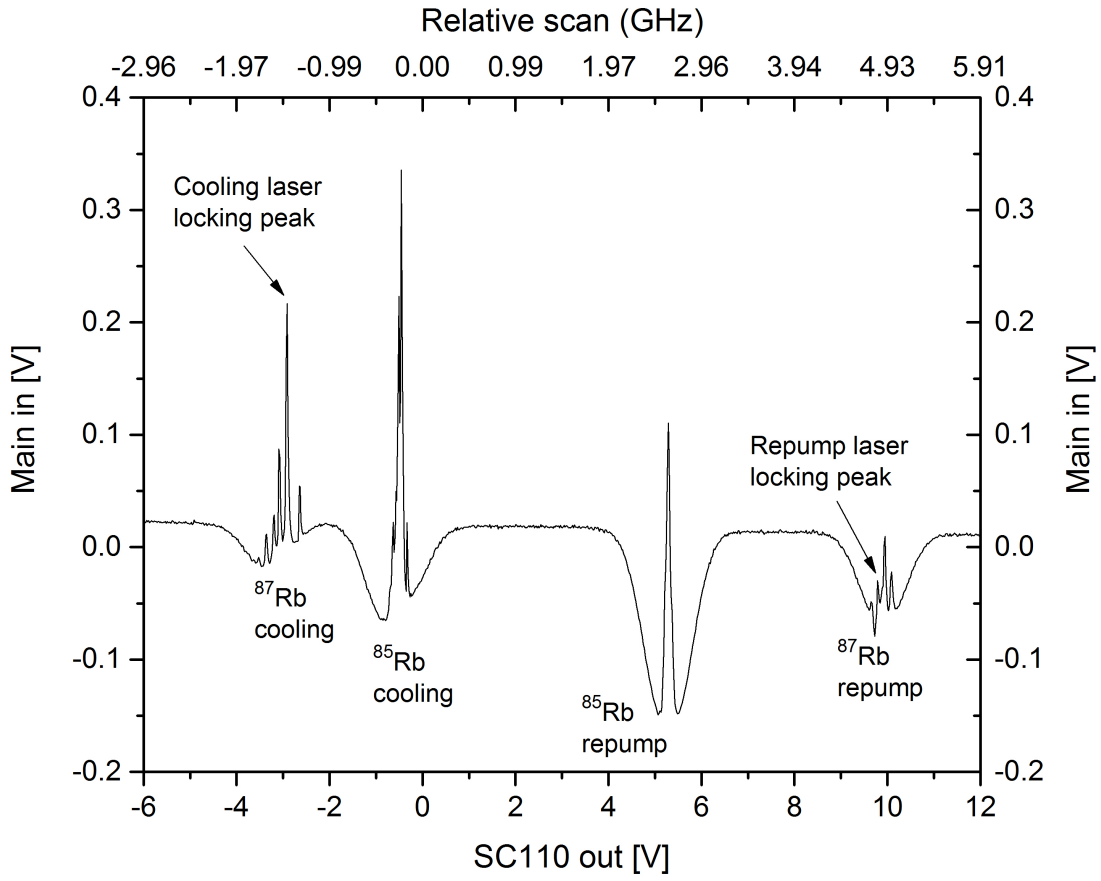


Figure 4.8: Saturable absorption spectrum of rubidium obtained from the locking interface (DigiLock, Toptica) showing the cooling and repump transitions of both isotopes with locking peaks for the cooling and the repump lasers. The upper x-axis has been converted to a frequency scan.

coils is 90 mm. Each coil has 200 turns of enamelled copper wire to support the flow of current. Since the two coils are identical to each other and the currents flow in opposite directions a total cancellation of the magnetic field at a half distance between the coils along the axis results. This is at the centre of the vacuum chamber. However, what is more important in this case is the magnetic field gradient near the trapping center. Considering the coil axis to be along the z-direction and the two coils to be placed symmetrically around the centre, $z = 0$, the magnetic field gradient along the z-axis can be given as [101]

$$\frac{dB}{dz} = \frac{48a_c^2 d_c \mu_0 I N_{coil}}{(4a_c^2 + d_c^2)^{5/2}}, \tag{4.16}$$

where a_c is the radius of the coils, d_c is the separation between them, μ_0 is the permeability of the vacuum, N_{coil} is the number of turns and I is the current flowing through the coils. The gradient is constant near the centre and proportional

to the applied current. 3.75 A of current results in a magnetic field gradient of 14 Gauss/cm in the axial direction and 7 Gauss/cm in the radial direction.

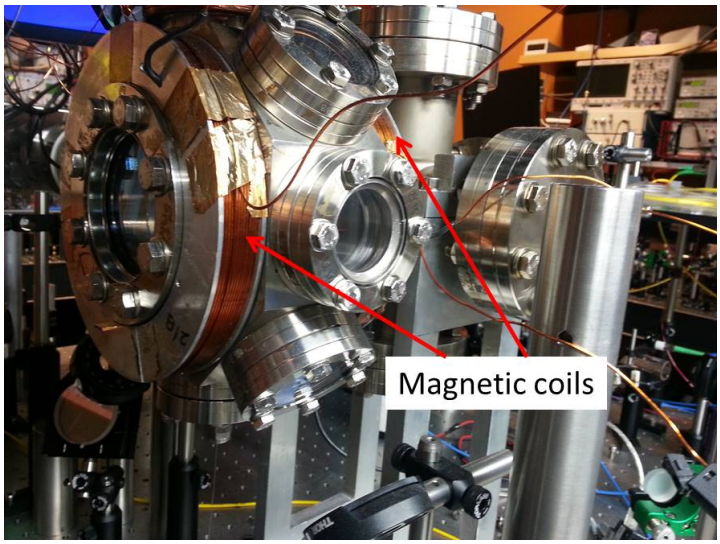


Figure 4.9: A picture of the vacuum chamber with the magnetic coils used for creating the MOT.

4.4.4 Ultra-high vacuum system

An ultra-high vacuum (UHV) is a requirement to trap atoms in a MOT. UHV is created using a combination of a scroll pump and a turbo-molecular pump ('TPS Compact' equipped with TV81M turbo-molecular pump, Agilent Technologies) initially and is maintained with the continuous operation of an ion-pump (VacIon Plus Starcell 55, Varian). The connection of the MOT chamber to the vacuum system is illustrated in Fig. 4.10. The MOT chamber is custom-made of steal with an octagonal geometry with 10 windows. Eight of these are along the circumference and are 2.75″ CF (conflate flange) viewports, whereas the front and back ports are 4.5″ CF. The back port is connected to a six-way cross (6X) which has all the six ports as 4.5″ CF flanges. The back port of the 6X is fitted with a 4.5″ CF viewport, which allows beam access to the MOT chamber. The viewports have anti-reflecting coating for near-IR wavelength. The top flange of the 6X is fitted with an electric feedthrough to attach the Rb dispensers and the bottom flange is connected to a T-gate-valve (rated to 10^{-12} mbar) with manual operation. On one side a four-way cross (4X) is fitted and a blank on the other. The gate valve gives access to the TPS pump via a flexible bellow, and the 4X gives access to the ion pump utilising another bellow. A vacuum gauge (Dual Filament Bayard-Alpert Pirani Gauge, FRG730CF35S, Agilent Technologies) is installed

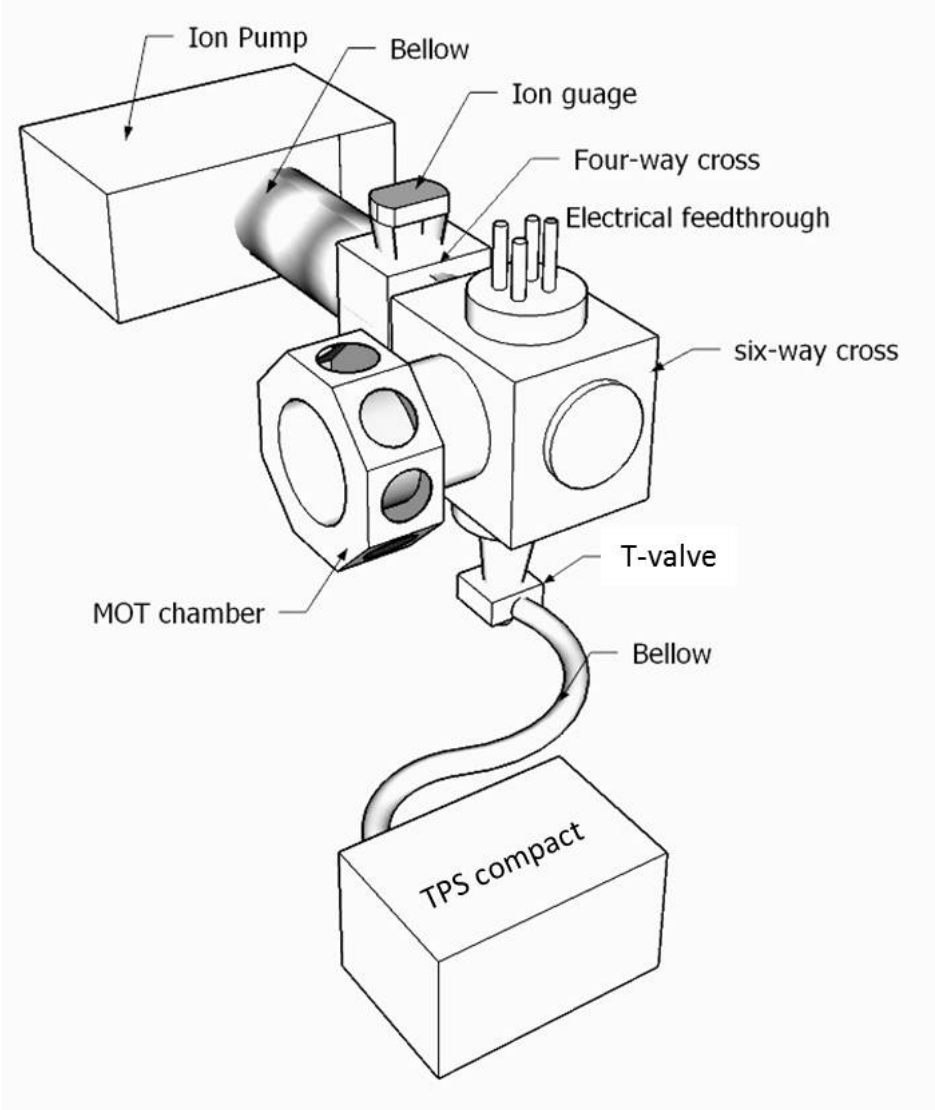


Figure 4.10: Illustration of vacuum components of the experimental setup.

on the top of the 4X, which operates in all the regions of vacuum (5×10^{-10} to 1000 mbar).

All the flanges are CF and copper gaskets are used to seal the vacuum. All the components are wiped with acetone using lint-free cloth before installation and due precautions are taken during handling to prevent any dirt/grease. The optical nanofibre is installed vertically in the MOT chamber with the help of a mounting system designed to hold the nanofibre [43]. The mount is U-shaped made from aluminum and with a length of 90 cm. The fibre to be placed in the chamber is glued on the legs of the mount in order to place the ONF at the centre of the chamber. The U-mount fits in a cylindrical base (59.5 mm long and 34 mm diameter) which gets attached to one of the flanges (top or bottom) of the vacuum

chamber. The cylindrical base has a hole along the axis which allows the fibre pigtail to pass through. The two pigtails are fed through the fibre feedthroughs connected at the top and/or bottom ports(s) of the MOT chamber using Teflon ferrule(s) [102]. The holes in the ferrule can be made using hand drills. The diameter of the holes is kept slightly larger than the fibre, e.g. for 225 μm fibre the holes are made with a 250 μm drill bit.

The T-valve connected at the bottom of the 6X opens or closes the access to the TPS pump as desired. The TPS pump is connected to the chamber using a flexible metal bellow. It has an inbuilt scroll pump which allows for operation from atmospheric pressure. When the system is switched on, the roughing pump kicks in to operation initially. After reaching the desired pressure it switches to the TMP automatically. This transition happens at a pressure in the range of 10^{-3} to 10^{-4} mbar. Finally a pressure of the order of 10^{-8} mbar is achieved after several hours of operation. At this point, baking of the whole vacuum chamber starts. The purpose of baking is to remove water and other hydrocarbons adsorbed on the internal surfaces which reduce achievable vacuum. For bake-out, heater tapes (ribbon heater, 1-5717-03 / 1-5717-01, AS ONE) with 20 mm width are wrapped around all components of the vacuum system and covered with aluminium foil to reduce heat radiation. The baking temperature is increased slowly (around 5°C every half an hour) up to 130°C. It is kept at this temperature for two days. The pressure in the chamber rises with the rise in temperature and then starts decreasing when kept at the final temperature due to cleaning of the chamber. Once bake-out is complete the temperature is reduced slowly. This reduces the pressure further to $\sim 10^{-9}$ mbar. At this stage the Rb dispenser (SAES Group) connected to the electrical feedthrough can be activated. First it must be cleaned by passing a slowly increasing current through it (around 0.5 A every 30 minutes) up to the point where degassing stops (typically 3.5-4 A). This can be identified by monitoring the pressure. With every increase in the dispenser current a sudden pressure increase can be noticed as the dispenser is not completely degassed. This continues untill maximum current reached. It is important not too have the dispenser directly facing the ion pump to avoid rapid loss of the Rb.

After the activation of the dispenser, the ion pump is switched on; it is kept at a distance of 1 m and connected to the 4X using a metal bellows. The bellows allows us to keep the ion pump away from the MOT chamber in order to minimise the effect of its strong permanent magnets. For a few hours, the TPS and the ion pump operate together. Finally the T-valve is closed tightly and the TPS is switched off. From this point only the ion pump is used to maintain pressure and

it can operate like this for years.

Some times it is possible that there is a leak in the system and the pressure does not drop as mentioned following the protocol described above. In such cases, the leak is identified by putting isopropyl-alcohol near the copper gaskets through the access grooves on the CF flanges. When alcohol is injected the pressure in the chamber rises quickly if there is a leak. In this case, the flange is further tightened. Also, the Teflon ferrule is a potential source for a leak. Often during the cooling down of the system towards the end of the bake-out, if there is no pressure decrease with the reduction in temperature, then most likely the leak is from the Teflon ferrule. In this case, after slightly tightening the Swagelok holding it (around one-fourth to half a turn), the pressure starts decreasing rapidly. Once the vacuum is created it remains stable, provided the pumping speed of the ion pump (in our case, 50 l/s) is appropriately chosen according to the volume of the vacuum chamber. In fact, no vacuum system can ever be absolutely vacuum-tight but the leak rate has to be low enough so that it can be pumped out without influencing the pressure in the vacuum chamber.

For creating the trap, the Rb dispenser is switched on at the operation current of 3.7 A (the current at which there is no degassing and enough atoms are in the chamber). It remains on as long as cold atoms are required. After around half an hour of switching on the dispenser (this could be hours for the first operation), cold atoms can be generated by switching on the magnetic field and allowing the lasers, locked at the appropriate transitions, to form the optical molasses. The cold atoms can be monitored using CCD/CMOS cameras.

4.5 Conclusion

This chapter describes laser cooling of atoms in a MOT and provides details of the MOT setup. The force exerted on an atom by near-resonant light is described and the theory is extended to describe the cooling of atoms in an optical molasses and magneto-optical trapping. Details of the experimental setup for cooling and trapping of ^{87}Rb atoms are provided.

Chapter 5

Temperature Measurement of Cold Atoms Using an Optical Nanofibre

5.1 Fluorescence Measurements Using an Optical Nanofibre

An ONF can be used for sensing cold atoms which are typically at sub-mK temperatures, mainly utilizing fluorescence or absorption techniques [41, 42, 44, 46]. A cold atom cloud is formed around the ONF in a MOT as described in Chapter 4. Two cameras imaging the cloud in orthogonal directions help to identify the position of the ONF in the cloud. The densest region is overlapped with the ONF precisely using additional, small magnetic coils which can shift the magnetic zero position in the vacuum chamber. This is optimised by changing the current through the alignment coils in order to maximise the atomic fluorescence collected by the ONF. A basic schematic of the setup is shown in Fig. 5.1(a) and an image of the cold atom cloud overlapped on an ONF can be seen Fig. 5.1(b).

5.1.1 MOT loading and effective number of atoms

Fluorescence coupled into the ONF is determined by connecting one of the fibre's pigtails to a single photon counting module (SPCM-AQR-14, Perkin and Elmer, quantum efficiency = 60% at 780 nm). Photons emitted by the atoms couple

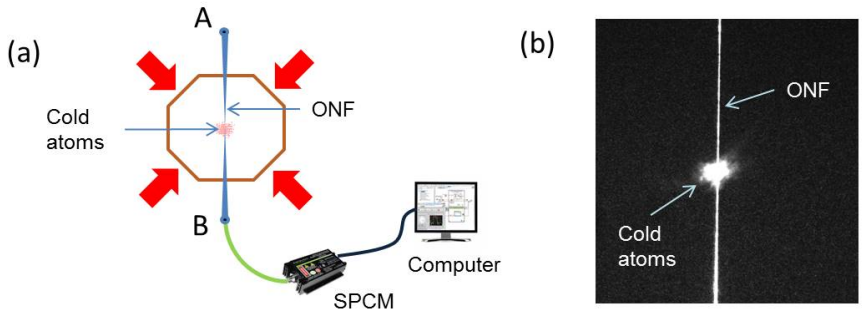


Figure 5.1: (a) Illustration of a basic setup with an ONF. A, B: pigtail ends. SPCM: Single photon counting module. ONF: Optical nanofibre. (b) An image of the cold atom cloud with the ONF taken using a CMOS camera (DCC1545M, Thorlabs). The fibre is visible due to MOT beams scattering off it.

to the guided modes of the ONF though its waist by evanescent field coupling and travel along the two pigtails where they can be detected. Along with the fluorescent photons, the MOT beams also couple to the ONF in a similar manner. The contribution due to MOT beams can be identified by taking the measurement with the MOT magnetic fields switched off, i.e. in the absence of the cold atom cloud. Fig. 5.2 shows an example of the fluorescence coupling illustrating the loading of the cloud from the background Rb vapour. A steady state is reached when the number of atoms being collected in the trap equalises the number lost from the trap due to collisions or optical interactions. The time constant to reach the steady state depends on the pressure in the chamber; however, the steady-state number of atoms does not [103].

The photon counts registered by the SPCM may differ depending on the density of the MOT and the overlap of the cloud with the ONF. The collected fluorescence is only from one of the pigtails, whereas a similar magnitude signal should be detectable at the other pigtail as well, since the photons that couple to the waist could travel in either direction along the fibre in equal proportion. Mainly those atoms within the evanescent field region of the ONF contribute to any signals obtained. The decay length, $d_l = 1/q$, (see Eq. 2.43) for 780 nm light for an ONF of diameter 350 nm is 268 nm. We can estimate the number of atoms present within the decay length region as follows and it is based on the number of atoms present in the trap. There are $\sim 10^7$ atoms in the MOT, estimated from the fluorescence from the cloud measured using a photodiode (DET36A, Thorlabs) with a convex lens placed at the aperture focussing on the MOT. The cloud diameter is 0.8 mm as measured by taking an image using the CMOS camera. The number density of atoms, $\rho_d(r, z)$, in the MOT can be taken as a Gaussian

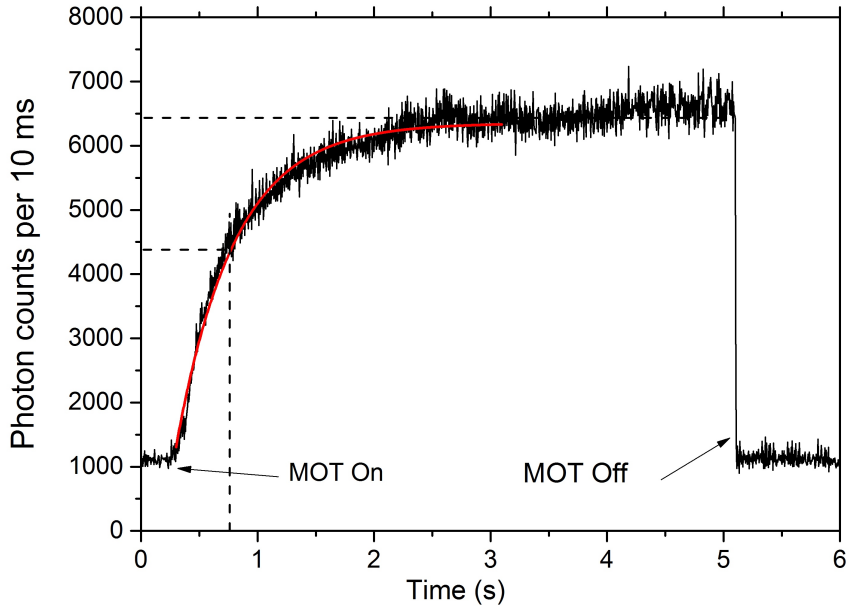


Figure 5.2: Photon counts registered by the SPCM during the loading of atoms in the MOT. The magnetic field for the MOT is switched on at $t = 0.25$ sec, and switched off at $t = 5.1$ sec. The loading of the MOT takes 0.5 sec as obtained by the exponential fit (solid red line) to the loading curve. The dashed vertical line is placed at the loading time position.

distribution modified due to the presence of the ONF, such that

$$\rho_d(r,z) = \frac{N}{\sigma_r^3(2\pi)^{3/2}} e^{-(r^2+z^2)/\sigma_r^2} g(r), \tag{5.1}$$

where r is the radial coordinate, z is the axial coordinate, σ_r is the radius of the cloud[1], N is the total number of atoms and $g(r) = 1 - \text{Arcsin}(a/r)/\pi$ is a modification factor due to the presence of the ONF [104]. Integrating Eq. 5.1 over r and z with the limits $a < r < (a + d_l)$ and $-\sigma_r < z < \sigma_r$, respectively, we get the effective number of atoms in the evanescent field region to be less than 2 (in fact 1.2, which we use in later calculations). The fluorescence photon count, n_p, collected by the ONF for these atoms can be estimated using the relation [41]

$$n_p = N_{eff}\eta_{ONF}\Gamma_s T_r \eta_D, \tag{5.2}$$

where N_{eff} is the effective number of atoms contributing to the signal, η_{ONF} is the averaged coupling efficiency of spontaneous emission to the guided mode of the ONF, Γ_s is the atomic scattering rate, T_r is the transmission of the ONF from the waist to one end and η_D is the detector quantum efficiency. N_{eff} can be taken as the number of atoms in the evanescent field region. η_{ONF} is $\sim 6\%$

[1] σ_r = FWHM/2.3548

based on the calculation with Cs atoms [23, 41]. This is an estimate value only for Rb as it is assumed it would behave similarly to Cs. $\Gamma_s = 1.8 \times 10^7$ calculated using Eq. 3.36 for the collective intensity of the six circularly polarised MOT beams as 36 mW/cm^2 with a red-detuning of 14 MHz. T_r and η_D are 0.91 and 0.6, respectively, for the ONF and detector used. This calculation provides n_p as 7×10^5/s, which reasonably agrees with observations presented in Section 5.2.

5.1.2 Temperature measurement by the release-recapture technique

The average temperature of the cold atom cloud can be measured using the fluorescence collected by the ONF in several different ways. Two different methods have been used in the group: (i) a forced oscillation method in which the cloud is oscillated by applying a periodic, spatially varying, magnetic field generated by the trapping coils while collecting the fluorescence during the oscillation [46], and (ii) a release-recapture (RR) method in which the cloud is allowed to expand by switching off the optical molasses and recapturing the atoms after a variable time [47]. Published work on this topic is given in Appendix A.

In this section, we focus on the RR technique and compare the results with the measured temperature by the more conventional technique of time-of-flight. In the RR technique, the MOT is turned off for a short duration (the 'release time') to allow the cloud to expand ballistically and then switched on again to recapture the atoms which could not escape the MOT region during the release time. The fraction of atoms recaptured as a function of the release time gives an estimate of the cloud temperature. Assuming a Maxwellian distribution of the atomic velocities in the sample, and neglecting the effect of gravity, the fraction of the total number of trapped atoms recaptured after a release time, t_r, is [105]

$$f_r = -\left(\frac{2}{\sqrt{\pi}}\right)\frac{v_c}{v_T}e^{-v_c^2/v_T^2} + \mathrm{Erf}\left(\frac{v_c}{v_T}\right), \tag{5.3}$$

where $v_T = \sqrt{2k_BT/M}$ is the thermal velocity of the the atoms at a temperature T and $v_c = R_c/t_r$ is the velocity of an atom that is high enough for it to escape from the trap during time t_r. R_c is the radius of the MOT beams characterising the trapping region. The recaptured fraction, f_r, is quantified by two methods: (i) the photon counts measured after the recapture process compared with the total counts obtained before releasing and (ii) comparing the amount of fluorescence

collected by a CMOS camera imaging the cloud after recapture and before release of the atoms. Experiments are performed for various release times in steps of 10 ms. The obtained data in both cases are fit with Eq. 5.3 to get the corresponding temperature values.

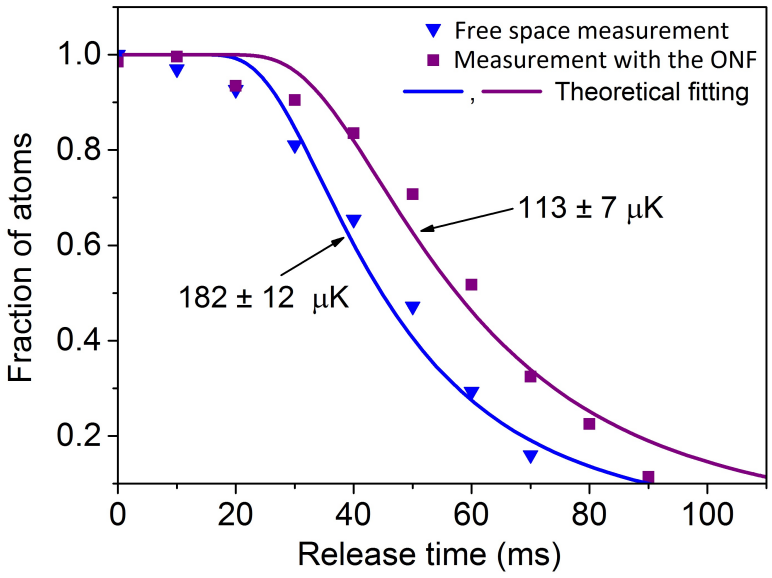


Figure 5.3: Normalised fraction of atoms remaining in the trap for different release times with their theoretical fittings using Eq. 5.3. The obtained data deviates slightly from the theoretical plot which could be due to the fact that the actual MOT centre is not at the centres of all the beams as it is required to move the cloud slightly in order to overlap the MOT centre onto the ONF.

The temperature measured by the ONF method and the direct camera are 113± 7 μK and 182±12 μK, respectively. The errors are based on fits to the data as shown in Fig. 5.3. The measured temperatures are of a similar order, but with some difference. This can be attributed to the fact that the ONF is mainly sensing the central part of the cloud (thereby the coldest atoms), whereas the camera is measuring the temperature of the whole cloud.

5.2 Absorption Measurements Using an Optical Nanofibre

Light propagating in an ONF extends outside the physical boundary and can be scattered by any atoms present in the evanescent field region [24]. The scattered light may couple back to the ONF (either in the guided modes or the radiation modes) or may be lost in free space. For a probe beam passing through an ONF, scattering into the radiation modes, or in the backward propagating guided

mode, would lead to a decrease in the transmission of the probe in the presence of the atoms (transmission loss due to the ONF profile should be accounted for separately). This decrease in the transmission is termed as absorption. Scanning the probe frequency can reveal the atomic absorption spectrum and transient absorption of a freely expanding cloud may give information about the local temperature of the cloud influenced by the probe light sent through the ONF.

5.2.1 Measurement of linewidth

Absorption measurements are done after ensuring the best coupling of the MOT to the ONF by maximising the fluorescence collection. A probe beam is sent through port A of the ONF (Fig. 5.1(a)). The probe beam is derived from an ECDL laser scanning across the hyperfine transition $5S_{1/2}F{=}2 \rightarrow 5P_{3/2}F'{=}3$. 60% absorption of the probe beam is obtained at resonance for a probe power of 0.5 pW (Fig. 5.4). The linewidth of the transition is found to be ∼13 MHz. The difference from the natural linewidth (6 MHz) can be attributed to the fact that the probed atoms are in the vicinity of the ONF and, hence, subjected to the atom-surface interactions, such as van der Waals effect, that modifies the spectral properties of the atoms near the fibre [32]. This lead to an enhancement in the spontaneous emission rate due to the presence of the ONF [23].

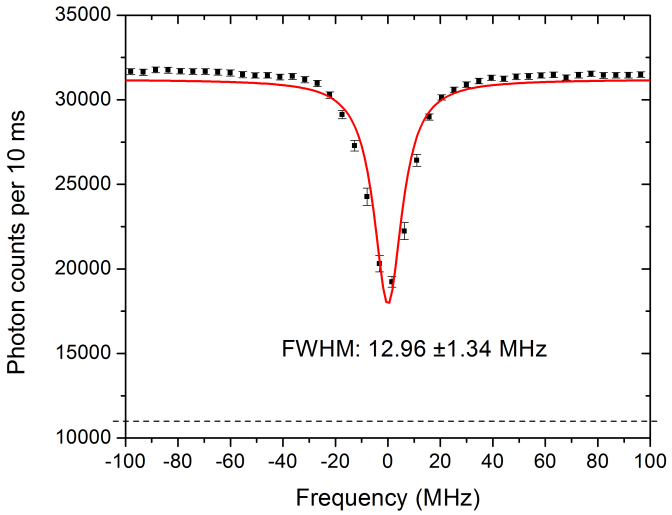


Figure 5.4: Absorption spectrum of cold ^{87}Rb atoms in a MOT for the probe sent through an ONF. Each data point is averaged over 50 runs. The red curve shows a Lorentz fit to the experimental data (black dots). The dashed horizontal line shows the background level due to the MOT fluorescence, MOT beams and room light.

5.2.2 Temperature measurement using transient absorption

The average temperature of a cold atom cloud can be measured using a transient absorption technique. When the cloud is allowed to expand freely by switching off the MOT beams, the absorption of the probe beam passing through the cloud reduces due to a decrease in the atomic density in the region covered by the probe. The time evolution of the absorption signal characterises the temperature of the cloud.

Consider a cloud with a Gaussian density distribution at $t = 0$, which expands ballistically. The density distribution evolves as [106]

$$\rho_d(r,t) = A(t)e^{-r^2/(w_0^2+\bar{v}^2t^2)}, \tag{5.4}$$

where r is the radial coordinate, w_0 is the initial Gaussian waist of the cloud, $\bar{v}$ is the average thermal velocity and $A(t)$ is the peak density at time t given as

$$A(t) = N/\left(\pi(w_0^2+\bar{v}^2t^2)\right)^{3/2}, \tag{5.5}$$

with N being the total number of atoms in the trap. However, the density of the atom cloud is modified by the presence of the ONF (of radius a) in the region close to it and it is required to introduce an additional factor, $g(r) = 1-\mathrm{Arcsin}(a/r)/\pi$, [104] to take this modification into account. Thus, the evolution of a ballastically expanding cloud in the presence of an ONF is given as

$$\rho_d(r,t) = \frac{\mathrm{N}e^{-r^2/(w_0^2+\bar{v}^2t^2)}}{\pi^{3/2}(w_0^2+\bar{v}^2t^2)^{3/2}}(1-\frac{\mathrm{Arcsin}(a/r)}{\pi}). \tag{5.6}$$

According to Beer's law, the differential change in the intensity of a probe passing through an absorbing medium is given by

$$dI = -\sigma_a\rho_d(r,t)I(r)dr, \tag{5.7}$$

where σ_a is the atom-light absorption cross-section and $I(r)$ is the evanescent field intensity at a radial distance, r, from the axis of the fibre due to the probe beam propagating through the ONF.

Experiments are performed for various input probe powers with a probe beam locked on resonance to the transition $5\mathrm{S}_{1/2}\mathrm{F}{=}2\rightarrow 5\mathrm{P}_{3/2}\mathrm{F}'{=}3$ (Fig. 5.5). The

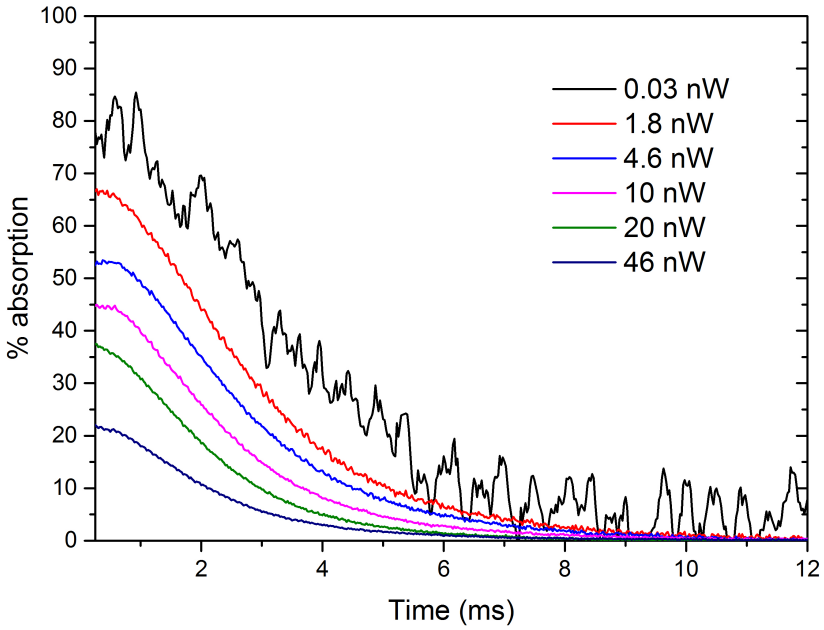


Figure 5.5: Transient absorption for different input probe powers through the ONF. Fluctuations in the background light is evident for the measurements with the lowest probe power, 0.03 nW.

maximum percentage absorption obtained for an unexpanded cloud reduces with power. Looking at the transient behaviour of the absorption during free expansion at various powers, we can estimate the temperature change of the cloud locally near to the ONF due to the probe beam. The ONF only senses the evanescent field region which is very small (250-300 μm) compared to the full cloud dimensions ($\sim$ 1 mm). Also, the probe beam is expected to have an affect in the evanescent field region only. Fitting the transient absorption curves with Eq. 5.6 provides the value for $\bar{v}$ for which the corresponding temperature is $T = M\bar{v}^2/3k_B$.

Fig. 5.6 shows the obtained theoretical fittings for the normalised absorption spectra. The effect of probe power on local temperature is evident from the calculated temperature values. The minimum probe power of 30 pW provides a temperature close to the overall cloud temperature as this creates a minimal heating effect due to the probe beam. As the probe beam is increased, the probe beam intensity in the evanescent field region becomes stronger, hence, the scattering force on the atoms due to the probe beam gets stronger leading to a heating of the atoms locally. The temperature increases rapidly with respect to the probe power and reaches a saturation (Fig. 5.7).

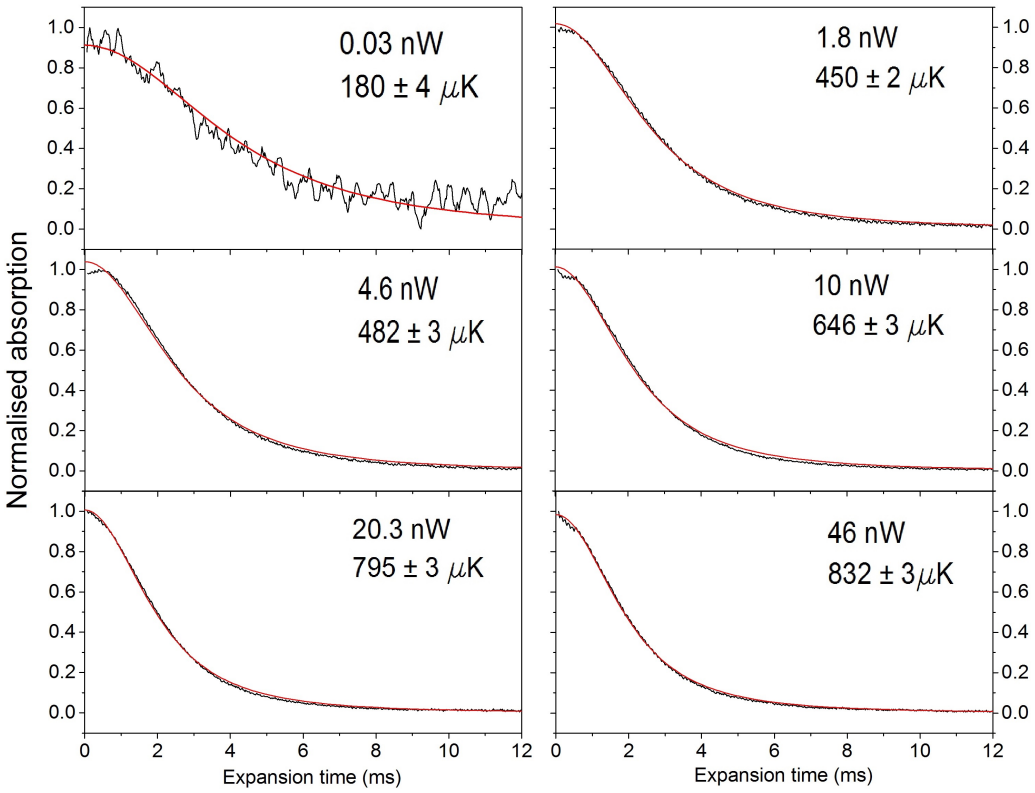


Figure 5.6: Transient absorption with theoretical fits for various probe powers. The corresponding temperature values found from the fits are shown with the standard error obtained from the fitting parameters.

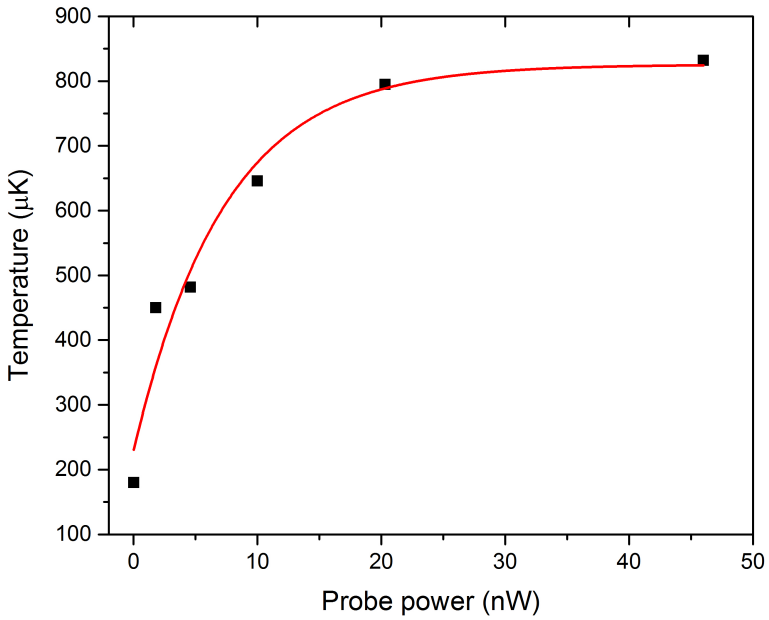


Figure 5.7: Temperature measured by the transient absorption technique with a probe propagating through the ONF. The red curve shows an exponential fit.

5.3 Conclusion

There are mainly two ways of detecting cold atoms using ONFs: (i) by collecting the fluorescence of atoms emitting around the waist of the ONF, (ii) by measuring the absorption of a probe beam sent through the ONF. The loading time of the MOT has been measured using fluorescence detection and the linewidth of a hyperfine transition has been measured using absorption detection. The ONF overlapping on a cold atom cloud has been used for measuring its temperature. Two different techniques, release-recapture and transient absorption, have been used for the temperature measurements based on fluorescence and absorption detection, respectively.

Chapter 6

Autler-Townes Splitting at Ultra-Low Power

The theory related to the Autler-Townes splitting in a three-level atom has been described in Section 3.2.1. This chapter details the experimental realisation with cold ^{87}Rb atoms, where the pump and the probe beams are sent through the ONF overlapping the cold atom cloud. The splitting is observed at unprecedented low power levels, demonstrating the capability of such a system for ultra-low power device fabrications. This is also the first observation of frequency up-conversion in cold atoms using excitation and detection using an ONF, in our knowledge.

The contents of this chapter have been published as an open access article in "R. Kumar, V. Gokhroo, K. Deasy and S. Nic Chormaic, *Autler-Townes splitting via frequency up-conversion at ultralow-power levels in cold ^{87}Rb atoms using an optical nanofiber*, Physical Review A, 91 (5), 053842 (2015)" .

RK contribution: Design and implementation of the experimental setup, data collection and analysis, theoretical modelling and paper writing.

Autler-Townes splitting via frequency upconversion at ultra-low power levels in cold ^{87}Rb atoms using an optical nanofibre *

Ravi Kumar[1,2], Vandna Gokhroo[1], Kieran Deasy[1], and Síle Nic Chormaic[1]

[1]*Light-Matter Interactions Unit, Okinawa Institute of Science and Technology Graduate University, Onna, Okinawa 904-0495, Japan*

[2]*Physics Department, University College Cork, Cork, Ireland*

Abstract

The tight confinement of the evanescent light field around the waist of an optical nanofibre makes it a suitable tool for studying nonlinear optics in atomic media. Here, we use an optical nanofibre embedded in a cloud of laser-cooled ^{87}Rb for near-infrared frequency upconversion via a resonant two-photon process. Sub-nW powers of the two-photon radiation, at 780 nm and 776 nm, co-propagate through the optical nanofibre and generation of 420 nm photons is observed. A measurement of the Autler-Townes splitting provides a direct measurement of the Rabi frequency of the 780 nm transition. Through this method, dephasings of the system can be studied. In this work, the optical nanofibre is used as an excitation and detection tool simultaneously, and it highlights some of the advantages of using fully fibred systems for nonlinear optics with atoms.

PACS numbers: 42.65.-k, 32.10.-f, 42.50.Hz, 42.81.-i

*Physical Review A, 91 (5), 053842 (2015)

6.1 Introduction

Subwavelength diameter optical fibres, also known as optical nanofibres (ONFs), have recently emerged as a very useful tool for probing [41, 43, 46] and trapping cold atoms [45, 107], particularly due to the functionality of such nanofibres in the development of atom-photon hybrid quantum systems [108, 109]. Aside from this research focus, ONFs have also been shown to be highly efficient tools for demonstrating nonlinear optics using very low light power levels in atomic systems [110]. More than a decade ago, Patnaik *et al.* [20] proposed a demonstration of slow light in an ONF surrounded by a nonlinear medium, such as atoms. More recently, two- photon absorption by laser-cooled atoms using an ONF was proposed [111]. Quantum interference effects, such as electromagnetically induced transparency (EIT) [53] and two-photon absorption [56], were demonstrated using an ONF in rubidium (Rb) vapor, and nW level saturated absorption in a Xe gas was observed with an ONF [58]. This versatility of ONFs for nonlinear optics arises from the very high evanescent field intensities that can be achieved as a result of the very tight light confinement within a very small mode area over long distances of a few mm and it is known that atoms experience an appreciable ac stark shift on their energy levels in the presence of an intense light field. Here, we study a two-photon excitation process, at 780 nm and 776 nm, in a cascade three-level configuration [112] in cold ^{87}Rb atoms using an optical nanofibre. We have observed frequency up-conversion for 776 nm probe power as low as 200 pW and Autler-Townes (A-T) splitting [61] for <20 nW of 780 nm coupling power. These power levels are several orders of magnitude lower than those used in free space experiments [113–115]. The effect of varying the coupling power on the obtained A-T spectra is investigated and sources of dephasing within the system are considered.

6.2 Experimental Details

We use laser-cooled ^{87}Rb atoms, in a standard MOT configuration, the details of which are described elsewhere [49]. We adopt a two-photon cascade three-level system where $5S_{1/2}$ ($|1\rangle$) is the ground state, $5P_{3/2}$ ($|2\rangle$) is the intermediate state, and $5D_{5/2}$ ($|3\rangle$) is the excited state. Relaxation of $|3\rangle$ via $6P_{3/2}$ ($|4\rangle$) generates 420 nm blue light (Fig. 6.1). A schematic of the experimental setup is shown in Fig. 6.2. A Rb vapor cell is used to provide the reference frequencies for

the two-photon transitions. A counter-propagating configuration is chosen since the linewidths are solely determined by the lifetime of the final state, $|3\rangle$ [116], and sharper peaks can be observed for reference purposes. The 420 nm blue fluorescence (ω_4) generated in the vapor cell is monitored using a photomultiplier tube (PMT) with the aperture covered by a 420 nm filter (FWHM of 10 nm). We do not detect the infrared 5.23 μm (ω_3) photons. All lasers used are extended cavity diodes (ECDL), one of which is locked to the $5S_{1/2}$ F=2 $\rightarrow$ $5P_{3/2}$ F$'$ = 2 and F$'$=3 crossover transition using a standard saturation absorption setup. This laser provides both the cooling beams for the MOT and the 780 nm coupling beam for the $|1\rangle \rightarrow |2\rangle$ transition (i.e., the $5S_{1/2}$ F=2 $\rightarrow$ 5 $P_{3/2}$ F$'$ = 3 transition). The second ECDL, at 776 nm, is scanned across the $|2\rangle \rightarrow |3\rangle$ probe transitions. A third ECDL (not shown in Fig. 6.2) is used for the 780 nm repump beam in the MOT.

The ONF is prepared from a commercial, single-mode optical fibre for 780 nm using a flame brushing technique [76]. It has a diameter of $\sim$350 nm, ensuring that only the fundamental mode propagates at 780 nm. Note that higher modes may propagate in the ONF for 420 nm light. Transmission through the ONF at 780 nm is measured to be 84%. The ONF is mounted on an aluminium u-shaped mount and installed vertically in the vacuum chamber [43]. The experiment is designed so that the cold atom cloud is centered on the waist of the ONF. The atom cloud diameter is $\sim$0.8 mm and the temperature is measured to be $\sim$200 μK using a time-of-flight technique. The cloud position is optimised using two magnetic shim coils in order to overlap the densest part of the cloud to the ONF. This is done while monitoring the spontaneous emission from the atoms coupling into the ONF. The cloud contains $\sim 10^7$ atoms; however, if we consider the evanescent field decay length for 780 nm light, there are typically $<$10 atoms in the evanescent field region, and the photon signals collected via the ONF can be considered to be directly related to emissions from such low atom numbers.

The 780 nm and 776 nm beams used in the vapor cell reference measurements (ω_1' and ω_2', respectively) are split in order to obtain the required frequencies (ω_1 and ω_2, respectively) for two-photon excitation in the cold atoms via the ONF. The 780 nm beam from the ECDL is double-passed through AOM2 (Fig. 6.2) using the '+1' order to obtain ω_1, which is 14 MHz red-detuned from the $5S_{1/2}$ F=2 to $5P_{3/2}$ F$'$=3 cooling transition. The 776 nm beam from the second ECDL is double-passed through AOM3 using the '-1' order to ensure that $\omega_1' + \omega_2' = \omega_1 + \omega_2$. This permits us to directly compare the spectra obtained from the cold atoms and the vapor cell in real time. Circular polarisation of the same handedness is

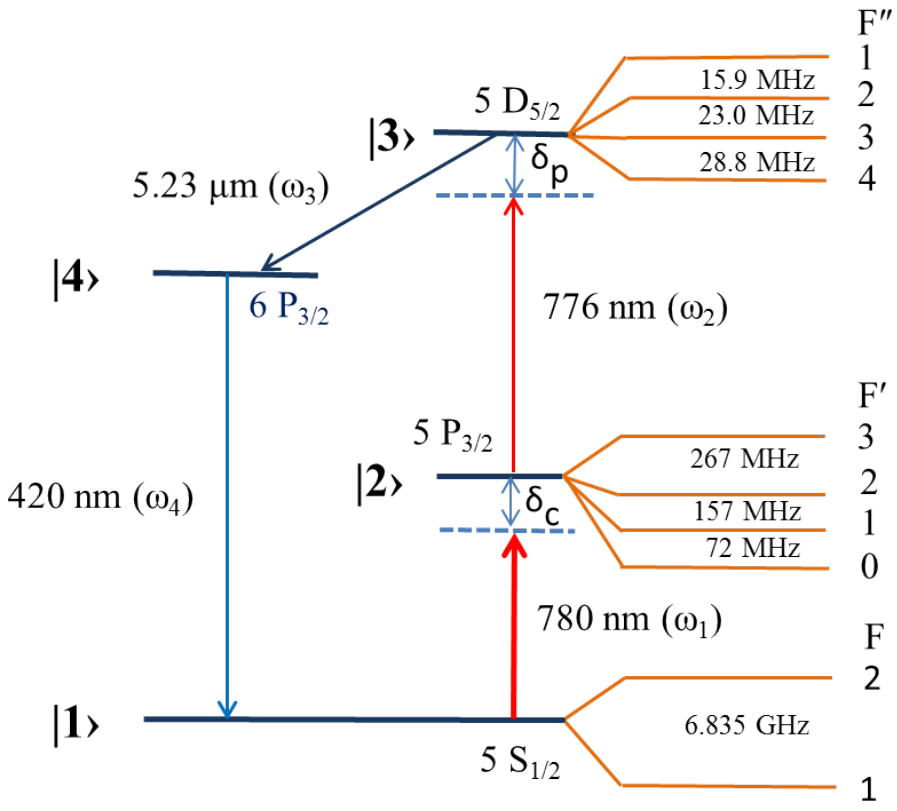


Figure 6.1: Energy level diagram for ^{87}Rb atoms showing the 780 nm coupling and 776 nm probe beams.

used for all 780 nm and 776 nm beams.

ω_1 is sent through port A of a 50:50 fibre beam splitter, while ω_2 passes through port B (Fig. 6.2). In order to excite the cold ^{87}Rb atoms from $|1\rangle$ to $|3\rangle$ in the two-photon cascade system via the ONF, one output port, D, of the fibre splitter is spliced to one pigtail of the nanofibre (Fig. 6.2). The other output port, C, is connected to a power meter to monitor beam powers. The measured power is proportional to the power at the nanofibre waist, any differences being due to the ONF transmission losses at a particular wavelength. Hence, if we assume equal losses at both sides of the taper, the measured power can be taken as 1.1 times the waist power for both 780 nm and 776 nm wavelengths.

6.3 Results and Discussion

A typical transmission spectrum of the 780 nm light (for input power of 1.8 nW) through the ONF is shown in Fig. 6.3 with no ω_2 present. As the laser is scanned

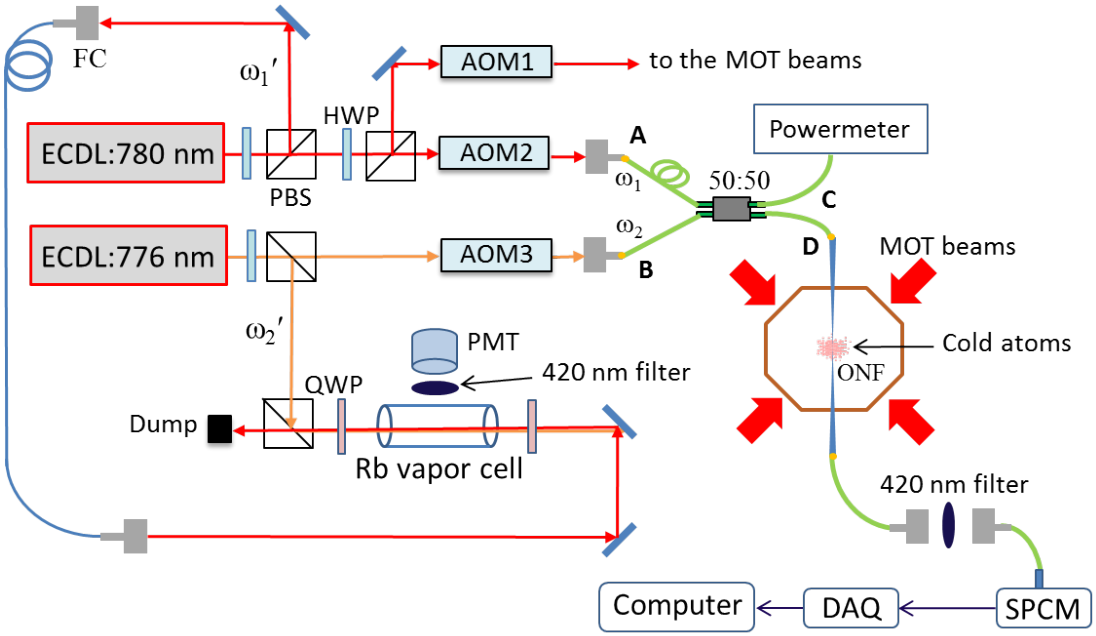


Figure 6.2: Schematic of the experimental setup. 780 nm and 776 nm light are co-propagating in the nanofibre to generate blue photons from the cold atoms. An SPCM is used to detect the blue photons exiting from the nanofibre pigtail after filtering in free space. 780 nm and 776 nm light counter-propagating in a Rb vapor cell are used to obtain the reference signal for identification of the peaks in the two-photon spectrum. SPCM: Single photon counting module, ECDL: Extended cavity diode laser, AOM: Acousto-optic modulator, QWP: Quarter waveplate, HWP: Half waveplate, PMT: Photo multiplier tube, MOT: Magneto-optical trap, ONF: Optical nanofibre, DAQ: Data acquisition card, FC: Fibre coupler.

across the $5S_{1/2}$ F=2 to $5P_{3/2}$ F′ transitions, absorption dips appear. If we add ω_2 into the nanofibre, 420 nm (blue) photons are generated within the atom cloud via four-wave mixing for co-propagating coupling and probe beams [117]. ω_1 and ω_2 excite the atoms from $|1\rangle$ to $|3\rangle$ via $|2\rangle$. In the relaxation process from $|3\rangle$ to $|4\rangle$ and from $|4\rangle$ to $|1\rangle$ ω_3 ($\vec{k}_{IR}$) and ω_4 ($\vec{k}_{blue}$) are generated, respectively. The decay probability from $|3\rangle$ to $|4\rangle$ is 35% and from $|4\rangle$ to $|1\rangle$ is 31% [118]. The four frequencies are related by the frequency-matching condition to satisfy conservation of energy, $\omega_1 + \omega_2 = \omega_3 + \omega_4$, whereas momentum conservation requires the phase-matching relation, $\vec{k}_{780} + \vec{k}_{776} = \vec{k}_{IR} + \vec{k}_{blue}$ to be satisfied [119]. In this system, the phase-matching condition must be satisfied since ω_1 and ω_2 co-propagate and the blue light, ω_4, must be produced in the forward direction. However, we did not try to observe the presence of blue photons in the backward direction due to constraints in the experimental setup. The blue photons couple into the nanofibre and propagate along it. The guided light is coupled out of the ONF and passed through a 420 nm (FWHM : 10 nm) filter before reaching the single photon counter (SPCM). The filter serves to eliminate

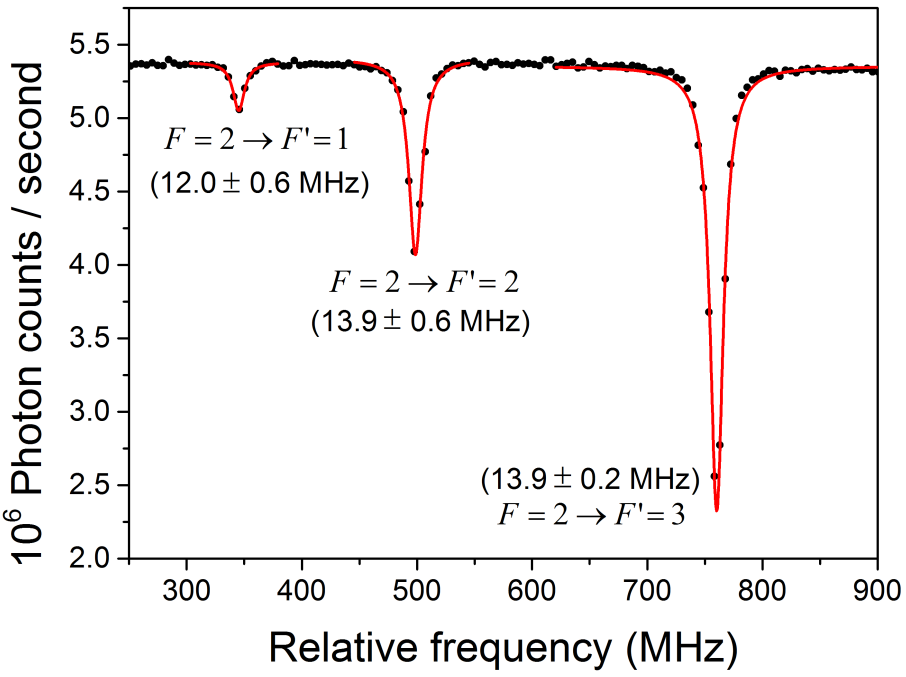


Figure 6.3: Transmission of 780 nm light passing through the ONF with cold ^{87}Rb atoms around the waist. The laser is scanning across the $5S_{1/2}$ F=2 to $5P_{3/2}$ possible transitions. This spectrum is obtained using an additional ECDL laser in scan mode. The data are fit (red curves) to Lorentzian profiles and the obtained linewidths for the relevant transitions are indicated at the peaks.

any residual excitation beams, or other 780 nm photons, coupled to the nanofibre from the atom cloud or the MOT beams. Detection of blue photons serves as a signature of the two-photon absorption process in the evanescent field region, hence the ONF acts as both the excitation and detection tool simultaneously.

To study the influence of coupling and probe power on the two photon process we start with no ω_1 light through port A of the 50:50 splitter (Fig. 6.2). ω_2 is sent through port B and we observe blue emission from the cold atom cloud. Hence, we deduce that excitation from $|1\rangle$ to $|2\rangle$ purely from the MOT beams is sufficient to initiate the two-photon process, which we observe for as little as 200 pW of power in ω_2. Fig. 6.4(a) shows the typical blue counts detected on the SPCM when ω_2 was scanned across the two-photon transition. The peak in the observed spectrum occurs at the same two-photon frequency detuning as that which gives rise to the strongest observed transition in the vapor cell. When we plot the peak blue photon count rate as a function of probe power in ω_2 we see there is saturation behavior even though we operate in the nW region (Fig. 6.4(b)).

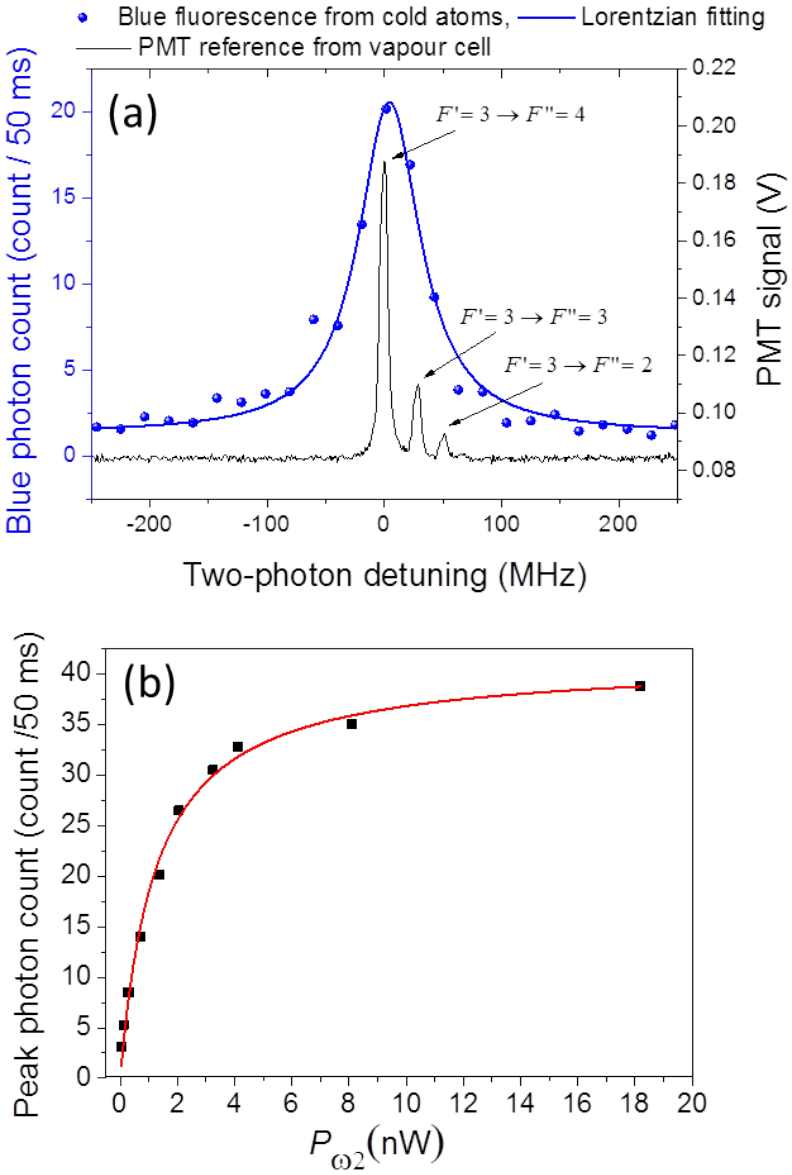


Figure 6.4: (a) 420 nm photon count rate (blue dots) as ω_2 is scanned across the $5P_{3/2}$ to $5D_{5/2}$ transition. An intermediate power (1.4 nW) of ω_2 is input into the nanofibre, whereas any 780 nm present is only from the MOT beams. The data are fitted (solid blue curve) to a Lorentzian profile. The black spectrum is the corresponding reference signal obtained from the vapor cell when the 780 nm and 776 nm beams are counter-propagating. The hyperfine transitions associated with each peak are indicated. (b) Maximum blue photon count (i.e. the peak value of the curve in (a)) for different powers of ω_2. Here, the 780 nm contribution is also only from the MOT beams. The red curve is a theoretical fit to yield the saturation power as 1.24±0.12 nW. This corresponds to ∼1.1 nW of 776 nm power at the waist.

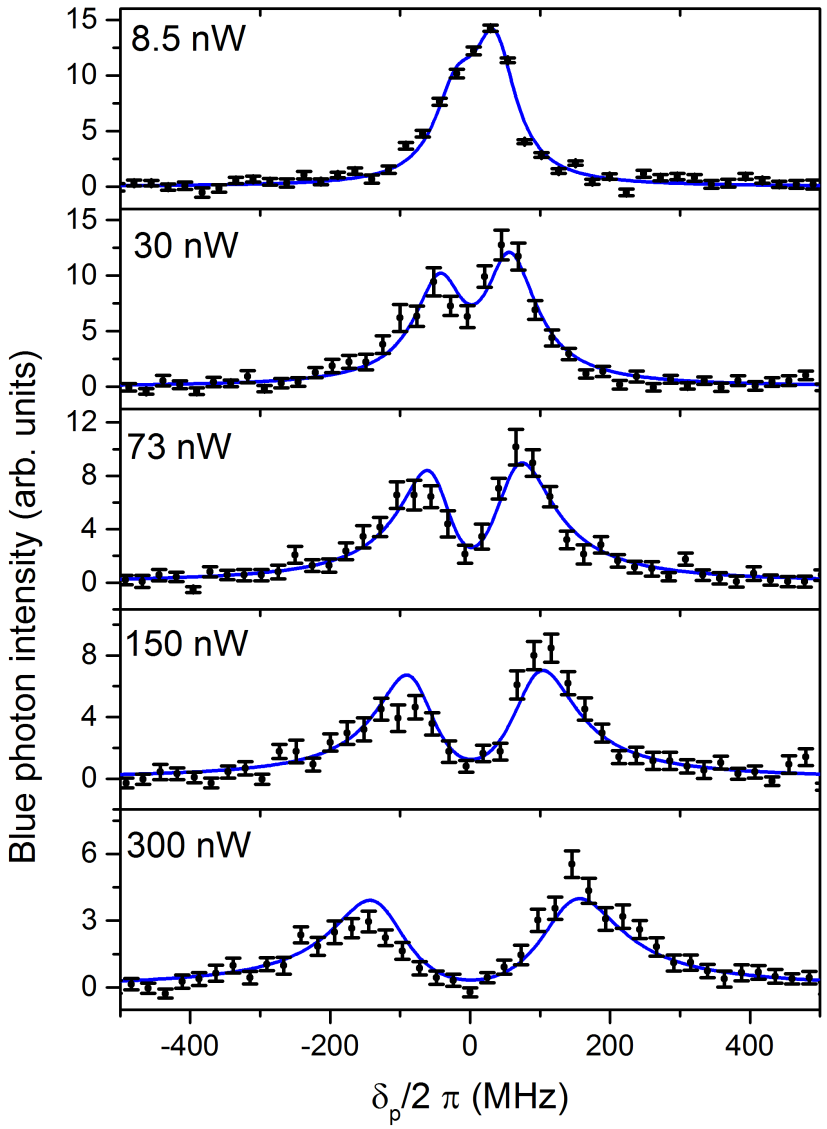


Figure 6.5: Blue fluorescence from the atoms collected via the ONF for different powers in ω_1, which is 14 MHz red-detuned from the $5S_{1/2}$ F=2 to $5P_{3/2}$ F′=3 transition, while ω_2 is scanned across the $5P_{3/2}$ F′=3 to $5D_{5/2}$ hyperfine levels. The power for ω_2 is fixed at 0.5 nW. δ_p is the detuning of ω_2 as indicated in Fig. 6.1. ω_1 is held at the same frequency as the cooling beams. Asymmetry in the observed A-T doublet is due to the fact that ω_1 is not on resonance. Solid lines are theoretical fits to the data using Eq.(1).

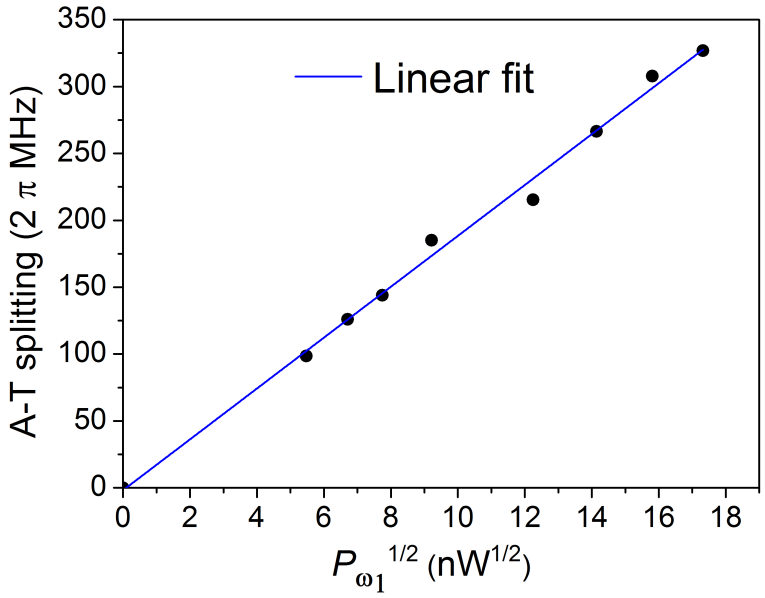


Figure 6.6: Measured A-T splitting as a function of the square-root of the power in the 780 nm coupling beam.

The linewidth obtained for the two-photon spectrum from cold atoms, see Fig. 6.4(a), is broader than the natural linewidths of the intermediate (∼5.9 MHz) and final levels (∼0.66 MHz). This could arise from dephasing introduced to both the levels due to the presence of MOT beams at all times during measurements. Power broadening and the ac Stark effect from the MOT beams would give partial broadening. The other contributions in the broadening may come from the presence of the $5D_{5/2}$ state manifold and atom-fibre surface interactions [31, 120]. Note that there is not much observable broadening when we only use a 780 nm probe beam for standard one-photon absorption (Fig. 6.3). This may be due to the effect of light-induced dipole forces on the atomic cloud [42]. In our case, we measure ∼14 MHz linewidth even when using nW of power.

Next, in order to study the effect of the very strong evanescent field intensities on atomic transitions, we introduce the coupling laser, ω_1, into the ONF via port A of the fibre coupler. The power in the coupling beam, P_{ω_1}, is varied while the probe power, P_{ω_2}, is fixed at 500 pW. This value was chosen to ensure that sufficient 420 nm photons are obtained for detection. We observe that the peak blue photon count increases with P_{ω_1} and the width of the spectrum broadens (data not shown here). For $P_{\omega_1} \sim 20$ nW, the obtained spectrum clearly splits into two peaks. The peak separation increases as P_{ω_1} increases (Fig. 6.5). This is known as Autler-Townes (A-T) splitting and is caused by the ac Stark effect of

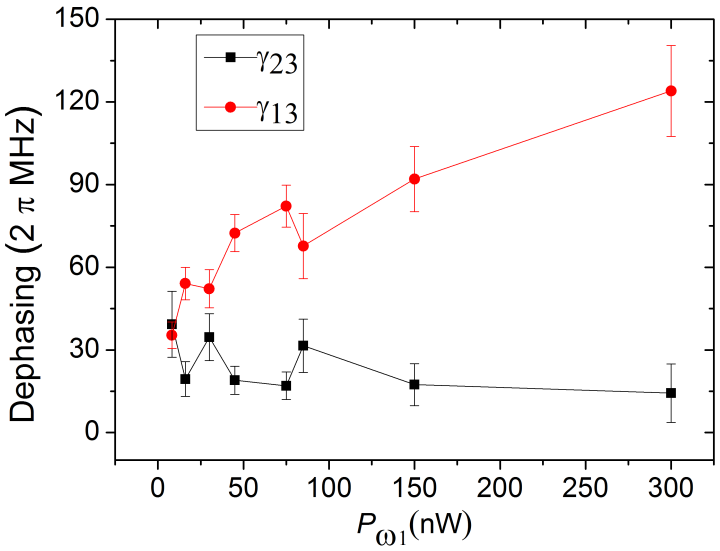


Figure 6.7: Variation of γ_{23} and γ_{13} as a function of coupling power, P_{ω_1}.

the 780 nm transition in the presence of a strong coupling beam [61]. The A-T splitting is plotted for different values of P_{ω_1} (see Fig. 6.6) and we see that it is directly proportional to the square-root of P_{ω_1} as expected.

The number of blue photons detected via the optical nanofibre due to decay of the $6P_{3/2}$ level is related to the absorption of ω_2 light by the atoms. Therefore, considering a simple three-level model, the observed A-T splitting spectrum is assumed to be proportional to the imaginary part of the density matrix term ρ_{32} [93],

$$\rho_{32} \propto \frac{i\frac{|\Omega_c^2|}{4}}{\gamma_{12}^2 + \delta_c^2 + 2\frac{|\Omega_c^2|}{4}} \frac{\gamma_{23} + i\delta_p}{[\gamma_{13} + i(\delta_p + \delta_c)][\gamma_{23} + i\delta_p] + \frac{|\Omega_c^2|}{4}} \tag{6.1}$$

where γ_{12}, γ_{13}, and γ_{23} are dephasings, δ_c and δ_p are coupling and probe detunings, and Ω_c is the Rabi frequency of the coupling transition.

Fitting Eq.(1) to the experimental data (Fig. 6.5), we obtain values for the dephasings and the Rabi frequency of the coupling transition. From the simplified model used, we find that γ_{13} is larger than γ_{23} and it increases with P_{ω_1} (Fig. 6.7). This behavior may be explained by the fact that the atom is a multi-level system and that very intense light fields are present; at higher P_{ω_1} there is a finite probability that atoms may be excited from $5S_{1/2}$ F=2 $\rightarrow$ $5P_{3/2}$ F$'$ = 2, 1, thereby providing a decay channel for $5S_{1/2}$ F=2, i.e., the lower hyperfine

state, $5S_{1/2}$ $F = 1$. This mechanism may contribute to dephasing of the ground state and this is reflected by the increasing value of γ_{13} for higher P_{ω_1}. In order to gain better insight into the exact origin of the dephasings a full theoretical description of a 4-level system in the presence of an evanescent field is required. For a given power, the evanescent field distribution outside the nanofibre, the excitation probabilities, and the coupling efficiency of the 420 nm photons from atoms positioned at different radial distances from the ONF surface, is needed. Heating of the atom cloud is also expected to play a role. As the power in ω_1 is increased, local temperature of the atom cloud should increase, thereby leading to a change in atom cloud density and a possible increase in atom-atom or atom-surface interactions.

6.4 Conclusion

In conclusion, we have observed frequency up-conversion and A-T splitting for ultra-low power levels (nW) in an atom-nanofibre system. The splitting is observed for ultra-low powers of the coupling field in the evanescent region of the nanofibre. If we consider 50 nW of coupling power propagating in the ONF, we can assume that there is typically less than one photon in the interaction volume at any given time [14, 56]. Such power levels are used frequently in nanofibre experiments and it is important to take into account any induced shifts in the energy levels that may arise [121]. In the high intensity regime, the Rabi frequency for the coupling transition is approximately equal to the A-T splitting [122] and this method allows us to measure it directly for an atom+nanofibre system. Otherwise, due to the difficulties in exactly determining nanofibre parameters such as the influence of fibre surface on energy levels, the effective position of the atoms in the evanescent field, waist size of the ONF etc., this could be challenging to estimate. The observation of nonlinear phenomena using an optical nanofibre in a cold atom system increases the versatility of such devices and may be useful for demonstrations of single photon all-optical switching [123], or quantum logic gates [124] at ultra-low powers. The efficiency of the process may be improved by optimizing the beam polarisations [125] at the nanofibre waist, a technique that relies on optimum control on light propagation in ultrathin fibres [49, 126, 127].

Chapter 7

Electromagnetically Induced Transparency with Optical Nanofibres

Theory related to the electromagnetically induced transparency has been described in Section 3.2.2. This chapter shows the experimental realisation with cold Rb atoms in a ladder-type system, where the coupling and the probe beams are sent through the ONF overlapping the cold atom cloud. A multi-peak EIT spectrum is observed related to the hyperfine levels, and further an all-optical-switch is demonstrated based on the EIT effect.

The contents of this chapter have been accepted for publication as an open access article, "R. Kumar, V. Gokhroo and S. Nic Chormaic, *Multi-level cascaded electromagnetically induced transparency in cold atoms using an optical nanofibre interface*, New Journal of Physics, 17, 123012 (2015)" .

RK contribution: Design and implementation of the experimental setup, data collection and analysis, theoretical modelling and paper writing.

Multi-level cascaded electromagnetically induced transparency in cold atoms using an optical nanofibre interface

Ravi Kumar[1,2], Vandna Gokhroo[1], and Síle Nic Chormaic[1]

[1]*Light-Matter Interactions Unit, Okinawa Institute of Science and Technology Graduate University, Onna, Okinawa 904-0495, Japan*

[2]*Physics Department, University College Cork, Cork, Ireland*

Abstract

Ultrathin optical fibres integrated into cold atom setups are proving to be ideal building blocks for atom-photon hybrid quantum networks. Such optical nanofibres (ONFs) can be used for the demonstration of nonlinear optics and quantum interference phenomena in atomic media. Here, we report on the observation of multilevel cascaded electromagnetically induced transparency (EIT) using an optical nanofibre to interface cold ^{87}Rb atoms. Intense evanescent fields can be achieved at ultralow probe (780 nm) and coupling (776 nm) powers when the beams propagate through the nanofibre. The observed multipeak transparency spectra of the probe beam could offer a method for simultaneously slowing down multiple wavelengths in an optical nanofibre or for generating ONF-guided entangled beams, showing the potential of such an atom-nanofibre system for quantum information. We also demonstrate all-optical-switching in the all-fibred system using the obtained EIT effect.

Keywords: Optical nanofibre, nonlinear optics, EIT, cold atoms, quantum optics

7.1 Introduction

A strong interaction between light and matter is one of the main requirements to successfully realise neutral atom-based quantum networks [7, 8, 128]. Atoms confined in a cavity provide one method of achieving strong coupling due to the small mode volume of the light field [129]. However, in order to ensure that photons can travel long distances - as would be desirable in quantum networks - such cavities need to be coupled to optical fibres [10, 130–132]. Therefore, if strong atom-photon coupling could be achieved in a system that is by itself inherently fibred, this would be a distinct advantage. Optical nanofibres (ONFs) offer a small optical mode volume in the evanescent field region and are, by default, fibre coupled, thereby providing an alternative method for exploring the strong coupling regime [50]. Light can be coupled to the pigtails and propagate through the nanofibre waist with extremely high transmission. A large fraction of the 'guided' light is contained within the evanescent field, which extends beyond the physical boundary of the fibre [15]. The evanescent field decays exponentially perpendicular to the light propagation direction, leading to a strong confinement of light in the transverse direction. Atoms surrounding the waist region couple to the evanescent field [24, 133]. Alternatively, spontaneous emission from the atoms may also couple to the guided modes of the ONF [23, 134–136]. This 'atom-nanofibre' system could serve as a node in a quantum network, with information being stored in the quantum states of the atoms and information being transferred via the guided light, which acts as the quantum bus. In 2009, Le Kien and Hakuta [30] proposed that light guided along a nanofibre, passing through a cold atom cloud, could be slowed down. More recently, such effects have been demonstrated experimentally [51, 52]. These demonstrations are based on electromagnetically induced transparency (EIT) in a Λ-type, three-level atomic system, generating a transparency window in the absorption profile of the probe beam leading to a reduction of the group velocity of the pulse guided by the nanofibre. Here, we use a ladder-type scheme in order to obtain multiple EIT windows, with the potential to support slow group velocities for multiple probe pulses at different frequencies simultaneously. Two light fields propagating with slow group velocities could be used to produce quantum entanglement [137]. Furthermore, a ladder type system is generally utilised to study Rydberg atoms [138], and multi-level EIT schemes may be useful for nonlinear light generation processes [139].

7.2 Experimental Methods

7.2.1 Optical nanofibre fabrication

A commercial optical fibre is used to fabricate a 350 nm diameter ONF using a heat-and-pull technique. In this method, an unjacketed part of an optical fibre is heated and stretched. There are various ways of heating the fibre including using an oxy-butane or oxy-hydrogen flame, a focussed CO_2 laser, microfurnaces, electric strip heaters or sapphire tubes. We use an oxy-hydrogen torch to heat the fibre using a pulling rig which is described elsewhere [76]. In order to maintain a high optical transmission, the pulling process must be adiabatic. We start with a 250 μm (cladding) diameter fibre and pull until a waist diameter of $\sim$350 nm is achieved. The prepared ONF has a transmission of $\sim$84% for 780 nm light and it remains the same during the experiments. The diameter of the nanofibre ensures that only the fundamental fibre-guided mode, LP_{01}, propagates for the wavelengths of light used in the experiments, i.e. 776 and 780 nm. The ONF is installed in a vacuum chamber - used for the magneto-optical trap - in such a way that its waist is aligned with the cloud of cold atoms [43].

7.2.2 Cold atoms

Atoms are cooled in a standard magneto-optical trap (MOT) to a temperature of $\sim$200 μK with three cooling beams in the retro-reflected configuration. The cooling beams are kept 14 MHz red-detuned from the 5 $S_{1/2}$ F=2 $\rightarrow$ 5 $P_{3/2}$ F$'$=3 transition, and the repump beam is kept at the 5 $S_{1/2}$ F=1$\rightarrow$ 5 $P_{3/2}$ F$'$=2 transition. The temperature of the cold atom cloud is measured using a time-of-flight technique by taking the fluorescence image of the cloud after different free expansion times. The cloud is overlapped with the ONF using two magnetic compensation coils. A small current in the compensation coils is adjusted while monitoring the fluorescence coupling to the ONF via a photon counter connected to one pigtail. A higher coupling rate indicates better overlap of the densest part of the atomic cloud with the ONF. An optical depth of 0.17 is achieved when the probe beam passes through the ONF during continuous operation of the MOT. Note that there are approximately two atoms in the evanescent field region of the ONF contributing to the observed signal.

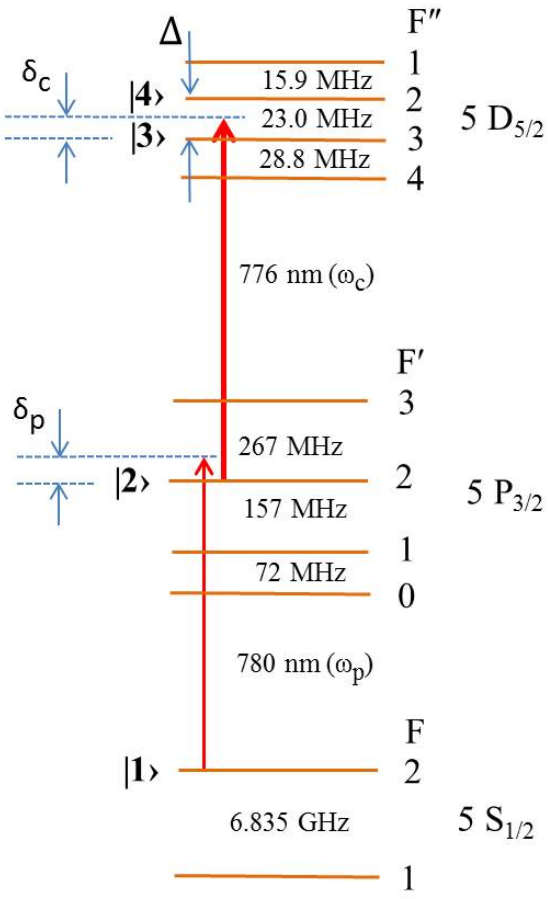


Figure 7.1: Energy level diagram for ^{87}Rb. The relevant levels for the EIT experiment are marked as $|1\rangle$, $|2\rangle$, $|3\rangle$ and $|4\rangle$.

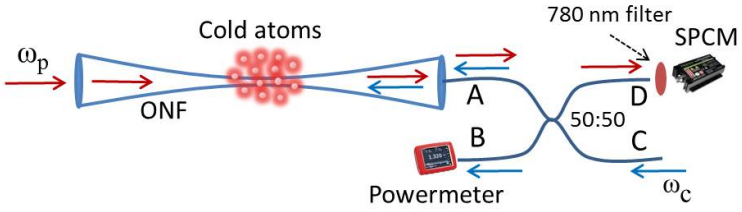


Figure 7.2: Schematic of the experimental setup. ONF: Optical nanofibre, SPCM: Single photon counting module, 50:50:fibre beam splitter with 50:50 split ratio. One port (port A) of the fibre splitter is spliced to one pigtail of the tapered fibre.

7.2.3 Ladder type electromagnetically induced transparency system

We consider a multilevel, cascaded EIT system as shown in Fig.7.1. An intense coupling beam at 776 nm (ω_c) drives the upper transition, 5 $P_{3/2} \rightarrow$ 5 $D_{5/2}$, and a weak probe beam (ω_p) at 780 nm drives the lower transition, 5 $S_{1/2} \rightarrow$ 5

$P_{3/2}$. Both the probe and coupling beams are sent through the optical nanofibre in a counter-propagating configuration (Fig. 7.2). A power meter connected to port B of a 50:50 fibre beam splitter measures the power level of the coupling beam sent into the tapered fibre pigtail connected to port A. The probe beam propagates in the opposite direction to the coupling beam and half of the probe power is obtained at port D, where it is out-coupled and passed through a 780 nm filter (FWHM: 3 nm) in free space and then directed to a single photon counter (SPCM). The filter prevents the 776 nm back-reflected light from reaching the detector.

7.3 Results and Discussions

EIT reduces the absorption of a weak probe beam in resonance with a dipole-allowed atomic transition due to the presence of a strong coupling beam on a linked transition. Optical properties of atomic samples are mainly associated with the energy levels and the imaginary part of the susceptibility, $\mathrm{Im}[\chi^{(1)}]$, determines the absorption of a probe beam passing through the atomic gas. The susceptibility is modified by the coupling beam which can be analysed by the the time evolution of the density matrix of the system [140–142]. Considering the multi-level system as shown in Fig. 7.1, the absorption coefficient for the probe beam, using the dipole- and rotating wave-approximations, can be given as [142],

$$\alpha \propto \omega_p \frac{B}{A^2 + B^2} \tag{7.1}$$

with

$$A = -\delta_p + \frac{A_{32}}{\gamma_{32}} + \frac{A_{42}}{\gamma_{42}}, B = \gamma_{21} + \frac{A_{32}}{\delta_p + \delta_c} + \frac{A_{42}}{\delta_p + \delta_c - \Delta},$$

$$A_{32} = \frac{\gamma_{31}(\delta_p + \delta_c)}{\gamma_{31}^2 + (\delta_p + \delta_c)^2} a_{32}^2 (\frac{\Omega_c}{2})^2, A_{42} = \frac{\gamma_{41}(\delta_p + \delta_c - \Delta)}{\gamma_{41}^2 + (\delta_p + \delta_c - \Delta)^2} a_{42}^2 (\frac{\Omega_c}{2})^2$$

where ω_p is the frequency of the probe beam, Ω_c is the Rabi frequency of the coupling beam, δ_p (δ_c) is the detuning of the probe (coupling) beam, Δ is the frequency difference between $|3\rangle$ and $|4\rangle$, γ_{ij} are the decay rates from $|i\rangle$ to $|j\rangle$ and a_{32} (a_{42}) is the relative transition strength between levels $|2\rangle$ to $|3\rangle$ ($|4\rangle$). Here, we have neglected the transition 5 $P_{3/2}$ F′=2 →5 $D_{5/2}$ F″=1 as this is weak and not observed in our experiments.

7.3.1 Multilevel electromagnetically induced transparency

We study multilevel EIT using the hyperfine levels of three fine structure levels, namely 5 $S_{1/2}$, 5 $P_{3/2}$, and 5 $D_{5/2}$ (Fig. 7.1). ω_c is kept at a fixed blue-detuning (δ_c = 7 MHz) from 5 $P_{3/2}$ F′=2 → 5 $D_{5/2}$ F″=3, whereas ω_p is scanned across 5 $S_{1/2}$ F=2 → 5 $P_{3/2}$ F′=2. In fact, in this situation the coupling beam is coupled to all hyperfine levels of 5 $D_{5/2}$ simultaneously with different detunings. While scanning the probe, EIT dips appear in the probe transmission when a resonant condition is met with any of the hyperfine transitions of the 5 $D_{5/2}$ level. The hyperfine levels in 5 $D_{5/2}$ are closer spaced than the hyperfine levels of 5 $P_{3/2}$. The probe scan does not cover any hyperfine levels of 5 $P_{3/2}$ other than $F' = 2$; however, it covers all the hyperfine levels of 5 $D_{5/2}$. The frequency reference is obtained using a vapour cell with a portion of the probe and coupling beams sent through it in a counter-propagating configuration while simultaneously monitoring the probe transmission in the vapour cell and through the nanofibre in the cold atoms experiment.

A typical EIT profile obtained in the cold atoms with 5 pW of power (P_p) in the probe beam and 200 nW of power (P_c) in the coupling beam through the ONF is shown in Fig. 7.3. Fitting cold atom data with equation 1 (orange curve in Fig. 7.3) we find that the curve does not fit the central part completely, but provides a very good fit for detunings higher than 25 MHz or lower than −25 MHz. Equation 1 is for free beam experiments where it is assumed that all the atoms contributing to the signal experience the same probe and coupling powers which is not true for our experiment. Symmetry of the evanescent field around the tapered region depends on the polarisation of light [15]. In principle, linear polarisation does not give a symmetrical field intensity around a nanofibre. In our experiment, the evanescent field of the coupling beam may not be overlapping with the probe due to their different polarisation orientations at the nanofibre waist. Hence, it is possible that some atoms may observe more 780 nm light, leading to single photon absorption of a portion of the 780 nm probe beam where the 776 nm presence is minimal due to azimuthal field dependence. This may introduce an additional absorption at the 5 $S_{1/2}$ F=2 → 5 $P_{3/2}$ F′=2 resonance with a Lorentzian profile. Hence, we add a Lorentz curve with a natural linewidth to equation 1 and get a reasonably good fit to the experimental data (blue curve in Fig. 7.3).

Parameters a_{32} and a_{42} in equation 1 are the relative transition strengths, which depend on the pump and probe polarisations and the distribution of atoms in

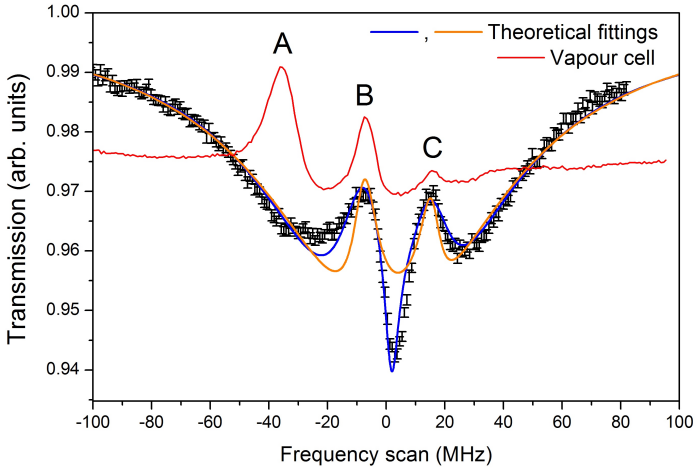


Figure 7.3: Transmission through the fibre as the frequency of the probe beam is scanned. The coupling beam is 7 MHz blue-detuned from the transition 5 $P_{3/2}$ F′=2 → 5 $D_{5/2}$ F″=3 and has a power of 200 nW. Black points: experimental data averaged for 200 runs. Orange curve: fitting using equation 1. Blue curve: fitting with a Lorentzian curve added to equation (1). Red curve: frequency reference obtained by a vapour cell. In the vapour cell, some atoms can make the transitions involving 5 $P_{3/2}$ F′=3 due to Doppler shift. Peak A corresponds to the transition 5 $P_{3/2}$ F′=3 → 5 $D_{5/2}$ F″=4, peak B due to 5 $P_{3/2}$ F′=3 → 5 $D_{5/2}$ F″=3 and 5 $P_{3/2}$ F′=2 → 5 $D_{5/2}$ F″=3, whereas, peak C is due to 5 $P_{3/2}$ F′=3 → 5 $D_{5/2}$ F″=2, 5 $P_{3/2}$ F′=2 → 5 $D_{5/2}$ F″=2 and 5 $P_{3/2}$ F′=1 → 5 $D_{5/2}$ F″=2. Peaks B and C have an equivalence in cold atoms as 5 $P_{3/2}$ F′=2 → 5 $D_{5/2}$ F″=3 and 5 $P_{3/2}$ F′=2 → 5 $D_{5/2}$ F″=2, respectively, but there is no peak corresponding to peak A since the atomic velocities are not sufficient to allow the 5 $P_{3/2}$ F′=3 transition to be within the range of the probe scan. The 5 $P_{3/2}$ F′=2 → 5 $D_{5/2}$ F″=1 transition is weak and not observable in either case.

magnetic sublevels. In reality, the polarisation pattern at the waist is complicated and cannot be taken simply as linearly polarisation even for linearly polarised light inputs, as in our case. In fact, the light does not even remain transverse, but acquires a longitudinal component at the waist region [15]. Also, aside from the birefringence of the ONF, the pigtails are not polarisation maintaining. Hence, these values must be determined from the experimental data. We fit the data for various coupling powers using a_{32} and a_{42} as free parameters and find that these values are almost constant with $a_{32} = 0.747$ and $a_{42} = 0.624$ with standard deviations of 0.036 and 0.124, respectively. Subsequently, we fit all the data while keeping these values fixed. The obtained fittings are shown in Fig. 7.4 for various coupling powers. The Rabi frequency is kept as a free parameter and we find that it varies linearly with the square root of the coupling power as expected (Fig. 7.5a).

The measured linewidths of the obtained peaks with respect to the coupling power are shown in Fig. 7.5b. There are two noticeable features: (i) broad linewidths,

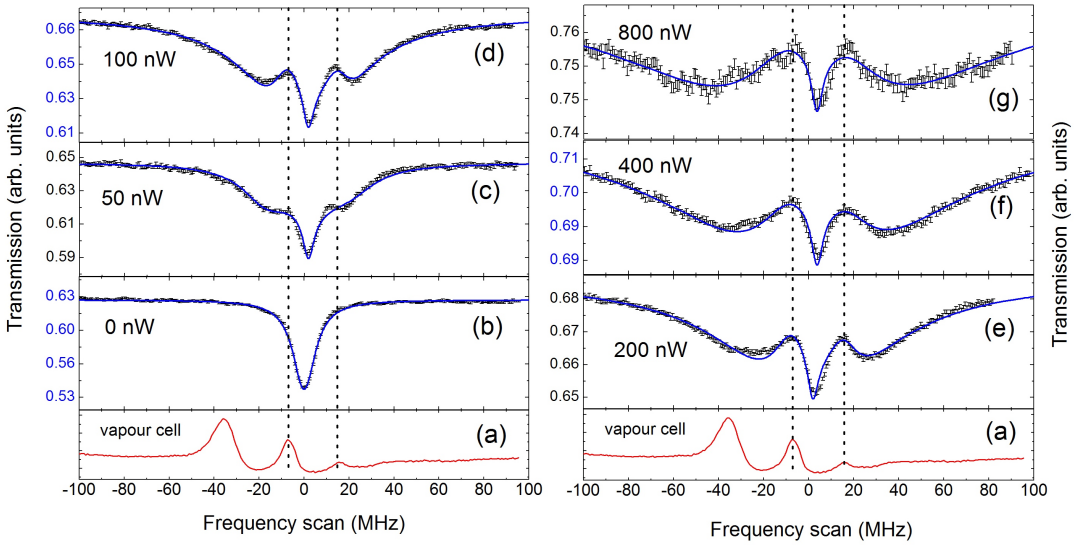


Figure 7.4: Multiple EIT peaks for coupling beam powers from 0-800 nW as indicated on the graphs. (a) The frequency reference signal obtained in a vapour cell (red curves) is used for frequency calibration.(b) At $P_c = 0$ nW an absorption signal is observed corresponding to the probe power of 5 pW. (c)-(g) EIT signals for $P_c = 50 - 800$ nW. The vertical dotted lines show the positions corresponding to the 5 $P_{3/2}$ F′=2 → 5$D_{5/2}$ F″=3 and F″=2 transitions. Black dots are experimental data and the blue curves are theoretical fittings.

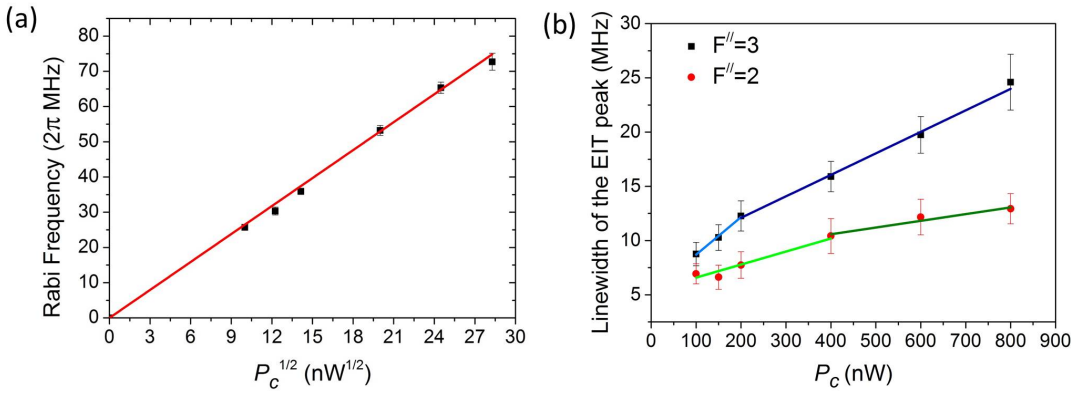


Figure 7.5: (a) Rabi frequency as a function of the square root of power in the coupling beam, determined from Fig. 7.4, for the strong coupling beam condition. The red line is a linear fit to the experimental data. (b) Linewidth of the two transparency peaks as a function of coupling power. The solid straight lines represent linear fits to the experimental data and two clear slopes are evident for each peak.

particularly at high P_c, compared to the natural linewidth of 6 MHz, and (ii) a linear increase in the width 'in sections' as a function of P_c. The broadness of the peaks may be due to several reasons. It is well known that the ratio of P_p/P_c and their polarisations affect the EIT profile significantly [143]. In any studies with an ONF, the atoms are distributed in the exponentially decaying

probe and coupling field intensities. Therefore, any particular probe and coupling power does not mean that all the participating atoms observe the same probe and coupling intensities. In other words, an effective P_p/P_c, as viewed by any particular atom, has a wide range of values. The polarisation of the two beams as observed by the atoms is also complex giving rise to the broadening of the peaks. Decoherence due to atoms hitting the ONF may also play a contributing role. The width of the EIT peaks increases linearly with P_c to a certain level and then a change in slope is observed for both the peaks, but at different power levels. The origin of this change in slope is yet to be understood via a full theoretical treatment of the problem, but is considered beyond the scope of this current work.

7.3.2 All-fibred-all-optical-switching

The observed EIT effects in the system are used for making an all-optical-switch. The probe beam is locked to 5 $S_{1/2}$ F=2 $\rightarrow$ 5 $P_{3/2}$ F$'$=2 and the coupling beam to 5 $P_{3/2}$ F$'$=2 $\rightarrow$ 5$D_{5/2}$ F$''$=2. The coupling beam is passed through two AOMs successively, one in "+1" order and other in "−1" order with the same frequency, in order to have the facility to switch on and off the beam, P_c, without any effective frequency shift. The coupling beam power is set to 80 nW and it is switched off and on at 10 kHz by modulating the AOM. The probe beam is continuously on and the transmission through the nanofibre is monitored. The transmission is higher when the coupling beam is on and lower when off. There is some leakage of the coupling beam due to back reflections on the detector even with the 780 nm filter in place. This back refection is determined by performing the same on and off switching sequence of the coupling beam in the absence of the cold atom cloud and is subtracted from the signal obtained when the cloud is present to get the change in transmission purely due to atoms as a switching medium. Fig. 7.6 shows the background-subtracted data and the electrical signal used to control the AOM modulation to switch the coupling beam on and off. One data point is collected every 25 μs. The switching speed could go higher with a denser cloud, making the data collection gate time even shorter.

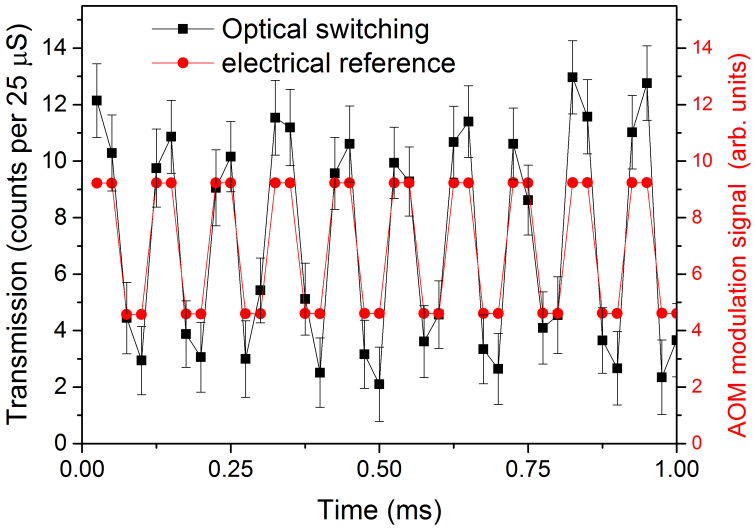


Figure 7.6: Transmission through nanofibre as a function of time to demonstrate all-optical-switching. Black: Photon counts obtained with 10 kHz on-off modulation of the coupling beam in the presence of cold atoms with background counts subtracted. Red: electrical reference signal used for switching on and off the coupling beam. The data is averaged for 150 runs.

7.4 Conclusion

We have demonstrated multi-level EIT in a cascaded system using an ONF for sending the probe and the coupling beams to a cold atomic cloud. This method could be used for storing two light pulses of different frequencies at the same time, and could also be used for generating entanglement with two different frequency beams. Using the EIT results, we have also demonstrated an all-fibred-all-optical switch which could be used for optical data processing in quantum systems. For analysing the EIT peaks, we have neglected optical pumping effects, such as double resonant optical pumping (DROP) [144], which is due to changes in the population of the ground level being probed. This can be justified as the probe beam we use is very weak and the MOT beams are continuously on during the experiment. Due to the presence of the cooling and the repump beams coupling to the two ground states (5 $S_{1/2}$ F=2 and 5 $S_{1/2}$ F=1), the population of these two states should be constant. Reduction of the DROP effect due to the presence of the repump beam has been studied for Rb vapour recently [145]. The width of the EIT signal is dependent on the coherence properties of atoms in the system. In our system, the atoms are moving in the MOT and the observation region is limited to the evanescent field region of the ONF. This can be transited by the atoms in a few 10s of μs. Also, the MOT is in continuous operation, hence the magnetic field and the MOT beams are on during the measurement leading to further boarding

of the obtained signals. However, we have obtained well-separated peaks (23 MHz apart) corresponding to the hyperfine transitions of the 5 $D_{5/2}$ level. If the atoms were in an ONF-based trap [45], the linewidths could be significantly lower and this would be a benefit for slowing down the light beams traveling through the ONF. Also, the signal strength could be higher as the number of atoms in the evanescent field region could be orders of magnitude higher than in the MOT case. This would be an advantage for all-optical-switching to obtain a higher contrast between the on and off states and could also lead to higher speed operation of the switch.

Chapter 8

Atom Interaction with Higher Order Modes of an Optical Nanofibre

Masalov and Minogin [38, 146] demonstrated that the spontaneous emission from a laser excited atom near an ONF supporting higher order modes would have about 5 to 10 times more pumping into the higher-order modes than the fundamental mode. A successful examination of this effect is presented in this chapter. The study is also extended to study the absorption property and higher absorption of the higher order modes is observed. This is the first and only work to date showing any interaction between ONF-guided higher-order modes and atoms. The profile of the ONF used for this work was exponential for which 32% transmission for the first family of higher order modes (LP_{11}) was achieved. However, later there have been significant advancements in the fabrication process utilising linear taper profiles, and then it was possible to achieve up to 95% transmission for the higher modes [76, 81]. Higher transmission fibres would be advantageous for further experiments in this line.

The contents of this chapter have been published as an open access article in "R. Kumar, V. Gokhroo, K. Deasy, A. Maimaiti, M. C. Frawley, C. Phelan and S. Nic Chormaic, *Interaction of laser-cooled* ^{87}*Rb atoms with higher order modes of an optical nanofibre*, New Journal of Physics, 17 (1), 013026 (2015)" .

RK contribution: Design and implementation of the experimental setup, data collection and analysis, paper writing.

The ONF used in this experiment was prepared by Aili Maimaiti (PhD student),

and the theoretical plots shown in the paper are works by Dr. Kieran Deasy, Dr. Ciarán Phelan and Aili Maimaiti.

Interaction of laser-cooled ^{87}Rb atoms with higher order modes of an optical nanofibre *

Ravi Kumar[1,2], Vandna Gokhroo[1], Kieran Deasy[1], Aili Maimaiti[1,2], Mary C. Frawley[1,2], Ciarán Phelan[1] and Síle Nic Chormaic[1]

[1] *Light-Matter Interactions Unit, OIST Graduate University, Onna, Okinawa 904-0495, Japan*

[2] *Physics Department, University College Cork, Cork, Ireland*

Abstract

Optical nanofibres are used to confine light to sub-wavelength regions and are very promising tools for the development of optical fibre-based quantum networks using cold, neutral atoms. To date, experimental studies on atoms near nanofibres have focussed on fundamental fibre mode interactions. In this work, we demonstrate the integration of a few-mode optical nanofibre into a magneto-optical trap for ^{87}Rb atoms. The nanofibre, with a waist diameter of ∼700 nm, supports both the fundamental and first group of higher order modes and is used for atomic fluorescence and absorption studies. In general, light propagating in higher order fibre modes has a greater evanescent field extension around the waist in comparison with the fundamental mode. By exploiting this behaviour, we demonstrate that the detected signal of fluorescent photons emitted from a cloud of cold atoms centred at the nanofibre waist is larger if higher order modes are also included. In particular, the signal from higher order modes appears to be about six times larger than that obtained for the fundamental mode. Absorption of on-resonance, higher order mode probe light by the laser-cooled atoms is also observed. These advances should facilitate the realisation of atom trapping schemes based on higher order mode interference.

Keywords: Optical nanofibre, Higher order fibre modes, Cold atoms, Atom trapping

*New Journal of Physics, 17 (1), 013026 (2015)

8.1 Introduction

Subwavelength diameter optical fibres, commonly known as "optical nanofibres (ONFs)", are proving to be of immense value for both fundamental and applied research with many different systems being investigated, such as cold atom manipulation and trapping [40, 43, 45, 107, 147, 148], colloidal particle manipulation [149–151], and sensing [152, 153]. ONFs have a large evanescent field extension outside their waist region, making them ideal for light-matter interactions studies. The integration of ONFs into atomic systems has been a focus of ever increasing research interest in recent years [154]. Earlier experiments, such as those reported in [40, 43, 45, 107, 147], focussed on (i) the interaction of the light guided in the fundamental fibre mode, HE_{11}, with atoms, or (ii) excitation of the HE_{11} mode through fluorescence coupling from resonantly excited atoms. While the latter experimental technique provides a means of characterizing the atoms near the surface of the optical nanofibre [13, 43, 44, 47], the former permits scenarios whereby atoms can be trapped around the optical nanofibre when far-detuned light is coupled into it [40, 45, 107]. Such ONFs can be termed as *single-mode ONFs (SM-ONFs)* since only the fundamental guided mode is supported [23]. The advantage of such a system is that, in addition to atom trapping applications, the nanofibre provides an optical interface that may be exploited for quantum communication using ensembles of laser-cooled atoms [148].

Other atom trapping geometries based on the use of higher order modes (HOMs) in a nanofibre have been proposed, permitting greater flexibility of atom position relative to the fibre and relative to other trapped atoms [28, 29, 155]. These schemes have the benefit of allowing for selective mode interference by adjusting the trapping parameters according to experimental requirements. Efficient guiding of HOMs in ONFs was a major technical challenge until our recent reporting of low-loss mode propagation in nanofibres fabricated from 80 μm diameter silica fibre [79]. Similar work using 50 μm fibre has since been reported [126]. We term such fibres *few-mode ONFs (FM-ONFs)* to distinguish them from the more conventional SM-ONFs. The crucial step in advancing such experiments was the result of a thorough study of the ideal parameters for fibre tapering, which revealed that reducing the fibre cladding-to-core diameter ratio relaxes the adiabatic criteria, thereby promoting efficient guiding of higher order modes [83]. The subsequent experimental achievements opened up a plethora of potential atom trapping scenarios, taking advantage of the few mode behaviour of the nanofibre. If one considers the field distribution of the first four true nanofibre modes (illus-

trated in Fig. 8.1), it is evident that the evanescent field for TE_{01}, TM_{01} and HE_{21} extends further into the surrounding medium than for HE_{11}. For a nanofibre of diameter 700 nm, as used for the experiments reported in this work, the fraction of light outside the nanofibre is higher for each of the TE_{01}, TM_{01} and HE_{21} modes as compared with HE_{11}. This phenomenon results in the evanescent light field for the higher order modes interacting with more atoms in the surrounding cloud than when studies are limited to the fundamental mode.

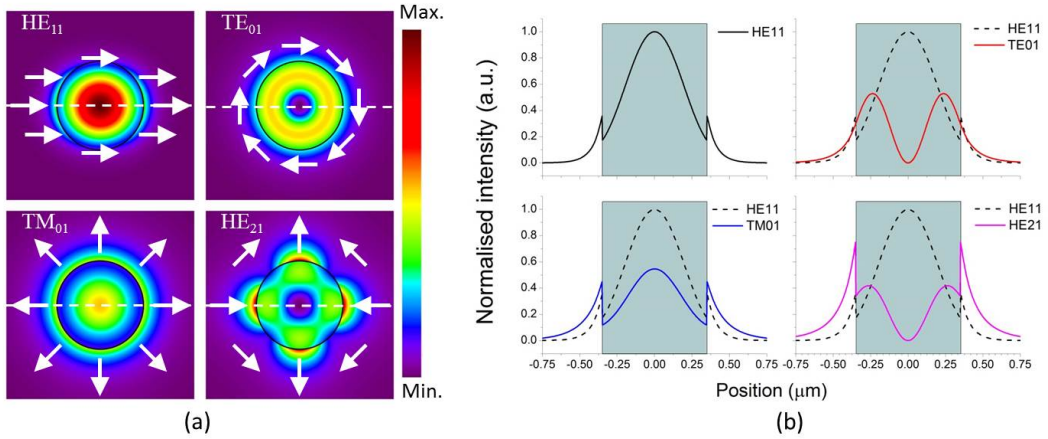


Figure 8.1: (a) Intensity distribution of the first four fibre modes (HE_{11}, TE_{01}, TM_{01}, and HE_{21}) of a nanofibre (radius 350 nm) for 780 nm light. Refractive indices of the nanofibre material and the surrounding medium are taken as 1.456 and 1 respectively. Black circles denote the nanofibre boundary. Arrows denote the polarisation of the light fields. The amount of power in each mode is identical and the four plots are normalised to the maximum intensity in the HE_{11} mode. (b) Intensity profile along the white dashed line in figure (a) with the zero position at the fibre axis. The shaded region denotes the fibre. The intensities are normalised to the maximum intensity in the HE_{11} mode. The profile of the HE_{11} mode is plotted along with the other modes for ease of comparison.

In this work, we present the first demonstration of a few-mode ONF integrated into a cloud of laser-cooled ^{87}Rb atoms. The higher order modes in the ONF were maintained despite the integration of the nanofibre into the ultra high vacuum system. We use the FM-ONF for two different studies to contrast the difference between the higher and fundamental modes: (i) we consider the count rate of atomic fluorescence coupled into the fibre through the nanofibre waist for both fundamental and higher modes, and (ii) we measure the atomic absorption of an on-resonance probe guided in the fundamental or in the higher modes. We show that the count rates for photons coupled into the nanofibre are larger when we include higher order guided modes in addition to the fundamental mode. This is in qualitative agreement with earlier theoretical predictions [38, 146]. Note that the theory is based on single atom coupling to the nanofibre, whereas our system

involves multiple atoms. Our studies also show that more atoms absorb light from the evanescent field when higher order modes are used, leading to better absorption signals (measured as a percentage of the probe light sent through the nanofibre). Aside from the impact this work will have on trapping schemes for cold atoms, it is also expected to drive progress in several other areas of research including optical communication, neutral-atom based quantum networks, particle manipulation, and sensing.

This paper is organised as follows. Section 2 describes the fabrication of the FM-ONF and the experimental details of the magneto-optical trap for ^{87}Rb. Section 3 presents the methods and results we obtained for three different experiments: (i) coupling of light (from MOT beams) to the nanofibre in the absence of an atom cloud, (ii) coupling of light to the nanofibre in the presence of an atom cloud, and (iii) absorption of a nanofibre-guided, probe beam by the laser-cooled atoms. The conclusion is presented in Section 4.

8.2 Experiment

8.2.1 Higher order mode optical nanofibre

Most published work on ONFs and atoms has focussed on SM-ONFs. Here, we used a FM-ONF which was fabricated from an 80 μm diameter, commercial, few-mode fibre for 780 nm (SM1250G80, Thorlabs) using the heat-and-pull technique, as previously described in [79]. We use 80 μm fibre in these experiments since it is easy to integrate with other fibre components using standard splicing techniques. The fibre pulling rig used was a hydrogen-oxygen flame-brushed system [76]. A 2 cm length of protective jacket was removed from the fibre and the two pigtails were clamped on translation stages on the pulling rig. The flame heated the fibre near to its phase transition temperature (1550 °C). The flame was brushed along the fibre for a particular set length (the "hot zone") while the fibre was simultaneously pulled by two translation stages moving in opposite directions with a constant speed (the "pulling speed"). The obtained taper profile was very close to exponential in the taper regions. Higher order mode propagation is extremely sensitive to the taper angle, which itself depends on the pulling speed and hot zone. A longer hot zone facilitates shallower exponential tapers, leading to a higher transmission, but this also elongates the taper length. If the nanofibre is too long, it is not suitable for integration into our cold atom setup. For these

reasons, and in order to achieve reasonably high transmission of the higher order modes through the nanofibre, an optimal hot zone of 7.7 mm and tapering speed of 0.125 mm/s were used. A photodetector and a charged coupled device (CCD) camera were placed at the output end of the fibre to monitor the transmission and mode profile during the tapering process.

Light propagating in the linearly polarised, LP_{11}, approximate mode in the non-tapered fibre segments must be described by the TE_{01}, TM_{01} and HE_{21} true modes in the nanofibre region, and LP_{01} has its equivalence as the HE_{11} mode. For ease of notation, in the following discussions, we refer to the LP_{11} approximate mode for indicating the family of true modes collectively, while recognising that the true modes provide us with the correct solutions. Solving Maxwell's equations for an optical fibre [156] yields a waveguide mode parameter, called the V-number, from which the number of modes supported by the fibre can be obtained. The V-number is given as

$$V = \frac{2\pi a}{\lambda}\sqrt{n_{core}^2 - n_{clad}^2}\ , \tag{8.1}$$

where a is the radius of the core, λ is the wavelength of the light propagating in the fibre, and n_{core} and n_{clad} are the refractive indices of the core and the cladding, respectively. The V-number for the specific fibre used in our experiments (when untapered) is 4.3, implying that it can support four linearly polarised mode groups, LP_{01}, LP_{11}, LP_{21}, and LP_{02}, for 780 nm light. When a nanofibre is fabricated, the cladding of the untapered fibre becomes the core for the nanofibre and the surrounding medium (e.g. air or vacuum) becomes the cladding. The V-number plot is shown in Fig. 8.2. The mode cutoff diameter is around 660 nm for the degenerate HE_{21} true modes and around 580 nm for both the TE_{01} and TM_{01} true modes.

In our experiments, the LP_{11} mode was excited by injecting a Laguerre-Gaussian (LG) beam into the untapered fibre pigtails [157]. A liquid-crystal-on-silicon spatial light modulator (Holoeye Pluto SLM) was used to create the LG beam [82]. A computer-generated vortex hologram was applied to the SLM and a vertically polarised, 780 nm laser beam was launched on to the SLM surface; the reflected beam formed a doughnut shape at the far field. This LG_{01} free space beam was coupled to the fibre to excite the LP_{11} mode which yielded a two-lobed beam profile at the fibre output, as expected. Along with the excitation of the LP_{11} mode, there was a small percentage of residual fundamental mode coupled into the fibre. This was mainly due to the purity of the generated LG beam and the efficiency of the fibre coupling. The level of the impurity was estimated by

sending an LG_{01} beam into the fibre during the tapering process and observing its transmission as a function of pulling distance (see Fig. 8.3(a)). The mode cutoff pull length for the higher modes (HE_{21}, TE_{01}, TM_{01}) and the fundamental mode can be defined from Fig. 8.3(a). Deducting the percentage of the remaining fundamental mode (Position 3) from the total intensity (Position 1), we estimated that the LP_{11} mode was excited in the few-mode fibre with a purity of 95%.

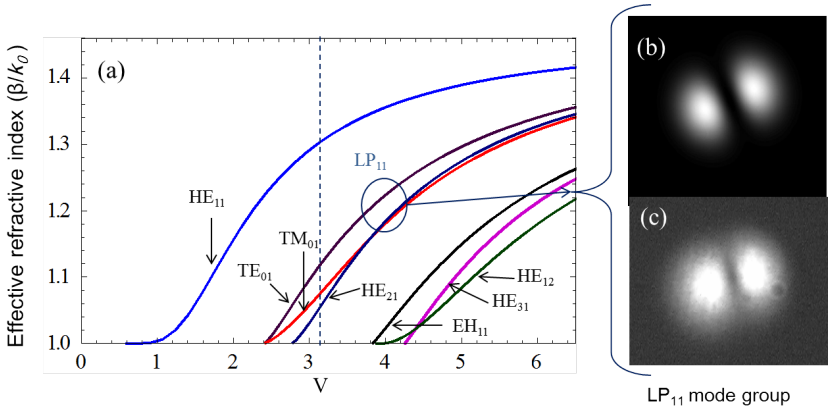


Figure 8.2: (a) V-number plot for different modes of the nanofibre with the V-parameter on the x-axis. The vertical line indicates the corresponding V-number for the nanofibre size used in the experiments; (b) Simulated profile for the LP_{11} mode exiting from a nanofibre pigtail; (c) Observed experimental profile for (b).

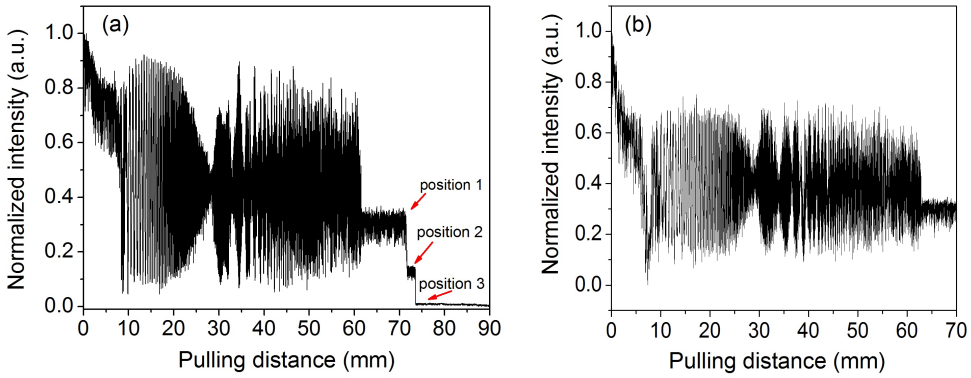


Figure 8.3: Observed transmission for light coupled to the LP_{11} mode of the fibre during tapering: (a) for a pull length of 90 mm to cut off all the higher modes and (b) for a 70 mm pulling length to ensure that the nanofibre supports only the TE_{01}, TM_{01}, HE_{21}, and HE_{11} modes. In (a) Position 1 is the cutoff point for the coupled HE_{21} modes, Position 2 is the cutoff for the TE_{01} and TM_{01} modes and Position 3 is the portion of the residual fundamental mode guided by the nanofibre.

First, a nanofibre was fabricated using a 90 mm pulling length in order to obtain a complete transmission profile including mode cutoffs. The transmission graph (Fig. 8.3(a)) suggested that the pulling distance should be between 62 and 71 mm to obtain a nanofibre supporting the LP_{11} family of modes and the fundamental

mode (Ref. [79] gives the details of the process). Since a smaller diameter fibre yields greater extension of the evanescent field into the surrounding medium, it is preferable to use a longer pulling length. For all other experiments reported here, we used a 70 mm pulling length to fabricate the nanofibre. This corresponded to ∼700 nm waist diameter determined from the calibration data of our pulling rig. Monitoring the mode profile until the end of the pulling process ensured that the prepared fibre still supported the LP_{11} mode. The nanofibre had 32% transmission for the LP_{11} mode group (see Fig. 8.3). The rest of the power was lost as it coupled to the cladding modes in the taper regions [126]. This fibre was highly adiabatic for the fundamental mode with 92% transmission. Using these values of total transmissions (and assuming both sides of the taper were equivalent as verified by measurement), we estimate that 96% of the input power was transmitted to the nanofibre waist for the fundamental mode and 56% for the LP_{11} mode group.

The nanofibre was glued to a U-shaped mount and installed vertically in an octagonal vacuum chamber used for the magneto-optical trap (MOT). The six cooling beams intersected at the nanofibre waist, four at 45° and two at 90° to the nanofibre axis. The fibre pigtails at either end of the nanofibre were passed through Teflon ferrules (with hand-drilled holes of 0.25 mm diameter) located on the top and the bottom flanges of the chamber. The ferrules were rendered vacuum tight by compressing Swagelok connectors [102]. A relatively simple experiment was carried out in order to test whether the distribution of power between the fundamental and the LP_{11} modes was affected by pressure on the tapered fibre via the Teflon ferrule. As described earlier, an LG_{01} mode was coupled to the fibre and the output was measured with a CCD camera. We observed minimal mode mixing as the ferrule was tightened. Note that it is crucial to keep the nanofibre straight to ensure minimal bending loss and distortion of the mode profiles of the light passing through it.

8.2.2 Magneto-optical trapping of atoms

^{87}Rb atoms were cooled and trapped using a standard magneto-optical trapping technique (for details see [47] though it was for ^{85}Rb). Base pressure in the vacuum chamber was 2×10^{-9} mbar and, when a current of 5 A was passed through a Rb dispenser, the pressure rose to 4×10^{-9} mbar and remained stable during the experiments.

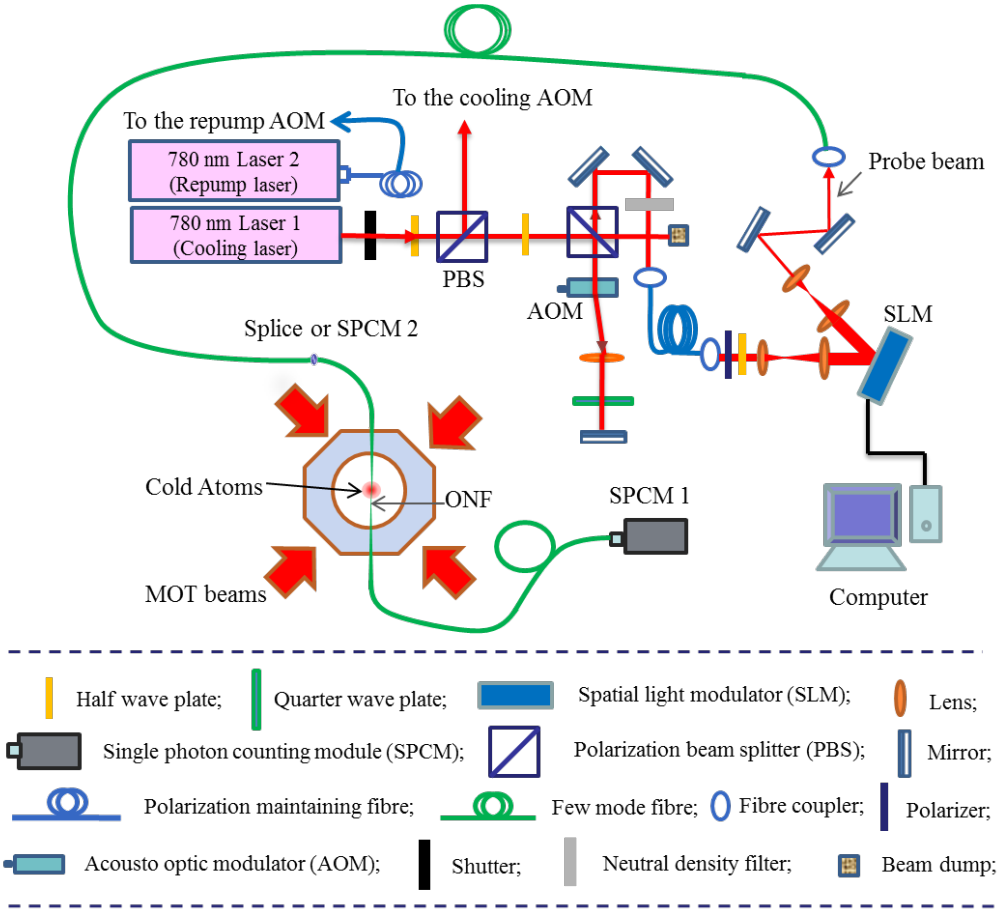


Figure 8.4: Schematic of the experimental setup. For absorption experiments one pigtail of the FM-ONF was spliced to a length of fibre (the same kind which was used to prepare the FM-ONF) transporting the probe light and another pigtail was connected to an SPCM. For fluorescence measurements, the pigtails were connected to different devices according to the experiment being conducted (see Section 3.2).

A 780 nm laser was locked to the $5\ ^2S_{1/2}F_g = 2 \rightarrow 5\ ^2P_{3/2}F_e = (2,3)_{co}$ crossover peak of ^{87}Rb for the cooling beam. The frequency was further shifted by an acousto-optical modulator (AOM) in a double-pass configuration so that it was 14 MHz red-detuned from the cooling transition, $5\ ^2S_{1/2}F_g = 2 \rightarrow 5\ ^2P_{3/2}F_e = 3$. The cooling beam was split into four beams, two of which were retro-reflected to get three pairs of σ^+ and σ^- beams for the MOT. Another laser, used as the repump, was locked to the $5\ ^2S_{1/2}F_g = 1 \rightarrow 5\ ^2P_{3/2}F_e = (0,2)_{co}$ peak and shifted to the repump transition, $5\ ^2S_{1/2}F_g = 1 \rightarrow 5\ ^2P_{3/2}F_e = 2$, using an AOM. The repump was overlapped with one of the cooling beams using a beam splitter. The magnetic field for the MOT was created by a pair of coils carrying equal currents of 3.5 A in opposite directions to generate a field gradient of 10 G/cm at the centre of the vacuum chamber. Each cooling beam had an intensity of 6 mW/cm^2 and a diameter of 18 mm. The cold atoms were trapped around the waist of the

FM-ONF. A compensation coil was used to generate a small magnetic field in the transverse direction to the MOT coils' axis in order to optimise the overlap between the centre of the atom cloud and the nanofibre. The diameter of the cloud was ∼1 mm and there were ∼3×10^6 atoms in the trap. The temperature of the cloud was measured to be ∼150 μK by taking a series of fluorescence images of the cloud for different expansion times.

8.3 Measurements and Results

8.3.1 Coupling of MOT beams to the nanofibre

As a first test, in the absence of cold atoms and probe light through the FM-ONF, an analysis of MOT beam coupling to the nanofibre was conducted. The mode profile of the coupled light was analysed at the output of one of the FM-ONF pigtails by focussing it onto a CCD camera (replacing the SPCM 2 by a CCD camera, in Fig. 8.4). The observed profile, as shown in Fig. 8.5, was doughnut shaped, but not completely dark at the centre. A fit of the observed intensity profiles using a combination of the LG_{00} and LG_{01} modes (where the LG_{00} mode corresponds to the LP_{01} fibre mode and the LG_{01} mode to the LP_{11} fibre mode) revealed that ∼55% of the light coming out from the nanofibre pigtail was in LG_{01}. Taking the transmission difference for the fundamental and the higher modes through the FM-ONF into consideration, we estimate that ∼67% of the light from the MOT beams that coupled into the nanofibre excited higher order modes.

8.3.2 Fluorescence measurements

Next, we looked at the fluorescence coupling into the FM-ONF from resonantly-excited atoms. The cold atom cloud was formed around the waist of the FM-ONF and both the output pigtails were connected to single photon counting modules (SPCMs). In this condition, light coupled into the nanofibre had a contribution from (i) the MOT beams and (ii) the atomic fluorescence. Photon counts were recorded on both the SPCMs and the signals were found to be equivalent, i.e. half of the photons coupled in to the nanofibre travelled in each direction. In order to estimate the contribution of the fundamental mode to the total photon count rate, one output pigtail was spliced to a section of single mode fibre (SMF, 780HP,

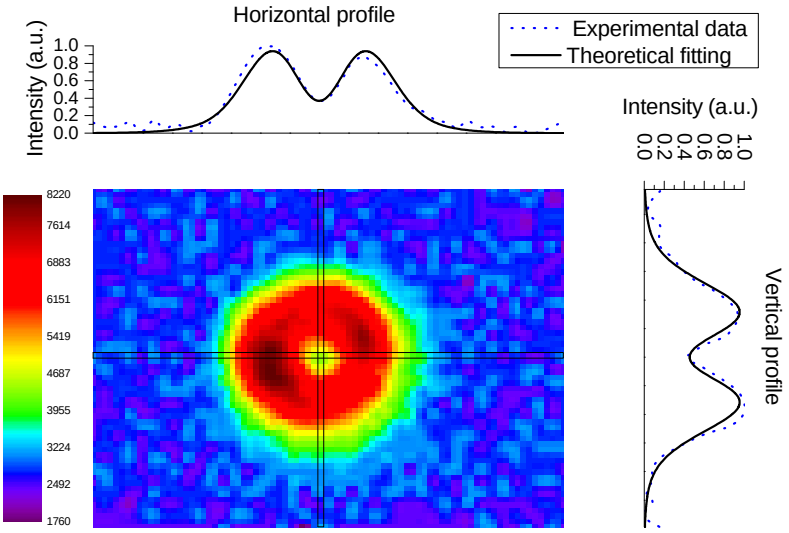


Figure 8.5: Intensity of the light collected by a CCD camera at one output of the nanofibre when only the MOT beams are on. Horizontal and vertical profiles are fitted using a combination of LG_{01} and the fundamental mode.

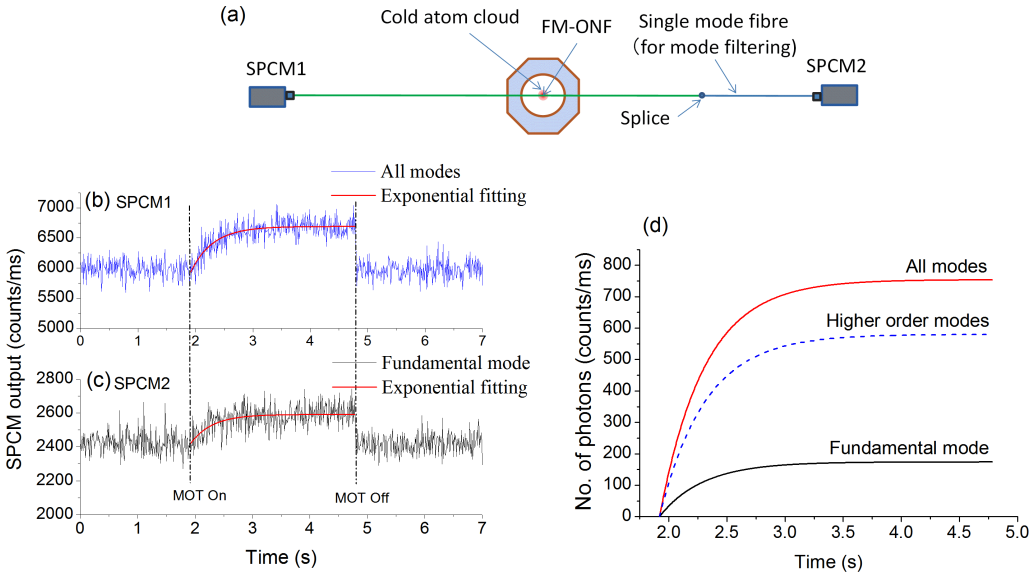


Figure 8.6: (a) Schematic of the experimental setup for the mode filtering experiment; (b) Cold atom cloud loading curve when light is coupled to the guided modes of the FM-ONF; (c) the same as (b) but only for the fundamental mode. When the MOT magnetic field is switched on, the cloud starts loading and the photon count increases exponentially until it reaches a steady state when the cloud is fully loaded. After reaching this level, the magnetic field is switched off. All the atoms leave the trap and the recorded photon count rate is purely due to the MOT beams coupling into the nanofibre; (d) Comparison of fluorescence counts based on the exponential fits to the loading curves in (b) and (c). The curve for the higher order modes (blue, dashed) is generated by subtracting the fundamental mode contribution from all modes.

Thorlabs). The SMF acted as a filter for any higher order mode propagation (Fig. 8.6 (a)) and only fundamental mode guiding survived. Simultaneously, the second SPCM recorded the total number of photons coupled into all the fibre modes, i.e. both the fundamental and higher orders, collectively. The MOT magnetic field was switched on and off at intervals of few seconds (to provide enough time for the cloud to reach steady state) in order to separate the photon count contribution from the atom cloud (as shown in Figs. 8.6 (b) and (c)) and that arising from the MOT beams. By comparing the total photon signal with that obtained for only the fundamental mode, we determined that ∼85% of the atomic fluorescence coupling to the nanofibre was coupled into the higher order modes. In other words, for every photon coupled into the fundamental mode, approximately six photons coupled into the higher fibre modes. Note that the different transmissions from the waist to the pigtail output for the fundamental mode (96%) versus the higher order modes (56%) were taken into consideration.

In order to confirm this result, the same test was repeated with a different method for filtering out the higher order modes contribution. A SM-ONF was spliced to the output pigtail of the FM-ONF in place of the mode filtering SMF. The SM-ONF was fabricated from the same few-mode fibre (SM1250G80) as the nanofibre in the chamber. Similar results were obtained (data not shown).

8.3.3 Absorption measurements

Next, we considered atom absorption of the light in the evanescent field to see how it varied depending on whether higher order modes or the fundamental mode were guided by the nanofibre. A fraction of the cooling laser beam was passed through a double-pass AOM so that its detuning could be changed as required. The output of the AOM was passed through a linear polarizer before reflecting from the phase imprinted SLM to generate an LG_{01} probe beam, which was coupled to the FM-ONF to excite the higher order modes. The computer-controlled SLM was used to switch the free-space probe beam between LG_{00} and LG_{01} depending on need.

The cold atom cloud was formed around the waist of the nanofibre, ensuring that the atoms in the cloud interacted with the guided light via evanescent field coupling. The MOT beams, i.e. the cooling and repump beams, and the photon counter were switched on and off using the timing sequence shown in Fig. 8.7 in order to check absorption of the probe beam by the cold atoms. The trapping

magnetic field and the probe beam were kept on at all times; however, the photons guided through the nanofibre were only counted during the 1 ms time when the MOT beams were off. A repetition rate of 5 Hz was used for the experiments to ensure that the atom cloud was fully loaded before proceeding with any measurements. This gave sufficient time for the cloud to return to its steady state by re-collecting any atoms lost in the 1 ms expansion during the detection phase. The photon counts were collected for 400 runs.

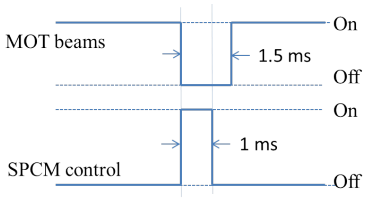


Figure 8.7: Timing sequence for the MOT beams and the SPCM during absorption experiments. A 5 Hz repetition rate was used.

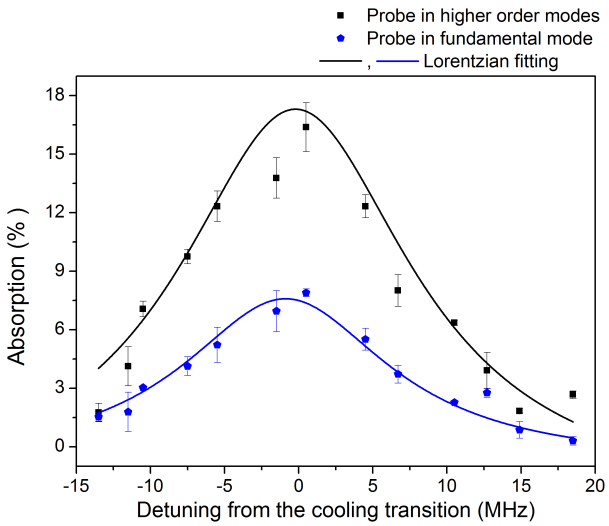


Figure 8.8: Absorption spectra obtained when either higher order modes (squares) or a fundamental mode (circles) probe beam was coupled into the FM-ONF. Probe power measured at the output end was maintained at $\sim$ 4.3 pW in both cases by changing the input power.

Next, the same collection sequence (Fig. 8.7) was repeated 400 times in the absence of MOT magnetic field, so as to determine the background signal. Using these two sets of data, the percentage absorption of the probe was calculated for a particular detuning with respect to the cooling transition of ^{87}Rb. The same experiment was repeated using different probe beam detunings in order to obtain the absorption spectrum for the ^{87}Rb cloud (Fig. 8.8). Finally, a similar experiment was performed for a fundamental mode probe in the nanofibre. We used the same power values at the output end of the nanofibre. Again, the

percentage absorption signal for the atom cloud was obtained. From Fig. 8.8 one can see that the absorption appeared more pronounced when the LP_{11} mode group was at the nanofibre waist. For all cases the probe power was maintained at 4.3 pW at the output end in the cloud-off condition. Taking the transmission difference for the LP_{00} and LP_{01} modes into account, the probe power at the waist of the nanofibre for the higher order mode case was 1.7 times higher than for the fundamental mode. The absorption percentage for the higher order modes still appeared to be higher (by a factor of $\sim$2). This reflects the fact that more atoms surrounding the waist of the nanofibre interacted with the evanescent field for higher order modes, since they extend further from the fibre surface. The linewidths obtained by Lorentzian fitting to the spectra are similar in both the cases (19 $\pm$ 5 MHz for the higher modes and 17 $\pm$ 2 MHz for the fundamental mode).

8.4 Conclusion

In this work, we have demonstrated, for the first time, the propagation of higher order modes (the LP_{11} mode group) in an optical nanofibre integrated into a magneto-optical trap for neutral atoms. We have studied fluorescence from atoms coupled into the optical nanofibre guided modes. Our preliminary results appear to be in qualitative agreement with earlier theoretical predictions [38, 146], but further studies are necessary to fully understand the effects. In particular, state selection of the atoms should be performed [39]. We also observed absorption of the higher modes and, for a particular output power level, absorption appeared to be higher than that for the fundamental mode. The work presented in this paper enables numerous heretofore theoretical atom trapping schemes to finally be realised, such as that relying on modal interference of far detuned higher order modes [28]. Future work will focus on trapping atoms around the nanofibre using higher order mode combinations and will include consideration of alternative complex mode patterns [155].

Chapter 9

Conclusions

Experiments presented in this thesis show the current trend of research with ONFs integrated to a MOT. Relevant theories are presented describing the light propagation through an ONF, light-atom interactions and magneto-optical trapping of atoms. Methods for fabricating ONFs of different kinds (SM-ONF and FM-ONF) are presented. Experiments with the SM-ONF (with a diameter of 350 nm) include the temperature measurement of cold atoms using a probe beam sent through the ONF, observation of Autler-Townes splitting, EIT, and all-fibred-all-optical-switching at ultra-low power levels. The experiments with the FM-ONF (with a diameter of 700 nm) provides evidence of higher pumping efficiency in higher-order modes, than for the fundamental mode, for emissions from laser-excited atoms surrounding the waist of the ONF and a higher percentage absorption of light propagating in higher-order modes than in the fundamental mode.

Measuring the temperature of the cloud for various probe powers through the ONF, it has been shown that near-resonant light at 780 nm through the ONF gives rise to a local temperature change of the cold atoms. The effect of this light is further investigated by introducing another beam of 776 nm (as a probe beam), along with the 780 nm (as a coupling beam), through the ONF in order to observe the Autler-Townes splitting the intermediate energy level due to the 780 nm beam. The splitting at ultra-low power, with less than one photon on average at any time in the interaction region, shows the strength of the evanescent field of an ONF and also provides a method for direct detection of the Rabi frequency of the coupling field. With a slight modification to the experimental setup by using the 780 nm light as a probe with lower intensity and the 776 nm light as a coupling

beam with higher intensity, it was possible to observe EIT in a ladder-type system. The obtained multi-peak EIT feature has a potential application of slowing down multiple frequencies at the same time in an ONF. Two light pulses propagating with slow group velocities in a coherently prepared atomic gas enables a single-photon pulse to coherently control or manipulate the quantum state of the other resulting in the generation of entangled states useful for quantum information processing [137]. Based on the observed EIT phenomenon, it was possible to perform an optical switching experiment in an all-fibred system where both the probe and the control are propagating in the fibre network. The switching speed of this prototype experiment was 10 kHz; however, it would be possible to go to higher switching speeds by using an optically denser medium, for instance, by elongating the cloud along the ONF axis leading to higher effective number of atoms or by using a fibre-based trap, which can have a few thousand atoms interacting with the evanescent field.

Next, the experiential demonstration of the interaction of atoms with the higher-order modes of an ONF provides an additional degree of freedom for information transfer and entanglement experiments. There have been theoretical proposals for trapping atoms using dipole forces generated by the light field propagating in the higher-order modes of an ONF [29, 155]. Such traps have been realised with the fundamental mode of an ONF using red- and blue-detuned beams passing through an ONF [45, 107]; however, a trap generated by the interference of different modes would provide more flexibility on the trapping geometry in three dimensions. A demonstration of the interaction of atoms with HOMs of an ONF also opens the possibility of manipulating atoms by the transfer of angular momentum of light [158–160]. Entanglement of orbital angular momentum (OAM) states is very promising for quantum information technologies [161, 162]. Terabit data transmission employing OAM multiplexing has been demonstrated in free space [163] and through a fibre [164]. Also, a quantum memory for OAM photonic qubits has been made successfully [165]. However, for a real quantum network system it would be very advantageous to perform an OAM-based qubit operation and this could be done using atoms coupled to an ONF. It is anticipated that such experimental goals could be reached in the future.

Appendix A

Other Published Works

A.1 Release-Recapture Temperature Measurement

The release-recapture method for the temperature measurement of cold atoms is well known. This chapter presents the first implementation of this technique for temperature measurements using the fluorescence collected through an ONF. This work was published in "L. Russell, R. Kumar, V. B. Tiwari, S. Nic Chormaic, *Measurements on release–recapture of cold 85 Rb atoms using an optical nanofibre in a magneto-optical trap*, Optics Communications 309, 313-317 (2013)".

RK contribution: Performing the experiment, data analysis and paper writing.

Optics Communications 309 (2013) 313–317

Contents lists available at ScienceDirect

Optics Communications

journal homepage: www.elsevier.com/locate/optcom

Measurements on release–recapture of cold ^{85}Rb atoms using an optical nanofibre in a magneto-optical trap

L. Russell [a,b,c,*], R. Kumar [a,b,c], V. B. Tiwari [a,b,d], S. Nic Chormaic [a,c,e]

[a] Physics Department, University College Cork, Cork, Ireland
[b] Tyndall National Institute, Lee Maltings, Propsect Row, Cork, Ireland
[c] Light-Matter Interactions Unit, OIST Graduate University, 1919-1 Tancha, Onna-son, Okinawa 904-0495, Japan
[d] Laser Physics Applications Section, Raja Ramanna Centre for Advanced Technology, Indore 452013, India
[e] School of Chemistry and Physics, University of Kwa-Zulu Natal, Durban 4001, South Africa

ARTICLE INFO

Article history:
Received 29 March 2013
Received in revised form
14 July 2013
Accepted 27 July 2013
Available online 9 August 2013

Keywords:
Laser cooling
Optical nanofiber
Rubidium
Release–recapture
Temperature

ABSTRACT

We have performed release–recapture temperature measurements of laser-cooled ^{85}Rb atoms using an optical nanofibre (ONF) in a magneto-optical trap (MOT). The effects of changing the cooling laser light-shift parameter on the temperature of the cold atoms and spring constant of the trap are studied. By varying the cold atom number density near the ONF, the onset of the multiple scattering regime is observed without the need for an estimation of the atom cloud size. Moreover, this sensitive ONF assisted release–recapture technique is easily able to detect any optical misalignment of the cooling laser beams in the MOT.

© 2013 Elsevier B.V. All rights reserved.

1. Introduction

Temperature is undeniably one of the most important characteristics of a laser-cooled sample of atoms that one can measure. By experimentally determining the ensemble temperature, T, quantities such as spring constant and diffusion coefficient can be estimated [1,2], temperature and density regimes can be mapped out [3], and a wealth of information regarding the efficiency of the trapping, cooling and compression scheme can be revealed [4,5]. Although there now exist many temperature measurement techniques, for example [6,7], the most commonly implemented methods use the thermal expansion of the cloud – time-of-flight (TOF) measurements – to estimate T [8,9]. In this paper, we focus on the release–recapture (RR) which is sensitive to the velocity distribution of the cloud. For temperatures at the Doppler limit (144 μk for ^{85}Rb) and above, as is the case in this work, the RR method is well-suited. At temperatures significantly below the Doppler limit, gravity begins to play a role in the thermal expansion of a cold cloud of atoms because the initial velocity of the atoms becomes small compared to the velocity acquired due to gravity during the expansion phase.

An optical nanofibre (ONF) [10,11] is generally made from standard optical fibre which is heated and simultaneously pulled to produce a subwavelength diameter fibre. ONFs can be used to couple light into optical resonators [12–15] and for characterising and guiding particles [16,17]. Spontaneous emission into the guided modes of an optical nanofiber is enhanced [18], making it an ideal high-sensitivity tool for channeling atomic fluorescence to a detector. Thus, in recent years, ONFs have also been shown to act as a measurement tool and delivery platform for cold atoms [19–26] and atomic vapours [27,28].

Here, the RR method is performed by positioning a cold cloud of ^{85}Rb atoms centrally around an ONF. Previous works show that, despite the presence of the hot ONF surface in the cloud of cold atoms, sub-Doppler temperatures can still be obtained with large red-detunings of the cooling laser beams [25].

2. Background

If a spherical cloud of atoms, with a Gaussian velocity distribution, is allowed to expand homogeneously from an initial finite diameter, the fraction of atoms, f_r, remaining after the release time, Δt_2, is given by

$$f_r = \frac{1}{\pi^{3/2}} \int_0^{v_c/v_T} e^{-u^2} u^2 \, du \cdot 4\pi, \tag{1}$$

* Corresponding author at: Physics Department, University College Cork, Cork, Ireland.
E-mail address: laura.russell@oist.jp (L. Russell).

0030-4018/$ - see front matter © 2013 Elsevier B.V. All rights reserved.
http://dx.doi.org/10.1016/j.optcom.2013.07.080

where $u^2 du \cdot 4\pi$ is the spherical polar coordinate for velocity. The thermal velocity of the atoms in the MOT at a temperature T is $v_T = \sqrt{2k_B T/m}$ and $v_c = R_c/\Delta t_2$ is the velocity at which the atoms just reach a position R_c in the time interval Δt_2. The capture region is characterised by the radius of the MOT beams, R_c. Integrating Eq. (1) yields

$$f_r = -\frac{2e^{-v_c^2/v_T^2} v_c}{\sqrt{\pi} v_T} + \mathrm{Erf}\left[\frac{v_c}{v_T}\right]. \quad (2)$$

Eq. (2) describes f_r as a function of Δt_2. This equation is fitted to the experimental data by taking R_c as known and v_T is the fitting parameter.

3. Experiment

The cold ^{85}Rb atom cloud is formed with a standard MOT configuration of three orthogonal, counter-propagating cooling beams intersecting at the centre of an inhomogeneous magnetic field. The cooling laser is locked to the crossover peak, $^2S_{1/2}F_g = 3 \rightarrow {}^2P_{3/2}F_e = (2,4)_{co}$ and then red-detuned from the cooling transition using an acousto-optical modulator (AOM). This detuning is controlled by the frequency input (0–10 V) to the AOM driver. Each beam has a maximum diameter of 24 mm (controlled via an aperture). The repumping laser is locked to the crossover peak, $^2S_{1/2}F_g = 2 \rightarrow {}^2P_{3/2}F_e = (1,3)_{co}$. The magnetic field is created by a pair of coils, each carrying currents of ~ 4 A in opposite directions, to generate an axial field gradient in the region of 15 G/cm at the centre of the MOT. Between 10^4 and 10^8 atoms are trapped in the MOT depending on experimental parameters.

To fabricate the ONF, the usual heat-and-pull-technique [29] is used with Fibercore SM750 fibre. For these experiments, the transmission of the ONF was $\sim 60\%$ and the waist diameter was ~ 1 μm (as determined with a scanning electron microscope). Further details about the experimental characteristics of an ONF can be found in [22]. The fibre pigtails are coupled into and out of the UHV chamber using a Teflon feed-through [30] and one end is connected to a single photon counting module (SPCM[1]). The cloud is aligned centrally around the ONF using imaging techniques and optimisation of the fluorescence coupling into the fibre guided modes is detected by the SPCM. Final adjustments to cloud position are made with magnetic coil currents.

3.1. Procedure

The cooling laser beams were switched on and off with an AOM in order to achieve the desired loading, release and recapture sequence (see Figs. 1 and 2). A recapture time, Δt_3, of 50 ms was used to ensure that no background vapour atoms are recaptured by the MOT. The loading time of the MOT is typically ~ 1 s. The magnetic field stays on at all times.

To perform a temperature measurement, the cloud of atoms was loaded for 10 s (Δt_1) to ensure that a steady-state number of atoms was reached. Then, the cooling laser was switched off using the AOM for a time Δt_2 to allow the cloud to expand freely. Δt_2 is varied each time the sequence is repeated: $\Delta t_2 = 5$ ms, 10 ms, 20 ms, … 150 ms. After the release time has passed, the cooling laser is switched on for $\Delta t_3 = 50$ ms to recapture the cloud. The cooling beams are switched off again with the AOM for 50 ms to provide a suitable contrast between the signal from the recaptured atoms and the background level. The sequence is recommenced for the next value of Δt_2. An image of the cloud is recorded using a CMOS camera and image analysis is performed to estimate the cloud radius.

Following this release and recapture process, fast atoms escape the MOT after a short release time and slower atoms are lost only after longer release times. To estimate the temperature of the atoms, the fraction of remaining atoms is calculated as a function of Δt_2. This is proportional to the fluorescence coupled into the nanofibre. This method is sensitive to the velocity distribution of the cloud.

4. Results and discussion

Temperatures approaching the Doppler limit have been observed at moderate detunings when the alignment of MOT beams has been particularly good. For example, for a detuning of -2.6Γ (where $\Gamma = 2\pi \times 5.9$ MHz is the natural linewidth of the $5^2S_{1/2} \rightarrow 5^2P_{3/2}$ transition in ^{85}Rb) with a cooling laser intensity per beam, I_{beam}, of $2.9I_s$ (where $I_s = 1.6$ mW/cm^2 for $\sigma^{\pm}$-polarised light on the ^{85}Rb cooling transition), T is estimated to be 167 μK (Fig. 3). Poor MOT beam alignment would mean that atoms may leave the capture region in a non-isotropic way, the signature of which is an immediate and sharp decrease in recaptured atoms. The importance of precise optical alignment and power equalisation in the MOT beams is well known [31,32]. For example, [31] reports a temperature and associated variation of (147 ± 25) μK depending on the alignment of the laser beams. By using the ONF as the detection tool, the effect of beam misalignment and power mismatching is detectable with a greater sensitivity than for fluorescence imaging techniques.

The temperature of the cold atoms as a function of I_{beam} was investigated (Fig. 4) and measurements show that a span of a few hundred μK can be observed when varying I_{beam} from 2.5 mW/cm^2 to 6.7 mW/cm^2 at a constant cooling laser red-detuning of $\sim 2\Gamma$. As expected, the temperature reduces as laser intensity is reduced [33].

Traditionally, R_c is the quantity with the greatest uncertainty. A small change in R_c (~ 2.5 mm) when fitting Eq. (2) to the data results in a temperature shift of the order of the error bars seen in Figs. 4–6.

In order to compare the RR temperature measurements with another technique, we have taken data directly from previous work which used the method of forced oscillations to estimate cloud temperature (see [25] for full details). Table 1 presents a comparison of results for temperature as a function of cooling laser red-detuning. The results found using each technique correlate quite well. In particular, for higher detunings, the T values which have been estimated with each method agree more strongly. Lower values of red-detuning were not easily examined with the ONF used for RR as the sacrifice in N_A was sufficient to lower the fluorescence coupling signal significantly.

From Fig. 5, it is clear that temperatures obtained with the RR technique increase linearly with the light-shift parameter, $\Omega^2/|\delta|\Gamma$, as expected [2]. The spring constant, κ, can be inferred from these temperature values. κ describes the restoring force in the MOT and is a particularly relevant quantity in relation to compressing atoms to high density. To determine κ it is assumed that, in thermal equilibrium, the atom cloud has a thermal energy given by $k_B T = \kappa\langle r^2\rangle = m\langle v^2\rangle$, where T is the experimentally determined cold atom cloud temperature, k_B is Boltzmann's constant, r is the radius of the atom cloud, and $\langle v^2\rangle$ is the mean square atomic velocity [1,4]. For each value of red-detuning, the cloud radius is estimated using image analysis. Fig. 6 shows that the spring constant increases with intensity at low intensity or detuning values and then levels off at some critical value of the light-shift parameter. Wallace et al. [2] report that the spring constant is not independent of I_{beam} until a moderately high value of the light-shift parameter is reached.

[1] Perkin and Elmer single photon counting module; model: SPCM-AQR-14; dark count = 100 counts s^{-1}; quantum efficiency = 60% at 780 nm.

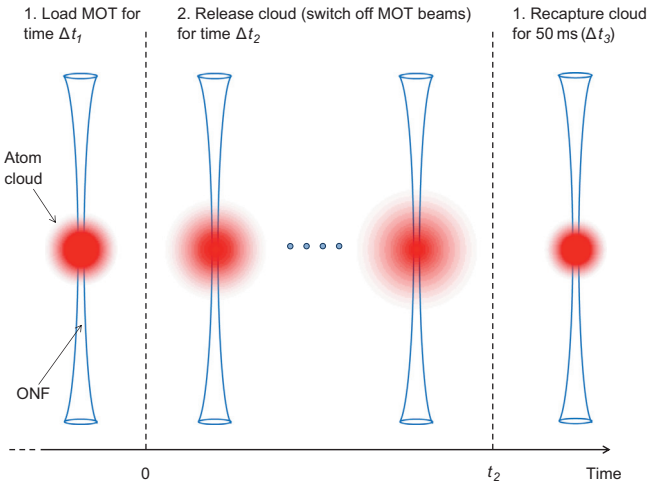


Fig. 1. Illustration of the release and recapture sequence as a function of time. The cloud is positioned centrally around the ONF. The cloud is loaded for a time Δt_1 and then released from the trap for a time Δt_2. Δt_2 is varied from sequence to sequence to build up a profile of the velocity of the atoms in the MOT. The recapture time, Δt_3, is set to 50 ms. The cloud is then released once more for 50 ms, before repeating the entire sequence.

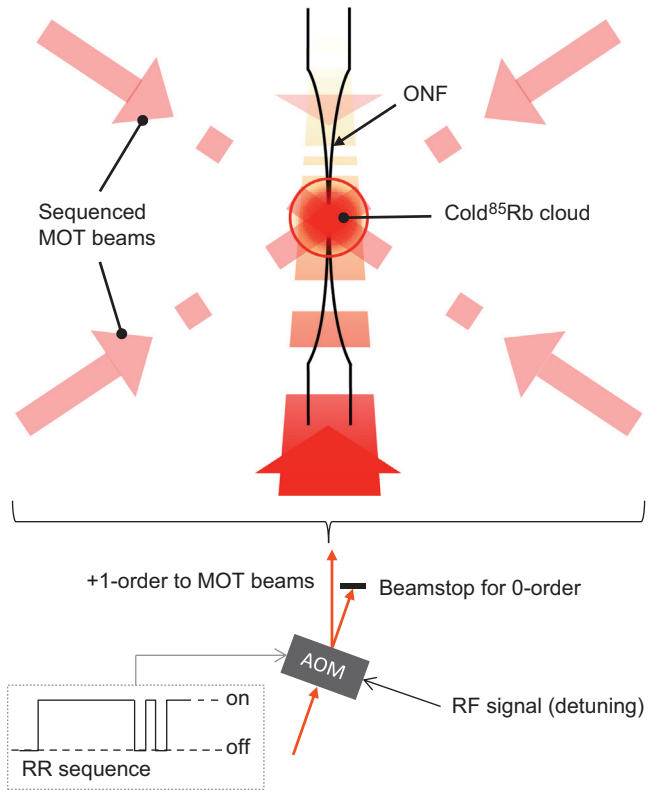


Fig. 2. Illustration of the experimental setup. The 1st-order beam from an AOM is expanded and split into three equal-intensity cooling beams for the MOT. The ^{85}Rb cloud is positioned centrally around the ONF. The cooling beams are switched on and off according to the sequence shown here with an AOM. Beam detuning is controlled via the tunable RF input on the AOM.

It is interesting to observe that, as evident in Fig. 6, κ levels off above light-shift parameter values of ≈ 1. As the most dense part of the cloud is being studied with the ONF, this may be an

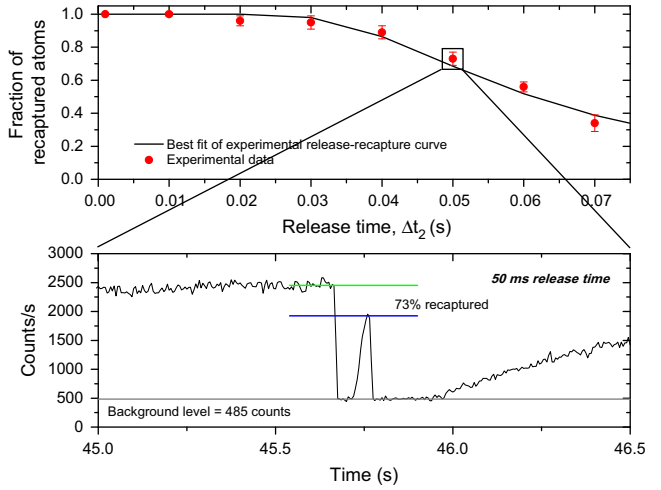


Fig. 3. Fraction of recaptured atoms estimated from the fluorescence data obtained from an optical nanofibre placed near the cold cloud of atoms. For a release time, Δt_2, of 50 ms, 73% of the expanded cloud was recaptured with $\delta = -2.6\Gamma$ and cooling laser intensity of $2.9 I_s$ (4.6 mW/cm^2) per beam.

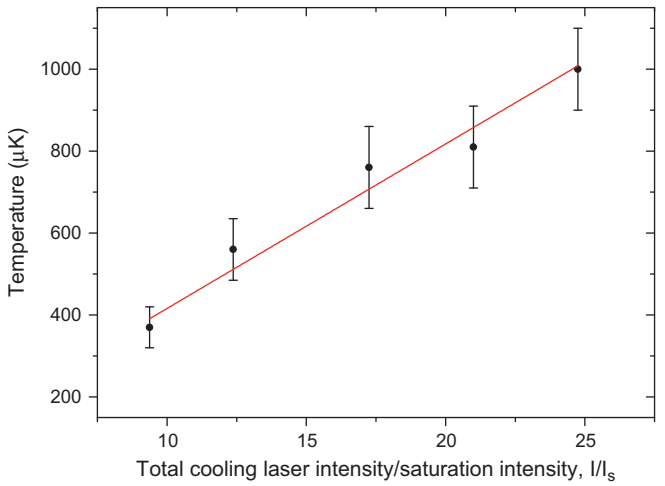


Fig. 4. Temperature as a function of cooling laser intensity normalised to the saturation intensity, I_s ($\delta = -2\Gamma$). The solid red line is a linear fit to the experimental data. (For interpretation of the references to color in this figure caption, the reader is referred to the web version of this article.)

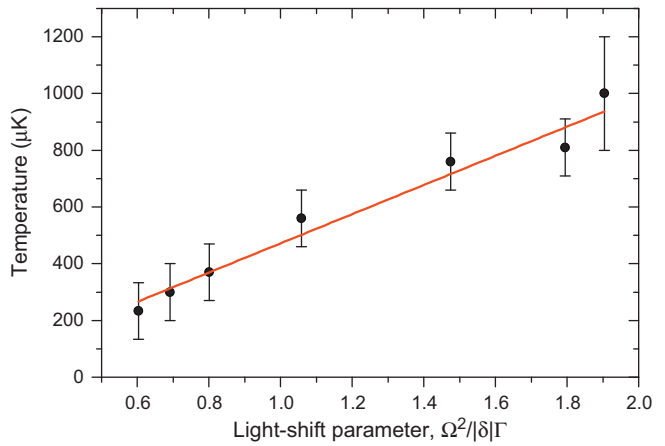


Fig. 5. Temperature of the cloud as measured with RR plotted against the dimensionless light-shift parameter $\Omega^2/|\delta|\Gamma$ (black circles) and a linear fit (red solid line) to the data. (For interpretation of the references to color in this figure caption, the reader is referred to the web version of this article.)

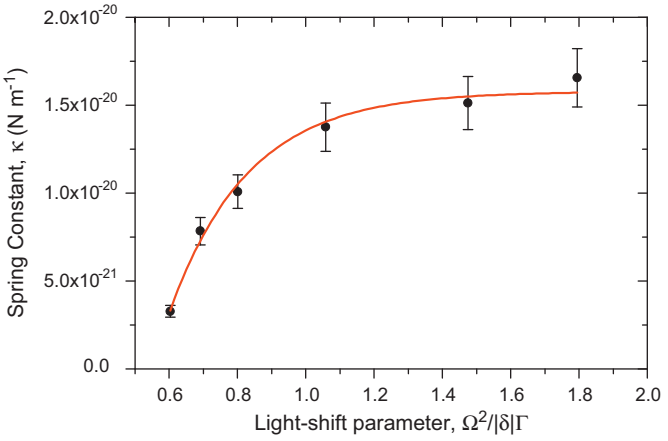


Fig. 6. Spring constant against dimensionless light-shift parameter $\Omega^2/|\delta|\Gamma$ (black circles) with a fit for a guide to the eye (red, solid line). (For interpretation of the references to color in this figure caption, the reader is referred to the web version of this article.)

Table 1
Variation of temperature with cooling laser red detuning in units of the natural linewidth using two different measurement techniques. I_{beam} was approximately $2.2I_s$ for release–recapture and $1.3I_s$ for forced oscillation. Forced oscillation data is taken directly from [25].

Method	Red detuning (Γ)	Temperature (mK)
Release recapture	1.1	1.80 ± 0.20
	2.0	0.56 ± 0.13
	3.5	0.23 ± 0.03
Forced oscillation	2.1	0.97 ± 0.08
	2.6	0.65 ± 0.06
	3.1	0.37 ± 0.04
	3.5	0.18 ± 0.02

interesting observation when compared to measurements done with photodiodes.

As atom number is increased in the MOT, the regime of operation transitions from temperature-limited (TL) to multiple-scattering (MS) [34–36]. In the TL regime, the cold atoms are essentially non-interacting because N_A is small (typically less than 10^4) and the density is low. The cloud acts as an ideal gas in this regime, and, as more atoms are loaded into the trap, the size of the cloud remains the same while the density increases linearly and its distribution remains Gaussian [37]. For larger N_A ($\geq 10^5$) the cloud begins operating in the MS regime and the density becomes largely independent of N_A [38]. Two effects are seen in this regime. Firstly, repulsive forces caused by the re-absorption of scattered photons lead to an increase in the cloud size while the density remains constant. This radiation trapping effect determines the density and temperature of cold atoms [3,39]. For example, at $N_A \sim 10^7$ the cloud density is maintained and the optical thickness is such that, on an average, each photon absorbed from the cooling laser beams will, after re-emission, scatter no more than once on its way out of the cloud. This determines the spatial growth of the cloud as N_A increases beyond 10^7 [40]. The second effect is due to an attenuation force which arises from the intensity gradients in the MOT beams and the absorption of such by the atoms [38,41]. This results in spatial compression of the cloud and a small reduction in spring constant of the trap [42]. When the MOT transitions from the TL to the MS regime, the atom distribution may or may not change from Gaussian to flat-topped. Thus, at higher cloud densities, cloud images may not be a direct indicator of density. Measurements using an ONF negate the use of imaging analysis to estimate cloud volume (for example, [39]) making it simpler to observe regime-change in the MOT via fluorescence coupling.

By considering an observation volume surrounding the ONF, cloud density can be studied as the light-shift parameter is varied. It is assumed that atoms within a hollow observation cylinder with an outer radius equal to the ONF radius + 300 nm are most likely to emit fluorescence into the guided mode of the ONF [19,22]. This number of effective atoms, n_{eff}, can be estimated at one end of the ONF using $n_{eff} = 2C_P/R_{sc}\eta_{ONF}Q\eta_{QD}$ where R_{sc} is the atomic scattering rate, η_{ONF} is the average coupling efficiency of photons into the guided ONF mode in one direction (estimated at 2% using previous work based on ^{133}Cs [43]), Q is the ONF transmission from the middle of the ONF waist to the detector (the transmission through the entire length of fibre is 60% so Q=77% for half the fibre length), and η_{QD} is the quantum efficiency of the SPCM (60%). The quantity C_P is the fluorescent count rate obtained by the SPCM and is obtained from the RR raw data. The scattering rate, R_{sc}, is described by [35]

$$R_{sc} = \frac{\Gamma}{2}\frac{C_1^2\Omega_{tot}^2/2}{\delta^2+\Gamma^2/4+C_2^2\Omega_{tot}^2/2}. \quad (3)$$

Here, Ω_{tot} is the Rabi frequency for all MOT beams and is taken to be six times that of any one of the trapping beams. C_1 and C_2 are average Clebsch–Gordan co-efficients. The values of C_1^2 and C_2^2 are assumed to be equal due to optical pumping among the Zeeman sublevels in the presence of strong coupling between atoms and the radiation field [35].

If N_{eff} is plotted as a function of light-shift parameter, saturation of the atom number commences from $\Omega^2/|\delta|\Gamma \sim 1.2$ onwards (Fig. 7). As the observation volume is fixed by the ONF radius, this saturation effect is due to the spatial expansion of the cloud while it maintains constant density and may also indicate the onset of the MS regime in the MOT.

5. Outlook and conclusion

The temperature of a cold ensemble of ^{85}Rb atoms has been measured using the RR method with an ONF. The RR sequence was applied to an AOM allowing the MOT beams to be switched off rapidly. The results presented here agree with those found by the forced oscillation method [25] and again reinforce the viability of placing the ONF in yet colder atomic samples. This work has highlighted the sensitivity of the cloud temperature to small changes in beam misalignment, detunings, and intensities, and

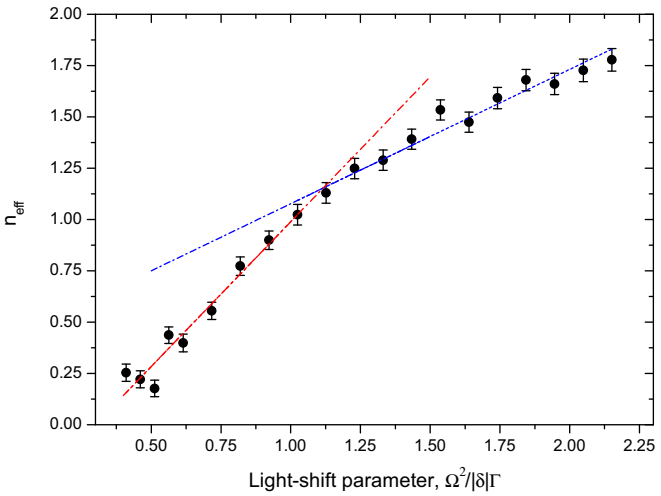


Fig. 7. Estimation of effective atom-number, n_{eff}, with increasing dimensionless light-shift parameter $\Omega^2/|\delta|\Gamma$ (black circles) with two linear fits to indicate the change in slope around a light-shift parameter 1.2.

demonstrates the ability to detect these temperature changes with the ONF. As the detector can be positioned anywhere in the cloud of atoms, a systematic temperature measurement, while exploring the entire parameter space, can be performed.

Free-space RR measurements show that, with the same variation in laser cooling intensity as we have used, a few hundred μK span can be observed. The results here display this trend and, additionally, provide detailed information about the velocity distribution of the atom cloud. In particular, with the ONF-based RR method, the system is sensitive to atoms near the fibre surface and, using data analysis, it is possible to generate a decay curve that shows how those near-surface atoms with a high velocity leave the capture region quickly and do not continue to contribute to the signal detected via the ONF.

Values for the springs constant of the MOT, inferred from temperature results, increase with cooling laser intensity until some critical value of the light-shift parameter is reached (≈ 1) and then begin to level out. Further, by examining coupling signal strengths while varying the light-shift parameter, the density regime in which the MOT is operating can be identified.

Acknowledgments

The authors wish to thank W. Cotter for help in creating the AOM sequencing programme. This work is partially supported by Science Foundation Ireland under Grant nos. 07/RFP/PHYF518 and 08/ERA/I1761 through the NanoSci-E+ Project NOIs, OIST Graduate University and the Higher Education Authority via the INSPIRE programme. LR acknowledges support from IRCSET under the Embark Initiative.

References

[1] P. Kohns, P. Buch, W. Suptitz, C. Csambal, W. Ertmer, Europhysics Letters (EPL) 22 (1993) 517.
[2] C.D. Wallace, T.P. Dinneen, K.Y.N. Tan, A. Kumarakrishnan, P.L. Gould, J. Javanainen, Journal of the Optical Society of America B 11 (1994) 703.
[3] A. Vorozcovs, M. Weel, S. Beattie, S. Cauchi, A. Kumarakrishnan, Journal of the Optical Society of America B 22 (2005) 943.
[4] A.M. Steane, C.J. Foot, Europhysics Letters (EPL) 14 (1991) 231.
[5] S. Tung, Y. Chen, C. Lin, L. Hsu, I. Yu, Chinese Journal of Physics 38 (2000) 395.
[6] D.R. Meacher, D. Boiron, H. Metcalf, C. Salomon, G. Grynberg, Physical Review A 50 (1994) R1992.
[7] R. Silva, K. Magalhaes, E. Henn, L. Marcassa, V. Bagnato, Optics Communications 265 (2006) 526.
[8] S. Chu, L. Hollberg, J.E. Bjorkholm, A. Cable, A. Ashkin, Physical Review Letters 55 (1985) 48.
[9] P.D. Lett, R.N. Watts, C.I. Westbrook, W.D. Phillips, P.L. Gould, H.J. Metcalf, Physical Review Letters 61 (1988) 169.
[10] J.D. Love, W.M. Henry, W.J. Stewart, R.J. Black, S. Lacroix, F. Gonthier, IEE Proceedings J, Optoelectronics (1991) 138 343.
[11] G. Brambilla, Journal of Optics 12 (2010) 043001.
[12] J.C. Knight, G. Cheung, F. Jacques, T.A. Birks, Optics Letters 22 (1997) 1129.
[13] M.L. Gorodetsky, V.S. Ilchenko, Journal of the Optical Society of America B 16 (1999) 147.
[14] J.M. Ward, S. Nic Chormaic, Applied Physics B 100 (2010) 847.
[15] A. Watkins, J. Ward, S. Nic Chormaic, Japanese Journal of Applied Physics 51 (2012) 052501.
[16] G. Brambilla, G.S. Murugan, J.S. Wilkinson, D.J. Richardson, Optics Letters 32 (2007) 3041.
[17] M.C. Frawley, A. Petcu-Colan, V.G. Truong, S. Nic Chormaic, Optics Communications 285 (2012) 4648.
[18] F. Le Kien, S. Dutta Gupta, V.I. Balykin, K. Hakuta, Physical Review A 72 (2005) 1.
[19] K.P. Nayak, P.N. Melentiev, M. Morinaga, F.L. Kien, V.I. Balykin, K. Hakuta, Optics Express 15 (2007) 5431.
[20] L. Russell, D.A. Gleeson, V.G. Minogin, S. Nic Chormaic, Journal of Physics B: Atomic, Molecular and Optical Physics 42 (2009) 185006.
[21] V.G. Minogin, S. Nic Chormaic, Laser Physics 20 (2009) 32.
[22] M.J. Morrissey, K. Deasy, Y. Wu, S. Chakrabarti, S. Nic Chormaic, The Review of Scientific Instruments 80 (2009) 053102.
[23] E. Vetsch, D. Reitz, G. Sagué, R. Schmidt, S.T. Dawkins, A. Rauschenbeutel, Physical Review Letters 104 (2010) 203603.
[24] L. Russell, M. Daly, S. Nic Chormaic, 1- and 2-photon absorption by laser-cooled Rb-85 using an optical nanofiber, in: Quantum Africa 2010: Theoretical and experimental foundations of recent quantum technology, vol. 1469, American Institute of Physics, 2010, pp. 82–90.
[25] L. Russell, K. Deasy, M.J. Daly, M.J. Morrissey, S. Nic Chormaic, Measurement Science and Technology 23 (2012) 015201.
[26] A. Goban, K.S. Choi, D.J. Alton, D. Ding, C. Lacroûte, M. Pototschnig, T. Thiele, N.P. Stern, H.J. Kimble, Physical Review Letters 109 (2012) 033603.
[27] S.M. Hendrickson, M.M. Lai, T.B. Pittman, J.D. Franson, Physical Review Letters 105 (2010) 173602.
[28] S.M. Spillane, G.S. Pati, K. Salit, M. Hall, P. Kumar, R.G. Beausoleil, M.S. Shahriar, Physical Review Letters 100 (2008) 231.
[29] J.M. Ward, D.G. O'Shea, B.J. Shortt, M.J. Morrissey, K. Deasy, S.G. Nic Chormaic, Review of Scientific Instruments 77 (2006) 083105.
[30] E.R. Abraham, E.A. Cornell, Applied Optics 37 (1998) 1762.
[31] P.V.D. Straten, H. Metcalf, The quest for BEC, in: Interactions in Ultracold Gases: From Atoms to Molecules, September, Wiley-VCH Verlag GmbH and Co., 2002, pp. 1–70.
[32] C.G. Townsend, N.H. Edwards, K.P. Zetie, C.J. Cooper, J. Rink, C.J. Foot, Physical Review A 53 (1996) 1702.
[33] P.D. Lett, W.D. Phillips, S.L. Rolston, C.E. Tanner, R.N. Watts, C.I. Westbrook, Journal of the Optical Society of America B 6 (1989) 2084.
[34] T. Walker, D. Sesko, C. Wieman, Physical Review Letters 64 (1990) 408.
[35] C.G. Townsend, N.H. Edwards, C.J. Cooper, K.P. Zetie, C.J. Foot, A.M. Steane, P. Szriftgiser, H. Perrin, J. Dalibard, Physical Review A 52 (1995) 1423.
[36] V.B. Tiwari, S. Singh, H.S. Rawat, M.P. Singh, Journal of Physics B: Atomic, Molecular and Optical Physics 41 (2008) 205301.
[37] I. Guedes, M.T.D. Araujo, D.M.B.P. Milori, G.I. Surdutovich, V.S. Bagnato, S.C. Zilio, Journal of the Optical Society of America B 11 (1994) 1935.
[38] D.W. Sesko, T.G. Walker, C.E. Wieman, Journal of the Optical Society of America B 8 (1991) 946.
[39] K.R. Overstreet, P. Zabawa, J. Tallant, A. Schwettmann, Optics Express 13 (2005) 9672.
[40] K. Lindquist, M. Stephens, C. Wieman, Physics Review A 46 (1992) 4082.
[41] J. Dalibard, Optics Communications 68 (1988) 203.
[42] J.A. Greenberg, M. Ori, A.M.C. Dawes, D.J. Gauthier, Optics Express 15 (2007) 17699.
[43] F. Le Kien, V.I. Balykin, K. Hakuta, Physical Review A 73 (2006) 013819.

A.2 Probing a Dark-Magneto Optical Trap with an Optical Nanofibre

One of the factors which limit the density of a bright-MOT is radiation pressure. This limitation can be overcome using a technique called a dark-MOT. This chapter presents the first measurement on a dark-MOT using an ONF. This work was published in "L. Russell, R. Kumar, V. B. Tiwari, S. Nic Chormaic, *Investigation of a* ^{85}*Rb dark magneto-optical trap using an optical nanofibre*, Measurement Science and Technology 25 (5), 055203 (2014)".

RK contribution: Performing the experiment, data analysis and paper writing.

IOP Publishing Measurement Science and Technology
Meas. Sci. Technol. **25** (2014) 055203 (8pp) doi:10.1088/0957-0233/25/5/055203

Investigation of a ^{85}Rb dark magneto-optical trap using an optical nanofibre

Laura Russell[1,2], **Ravi Kumar**[1,2], **Vibhuti Bhushan Tiwari**[1,3] **and Sìle Nic Chormaic**[1,2,4]

[1] Department of Physics, University College Cork, Cork, Ireland
[2] Light-Matter Interactions Unit, OIST Graduate University, 1919-1 Tancha, Onna-son, Okinawa 904-0495, Japan
[3] Laser Physics Applications Section, Raja Ramanna Centre for Advanced Technology, Indore 452013, India
[4] School of Chemistry and Physics, University of KwaZulu-Natal, Durban 4001, South Africa

E-mail: ravi.kumar@oist.jp

Received 20 October 2013, revised 22 December 2013
Accepted for publication 4 February 2014
Published 19 March 2014

Abstract

We report here the first measurements on a dark magneto-optical trap (DMOT) of ^{85}Rb atoms using an optical nanofibre (ONF) with a waist of $\sim$1 μm. The DMOT is created using a doughnut-shaped repump beam along with a depump beam for efficient transfer of cold atoms from the bright hyperfine ground state ($F = 3$) into the dark hyperfine ground state ($F = 2$). The fluorescence from the cold ^{85}Rb atoms of the DMOT is detected by coupling it into the fibre-guided modes of the ONF. The measured fractional population of cold atoms in the bright hyperfine ground state (p) is as low as $\sim$0.04. The dependence of the loading rate of the DMOT on cooling laser intensity is investigated and also compared with the loading rate of a bright MOT. This work lays the foundation for the use of an ONF for probing a small number of atoms in an optically-dense cold atomic cloud.

Keywords: laser-cooling, dark MOT, rubidium, tapered optical nanofibre, atom cloud density

(Some figures may appear in colour only in the online journal)

1. Introduction

The optical nanofibre (ONF), or optical microfibre depending on the waist diameter, is an ultrathin wave guide usually fabricated from commercially-available fibre using a heat-and-pull technique [1]. The enhancement of the spontaneous emission from atoms surrounding an ONF into its guided modes is well known [2], making it an ideal high-sensitivity tool for channelling atomic fluorescence to a detector. In recent years, ONFs have been used as probes for cold atoms [3–6] and hot atomic vapours [7–9]. A number of proposals for trapping neutral atoms around ONFs have been made [10–14] and two-colour trapping of caesium has been achieved [15, 16]. Some of the advantages of ONFs are that, in addition to trapping applications, the nanofibre provides an interface that can be exploited for quantum communication using ensembles of laser-cooled atoms or for studying atom–surface interactions [17, 18]. A review on recent advances in this field is contained in Morrissey *et al* [19].

In the work reported here, atom cloud density enhancement techniques for a sample of laser-cooled ^{85}Rb atoms are studied in order to increase the fluorescence and/or absorption signals obtainable with ONFs. The density of atoms in a standard magneto-optical trap (MOT) is limited to $\sim 10^{11}$ atoms cm^{-3} for two reasons. First, a transfer of kinetic energy occurs when a ground state atom collides with an excited state atom leading to a trap loss rate that is proportional to the number of atoms trapped. The second limitation is due to laser-cooled atoms in the MOT reabsorbing scattered photons, a phenomenon known as radiation pressure. The outward radiation pressure of the fluorescent light balances the confining forces of the trapping laser beams at a particular density and, at this point, if the number of atoms is increased, the atom cloud simply grows in size rather than in density.

 © 2014 IOP Publishing Ltd Printed in the UK

For ONFs, this is a major consideration; if one wishes to do absorption experiments using ONFs, as many atoms as possible are required to fill the evanescent field region around the fibre in order to optimize the signal quality.

In 1993 Ketterle *et al* [20] demonstrated a MOT configuration, known as the dark MOT (DMOT), which confined sodium atoms in the lower (or dark) hyperfine ground level, where they are unperturbed by the cooling beams and, thus, the DMOT is free from the density limitations of a standard bright MOT (BMOT). By reducing the intensity of the repump beams used in the standard BMOT configuration almost all the atoms are transferred from the bright hyperfine level, $F = 2$, to the dark hyperfine level, $F = 1$, of the $3S_{1/2}$ ground state of Na. Although a small excitation rate is optimal for confining large numbers of atoms at a high density, the maximum possible excitation rate is required to efficiently capture atoms from a vapour and load them into a MOT. By using bright and dark regions in the repump beam simultaneously, both of these requirements can be fulfilled; a doughnut-shaped (or hollow) repump beam can be used for this as it consists of a bright outer ring of light and a dark inner circle. An atom which encounters the dark region (i.e. the region with negligible repump intensity) will only spend a very short time in the cooling cycle before being shelved into the dark hyperfine level. Alternative methods of creating a DMOT have been demonstrated. For example, Muniz *et al* [21] tuned the frequency of the repump laser to create a DMOT from an intense flux of slowed Na atoms. In the last decade, a more complete understanding of the DMOT has been formed [22–24] and recently extended to studies with ultracold atoms and molecules [25].

One way of working with a BMOT and DMOT is by generating them sequentially in time using triggered mechanical shutters and acousto-optic modulators (AOMs). However, an alternative approach is to simultaneously generate the BMOT and DMOT in different spatial regions of the trap, as achieved using the aforementioned doughnut-shaped repump beam. The spatially-generated DMOT has advantages since atoms can be continuously loaded into the dark region from the outer BMOT where the usual processes occur. In fact, although the inner, dark region is not really a MOT, the outer bright region still captures background atoms and feeds the dark section. In other words, experimental parameters for the atoms at the trap centre can be monitored and adjusted, while simultaneously maintaining the high loading rate achievable with the BMOT. This is possible because the trapped atom cloud is localized near the minimum of the magnetic field, whereas the capture of atoms occurs throughout the whole intersection volume of the cooling laser beams. Note that only the spatial DMOT is considered in the work that follows. This arrangement is very appealing for ONF-based work. For example, the possibility of continuous absorption measurements via an ONF probe becomes available. Permyakova *et al* [26] report that, even with moderate beam powers of the order of 6 mW, the dark MOT can capture a large number of atoms and achieve optical densities as high as 9. Thus, by using low cooling laser intensities (for confining large numbers of atoms at a high density) in a DMOT scheme, high signal-to-noise ratios for the fluorescence coupling should be achievable for minimal beam powers. This leads to the potential demonstration of nonlinear optical effects in the atom cloud without requiring high laser powers.

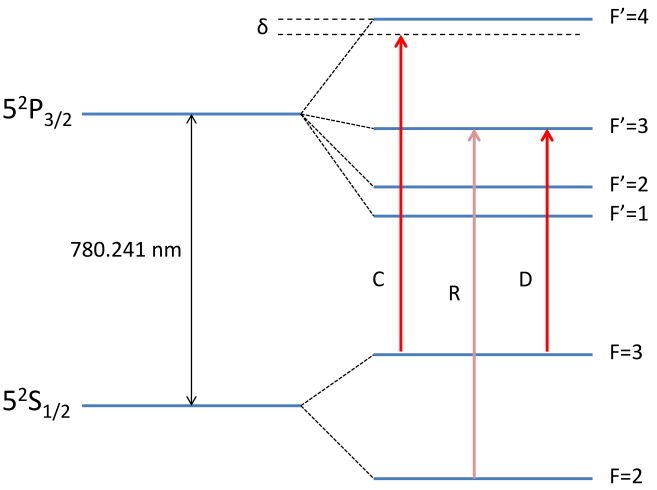


Figure 1. Energy levels used in the dark MOT for ^{85}Rb. 'C' represents the cooling laser, 'R' represents the repump beam, and 'D' represents the depump beam. δ is the red-detuning of the cooling laser.

2. Experimental technique

2.1. Laser configuration

Earlier, Townsend *et al* [27] demonstrated atom densities of nearly 10^{12} cm^{-3} in a dark MOT for caesium. Prior to this, no report of similar density enhancements in MOTs for elements other than sodium had been reported. Excited state hyperfine splitting is large for heavier alkali-metal atoms which makes it difficult to get the atoms in the dark state, while still maintaining enough atoms in the trap, by transient reduction of repump beam intensity as done in case of Na atoms. Hence, Townsend *et al* used a technique of partially blocking the repump beam to create a low repump intensity region at the centre surrounded by a higher repump intensity, and directed a depump beam to the dark region to increase the rate of decay to the dark ground state. We follow the same scheme for creating a DMOT for ^{85}Rb. The depump beam is tuned to the $F = 3 \rightarrow F' = 3$ transition of ^{85}Rb. Rb atoms (see figure 1) undergo many cooling cycles ($F = 3 \rightarrow F' = 4$) before falling to the dark ground state ($F = 2$) due to spontaneous Raman processes if no depump beam is used. The addition of a depump beam accelerates ground state pumping of atoms.

In the work reported here, a retro-reflected three beam MOT configuration is used for laser-cooling and trapping ^{85}Rb atoms. The doughnut-shaped repump beam is generated in the following manner. First, the laser beam is expanded in a telescope setup to a diameter of 25 mm (see figure 2). A separate, unit magnification telescope is used to place a shadow in the beam and project it on to the atom cloud. A glass slide with an opaque circle as the shadow is placed near the focal point of the telescope and aligned to create the

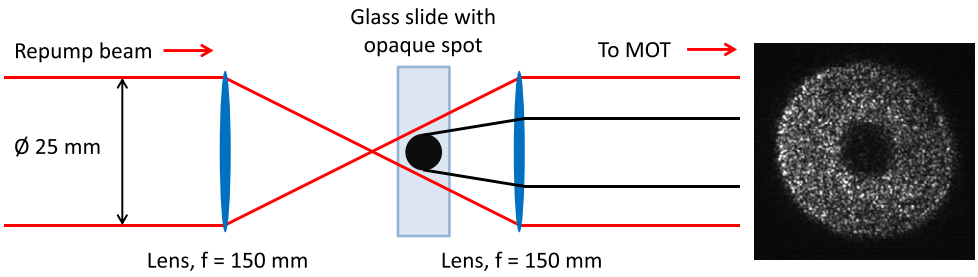


Figure 2. Left: experimental setup used to create the doughnut repump beam using a unity magnifier with an opaque circle positioned near the centre of two lenses. This imaging setup reduces Fresnel diffraction in the beam at the position of the MOT. Right: repump beam profile obtained using a CCD camera.

doughnut-shaped repump beam at the MOT. The opaque circle has a transmission of 10^{-4} as determined experimentally. If the circle were placed in the beam without being incorporated into a telescope system, Fresnel diffraction effects would occur at the trap centre. This would diminish the efficiency of the dark MOT in shelving atoms into $F = 2$. To facilitate switching from a DMOT to a BMOT, the slide with the shadow in the optical path of the repump beam can be easily removed from its holder, turning the doughnut beam into a standard Gaussian repump beam.

Rather than directing the doughnut repump beam along a path which copropagates with a cooling beam, a separate path is used. The reason for this is due to the retro-reflecting mirrors in the cooling beam path for the MOT design. If the repump beam were aligned such that it passed centrally through the cloud, but reflected back off a retro-reflecting mirror, the back-reflected dark spot may not align perfectly with the forward propagating one and could destroy the DMOT.

2.2. Quantifying the DMOT quality

To quantify the 'darkness' of the trap, Ketterle *et al* [20] introduced a quality parameter, p, that denotes the fraction of atoms in the bright, ground hyperfine level compared to the total number of atoms in the ground state, where

$$p = \frac{N_b}{N_b + N_d}. \tag{1}$$

For ^{85}Rb, N_b is the number of atoms in the bright $F = 3$ level and N_d is the number of atoms in the dark $F = 2$ level of the ground state. The quality of the DMOT is determined from p, where $p = 1$ represents a 100% BMOT and $p = 0$ is a 100% dark MOT. For the measurements of p reported here an ONF with diameter $\sim$1 μm is passed through the centre of the atom cloud. Fluorescence emitted from the laser-cooled atoms couples into the guided modes of the ONF and is subsequently measured at one fibre pigtail end using a single photon counting module (SPCM). The recorded count rate is proportional to the number of atoms in whichever hyperfine ground level is probed, thereby enabling a measurement of p to be performed. Alternatively, p can be estimated from the magnitude of observed absorption dips if free-space spectroscopy is performed.

3. Results and discussions

3.1. Free-space spectroscopy of the DMOT

The experimental setup is shown in figure 3. Initially, a free-space probe beam is passed through the atom cloud for absorption spectroscopy measurements, as illustrated in figure 3(a). The free-space probe beam is aligned with the centre of the cloud so that it passes through the DMOT. The probe beam is obtained from a 780 nm extended cavity diode laser (ECDL) operating in scanning mode and frequency tuned via saturated absorption spectroscopy. The beam, after passing through the cloud, is directed on an avalanche photodiode (Hamamatsu model: C5460-01), connected to a computer.

Figure 4 (upper plot) shows the absorption spectrum obtained using the free-space method to obtain a BMOT. The lower plot in figure 4 shows the spectrum for the DMOT (with the doughnut repump beam and the depump beam). It is evident that the magnitude of the $F = 2 \rightarrow F' = 1, 2, 3$ dips has doubled for the DMOT compared to the BMOT, while the magnitude of the $F = 3 \rightarrow F' = 2, 3, 4$ dips has approximately halved, indicating a clear enhancement of the atom population in the $F = 2$ hyperfine level for the DMOT compared to the BMOT.

3.2. Characterizing the DMOT with an ONF

By using beam stops to block and unblock the depump beam and/or the probe beam, different populations of atoms can be studied using an ONF. To fabricate the ONF, a heat-and-pull-technique is used [1, 28, 29]. Commercially-available SM780 (Fibercore) optical fibre is heated using an oxygen-butane flame and pulled using a pair of motorized translational stages. For these experiments, the final transmission of the ONF was $\sim$60% from end to end and the waist diameter was $\sim$1 μm. After fabrication, the ONF is fixed in a vertical orientation to an aluminium U-shaped mount with UV-curable glue. The nanofibre is aligned centrally in the MOT and the fibre pigtails are coupled into and out of the UHV chamber using a teflon feedthrough [30, 31]. A SPCM is connected to one pigtail of the ONF so that fluorescence from the atom cloud can be recorded. The setup is shown in figure 3(b). In the previous section, a probe beam generated by an ECDL was used (figure 3(a)). Now, the probe beam is derived from the repump beam of the MOT and aligned, in free-space, with the centre of the atom cloud (figure 3(b)). The frequency of this

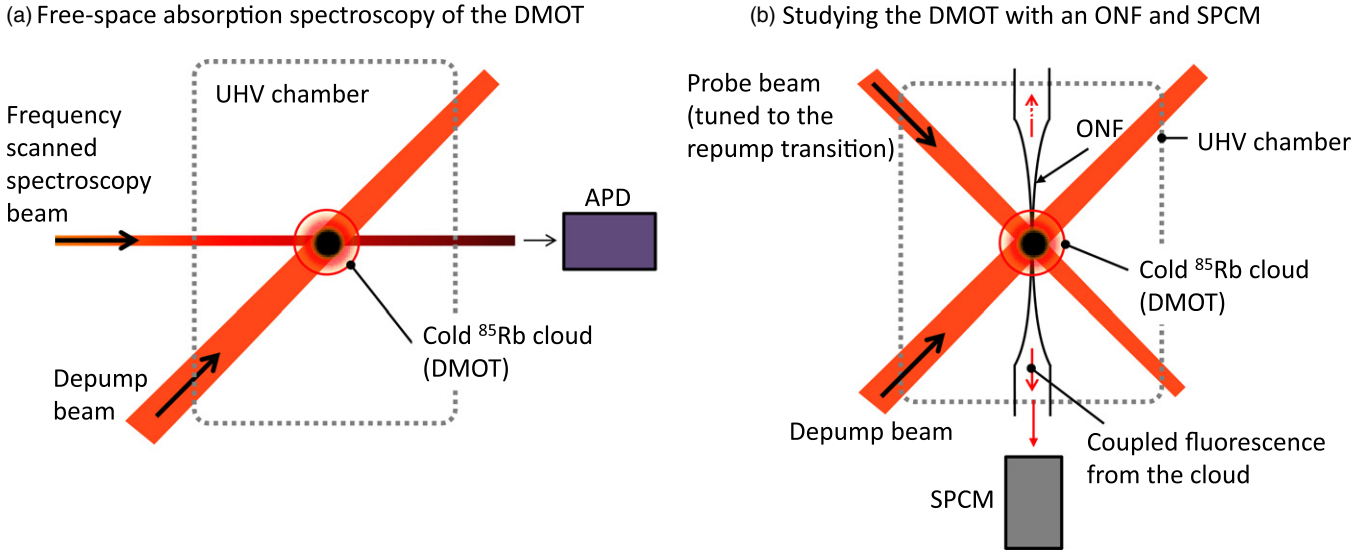


Figure 3. Schematic of the experimental setup. (*a*) Free-space spectroscopy on the DMOT incorporating a frequency-scanned probe beam, APD: avalanche photodiode, UHV: ultrahigh vacuum. (*b*) Probing the DMOT with an optical fibre, ONF: optical nanofibre, SPCM: single photon counting module.

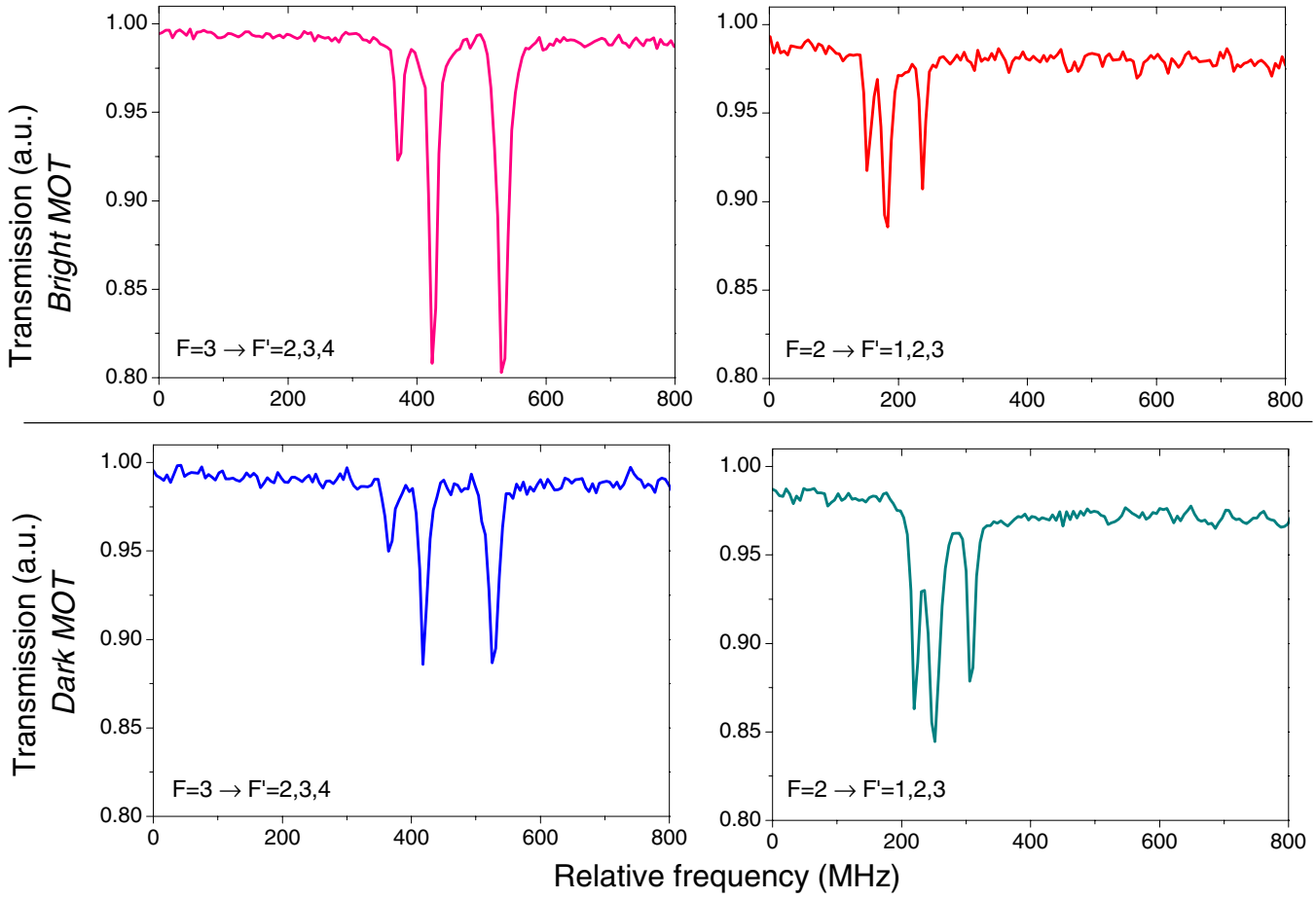


Figure 4. Upper traces: free-space absorption spectroscopy on a BMOT. Lower traces: free-space absorption spectroscopy on an optimized DMOT. The DMOT here is created using a doughnut repump MOT beam and a depump beam. There is a higher population in the $F = 2$ lower hyperfine level for the DMOT compared to the BMOT.

probe beam is fixed with an AOM and tuned to the repump transition of ^{85}Rb. Figure 5 shows two loading curves: the upper (red) plot is for a BMOT and the lower (black) plot is for a DMOT. The DMOT in this instance has no depump shining on it and, thus, it is not extremely dark (i.e. p is not very low). This explains why the resulting fluorescence count from the DMOT

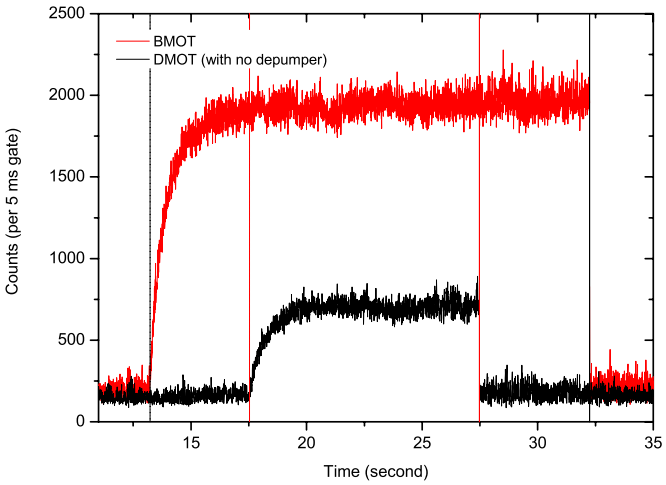


Figure 5. Loading curves for a BMOT (red, upper) and a DMOT (black, lower). The vertical lines show the switch on and switch off of the electric coils for the magnetic field. This plot shows the residual fluorescence coupling that can be obtained using a DMOT of modest p value. In this case, the DMOT has been created with the doughnut repump beam only (no depump light has been used).

(∼750 counts/5 ms) is non-negligible in comparison with that for the BMOT (∼2000 counts/5 ms). With the assumption that fluorescence from the probe transition ($F = 2 \rightarrow F' = 3$) is negligible compared to the fluorescence from the MOT trapping beams (reasonable in the case of this work) the steady state count rates for both curves are proportional to the number of atoms in $F = 3$. However, the distribution of atoms between both hyperfine ground states, $F = 2$ and $F = 3$, is different in each case. Furthermore, these two sets of data are not sufficient to determine the population of each ground state or the darkness of the DMOT. To determine the value of p with the SPCM and ONF two sets of data must be recorded and analysed, as described in the following section.

Figure 6(*a*) shows the fluorescence count rate through the fibre for a DMOT created with a doughnut repump beam (and no depumping beam). The black, vertical line at ∼7.5 s indicates the point at which the trapping magnetic field is switched on to allow the DMOT to load. The fluorescence level increases from 125 counts/2 ms (indicated by the red line that shows the background light coupling into the fibre) to ∼275 counts/2 ms due to the residual bright atoms in the DMOT. In other words, the $F = 3$ atoms contribute ∼150 counts/2 ms to the signal. This is the numerator of p as given in (1). In figure 6(*b*), the fluorescence signal is recorded for a DMOT created with the doughnut repump beam and the depumper. This yields a baseline count rate of 175 counts/2 ms (blue line, figure 6(*b*)) and the numerator of p in this case is 50 counts/2 ms. Furthermore, in this plot, the probe beam is added to the optical configuration. This probe beam is tuned to the repumping transition of ^{85}Rb ($F = 2 \rightarrow F' = 3$) and aligned with the dark region of the cloud. Thus, it 'fills in' the dark central region of the doughnut-shaped repump beam, thereby recreating a standard BMOT configuration. The probe switches on for 100 ms at 1 Hz repetition rate, while the depump switches off at the same time and with the same rate. The observed spikes in the fluorescence count rate (∼1150 counts/2 ms) coupled into the ONF are from atoms in both the ground state hyperfine levels, $F = 2$ and 3. This is the denominator of p. By taking the ratio of the baseline (125 counts/2 ms) in figure 6(*a*) to the peak counts in figure 6(*b*), and correcting for the background level, the value for p is determined as ∼0.10 in the DMOT without the depumper. However, with the inclusion of the depumper the dark MOT is improved and a value of $p \sim 50/1150 \approx 0.04$ is obtained.

3.3. DMOT loading times

Loading curves were analysed for the DMOT and BMOT via the ONF with a methodology similar to that described in [32]. Figure 7(*a*) shows a loading curve for a BMOT (red plot) and a loading curve for a DMOT (black plot). Both curves have been background-corrected. The BMOT curve yields a loading rate, R_B, of 15×10^4 counts s^{-1} by fitting it with $N(t) = R_B/\Gamma(1 - e^{-\Gamma t})$ where Γ is the collisional loss rate in the MOT. The black plot in figure 7(*a*) represents the loading for a DMOT which has been created with a doughnut repump beam and a depumper. The spikes in fluorescence occurring at 1 Hz (for 100 ms duration) are due to simultaneously switching off the depumper and switching on the probe beam for detection purposes. As discussed previously, these conditions (depumper off and probe on) recreate the conditions for a BMOT and provide a measurement of the denominator of p. These peaks in the DMOT plot reach values of $\sim 1 \times 10^5$ counts s^{-1}, matching the steady state count rate of the BMOT loading curve. The baseline curve of the DMOT plot represents the loading of the fraction of $F = 3$ atoms present in the DMOT. The DMOT does not contribute to the loading process so the loading rate cannot be larger in the DMOT than in the BMOT. In figure 7(*b*) one can see that the loading rate of the DMOT, R_D, is $\sim 0.2\,R_B$. For this DMOT, $p = 0.22$.

The change in R_D can be examined as a function of p. In figure 7(*b*), p is varied (using different depumper intensities) over the range 0.08–0.50. The loading rate of the DMOT decreases for lower p values as expected [33]. Loading rates for the BMOT and DMOT can be explored by varying the cooling laser intensity (per MOT beam, I_{beam}) and recording the same data as shown in figure 7(*a*) for each I_{beam}. This study is shown in figure 8. As expected, the DMOT loading rate, R_D, is consistently lower than the BMOT loading rate R_B.

3.4. Effective number of atoms

In the context of our earlier work [6], by considering an observation volume surrounding the ONF, the effective number of atoms near the ONF can be studied as the cooling laser intensity is varied. It is assumed that atoms within a hollow observation cylinder with an outer radius equal to the ONF radius + 300 nm are most likely to emit fluorescence into the guided mode of the ONF [3, 4]. This number of effective atoms, n_{eff}, can be estimated at one end of the ONF using $n_{\text{eff}} = 2C_P/R_{\text{sc}}\eta_{ONF}Q\eta_{QD}$ where R_{sc} is the atomic scattering rate, η_{ONF} is the average coupling efficiency of photons into the guided ONF mode in one direction (estimated at 2% using previous work based on ^{133}Cs [34]), Q is the ONF transmission from the middle of the ONF waist to the detector

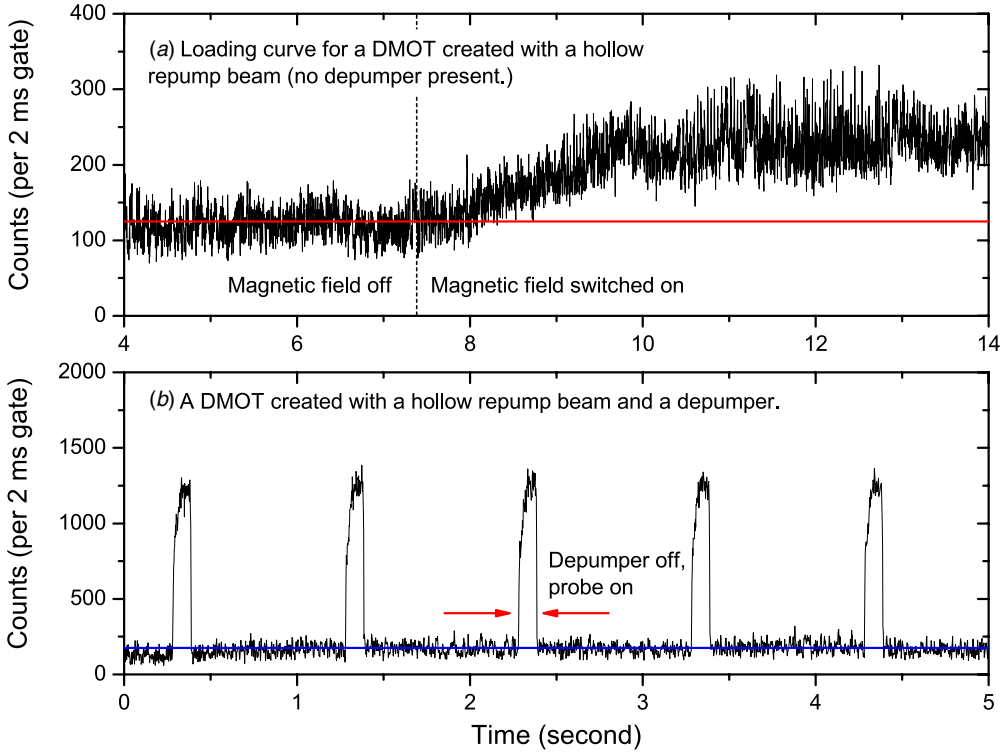


Figure 6. Florescence count rate coupled into the ONF for: (*a*) a DMOT created with a doughnut repump beam and no depump light, (*b*) a DMOT created with a doughnut repump beam and the depump beam. The depumper is switched off for 100 ms at 1 Hz repetition rate. Additionally, there is also a probe beam that switches on when the depump is off. For both plots, the doughnut-shaped repump beam is on at all times. By taking the ratio of the baseline counts in plot (*a*) to the peaks in plot (*b*) the value for p is determined to be ∼0.10. However, by including the depumper, p is determined using the baseline of plot (*b*) (blue line) to be $50/1150 \approx 0.04$.

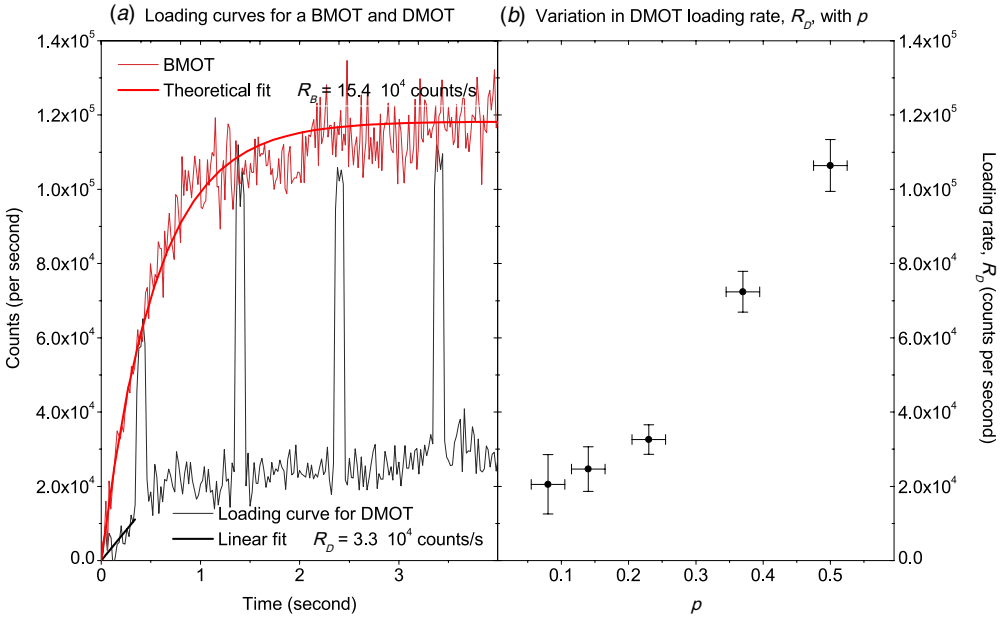


Figure 7. Background-corrected loading curves for the BMOT and DMOT are shown in (*a*) with theoretical fits to determine the loading rates: $R_B = 15 \times 10^4$ counts s^{-1}, $R_D = 3 \times 10^4$ counts s^{-1}. In this case, $p = 0.22$ for the DMOT. (*b*) As the DMOT becomes darker (i.e. as p reduces) the loading rate R_D decreases.

(the transmission through the entire length of fibre is about 60% and we estimate that $Q \sim 77\%$ for half the fibre length), and η_{QD} is the quantum efficiency of the SPCM (60%). The quantity C_P is the fluorescence count rate obtained by the SPCM and is obtained from the fluorescence coupling data. The scattering rate, $R_{\rm sc}$, is described by [35]

$$R_{\rm sc} = \frac{\Gamma}{2} \frac{C_1^2 \Omega_{\rm tot}^2/2}{\delta^2 + \Gamma^2/4 + C_2^2 \Omega_{\rm tot}^2/2}. \qquad (2)$$

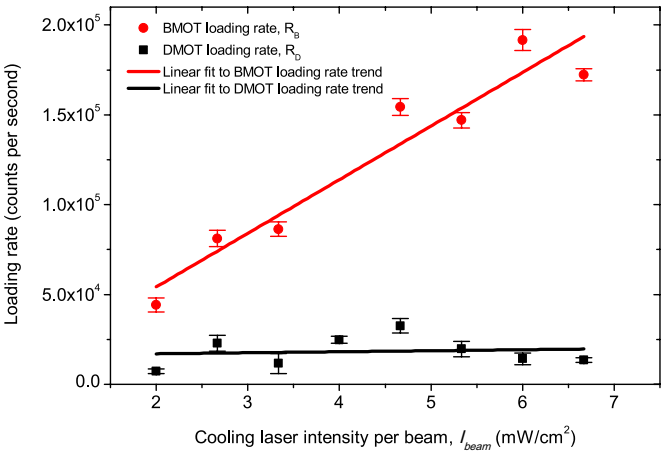


Figure 8. The red (black) data points show the trend in loading rates for the BMOT (DMOT) while varying the cooling laser intensity per MOT beam, I_{beam}. As the doughnut repump beam and the depumper do not help the loading process, the loading rates for the DMOT are lower than those of the BMOT. Linear fits have been applied to each series as a guide to the eye. The error bars are calculated from the loading curve fits.

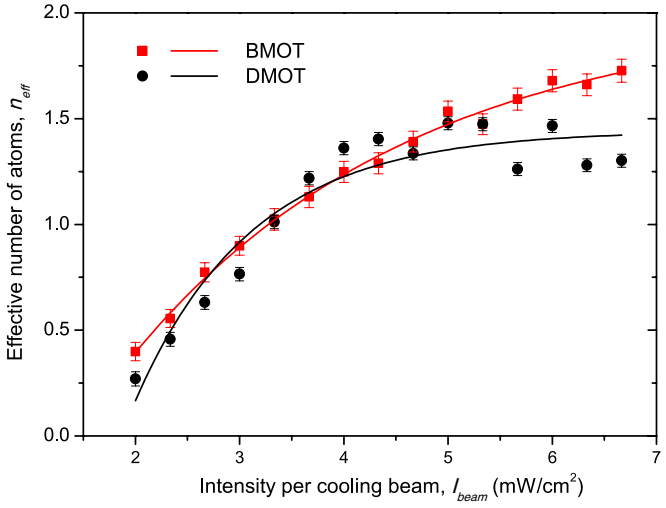


Figure 9. The black (red) data points show the variation in n_{eff} as the cooling laser intensity per beam (I_{beam}) is increased for the DMOT (BMOT) based on fluorescence coupling to the nanofibre. The solid lines are fits as a guide for the eye.

Here, Ω_{tot} is the Rabi frequency for all MOT beams and is taken to be six times that of any one of the trapping beams. C_1 and C_2 are average Clebsch–Gordan coefficients. The values of C_1^2 and C_2^2 are assumed to be equal due to optical pumping among the Zeeman sublevels in the presence of strong coupling between atoms and the radiation field [35].

Figure 9 shows the behaviour of n_{eff} for the BMOT and DMOT as I_{beam} is varied. As expected, n_{eff} increases for increasing I_{beam} due to the enhanced collection efficiency. However, a saturation effect occurs at higher intensities. As the observation volume is fixed by the ONF radius, this saturation effect is due to the spatial expansion of the cloud while it maintains constant density and may also indicate the onset of the multiple scattering regime in the MOT [35–37]. This saturation effect occurs at a lower I_{beam} for the DMOT ($\approx$4 mW cm^{-2}) compared to the BMOT, which implies the MOT may be transitioning to the multiple scattering regime earlier than it did for the BMOT.

Finally, we note that a density measurement via the ONF is non-trivial. For example, it is the number of atoms within the fluorescence coupling region of the ONF that contribute to the magnitude of the fluorescence signal. By creating a DMOT, the total number of atoms is sacrificed (due to the disruptive presence of the dark shadow and depumper). Then, even though there may be a density enhancement when the DMOT is in place, the fluorescence signal magnitude may be the same or lower than that in the case of the BMOT due to the lower atom number. This indicates why the BMOT atom number appears higher than those of the DMOT when examining the fluorescence coupling signals and the data points in figure 9.

4. Conclusion

This work examined the implementation of a DMOT in order to circumvent the density-limitations of a BMOT and is, to the authors' best knowledge, the first experimental study of a DMOT with an ONF.

The variation in DMOT loading rate, R_D, for changing p was measured via the ONF, with the lowest values of R_D obtained for the darkest DMOTs as expected. This alternative technique for measurement of DMOT parameters using an ONF has the advantage that it can be used to probe different local regions of a DMOT. For example, the loss of dark state cold atoms due to collisions around the central region and near the interface between bright and dark regions of a DMOT can be studied using an ONF. This would be extremely difficult to achieve using other commonly employed methods of fluorescence detection, i.e., using photodetectors. In general, the ONF provides an accurate measurement of even the lowest p values due to its sensitivity.

The findings of this work lay the foundation for future work with ONFs and optically-dense atomic samples. If one wishes to do absorption experiments using an ONF, for example, signal quality will be improved dramatically by forcing as many atoms as possible to fill the evanescent field region around the fibre. Although there will still be collisional losses in a DMOT (unless $p = 0$), the reabsorption of scattered photons is no longer a major problem. By packing more atoms closer to the fibre surface, absorption of the light passing through the nanofibre can be enhanced as the number of atoms in the evanescent field region is increased. A density improvement is critical to achieve high optical densities, thereby allowing demonstrations of nonlinear effects such as electromagnetically induced transparency and slow light [38, 39].

Acknowledgments

This work was supported by Science Foundation Ireland under grant no 08/ERA/I1761 through the NanoSci-E+ Transnational Programme, NOIs, and OIST Graduate University. LR acknowledges support from IRCSET through the Embark Initiative.

References

[1] Ward J M, O'Shea D G, Shortt B J, Morrissey M J, Deasy K D and Nic Chormaic S 2006 Heat-and-pull rig for fiber taper fabrication *Rev. Sci. Instrum.* **77** 083105

[2] Le Kien F, Dutta Gupta S, Balykin V I and Hakuta K 2005 Spontaneous emission of a cesium atom near a nanofiber: efficient coupling of light to guided modes *Phys. Rev.* A **72** 032509

[3] Nayak K P, Melentiev P N, Morinaga M, Le Kien F, Balykin V I and Hakuta K 2007 Optical nanofiber as an efficient tool for manipulating and probing atomic fluorescence *Opt. Express* **15** 5431

[4] Morrissey M J, Deasy K, Wu Y, Chakrabarti S and Nic Chormaic S 2009 Tapered optical fibers as tools for probing magneto-optical trap characteristics *Rev. Sci. Instrum.* **80** 053102

[5] Russell L, Deasy K, Daly M J, Morrissey M J and Nic Chormaic S 2012 Sub-Doppler temperature measurements of laser-cooled atoms using optical nanofibres *Meas. Sci. Technol.* **23** 015201

[6] Russell L, Kumar R, Tiwari V B and Nic Chormaic S 2013 Measurements on release-recapture of cold ^{85}Rb atoms using an optical nanofiber in a magneto-optical trap *Opt. Commun.* **309** 313

[7] Spillane S M, Pati G S, Salit K, Hall M, Kumar P, Beausoleil R G and Shahriar M S 2008 Observation of nonlinear optical interactions of ultralow levels of light in a tapered optical nanofiber embedded in a hot rubidium vapor *Phys. Rev. Lett.* **100** 233602

[8] Hendrickson S M, Lai M M, Pittman T B and Franson J D 2010 Observation of two-photon absorption at low power levels ssing tapered optical fibers in rubidium vapor *Phys. Rev. Lett.* **105** 173602

[9] Watkins A, Tiwari V B, Ward J M and Nic Chormaic S 2013 Observation of Zeeman shift in the rubidium D_2 line using an optical nanofiber in vapor *Proc. SPIE* **8785** 87850S

[10] Balykin V I, Hakuta K, Le Kien F, Liang J Q and Morinaga M 2004 Atom trapping and guiding with a subwavelength-diameter optical fiber *Phys. Rev.* A **70** 011401

[11] Le Kien F, Balykin V I and Hakuta K 2004 Atom trap and waveguide using a two-color evanescent light field around a subwavelength-diameter optical fiber *Phys. Rev.* A **70** 063403

[12] Sagué G, Baade A and Rauschenbeutel A 2008 Blue-detuned evanescent field surface traps for neutral atoms based on monde interference in ultrathin optical fibres *New J. Phys.* **10** 113008

[13] Reitz D and Rauschenbeutel A 2012 Nanofiber-based double-helix trap for cold atoms *Opt. Commun.* **285** 4705

[14] Phelan C F, Hennessy T and Busch T 2013 Shaping the evanescent field of optical nanofibers for cold atom trapping *Opt. Express* **21** 27093

[15] Vetsch E, Reitz D, Sagué G, Schmidt R, Dawkins S T and Rauschenbeutel A 2010 Optical interface created by laser-cooled atoms trapped in the evanescent field surrounding an optical nanofiber *Phys. Rev. Lett.* **104** 203603

[16] Goban A, Choi K S, Alton D J, Ding D, Lacroûte C, Pototschnig M, Thiele T, Stern N P and Kimble H J 2012 Demonstration of a state-insensitive, compensated nanofiber trap *Phys. Rev. Lett.* **109** 033603

[17] Russell L, Gleeson D A, Minogin V G and Nic Chormaic S 2009 Spectral distribution of atomic fluorescence coupled into an optical nanofibre *J. Phys. B: At. Mol. Opt. Phys.* **42** 185006

[18] Minogin V G and Nic Chormaic S 2010 Manifestation of the van der Waals surface interaction in the spontaneous emission of atoms into an optical nanofiber *Laser Phys.* **20** 32

[19] Morrissey M, Deasy K, Frawley M, Kumar R, Prel E, Russell L, Truong V G and Nic Chormaic S 2013 Spectroscopy, manipulation and trapping of neutral atoms, molecules, and other particles using optical nanofibers: a review *Sensors* **13** 10449

[20] Ketterle W, Davis K B, Joffe M A, Martin A and Pritchard D E 1993 High densities of cold atoms in a dark spontaneous-force optical trap *Phys. Rev. Lett.* **70** 2253

[21] Muniz S R, Magalhães K M F, Henn E A L, Marcassa L G and Bagnato V S 2004 Creating a self-induced dark spontaneous-force optical trap for neutral atoms *Opt. Commun.* **235** 333

[22] Chapovsky P L 2006 Spectral characteristics of cold rubidium atoms in a dark magneto-optical trap *J. Exp. Theor. Phys.* **103** 711

[23] Chapovsky P L 2007 Observation of nonlinear optical recoil-induced resonances in a dark magneto-optical trap *J. Exp. Theor. Phys.* **86** 78

[24] Singh S, Tiwari V B and Rawat H S 2010 Efficient loading of a Rb dark magneto-optical trap by controlling current through a getter source *J. Exp. Theor. Phys.* **111** 371

[25] Li-Rong W, Zhong-Hua J, Jin-Peng Y, Yan Y, Yan-Ting Z, Jie M, Lian-Tuan X and Suo-Tang J 2012 Investigation of ultracold atoms and molecules in a dark magneto-optical trap *Chin. Phys.* B **21** 113402

[26] Permyakova O I, Yakovlev A V and Chapovskii P L 2008 Measurement of the lifetime of rubidium atoms in a dark magneto-optical trap *Quantum Electron.* **38** 884

[27] Townsend C G, Edwards N H, Zetie K P, Cooper C J, Rink J and Foot C J 1996 High-density trapping of cesium atoms in a dark magneto-optical trap *Phys. Rev.* A **53** 1702

[28] Kenny R P, Birks T A and Oakley K P 1991 Control of optical fibre taper shape *Electron. Lett.* **27** 1654

[29] Brambilla G, Finazzi V and Richardson D 2004 Ultra-low-loss optical fiber nanotapers *Opt. Express* **12** 2258

[30] Abraham E R I and Cornell E A 1998 Teflon feedthrough for coupling optical fibers into ultrahigh vacuum systems *Appl. Opt.* **37** 1762

[31] Cowpe J and Pilkington R 2008 Swagelok ultra-torr based feed-through design for coupling optical fibre bundles into vacuum systems *Vacuum* **82** 1341

[32] Anderson M H, Petrich W, Ensher J R and Cornell E A 1994 Reduction of light-assisted collisional loss rate from a low-pressure vapor-cell trap *Phys. Rev.* A **50** R3597

[33] Kim J Y and Cho D 2001 Dark-spot magneto-optical trap of cesium atoms *J. Korean Phys. Soc.* **39** 864

[34] Le Kien F, Balykin V I and Hakuta K 2006 Scattering of an evanescent light field by a single cesium atom near a nanofiber *Phys. Rev.* A **73** 013819

[35] Townsend C G, Edwards N H, Cooper C J, Zetie K P, Foot C J, Steane A M, Szriftgiser P, Perrin H and Dalibard J 1995 Phase-space density in the magneto-optical trap *Phys. Rev.* A **52** 1423

[36] Walker T, Sesko D and Wieman C 1990 Collective behavior of optically trapped neutral atoms. *Phys. Rev. Lett.* **64** 408

[37] Tiwari V B, Singh S, Rawat H S and Singh M P 2008 Measurements on impulsive force-induced dynamics of a cold ^{85}Rb atom cloud in a magneto-optical trap *J. Phys. B: At. Mol. Opt. Phys.* **41** 205301

[38] Braje D, Balić V, Yin G and Harris S 2003 Low-light-level nonlinear optics with slow light *Phys. Rev.* A **68** 041801(R)

[39] Hakuta K 2008 Single atoms on an optical nanofiber: a novel work system for slow light *Proc. SPIE* **6904** 690406

A.3 Optical Nanofibre Facilitated Nonlinear Optics Effects

This chapter is part of the work done with four-wave mixing described in Chapter 6, and was published in "V. Gokhroo, R. Kumar, S. Nic Chormaic, *Optical nanofiber facilitated nonlinear optics effects in cold atoms*, Proc. SPIE 9503, Nonlinear Optics and Applications IX, 95030D (2015)".

RK contribution: Design and implementation of the experimental setup, data collection and analysis, theoretical modelling and paper writing.

Optical nanofiber facilitated nonlinear optics effects in cold atoms

Vandna Gokhroo[a], Ravi Kumar[a,b] and Síle Nic Chormaic[a]

[a]Light-Matter Interactions Unit, Okinawa Institute of Science and Technology Graduate University, Onna, Okinawa 904-0495, Japan;
[b]Physics Department, University College Cork, Cork, Ireland

ABSTRACT

In this paper, we describe an experiment for two-photon excitation in laser-cooled ^{87}Rb using an optical nanofiber. A brief description of the multilevel atom scheme is followed by experimental results on two-photon absorption and observation of Autler-Townes splitting in cold atoms. These experiments use powers several orders of magnitude lower than those used in free space experiments.

Keywords: Optical nanofibers, laser-cooled atoms, quantum interference effects, Autler-Townes splitting, frequency upconversion

1. INTRODUCTION

Subwavelength diameter optical fibers, otherwise known as optical nanofibers (ONF), have recently come to the fore as tools for cold, neutral atom-based quantum networks. To date, optical nanofibers have been used for spectroscopy, manipulation, and trapping of cold atoms. The intense evanescent field generated at the waist region, even for ultralow input powers in the pW-nW range, lend such fibers to studies of nonlinear optics and quantum interference effects in cold atoms. Nonlinear optics phenomena, such as electromagnetically induced transparency[1] and two-photon absorption,[2] were previously demonstrated using optical nanofibers in rubidium vapor, but work on cold atoms, though appearing in proposals,[3] was very limited until recently.[4–6]

In this work, we report on a 2-photon excitation process in laser-cooled ^{87}Rb that gives rise to frequency up-conversion. Thence, we study the impact of the high intensity evanescent field on the ground to intermediate state transition at 780 nm. A second transition from the intermediate state to the excited state at 776 nm is used as a probe. It is worth noting that the very high intensity evanescent field can give rise to an observable AC Stark effect on the hyperfine energy levels. We show the first demonstration of Autler-Townes splitting in the probe absorption spectrum from atoms around an optical nanofiber and this is achieved for excitation powers as low as 20 nW, while frequency up-conversion has been observed for powers as low as 200 pW of 776 nm. These powers are significantly lower than those required when using free-space excitation and probe beams.

2. EXPERIMENTAL SCHEME

2.1 Optical nanofiber and cold atoms

The optical nanofiber is fabricated by heating and simultaneously pulling a commercial optical fiber. Here, we use single mode fiber (780HP, Thorlabs) with core and cladding diameters of 125 μm and 4.4 μm, respectively. An oxygen-hydrogen flame is used in a flame-brushing configuration whereby the flame moves back and forth around the center position along the fiber axis while the fiber is simultaneously pulled by two motorized stages.[7] Exponential tapering is used to make a fiber with a waist of $\sim$400 nm. After the pulling process, the core becomes negligibly small at the waist region and light propagates in the cladding-vacuum interface. The pulling parameters, i.e. pulling length, heater distance and hot zone, were 40 mm, 3 mm and 17.6 mm, respectively. Transmission of the fiber for 780 nm light was $\sim$84% at the time of pulling and this value was maintained after

E-mail: sile.nicchormaic@oist.jp; groups.oist.jp/light

installation in the ultrahigh vacuum (UHV) chamber. The fiber is glued on a U-shaped mount by UV cured epoxy and then installed vertically in the chamber. Fiber ends exit through the top and the bottom flanges of the science chamber via 300 μm drilled holes in Teflon ferrules.[8]

The number of supported modes in the waist region of the nanofiber can be determined by the V-parameter, which is given by $V = \frac{2\pi a}{\lambda}\sqrt{n_{clad}^2 - n_{vac}^2}$ where a is the fiber radius, λ is the wavelength of light propagating in the fiber, and n_{clad} and n_{vac} are the refractive indices of the cladding and vacuum, respectively. The nanofiber in our experiments can support only the fundamental (HE_{11}) mode for 780 nm and 776 nm wavelengths, but four modes for 420 nm. The characteristics of the modes in the fiber are dependent on the fiber radius and propagating wavelength. For the linear polarization (LP) approximation, the evanescent field decay length is given by the inverse of a parameter, q, which is determined by the fiber eigen-equation.[9] For a 400 nm diameter ONF, the decay length for the fundamental mode is ~270 nm from the fiber surface for 780 nm propagating light (or ~80 nm for 420 nm light). From this, and using the density of our atom cloud, we determine that there are less than 10 atoms in the evanescent field region contributing to the signals.

The cold atom cloud is created around the waist of the ONF using a standard magneto-optical trap (MOT) with three retro-reflected beams of 18 mm diameters and a beam intensity of 4 mW/cm^2 each. Vapor pressure of Rb in the vacuum chamber is maintained at $\sim 5 \times 10^{-9}$ mBarr. A magnetic field gradient of $\sim$ 11 G/cm for the MOT is created by passing 2.75 A current in the anti-Helmholtz coils. Two additional compensation coils are used to overlap the MOT center with the ONF. Typically, there are $\sim 5 \times 10^6$ atoms in the cloud with a number density of ~2×10^{10} atoms/cm^3 in a 0.8 mm diameter sphere. The temperature of the atoms is estimated to be $\sim$ 200 μK by a time-of-flight technique using fluorescence imaging. Here, the MOT magnetic field and trapping beams are switched off and expanded cold atom cloud images are taken at intervals of 1 ms.

2.2 Two-photon excitation scheme

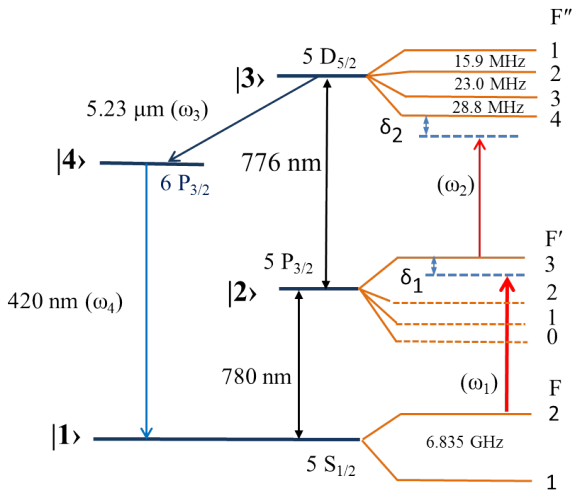


Figure 1. Hyperfine energy level diagram of ^{87}Rb. ω_1 and ω_2 represent the two-photon excitation beams for the cold atoms. δ_1 and δ_2 are the detunings from the F′=3 and F″=4 levels, respectively.

In this work, we demonstrate two-photon absorption in a cold, atom cloud using an ONF as the excitation and detection tool. A cascade three-level system is chosen with $5S_{1/2}$F= 2 as a ground state, $|1\rangle$, $5P_{3/2}$ F′ = 3 as an intermediate state, $|2\rangle$, and $5D_{5/2}$ F″ as the final excitation state, $|3\rangle$. Relaxation of $|3\rangle$ via $6P_{3/2}$, i.e. $|4\rangle$ generates 5.23 μm and 420 nm blue photons. The 780 nm (ω_1) and 776 nm (ω_2) beams propagate along the optical nanofiber and they excite the cold atoms from $|1\rangle$ to $|3\rangle$ via two-photon excitation (see Fig. 1 for the transitions involved). Emitted blue photons couple into the ONF through evanescent field coupling and they are detected at one end. Note that the energy levels of the hyperfine lines of the $5D_{5/2}$ state are inverted, i.e.

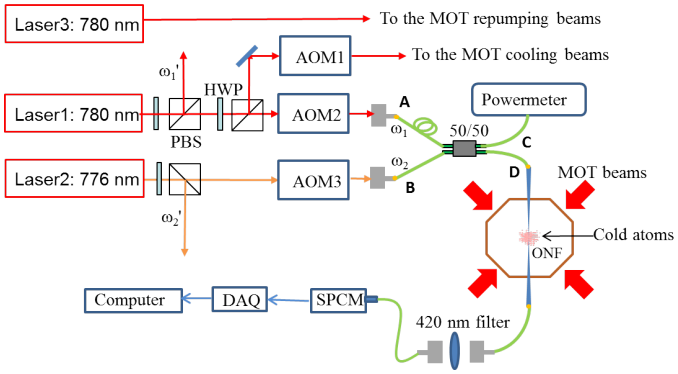


Figure 2. Schematic of the two-photon excitation and detection scheme in cold atoms via an ONF. PBS: Polarizing beamsplitter, HWP: Half waveplate, SPCM: Single photon counter module, DAQ: Data acquisition card, 50/50: Fiber optic coupler.

higher values of F″ have lower energy, in contrast to the cases for F and F′ (Fig. 1). This inverted hyperfine spectrum is due to the fact that the magnetic dipole interaction constant is negative. This arises from the strong polarization effects induced in the core due to the presence of the valence electron.[10]

2.3 Laser set-up

Three external cavity diode lasers (DL100 pro, Toptica) are used to generate all the beams needed for the experiment and a schematic is presented in Fig. 2. Laser1 is locked to the 5 $S_{1/2}$ F=2 → 5 $P_{3/2}$ F′=2, 3 crossover using saturation absorption spectroscopy. One direct beam (ω_1') from Laser1 is used for two-photon spectroscopy in a reference vapor cell. Cooling beams for the MOT and a two-photon excitation beam for the excitation via the ONF (i.e. ω_1) are also obtained from the same laser by up-shifting the frequency. Two independent acousto-optical modulators (AOM) in double pass configuration are used to bring the cooling and ω_1 frequencies close to that of $5P_{3/2}$ F′=3.

A second laser, Laser2, is tuned to ∼776.976 nm (in vacuum). A direct beam from Laser2, ω_2', when passed through the vapor cell counter-propagating with ω_1' yields the two-photon excitation peaks when ω_2' is scanned. Since ω_1' is locked at the crossover, which is 133 MHz red detuned from the $5P_{3/2}$ F′=3 level, two-photon resonances are shown for ω_2' 133 MHz higher than ω_{fi}, where ω_{fi} is the atomic transition frequency between the final and the intermediate level. Another beam from Laser2 is frequency downshifted via an AOM in double pass configuration and it provides another two-photon excitation beam, ω_2, which is used for the excitation of cold atoms via the ONF. Using this arrangement two-photon resonance peaks in the reference vapor cell and in the cold atoms can be obtained simultaneously and an accurate frequency calibration is obtained. Both the excitation beams, ω_1 and ω_2, obtained from the AOMs, gives the freedom of independent tunability of their frequencies and intensities. The third laser, Laser3, is locked to the $5S_{1/2}$ F=1 → $5P_{3/2}$ F′=2 transition. This provides the repump beam for the MOT.

2.4 Frequency reference for the two-photon excitation

The frequency reference for the $5S_{1/2}$ to $5P_{3/2}$ hyperfine levels (780 nm transition) is obtained by standard saturation absorption spectroscopy in-built with the laser system. The reference for the $5P_{3/2}$ to $5D_{5/2}$ hyperfine levels (776 nm transition) is done via two-photon spectroscopy in a reference vapor cell. ω_1' and ω_2' pass through the vapor cell in a counter-propagation configuration as shown in Fig. 3. In this configuration, unlike for single photon absorption where the spectrum is Doppler broadened, spectral linewidths are very narrow.[11] When beams are counter-propagating, a non-relativistic Doppler shift ($\Delta\omega = \omega v/c$) observed by an atom moving with velocity 'v' in the ω_1' beam is approximately the same in magnitude but opposite in sign as the Doppler shift seen for the ω_2' beam. The small difference between the two shifts arises due to the difference in the frequencies ω_1' and ω_2'. Hence, atoms moving with any velocity will absorb the maximum amount of light whenever ω_1' +

ω_2' is equal to the two-photon resonance frequency (ω_{gf}) and the resultant spectrum will be Doppler-free. The lineshape of the spectrum is Lorentzian and the linewidth is given by:[11]

$$\Delta\omega_f + |(\omega_2 + \epsilon\omega_1)/\omega_{ig}|\,\Delta\omega_i \tag{1}$$

where, $\Delta\omega_f$ and $\Delta\omega_i$ are natural linewidths of the final and intermediate states, $\epsilon = -1$ for the counter-propagating scheme and ω_{ig} is the atomic transition frequency between the intermediate and ground levels.

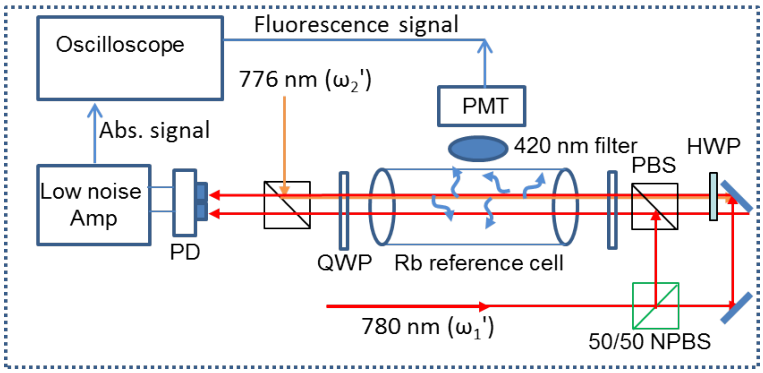


Figure 3. Vapor cell spectroscopy for two-photon excitation with ω_1' locked and ω_2' in scan mode. Counter-propagating ω_1' and ω_2' beams excite the atoms to $5D_{5/2}$ F'' states. This is detected either by monitoring the blue photons on the photomultiplier tube (PMT) or the absorption of ω_1' on a photodiode. QWP: quarter waveplate, NPBS: non-polarizing 50-50 beamsplitter, PD: photo detector, PMT: photo multiplier tube.

Two-photon spectroscopy can be performed either by fluorescence or absorption methods (see Fig. 3). In the fluorescence method, emitted blue photons are collected by a photomultiplier tube (PMT, PMM01, Thorlabs) after passing through a 420 nm bandpass filter (FB420-10, Thorlabs). In the absorption detection technique, balanced detection of the ω_1' beam is performed while scanning ω_2' (Fig. 3). Typically, the powers in ω_1' and ω_2' are 0.2 mW and 0.5 mW, respectively, and the beams have ~1.5 mm diameter.

2.5 Two-photon excitation in cold atoms

The beams for two-photon excitation in cold atoms (ω_1, ω_2) are combined at a 50:50 fiber beam splitter and one arm of the splitter is spliced to one pigtail of the ONF as shown in Fig. 2. A power meter at port C monitors the input power going into the ONF. The actual power at the nanofiber waist region differs due to the ONF transmission loss. ω_1 is locked to a fixed frequency, while ω_2 is kept in scanning mode. When $\omega_1 + \omega_2$ matches with the two-photon resonance frequency (ω_{fg}) the maximum blue photon signal is obtained by coupling to the ONF and collection at the opposite fiber pigtail. A single photon counting module (SPCM, COUNT-100B-FC, Laser Components) is used to detect the blue photons. In order to get the measurable blue photon count rate, the MOT is kept on all the time. Therefore, even in the absence of ω_1, the MOT beams contribute to the two-photon excitation. A 420 nm filter is used before the SPCM in order to monitor the blue photon emission and eliminate the undesirable strong background coming from ω_1, ω_2 and the MOT beams coupling into the ONF.

Laser2 is frequency scanned at a slow rate of 0.5 Hz. A data acquisition card (DAQ) is used to count the pulses from the SPCM. An additional pulse generator is used to create n pulses in the duration of one frequency scan, i.e. the *scan time*. The rising edge of the pulses initializes the counter and the counting time window is determined by the number of pulses and scan time by *scan time*/n. The timing sequence of the different devices during data collection is shown in Fig. 4. Data is averaged over 50 cycles of scan periods. LabVIEW is used to generate and control the timing sequence (Fig. 4).

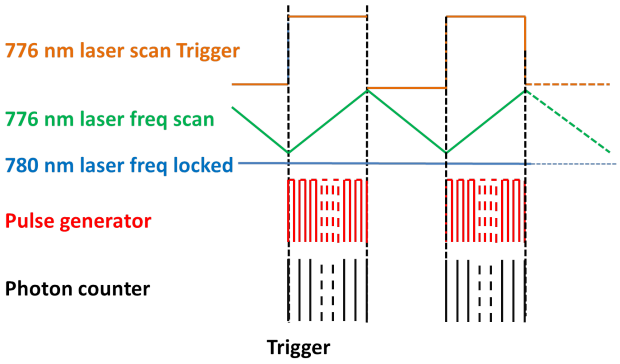


Figure 4. Synchronization of the devices during data collection. Various components are triggered by Laser2 scan trigger.

2.6 3-level system and Autler-Townes splitting

Two-photon excitation in a three-level ladder type system can be used to study the effect of strong light fields on the atomic transitions. We consider a case when the lower two states, $|1\rangle$ and $|2\rangle$, are coupled via a strong light field, P_{ω_1}, and the upper two levels, $|2\rangle$ and $|3\rangle$, are coupled via a weak probe beam, P_{ω_2}, so that $P_{\omega_1} \gg P_{\omega_2}$. The time evolution of the density matrix of the system is governed by the following equation:

$$\dot{\rho} = -\frac{i}{\hbar}[H, \rho] + \Gamma, \tag{2}$$

where ρ is the density matrix of the three level atom, H is the Hamiltonian and Γ is the decay matrix . In the steady state, $\dot{\rho} = 0$ and Eqn.2 can be solved for ρ_{23}. The real and imaginary parts of ρ_{23} are related to dispersion and absorption of the probe beam. Absorption of the probe beam can be given by the following relation:[12]

$$A = -Im(\rho_{23}\Gamma_2/\Omega_2), \tag{3}$$

where Γ_2 is half of the spontaneous decay rate of the upper most, or final, level and Ω_2 is the Rabi frequency of the probe beam.

When the first transition is tuned to resonance, i.e. $\delta_1 = 0$, the absorption spectrum of the probe (ω_2) beam shows the splitting at $\pm\ \Omega_1$, where Ω_1 is the Rabi frequency of the coupling transition. This is called Autler-Townes splitting.[13] At non-zero detuning of the coupling laser (i.e. $\delta_1 \neq 0$), the absorption spectrum is not symmetric. At the high intensity limit, when the power in ω_1 is much greater than the detuning, $\Omega_1 \gg \delta_1$, the resonance positions are[14]

$$\delta_2 = \begin{cases} +\frac{\Omega_1}{2} - \frac{\delta_1}{2} + \frac{\delta_1^2}{4\Omega_1} \\ -\frac{\Omega_1}{2} - \frac{\delta_1}{2} - \frac{\delta_1^2}{4\Omega_1} \end{cases}.$$

Due to the linear AC Stark effect the coupling of high intensity light to atomic states modifies the energy eigenstates of the system. For the system being considered here, with ω_2 being reasonably far from the stronger ω_1 frequency, we assume that there is no modification to the states caused by the weak probe beam. Instead, by sharing a common level (i.e. the intermediate level) ω_2 probes the effect caused by ω_1. In the presence of the strong coupling beam (ω_1) the new resonance position is split in two parts, showing a doublet structure (known as the Autler-Townes doublet) in the probe absorption.[15]

3. RESULTS

3.1 Vapor cell spectroscopy

A two-photon excitation spectrum obtained from atoms at room temperature is shown in Fig. 5. This spectrum serves as a reference for the experiments with cold atoms. The plot shows the hyperfine states of $5D_{5/2}$ from the vapor cell spectroscopy. Peaks are observed when $\omega_1' + \omega_2'$ matches with $5S_{1/2}$ F=2 to $5D_{5/2}$ F$''$ energy levels. The blue fluorescence signal collected from the PMT is plotted as a function of ω_2'. The widths of the hyperfine transitions are larger than the final level natural linewidth (0.66 MHz) due to the contribution of power broadening and the small Doppler effect present, as discussed earlier.

Even though ω_1' is 133 MHz red-detuned from the $5P_{3/2}$ F$'$=3 level, the signal is prominent due to the presence of thermal atoms having velocities large enough to compensate the detuning with the Doppler shift. If the cell is kept transverse to the light propagation direction, an extra small peak (shown by the dashed circle in Fig. 5) is also observed at the lower frequency side. The reason for this is that either the ω_1' or ω_2' beam reflects from the cell surface making a co-propagating configuration with the other beam. As ω_1 is locked at the crossover, atoms with a velocity magnitude that can compensate the 133 MHz red detuning will observe the same shift in ω_2' (with the same sign) and will therefore absorb light at a frequency 267 MHz lower than that absorbed in the counter-propagation case.

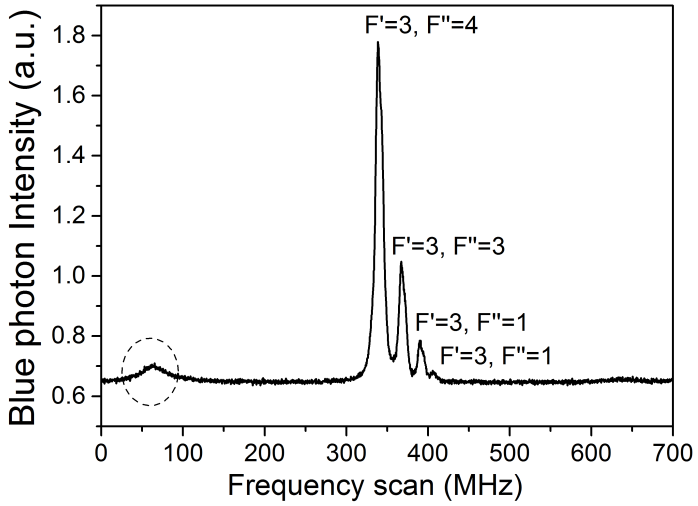


Figure 5. Hyperfine spectrum of the $5D_{5/2}$ F$''$ levels from two-photon excitation in a vapor cell. The spectrum is obtained from blue photon fluorescence detected using a PMT.

3.2 Two-photon excitation and Autler-Townes effect in cold atoms using an ONF

For the on-resonance two-photon excitation ω_1 is kept at the $5S_{1/2}$ F=2 $\rightarrow$ $5P_{3/2}$ F$'$= 3 transition. In the absence of ω_1, the MOT beams, which are 14 MHz red-detuned (i.e. -14 MHz) from the cooling transition, contribute to the two-photon excitation. Under this condition, $\sim$ 200 pW of ω_2 is enough to provide a detectable blue photon signal, which peaks when the ω_2 detuning (δ_2) is 14 MHz blue-detuned from the two-photon resonance.

If we select ω_1 so that it is also -14 MHz detuned (i.e. similar to the cooling beams) then the contribution from the MOT beams and ω_1 are added and the blue signal is enhanced. With ω_1 at resonance and for low powers there are two supplementary two-photon excitation processes. As the power, P_{ω_1}, is increased the contribution from the MOT beams reduces and ω_1 takes over.

For around 10 nW of P_{ω_1}, the blue photon spectrum splits into two parts and this splitting increases with P_{ω_1} (Fig. 6). This effect is known as Autler-Townes splitting and it scales linearly with the square root of P_{ω_1}, as theoretically predicted. The two-photon excitation process is also observed by monitoring the fluorescence

from the MOT atoms coupling into the ONF. In this measurement, ω_1 is not sent through the ONF. In other words, only ω_2 is sent into one pigtail of the ONF and a SPCM detector is placed at port C (see Fig. 2). In the presence of ω_2, atoms around the ONF can be excited to $|3\rangle$, which may decay via $|4\rangle$. This leads to fewer atoms going directly from $|2\rangle$ to $|1\rangle$, resulting in a decrease in the 780 nm fluorescence collected by the ONF. As ω_2 approaches the two-photon resonance condition, the MOT fluorescence signal collected by the ONF drops to a minimum value, as shown in Fig. 7.

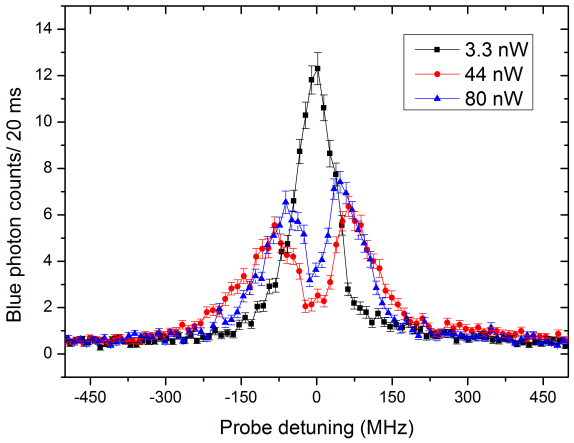


Figure 6. Two-photon excitation and Autler-Townes splitting in the presence of an on-resonance ω_1 coupling beam, for different powers. The probe power is kept at 500 pW. The splitting separation increases with an increase in the coupling power as shown by the blue and red curves. Data points are joined by the solid lines as guides to the eye.

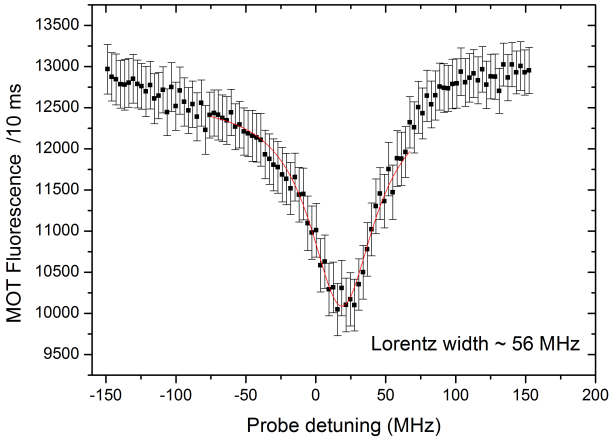


Figure 7. Fluorescence of the MOT atoms collected by the ONF while scanning the 776 nm probe beam. The dip around the center of the scan corresponds to the two-photon resonance condition. Red curve is the Lorentzian fitting.

4. CONCLUSION AND OUTLOOK

In this work, we have demonstrated two-photon excitation in cold ^{87}Rb atoms at ultralow excitation beam powers. Tight confinement of the evanescent field of an ONF provides high intensities at the waist region for such low powers. We observed the AC Stark effect of light on atomic transitions in terms of the Autler-Townes doublet. This shows the potential of such a system for nonlinear optics studies at ultralow powers. In the applied area, this study may be useful for all optical switching and quantum logic gates at ultralow powers.

ACKNOWLEDGMENTS

The work is funded by the Okinawa Institute of Science and Technology Graduate University, Okinawa, Japan.

REFERENCES

[1] Spillane, S. M., Pati, G. S., Salit, K., Hall, M., Kumar, P., Beausoleil, R. G., and Shahriar, M. S., "Observation of nonlinear optical interactions of ultralow levels of light in a tapered optical nanofiber embedded in a hot rubidium vapor," *Phys. Rev. Lett.* **100**, 233602 (2008).

[2] Hendrickson, S. M., Lai, M. M., Pittman, T. B., and Franson, J. D., "Observation of two-photon absorption at low power levels using tapered optical fibers in rubidium vapor," *Phys. Rev. Lett.* **105**, 173602 (2010).

[3] Russell, L., Daly, M., and Nic Chormaic, S., "1- and 2-photon absorption by laser-cooled 85Rb using an optical nanofiber," in [*Quantum Africa 2010: Theoretical and experimental foundations of recent quantum technology*], Bruning, E., Konrad, T., and Petruccione, F., eds., *AIP Conf. Proc.* **1469**, 82 (2012).

[4] Kumar, R., Gokhroo, V., Deasy, K., and Nic Chormaic, S., "Autler-townes splitting via frequency upconversion at ultra-low power levels in cold ^{87}Rb atoms using an optical nanofiber," *arXiv:1502.01123* .

[5] Sayrin, C., Clausen, C., Albrecht, B., Schneeweiss, P., and Rauschenbeutel, A., "Storage of fiber-guided light in a nanofiber-trapped ensemble of cold atoms," *arXiv:1502.01151* .

[6] Gouraud, B., Maxein, D., Nicolas, A., Morin, O., and Laurat, J., "Demonstration of a memory for tightly guided light in an optical nanofiber," *arXiv:1502.01458* .

[7] Ward, J. M., Maimaiti, A., Le, V. H., and Nic Chormaic, S., "Optical micro- and nanofiber pulling rig," *Rev. Sci. Instrum.* **85**, 111501 (2014).

[8] Abraham, E. R. and Cornell, E. A., "Teflon feedthrough for coupling optical fibers into ultrahigh vacuum systems," *Appl. Opt.* **37**, 1762 (1998).

[9] Tong, L. M. and Sumetsky, M., [*Subwavelength and Nanometer Diameter Optical Fibers*], Zhejiang University Press, Springer (2009).

[10] Lindgren, I., Lindgren, J., and Martensson, A., "Many-body calculations of the hyperfine interaction of some excited states of alkali atoms, using approximate brueckner or natural orbitals," *Z. Physik A* **279**, 113 (1976).

[11] Bjorkholm, J. E. and Liao, P. F., "Line shape and strength of two-photon absorption in an atomic vapor with a resonant or nearly resonant intermediate state," *Phys. Rev. A* **14**, 751 (1976).

[12] Vemuri, G., Agarwal, G. S., and Nageswara Rao, B. D., "Sub-Doppler resolution in inhomogeneously broadened media using intense control fields," *Phys. Rev. A* **53**, 2842 (1996).

[13] Autler, S. H. and Townes, C. H., "Stark effect in rapidly varying fields," *Phys. Rev.* **100**, 703 (1955).

[14] Stigholm, S., [*Foundations of Laser Spectroscopy*], John Wiley and Sons, New York (1984).

[15] Cohen-Tannoudji, C. and J. Dupont-Roc, G. G., [*Atom - Photon Interactions: Basic Process and Applications*], Wiley Interscience, New York (1992).

A.4 Spectroscopy, Manipulation and Trapping Using Optical Nanofibres

ONFs have been used extensively for spectroscopy and manipulation of atoms, molecules and other particles. The following is a review article published in "M. J. Morrissey, K. Deasy, M. Frawley, R. Kumar, E. Prel, L. Russell, V. G. Truong and S. Nic Chormaic, *Spectroscopy, manipulation and trapping of neutral atoms, molecules, and other particles using optical nanofibers: A review*, Sensors, 13, 10449-10481 (2013)".

RK contribution: Collecting references for Section 4 of the article and writing this section.

Sensors **2013**, *13*, 10449-10481; doi:10.3390/s130810449

OPEN ACCESS

sensors

ISSN 1424-8220
www.mdpi.com/journal/sensors

Review

Spectroscopy, Manipulation and Trapping of Neutral Atoms, Molecules, and Other Particles Using Optical Nanofibers: A Review

Michael J. Morrissey [1], Kieran Deasy [2], Mary Frawley [2,3], Ravi Kumar [2,3], Eugen Prel [2,3], Laura Russell [2,3], Viet Giang Truong [2] and S le Nic Chormaic [1,2,3,*]

[1] School of Chemistry and Physics, University of KwaZulu-Natal, Durban 4001, South Africa; E-Mail: morrissey@ukzn.ac.za

[2] Light-Matter Interactions Unit, OIST Graduate University, 1919-1 Tancha, Onna-son, Okinawa 904-0495, Japan; E-Mails: kieran.deasy@oist.jp (K.D.); mary.frawley@oist.jp (M.F.); ravi.kumar@oist.jp (R.K.); eugen.prel@oist.jp (E.P.); laura.russell@oist.jp (L.R.); v.g.truong@oist.jp (V.G.T.)

[3] Physics Department, University College Cork, Cork, Ireland

***** Author to whom correspondence should be addressed; E-Mail: sile.nicchormaic@oist.jp; Tel.: +81-98-966-1551.

Received: 31 May 2013; in revised form: 18 July 2013 / Accepted: 1 August 2013 / Published: 13 August 2013

Abstract: The use of tapered optical fibers, *i.e.*, optical nanofibers, for spectroscopy and the detection of small numbers of particles, such as neutral atoms or molecules, has been gaining interest in recent years. In this review, we briefly introduce the optical nanofiber, its fabrication, and optical mode propagation within. We discuss recent progress on the integration of optical nanofibers into laser-cooled atom and vapor systems, paying particular attention to spectroscopy, cold atom cloud characterization, and optical trapping schemes. Next, a natural extension of this work to molecules is introduced. Finally, we consider several alternatives to optical nanofibers that display some advantages for specific applications.

Keywords: optical nanofiber; taper; evanescent field; cold atoms; atomic vapor; single particle detection; optical cavities; laser cooling; spectroscopy; whispering gallery resonators

1. Introduction

Quantum mechanics plays a crucial role in the development and understanding of future technologies governed by quantum rules. The isolation of single atoms allows researchers to directly observe quantum properties of light-matter interactions. In recent years, researchers have been investigating the possibility of detecting, controlling, and manipulating quantum systems, such as cold atoms [1–4], trapped ions [5,6], and molecules [7], close to the surface of nanostructured devices. These devices include microcavities [8], atom chips [9], superconducting circuits [7], and optical nanofibers [1]. The interest in these devices primarily arises from their potential to offer methods by which single atoms/particles can be trapped, probed, and manipulated, thereby providing a useful tool for advancing quantum engineered devices.

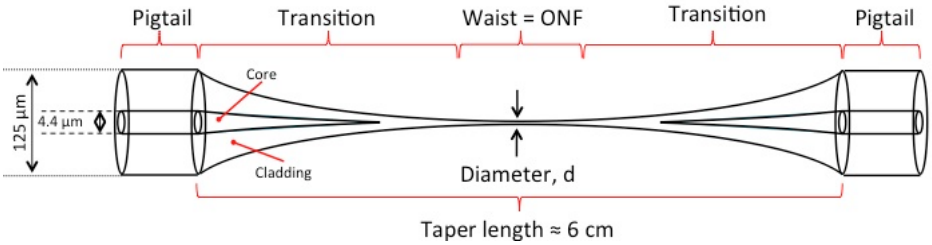
The focus of this review paper is on the application of optical nanofibers (ONFs) [10–13] for the detection, manipulation, and trapping of laser-cooled atoms and the role they play in this, and related, research fields. Optical fiber sensors are a well-established tool [14] and, more recently, the versatility of ONFs as sensing tools [15,16] for very small numbers of particles is also becoming evident. We begin by presenting the basic concept of the ONF and its fundamental properties. Section 2 introduces the ONF as a probe for either a cloud of magneto-optically trapped atoms or for atoms in a vapor. In these cases, the nanofiber can act as either a bright or dark probe with regard to the atoms. A bright nanofiber probe is generally used for absorption-type measurements, such as manipulation and trapping of atoms using light fields or for nonlinear optics with an atomic medium. In this case, light—usually tunable across an atomic transition of interest—is coupled into the optical fiber in the usual manner. This light propagates through the fiber, interacts with the surrounding medium at the narrowest region of the fiber (known as the waist), and then continues to propagate through the fiber until it is detected at the other end. Changes in the output intensity arise when interactions with the surrounding medium have occurred. In stark contrast, for a dark nanofiber, there is no initial light beam coupled into the fiber and any light detected at the output arises from fluorescence coupling from the surrounding medium into the nanofiber at the waist. The various techniques proposed to precisely trap and manipulate atoms are presented, as well as the atom-surface effects under such conditions. Aside from the progress in cold atom-fiber interaction experiments, ONFs have also found applications in sensing molecules, quantum dots, and nanodiamonds—areas that are reviewed in Section 3. In Section 4 some alternative systems for single atoms and molecules based on micro- or nanostructuring within the ONF itself are presented. The paper concludes with some comments on the future directions of this research field.

1.1. Properties of an Optical Nanofiber

An ONF is a circular dielectric waveguide with a diameter smaller than the wavelength of the light which propagates within it. Such an ONF can be realized at the waist of a biconical tapered optical fiber consisting of three distinct regions: (i) the normal fiber, (ii) the transition or taper region, and (iii) the waist, as illustrated in Figure 1. To fabricate such a device the same general fabrication technique is typically applied, involving the heating of an optical fiber to a molten state while elongating it to create a tapered optical fiber. Until now, a number of different heat sources have been

used for this process, including a gas flame [16,17], a CO_2 laser [18], a microheater [19], or an electrical strip heater [20]. Independent of the type of heat source, a pair of parameters are vital for determining the shape of the tapered region, along with the length and diameter of the ONF waist region [21,22]. These parameters are: (i) the size of the hot zone and (ii) the elongation length of the fiber. For this reason the flame brushing procedure is usually considered to be the preferred technique for incorporating optical nanofibers into cold atoms systems [16], since both of these parameters can be controlled with relative ease.

Figure 1. Schematic illustration of an optical nanofiber with a 125 μm outer diameter and a core diameter of 4.4 μm. The narrowest region has a diameter in the range of hundreds of nanometers. Typical taper lengths are ~6 cm, with the waist region being a few mm in length.



Another important factor in the fabrication of high performance ONFs is that optical losses due to the tapered regions should be kept to a minimum. To achieve this goal the adiabaticity criteria should be met [23]. These criteria take into account the changing profile of the fiber within the transition region and determine the best profile available. Assuming the diameter of the core and cladding decrease at the same rate, the core is reduced in size to the point where it has negligible influence on the guided modes within the ONF [24]. Thus, the guiding properties of the ONF are determined by the difference in the refractive indices between the cladding, n_{clad}, and the ambient environment, n_{amb}.

In many applications of ONFs the fiber should be single-mode, although interest in higher order mode propagation is increasing due to some advantages offered by modal interference for particle trapping [25–27]. The condition for a fiber to be single-mode is given by the *V*-number which depends on the fiber diameter, *d*, as well as the numerical aperture of the fiber, such that:

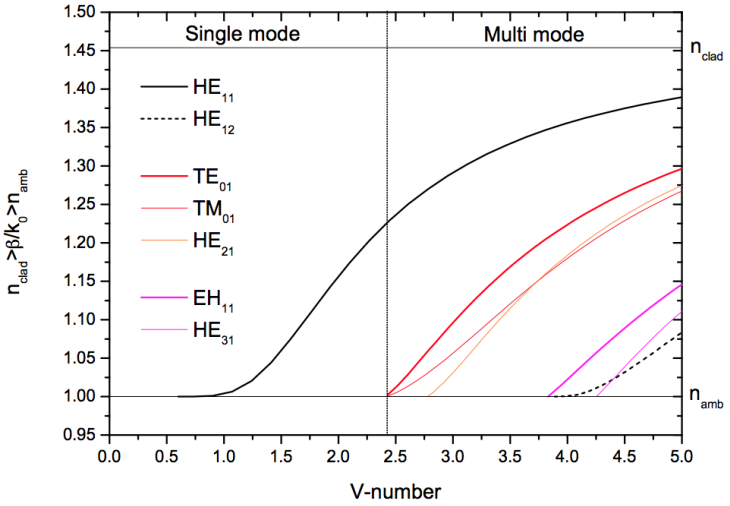
$$V = \frac{k_0\, d\sqrt{n_{clad}^2 - n_{amb}^2}}{2} < 2.405 \quad (1)$$

where $k_0 = 2\pi/\lambda$ is the free space wave-number. This single-mode condition is illustrated in Figure 2, where only the fundamental, HE_{11}, mode exists for values of the V-number lower than 2.405. This condition is met experimentally by ensuring the ONF diameter is below the single-mode cut-off diameter.

Due to the sub-wavelength diameter of the ONF, the evanescent field [28] extends further into the optically rarer medium, such as a surrounding atom vapor, than in a conventional optical fiber. The light intensity on the surface can easily exceed the intensity inside the ONF if its diameter is small enough. Moreover, the polarization dependence of the decaying behavior in the evanescent field is more distinct in this case, and the field intensity varies azimuthally around the fiber, depending on the polarization of the propagating light. The enhancement of the evanescent field lays a favorable

platform for the interaction of light with matter and also permits ONFs to be used for ultra-sensitive sensing applications.

Figure 2. A plot of the effective index of refraction, $n_{eff} = \beta/k_0$, against V-number for an optical fiber with cladding and core refractive indices as 1.4537 and 1.000, respectively. β represents the propagation constant. The vertical line indicates the boundary between single- and multimode guidance in the fiber (V = 2.405).



1.2. Optical Nanofibers for Emerging Quantum Technologies

In many areas of atomic physics, in particular for the development of quantum technologies, nonlinear optics provides a means of controlling the quantum states of light using atoms. While the focus of this paper is on sensing and manipulation of single or small numbers of particles around optical nanofibers, the overall motivation behind much of this work relates to emergent technologies in quantum networking using atoms and light, such as developing quantum logic gates via electromagnetically induced transparency (EIT) [29,30]. In any nonlinear system, in order to increase observable effects, there are two criteria which can be exploited, one of which is the nonlinearity of the medium and the other is the intensity of the light used. The optical depth of a medium, *OD*, is a unitless quantity that is related to the strength of the interaction between the medium and light, such that $OD = \eta\sigma L$, where η is the density of the medium, σ is the absorption cross-section of the atoms in the medium, and L is the interaction length.

In an atomic system, η is limited if one wants to avoid dephasing effects arising from atomic collisions. To maximize σ, the alkali atoms (such as Cs, Na, Li, and Rb) offer some of the highest absorption cross-sections available. Therefore, aside from choosing an alkali atom for observations of nonlinear effects, the obvious manner in which we can increase the optical depth is through increasing L, the interaction length. The optical nanofiber provides an ideal manner by which this can be achieved as the evanescent light field interacts with the surrounding medium over the taper length (typically several mm). This is in contrast to the interaction that can be achieved using, for example, a very tightly focused laser beam (as is necessary to achieve a high intensity), where the interaction length is limited by the diffraction of the beam. As an example, a laser beam tightly focused to a waist of 2.3 μm which interacts with a cloud of cold Cs atoms (transition wavelength ~850 nm) has a Rayleigh

length of ~20 μm [31], orders of magnitude shorter than the few mm interaction length attainable with optical nanofibers.

The other parameter that can be optimized is the intensity of the laser used; ideally, the beam mode area should be proportional to the wavelength of light in order to maximize the available intensity. As mentioned above, for a free-space laser beam a high intensity can be achieved using a very tight focus, but this will reduce the interaction length, *L*, that can be achieved [31]. The optical nanofiber again provides an ideal platform for obtaining high intensities while maintaining a relatively long interaction length since the mode is confined within the evanescent field and very high intensities can be achieved for very low power inputs on the order of mW or less. The strong transverse mode confinement, in combination with the longer interaction length, would appear to suggest that nonlinear optics using optical nanofibers embedded in atomic systems may be an ideal tool for such studies. By increasing the fiber waist length through alternative profile shaping to the standard exponentially shaped taper [26] the system becomes even more favorable.

Aside from the advantages with regards to nonlinear optics, optical nanofibers are also extremely efficient devices for coupling fluorescence from surrounding particles, with up to 28% coupling efficiency achievable for a Cs atom near a 400 nm diameter ONF [32]. Coupling of light into subwavelength-sized structures is a major technical challenge, usually involving plasmonics [33,34], but the ONF influences the spontaneous emission from the atom, thereby leading to such high efficiencies in theory. It is also far easier technically to place atoms *around* a nanofiber than to place them *into* a fiber, as, for example, has been done by Ghosh *et al.* using Rb vapor in a photonic band-gap fiber (PBGF) [30]. The advantages offered by PBGF are similar to those for the ONF—a large interaction length, *L*, and confinement of the light to an area comparable to the atomic scattering cross-section, $3\lambda^2/2\pi$, but the technical challenge of pumping the vapor into the fiber diminishes its functionality.

A drawback in using the optical nanofiber is the fact that surface interactions, such as van der Waals and Casimir-Polder, come into play and can affect both the resonance line shape and the central position in relation to free-space studies. A full understanding of the influence of surface interactions on line shape is essential in order to be able to distinguish this effect from others of interest and, while several theoretical studies have been conducted [35–37], further conclusive and substantiated experimental measurements are still required [38,39].

2. Neutral Atoms

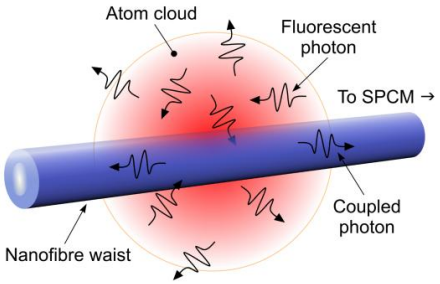
The potential for using cold atomic ensembles in the evolution of quantum technologies is undisputed. However, it is clear that further advances in the precision control and manipulation of cold atoms are essential. Since the development of laser cooling of neutral atoms in the 1980's, many techniques have been successfully developed to trap [9,40–43], manipulate [44–50], and probe [51–53] cold atoms. Both trapping and manipulation of atoms can be performed using either magnetic fields or far-off resonance laser light, while probing is most conveniently performed with near- or on-resonant light. In recent years, ONFs have attracted considerable interest in the field of atom optics due to their ability to efficiently couple light and matter, thus having the ability to simultaneously trap, manipulate

and probe neutral atoms [54]. There has also been a proposal on incorporating an ONF into an optical lattice to create small, cold atom samples with control over the final atom number [55].

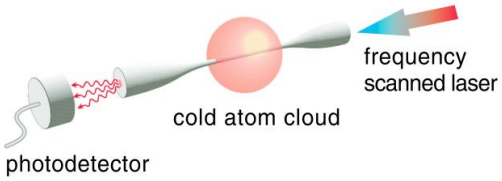
Spontaneous emission from cold, neutral atoms that are sufficiently close to a subwavelength diameter fiber can couple into the guided modes of the fiber [32,56]. Due to multiple surface effects, which are described in Section 2.1, this emission can be strongly enhanced and the resultant fluorescence can be utilized to probe atoms in the vicinity of the ONF surface, as described in Section 2.2. The ONF can also be used as a detection device in a bright probe manner, whereby near- or on-resonant light propagating in the fiber creates an evanescent field, a portion of which is absorbed by the neutral atoms and this is covered in Section 2.3. These cold atom probing techniques are illustrated in Figure 3. To distinguish between the cases of fluorescence detection directly from a laser-cooled sample, as opposed to that where an additional free-space laser is incorporated into the setup, we will use the terms emission fluorescence detection for the former (Figure 3a) and laser-induced fluorescence (LIF) detection for the latter (Figure 3c). The absorption detection method, illustrated in Figure 3b can also be extended to the detection of atoms in a vapor cell, as described in Section 2.4. By taking advantage of the evanescent field properties of the ONF, the combination of far-off-red and blue-detuned evanescent fields can be used to create two-color optical potentials, which can be used to trap and manipulate cold atoms. Variations of such techniques are described in Section 2.5.

Figure 3. Three techniques to detect neutral atoms using ONFs. (**a**) Emission fluorescence detection; (**b**) Absorption detection. Reprinted with permission from [57]. Copyright 2007 American Physical Society; (**c**) Laser induced fluorescence detection. Reprinted with permission from [58]. Copyright 2008 Institute of Physics. Note that in (c) an additional probe laser is used to excite the laser-cooled atoms, compared to the setup in (a).

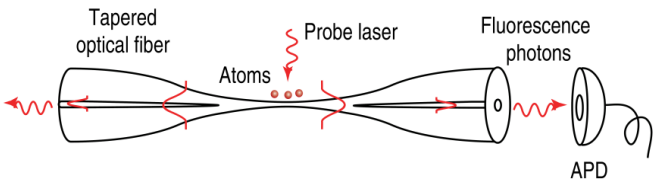
(**a**) Emission fluorescence detection



(**b**) Absorption detection



(**c**) Laser-induced fluorescence detection



2.1. Cold Atom-Surface Interaction

The study of individual neutral atoms in the vicinity of dielectric surfaces has gained renewed interest in recent year [32,58–60]. Regarding ONFs, this is primarily due to their ability to manipulate atoms near their surfaces making them ideal for the development of devices in quantum optics and nanotechnology. In order to develop these technologies it is imperative to have a thorough understanding of how the presence of the ONF dielectric surface affects the behavior of the atom.

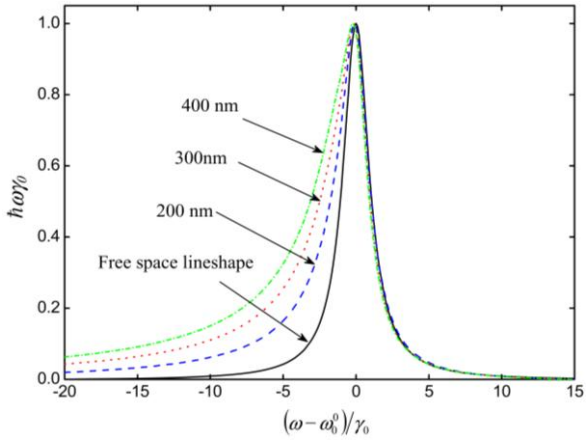
It is well known that the presence of any material body can substantially modify the spontaneous decay rate of an atom [32,61–64]. Spontaneously emitted photons close to the surface of the ONF can be radiated into space or they can be coupled into the guided modes of the ONF [65]. The presence of the ONF itself increases the coupling into the guided modes. The enhancement of the decay rates is largest when the atom is on the fiber surface and the effect reduces as the atoms are positioned further from the ONF surface. The decay rates not only depend on the position of the atom relative to the fiber surface, but also on the fiber size itself. The increase in coupling efficiency becomes significant when the diameter of the ONF is small in comparison with the radiation wavelength [32]. It also slightly varies for different magnetic sublevels. In a realistic system, a coupling efficiency of up to 28% of the spontaneously emitted photons can be achieved for a Cs atom near the surface of an ONF [32]. Such a high efficiency offers a promising technique for single atom detection.

The dominant electromagnetic interactions that take place in this context are the van der Waals [36] and Casimir-Polder forces [35]. The van der Waals force for ONFs can be viewed as an attractive force that pulls atoms towards the surface of the fiber and operates at distances $< \lambda/10$ from the fiber surface, where λ is the wavelength of the radiation. The Casmir-Polder force is also an attractive force, but only becomes significant at distances $> \lambda/10$ from the surface. In the context of cold atoms, these forces have been measured for several surfaces [66,67] and can be exploited to create trapping potentials as discussed in Section 2.5.

The aforementioned atom-surface interactions cause a shift or perturbation in the spectral emission of excited atoms close to the surface of the ONF. Russell *et al.* [35] theoretically studied this effect by modeling the spectral properties of atoms whose spontaneous emission couples to the guided mode of the ONF, with the assumption that only the fundamental mode is excited. Here, the fiber was treated as a planer surface. It was determined that, for typical ONF diameters (200–600 nm), the fluorescence excitation spectrum exhibits a well-pronounced asymmetry with red-side broadening and a red-detuned shifting of the peak position caused by the van der Waals effect. The inclusion of the Casimir–Polder effect has minimal influence on the asymmetry of the line shape, but slightly reduces the red-shift of the peak position. Figure 4 shows the contribution from both the van der Waals and Casimir-Polder effects to the line shape in the presence of an optical nanofiber for three different fiber diameters. In addition, it was determined that the asymmetry becomes more pronounced for atomic ensembles that are tightly confined around the optical nanofiber. Later, Frawley *et al.* [37] considered the effect of the fiber curvature on the van der Waals interaction with an atom.

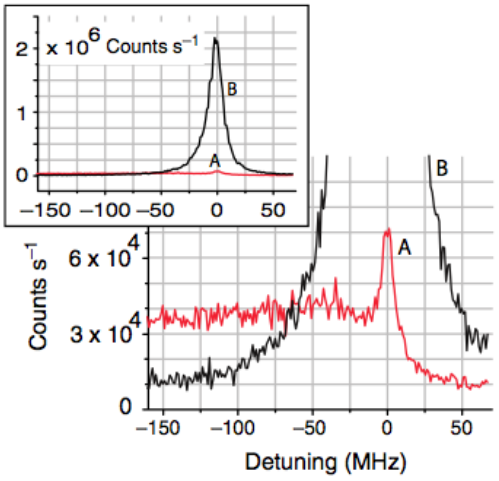
The predicted red-side-broadening effect has been experimentally observed by Sagué *et al.* [57] using absorption detection (see Section 2.3 for more details). Here, the asymmetries in the absorption profile of atoms interacting with the evanescent field of an ONF have been attributed to the van der Waals frequency shift.

Figure 4. Frequency dependence of the fluorescence power from a Cs cloud coupled into an ONF, including contributions from the van der Waals and the Casimir-Polder effects. For this calculation a cloud radius of 400 nm has been used. The nanofiber radius is varied from 200 nm to 400 nm for the different plots. The solid line shows the expected free space line shape as a comparison. Note that all lines are normalized. Reprinted with permission from [35]. Copyright 2009 Institute of Physics.



The red-shifted profile was also observed by Nayak *et al.* in 2008 [58], when Cs atoms were probed by scanning a laser perpendicular to the nanofiber through the closed-cycle transition $6S_{1/2}$ F = 4 ↔ $6P_{3/2}$ F' = 5 (see Figure 3c for a schematic of the LIF detection setup). The LIF spectra were coupled into the guided modes of the fiber and a long red tail was observed, as represented by Trace A in Figure 5. This was initially attributed to the presence of atoms close to the surface and seemed to agree with theoretical predictions [68,69].

Figure 5. Laser induced fluorescence spectra from Cs measured through an optical nanofiber for the closed-cycle transition, 6S $F = 4 \leftrightarrow$ 6P $F = 5$. Traces A and B correspond to without and with the effect of violet laser irradiation, respectively. The violet irradiation was used to remove Cs that had adhered to the surface of the fiber. Reprinted with permission from [58]. Copyright 2008 Institute of Physics.



However, when Nayak *et al*. [70] performed a more systematic investigation of atoms in a surface-bound potential, this effect was found to be due to atoms on the surface itself rather than free, cold atoms. The authors first measured the LIF spectrum of cold atoms and investigated how this evolved over time for changing fiber surface conditions. The line shape of the spectrum changes from Lorentzian for free, cold atoms and, over time, the spectrum broadens to a large red tail line shape. This implies that, as time progresses, more and more atoms form bound-states with the fiber and induce a spectral line broadening effect. The narrow peak near the atomic resonance is due to the contribution from free atoms with the broad spectrum in the red-detuned side due to the bound atoms. The effect plays a crucial role in determining the surface conditions and leads to a reduction in the amount of laser induced fluorescence that is coupled to the guided modes of the fiber. In fact, it is suggested that the main source of the red tail is produced by room temperature atoms falling into the surface potential rather than the cold atoms themselves. Thus, the background density determines the speed at which atoms fall into the surface potential. The atoms can be removed from the bound potential with the aid of a violet laser and this can be used to control the surface conditions. In this manner the observed spectrum returns to its original state and the expected Lorentzian-shaped excitation spectrum is once again achieved. This provides a method by which the effect of surface conditions can be reduced or even eliminated.

2.2. Fluorescence Detection of Cold Atoms

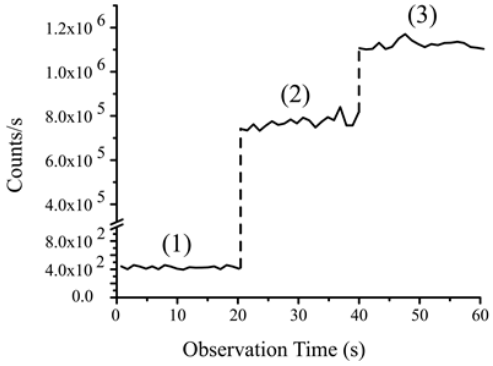
The detection and quantitative analysis of cold atomic ensembles are essential analytical tools required in the development of quantum technologies. The simplest method for cold atom detection is fluorescence imaging, where the atoms are irradiated with resonant laser light and the resultant fluorescence from the atoms is focused on either a CCD camera or a photodiode. Using a combination of these devices, parameters such as size, number of atoms, and atom density profile can be easily determined with sufficient accuracy for most experiments. Dynamic properties of the experimental setup, such as loading rate, lifetime, and decay rate can also be determined.

For normal operational parameters of a magneto-optical trap (MOT), atoms in the cloud absorb light from the cooling laser beams exciting the atoms to a higher state. For atoms that are close to the surface of the ONF, a portion of the resultant spontaneous emission as the atoms decay back to the lower level can couple directly into the guided modes of the fiber waist [2,71]. With the aid of a single photon counter module (SPCM) attached to the end of the fiber, fiber-guided photons can be detected and the specific attributes of the cold atom system can be determined. The high coupling efficiency of fluorescence photons to the guided modes enables fluorescence measurements from a very small number of atoms. This is done while the atoms are continuously trapped in the MOT and thus a continuous real-time measurement is obtainable. This fluorescence detection scheme for cold atoms is illustrated in Figure 3a.

The detection technique was first implemented by Nayak *et al.* [38] whereby the coupling of the fluorescence from Cs atoms into the ONF was observed simply by monitoring the signal on the SPCM as the laser beams and magnetic field are sequentially switched (see Figure 6). An increase in photon count rate was observed when the MOT laser beams and the magnetic-field were switched on due to the spontaneous emissions from the cloud of Cs atoms coupling to the guided modes. From

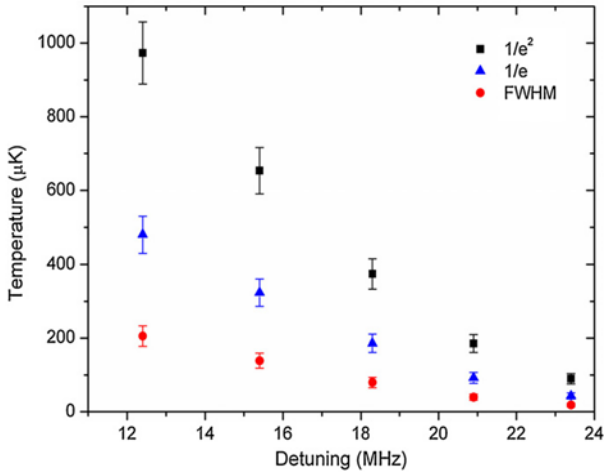
experimental parameters of the setup, it was determined that the effective number of atoms contributing to the signal at any given time was five. This accurately agreed with the photon count amplitude observed due to the presence of cold atoms around the fiber, indicating the potential of such devices for detection of a low number of atoms. Again, using this technique, the density profile, size and shape of the atomic cloud was determined by magnetically translating the cold atom cloud across the waist of the ONF and measuring the photon count rate as a function of cloud position. All the fiber fluorescence imaging results were compared to those achieved using standard fluorescence imaging techniques with photodiodes and CCD cameras and were found to be in good agreement.

Figure 6. Photon count rate through an optical nanofiber (diameter 400 nm) in a Cs MOT setup. (1) MOT laser beams and magnetic fields are off; (2) MOT laser beams are on, magnetic fields are off; (3) MOT laser beans and magnetic fields are on. Reprinted with permission from [38]. Copyright 2007 Optical Society of America.



This emission fluorescence detection method was adopted by Morrissey *et al.* [72] where the technique was used to determine the dynamic loading rates and life-times of ^{85}Rb in a MOT, with a fiber of diameter 600 nm. This was done by monitoring the coupled photons as a function of time as the MOT loaded from the background vapor and the photon signal decayed due to internal atom collisions when the atom source was switched off. The results were compared to those taken simultaneously using standard MOT measurement techniques and were found to be in good agreement. Using this same fiber fluorescence detection technique Russell *et al.* [3,73] measured ^{85}Rb temperatures above and below the Doppler limit of 144 μK using two different methods, one being that of forced oscillations [3] and the other being that of release-recapture [73]. Observed temperature variation corresponds with the limits of normal MOT behavior. Again, good agreement was found between temperature measurements made using the optical nanofiber and conventional fluorescence imaging methods with a photodiode. Figure 7 shows a plot of temperature obtained for a cloud of ^{85}Rb using the forced-oscillation technique [3] for an optical nanofiber with a diameter of 700 nm. Since the definition of cloud radius is required to determine the temperature using this technique, all three definitions commonly used in the literature ($1/e^2$, $1/e$ and FWHM) were tested in order to determine the viability of achieving sub-Doppler temperatures (<144 μK) in the presence of the "hot" nanofiber. This was achieved when the cooling beams were significantly detuned from resonance.

Figure 7. Atom cloud temperature as a function of detuning of the cooling laser beams for three standard definitions of cloud radius. The measurements were made using the forced oscillation technique and indicate that sub-Doppler temperatures <144 μK can be achieved in the presence of an ONF. Reprinted with permission from [3]. Copyright 2012 Institute of Physics.



Nayak *et al.* [38] developed an alternative technique to measure the fluorescence of cold atoms with the aid of an ONF, which we've termed laser induced fluorescence detection to distinguish from the fluorescence methods already described. Once the cold atoms are prepared in the MOT, the trapping beams are switched off and, for a short period of time, the cold atoms are excited by a free-space, resonant probe beam. During this excitation period the atoms absorb from the probe beam resulting in the spontaneous emission of photons, some of which couple to the guided modes of the fiber and are counted by an avalanche photodiode (APD). The probe beam is then switched off and the MOT beams are switched on allowing the atomic cloud to reload from the background. This experimental setup is illustrated in Figure 3c. The observation is accumulated over many cycles. In this excitation fluorescence experiment the estimated atom number in the observation region is reduced by a factor of 70 when compared to direct emission fluorescence detection. This is due to the expansion of the atom cloud while the cooling beams are off during the excitation period. However, this method has the advantage of being insensitive to scattering from the irradiating light.

Using this technique, Nayak *et al.* [58] were able to measure the LIF spectrum and detected surface effects which have already been referred to in Section 2.1 [38,70]. This method can be extended to the detection of single atoms around the ONF [58]. In this case, the atom number is dramatically reduced by varying experimental parameters of the MOT. The excitation fluorescence that couples into the guided modes is split at the fiber output using a 50/50 nonpolarizing beam splitter and detected using two separate SPCMs. The photon correlation between the two channels is measured by performing a Hanbury-Brown and Twiss experiment. The photon coincidences clearly display anti-bunching effects, confirming the detection of single atoms using the ONF. Under these conditions the LIF spectrum was measured to further understand the atom behavior. For a low intensity of the probe beam the spectrum exhibits almost a Lorentzian shape, but is slightly asymmetric with a small red tail with no power broadening observed. This indicates that the spectrum is induced by free atoms in the vicinity of the ONF. However, there exists a small dip at the central peak. This dip is more pronounced for larger

probe intensities and an additional broadening effect is observed. This dip was attributed to the mechanical effect due to scattering from the probe beam. It is worth noting that single atom behavior was only observed for clean fibers (after irradiation using a violet laser)—a further indication of the crucial role of surface interactions in such experiments.

2.3. Absorption Detection of Cold Atoms

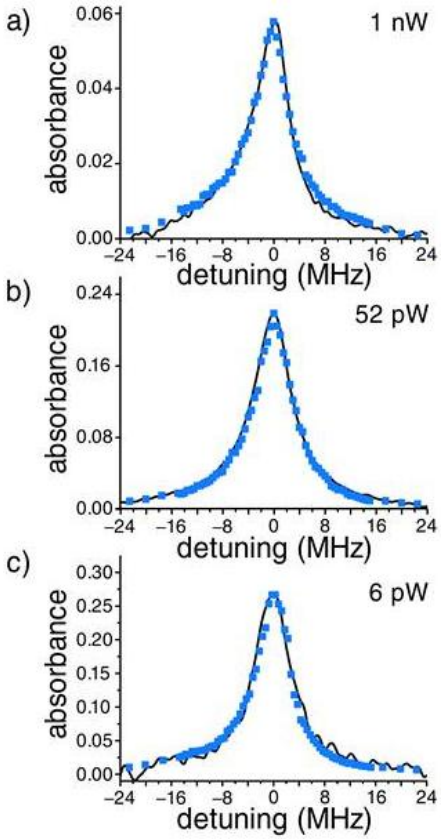
Absorption imaging is a standard detection technique in cold atom physics whereby properties of the cold atom ensemble can be determined by measuring the absorption of a resonant light field. The strong evanescent field surrounding the waist of a sub-wavelength tapered fiber allows light-matter interactions with media surrounding the fiber, therefore facilitating in-fiber spectroscopy on the cold atom ensemble which surrounds the ONF. Given that the evanescent field decays exponentially from the surface, typically within a distance of $\lambda/2\pi$, this method can also be used to investigate surface interactions.

Work published in 2006 by Kien *et al.* [74] highlights the need for knowledge regarding the optical response of an atom in a resonant field which propagates along the surface of a fiber. The authors demonstrate that, for low field intensity of the evanescent field, when the atom is in close vicinity to the fiber surface, the scattered power can be up to 60% of the propagating power. When the fiber diameter is comparable to the wavelength of propagation, the light is mainly scattered into free-space, while scattering into the guided modes is weak. In the case of high propagation powers, a further increase in the propagation power will lead to a dramatic decrease in the scattering efficiency due to the saturation effect. This is a positive outcome as, even with small input powers, circulation intensities of the probe beam at the ONF waist are very high, as discussed in Section 1.2. This implies that a wide range of nonlinear effects are obtainable with minimal probe powers.

The first experimental demonstration of in-fiber spectroscopy of a cold atomic sample was published in 2007 by Sagué *et al.* [57]. Atoms are first captured and cooled in a standard MOT while the probe laser is switched off. The MOT cooling and repump laser beams, as well as the magnetic field, are switched off and the probe laser is switched on. During this time period the probe beam frequency is scanned around the atomic cooling transition, allowing the atoms to absorb the light propagating in the evanescent field, and the signal is measured on an APD. This measurement technique is illustrated in Figure 3b. A series of absorption spectra are shown in Figure 8 for three evanescent field intensities. The presence of a mode propagating through the fiber increases spontaneous emission by approximately 57% at the surface—an effect that had not been observed before to such an extent without a cavity. For probe powers larger than 100 pW, the line shapes are narrower than expected. This is explained by the effect of the light-induced dipole forces on the density of the atomic cloud. For distances smaller than 370 nm, *i.e.*, in the region that contains more than 75% of the evanescent field power, the largest integrated density of the atomic cloud is predicted in the case of zero detuning. For blue (+3 MHz) and red (−3 MHz) detunings, this integrated density is lowered due to the effect of the light-induced dipole forces. This results in reduced absorbance and leads to an effective line narrowing. The measured linewidths approach 6.2 MHz for vanishing powers. This result exceeds the natural Cs D_2 linewidth in free space by almost 20%. This broadening can be explained by surface interactions detailed in Section 2.1, *i.e.*, the van der Waals shift of the Cs

D_2 line and the modification of the spontaneous emission rate of the atoms near the fiber. Both effects have the same magnitude and only their combination yields the very good agreement between the theoretical model and the experimental data. Other surface effects, such as the red-detuned-shifting of the center of the absorption profile, could not be measured due to the drift of the probe laser frequency. The authors conclude by highlighting that the subwavelength diameter fiber can be used to detect, spectroscopically investigate, and mechanically manipulate extremely small samples of cold atoms. On resonance, as little as two atoms, on average, coupled to the evanescent field surrounding the fiber and absorbed 20% of the total power transmitted through the fiber.

Figure 8. Line shapes obtained from an evanescent field around a nanofiber embedded in a laser-cooled sample of Cs. The measured linewidths approach the natural linewidth (6.2 MHz) for vanishing probe powers. Reprinted with permission from [57]. Copyright 2007 American Physical Society.



Due to the strong interaction between a few atoms and a relatively high intensity evanescent field, single and few atoms in the evanescent region can behave as an optically dense system. This is the subject of the work by Hakuta *et al.* [75]. They explore the atom-field interaction around a nanofiber using laser-cooled, Cs atoms and find that the atom/nanofiber interaction may open a new technique to trap single atoms without any external field. By using this trapping technique, they experimentally investigate small numbers of atoms by observing the fluorescence excitation spectrum.

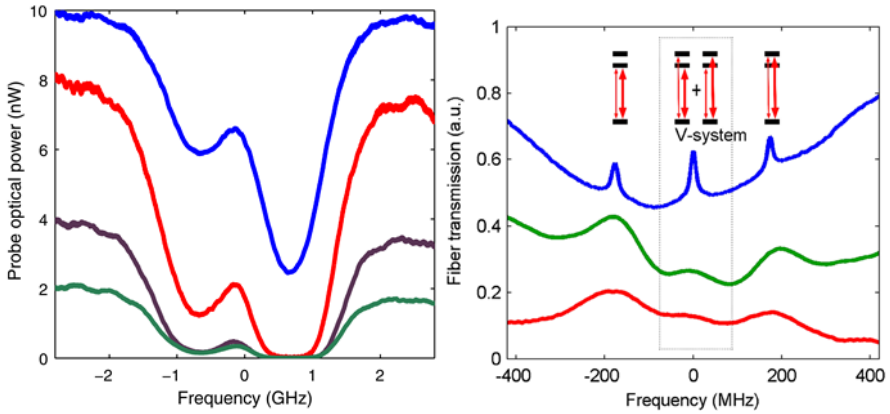
Work published in 2008 by Nayak *et al.* [58] highlighted that, since an appreciable amount of propagating radiation is distributed in the evanescent region, single atoms in this region work as a good nonlinear medium due to their optical density. The photo-absorption spectrum is measured for a

small number of atoms, revealing the possibility of realizing an optically dense system using hundreds of atoms. For example, photo-absorption through the nanofiber reaches about 50% when one atom sits on the surface; if several atoms are prepared on the nanofiber surface, the system may become optically opaque. It should be noted that, when the atom is positioned away from the surface, the absorption becomes smaller, obviously, and one may need more atoms to realize an optically dense medium.

2.4. Absorption Detection of Vapor Gas

The concept of in-fiber spectroscopy for cold atoms can be easily extended to include atoms in a vapor. Due to the finite interaction time between the particle and the field compared to that for trapped atoms, transit-time broadening of the line shapes in spectroscopic measurements is observed [39,76]. A hot atom passes through the evanescent field in under 1 nanosecond, compared to a cold atom which has a transit time on the order of microseconds. A very insightful and early discussion on the effects of atom-light beam interaction time (*i.e.*, transit time) in spectroscopy is contained in [76]. In 2008, Spillane *et al.* [77] discussed the observation of nonlinear interactions of a Rb vapor with an ONF-generated evanescent field using very low levels of input light. In fact, they were able to saturate the vapor using an input power level of 8 nW as shown in Figure 9(left) and observed electromagnetically induced transparency (EIT), plotted in Figure 9(right).

Figure 9. (**Left**) Transmission spectrum for a nanofiber in a vapor cell for increasing probe powers (2, 4, 8, and 10 nW) for the Rb D_2 transition; (**Right**) Saturated absorption spectrum with cross-polarized pump and probe beams for a Rb vapor cell (upper, blue) and a Rb nanofiber system (middle, green and lower, red) for the D_1 manifold of ^{85}Rb. The two side peaks correspond to the Doppler-free F = 3 → F' = 2 and F = 3 → F' = 3 hyperfine transitions. The center peak represents a V-system EIT signal. Reprinted with permission from [77]. Copyright 2008 American Physical Society.

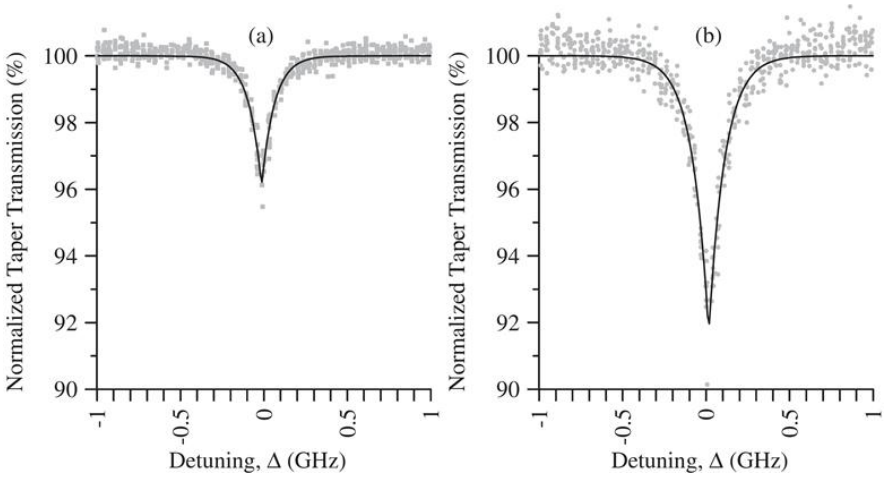


In 2009, Hendrickson *et al.* [78] observed transmission through a tapered fiber which was a nonlinear function of the incident power. This effect can also allow a strong control beam to change the transmission of a weak probe beam. This, once again, indicates that the ONF-atom interface can be used for nonlinear effects, such as EIT, slow light *etc.* For example, in 2010, Hendrickson *et al.* [79] published work about their observation of two-photon absorption in the ONF-vapor system using input

light at levels below 150 nW. The transit-time broadening resulting from the fast atoms passing the nanoscale waveguide produces two-photon absorption spectra with sharp peaks that are very different from conventional line shapes (see Figure 10). Russell *et al.* [80] have since proposed using the ONF in a cloud of cold atoms for the demonstration of 1- and 2-photon absorption.

One issue associated with the use of the ONF in a vapor system is the degradation that the fiber transmission undergoes almost as soon as the vapor is introduced. This is a result of atoms adsorbing onto the fiber surface and has an impact on the lifetime of the fiber for experimental measurements. Recently [81], a systematic study has been conducted on the degradation effects, and methods of preserving the transmission by the incorporation of a microheater near the ONF have been demonstrated. This improves the future prospects of the ONF as a tool for technological advances in atom-based studies.

Figure 10. Resonant two-photon absorption in an ONF vapor system for Rb. The percent transmission of the 776 nm signal through the nanofiber is plotted as a function of its detuning from the upper atomic state. (**a**) 780 nm power level of 146 nW. (**b**) 780 nm power level of 726 nW. Reprinted with permission from [79]. Copyright 2010 American Physical Society.



2.5. Trapping of Neutral Atoms with ONFs

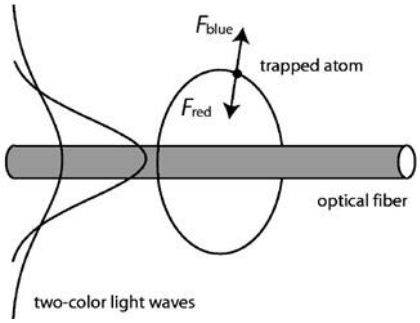
As mentioned previously, the extension of the evanescent field from the ONF surface is very small and, thus, creates a high radial intensity gradient. This leads to a large gradient force on the atoms around the ONF in the transverse direction which can be utilized to create a dipole trapping potential. For red-detuned light, the optical force becomes attractive and blue-detuned light creates a repulsive force. By combining these forces along with the van der Waal's force, a dipole trapping potential for atoms around the ONF can be created. To date, several trapping schemes and configurations have been developed to trap, guide, and probe neutral atoms using ONFs, making it a powerful tool in this research area.

The first proposal regarding the trapping of neutral atoms around an ONF was written by Balykin *et al.* [82] and used a single frequency of light passing through the fiber. In this paper it was proposed to use a red-detuned evanescent field propagating through a subwavelength diameter ONF to

create an optical potential attracting atoms towards the surface. For ONFs with a diameter two times smaller than the wavelength of propagating light, this attractive force can be counter-balanced by the centrifugal force of atoms moving in a circular motion around the TOF, thereby trapping the atoms close to the fiber surface.

Shortly after this theoretical publication, Le Kien *et al.* [83] proposed that neutral atoms can be trapped close to the surface of the ONF using two-color evanescent light fields. A simple schematic of the setup is shown in Figure 11. This proposed technique utilized a red-detuned light field, as well as the van der Waals force, to attract atoms towards the nanofiber, while a blue-detuned light field repels the atoms from the fiber. Due to the fact that the decay length of the evanescent field is wavelength dependent, by choosing the respective powers of the red- and blue- detuned beams a radial potential close to the nanofiber surface is created. If one or both fields are linearly polarized, two local minima are formed azimuthally around the fiber. This configuration allows atoms to be confined in two lines parallel to the fiber axis. If the input light fields are circularly polarized, a ring shaped potential is formed around the fiber resulting in atoms being confined to a cylindrical shell around the fiber.

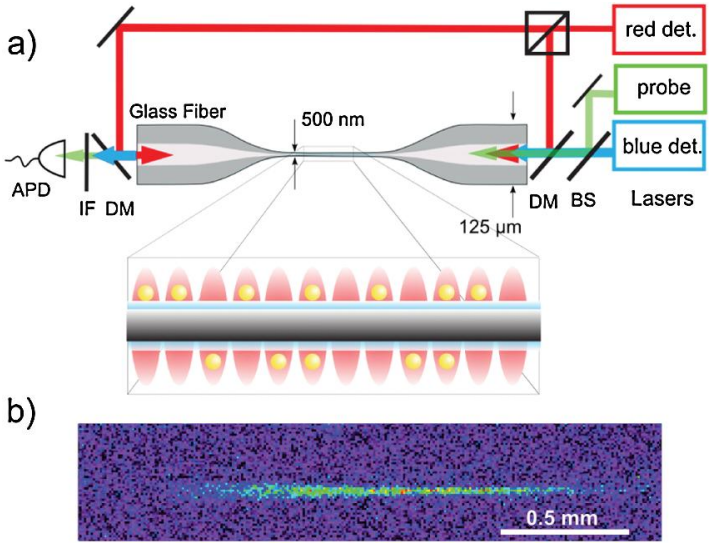
Figure 11. Schematic representation of atom trapping and guiding around an optical nanofiber using two-color evanescent light fields. Reprinted with permission from [83]. Copyright 2004 American Physical Society.



In 2010, Vetsch *et al.* [1] experimentally realized the two-color evanescent field setup to create a one dimensional optical lattice to trap Cs atoms around an ONF, work that was advanced by Dawkins *et al.* [84]. Two far-red-detuned lasers were counter-propagated through the ONF, producing an evanescent standing wave which creates an attractive force towards the fiber surface. This attractive force is balance by a single far-blue-detuned laser field. By choosing the correct power ratio between the red- and blue-detuned light fields, a minimum potential is achieved at a distance of a few 100 nm from the surface of the fiber, yielding trapping frequencies of 200, 313, 400 kHz in the radial, axial, and azimuthal directions, respectively. The atoms are confined in trapping sites along the axis of the fiber by the standing wave and radially confined by the potential created by the red-and blue-detuned laser fields. All the laser fields were linearly polarized, thereby confining the atoms azimuthally. This experimental setup is depicted in Figure 12a, which includes an illustration of the lattice. Figure 12b shows a fluorescence image of the trapped atoms. The atoms were confined in a one dimensional optical lattice approximately 200 nm from the surface of the ONF, with each lattice site separated by 500 nm. The average occupancy was 0.5, limiting the trap to about 2,000 atoms per millimeter. When spectral properties of the atoms were investigated it was found that their linewidth was slightly larger than the atomic linewidth and this was apportioned to atom-surface interactions. This trapping

technique can be easily adapted to create other configurations. Schneeweiss *et al.* [85] manually tuned the relative phase between the counter-propagating beams of the standing waves with the aid of acousto-optic modulators to demonstrate the optical transport of cold atoms along the nanofiber. Reitz *et al.* [86] proposed a double helix potential for the cold atoms using the same beam configuration as in [1], only with circularly polarized beams. The helical confinement arises from the beam intensity variations in the azimuthal direction [87]. Such a configuration would be extremely difficult to achieve using free space optics.

Figure 12. (**a**) Experimental setup of the ONF two-color atom trap. The blue-detuned running wave in combination with the red-detuned standing wave creates a trapping potential. A resonant laser is used for probing the atoms via the evanescent field. (**b**) Fluorescence image of the trapped atoms. Reprinted with permission from [1]. Copyright 2010 American Physical Society.



In 2012 Goban *et al.* [4] realized a two-color optical trap, which utilizes a so-called 'magic compensation' that traps the $6S_{1/2}$ ground and $6P_{3/2}$ excited states of Cs. Similar to traps mentioned above, this configuration is created by two counter-propagating beams, which are red-detuned to the magic wavelength, λ_{red} = 937 nm, creating a standing wave along the length of the ONF. This attractive force is balance by a second pair of counter-propagating beams blue-detuned to the magic wavelength, λ_{blue} = 686 nm. Both beams are co-linearly polarized, resulting in a three-dimensional, state-insensitive, optical trap with approximately 224 atoms at a distance of 215 nm from the fiber surface. The power required for the red- and blue-detuned beams are 0.4 and 5 mW respectively, creating trapping frequencies of 199, 273, and 35 kHz in the radial, axial, and azimuthal axes, respectively. The trapped atoms were analyzed using the absorption techniques mentioned in Section 2.3 where a probe beam propagates through the fiber, interacts with the trapped atoms in the ONF section of the fiber, and is measured at the other end by an APD. Due to the operation of the magic wavelength compensated trap, no appreciable shift in the transition frequency (0 ± 0.5 MHz) or broadening of the linewidth (0.5 ± 0.1 MHz) was observed. This is in contrast to the noncompensated trap [1], where a considerable shift in the transition frequency (13 MHz) and broadening of the linewidth (14.8 MHz broader than the natural linewidth) were observed.

As an alternative to single or two-color trapping, Saguéet *al.* [25] proposed alternative techniques to trap atoms based on two-mode interference of a blue-detuned evanescent field of an ONF. The advantage of higher order mode interference for atom trapping around the fiber is that a higher level of control on the trapping sites can be achieved compared with one or two-color trapping. However, technical challenges associated with transmitting a higher order mode through the fiber with high survival rates still remain and solutions involving choice of core-to-cladding ratio of the pretapered fiber and nonexponential profile of the nanofiber are being pursued by several research groups [26,27,88]. The difference in phase velocities of two modes simultaneously copropagating through the fiber allows for the creation of a stationary evanescent interference pattern along the length of the fiber at a specific distance from the surface. Controlling the power distribution between the modes enables the modification of the evanescent field of each mode. This allows the creation of field minima where the two fields cancel due to destructive interference. The atoms are thus radially trapped due to the varying decay length of the modes, axially trapped due to the different phase velocities of the modes, and azimuthally trapped due to the polarization matching of the modes. Combining (for example) the HE_{11} and TE_{01} modes, or the HE_{11} and HE_{21} modes, results in two periodic arrays of traps on either side of the fiber in the axial direction. The site separation in the axial direction is determined by the beat length of the modes and the radial modes are axially offset from each other by an amount inversely proportional to the beat length. The HE_{21} and TE_{01} mode combination creates four axial arrays of traps, which are elongated due to the larger difference in the beat lengths. According to theory, the atoms are trapped about 100–200 nm from the surface of the ONF. The parameters of the trap are such as to achieve trap depths of 1 mK, a trap lifetime of 100 s, with an initial kinetic energy corresponding to 100 μK. Depending on the mode combination the traps can be set up using powers of 25–50 mW.

3. Molecules and Other Particles

Considering the aforementioned successes in using optical nanofibers for atom sensing, it is not surprising that they have also been used in experiments with molecules and other particles. This section gives a description of such advances, beginning with the use of nanofibers to examine spectroscopic properties of surface adsorbed particles. This offers a novel method for probing molecular photo-response, spectroscopic changes due to molecule-surface interactions, the dynamics of surface agglomeration, and thin-film formation. The section then develops to encompass advances in controlled microparticle, quantum dot, and nanodiamond deposition onto nanofiber surfaces. Such particles can then be site-addressed to obtain a myriad of spectroscopic and behavioral data through the fiber. Furthermore, quantum dot and (in particular) nanodiamond coupling to nanofibers have promising applications in the creation of fiber output single photon sources.

3.1. Molecular Spectroscopy

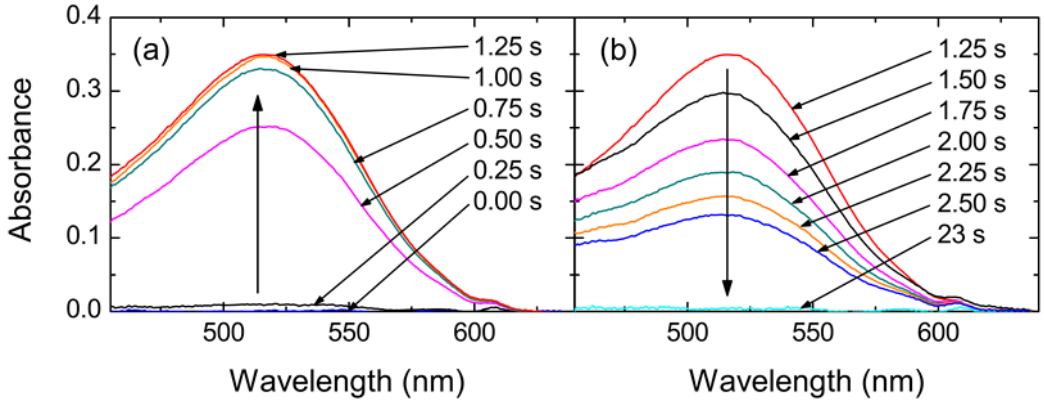
Nanofiber-based surface absorption spectroscopy of molecules was first examined by Warken *et al.* [89], who showed that the sensitivity of such a system is orders of magnitude higher than previous free-space techniques. Due to the their spectral sensitivity to molecular surface arrangement, 3,4,9,10-perylenetetracarboxylic dianhydride molecules (PTCDA) were selected for experiment. These

crystals were heated below a nanofiber, and sublimated molecules were adsorbed onto its surface. Absorption spectra were obtained through the fiber for various deposition times (0.5 to 2.3×10^7 molecules), showing clear vibronic progression. Additionally, molecular condensation and agglomeration over time resulted in transmissional line shifts, allowing the authors to investigate the post-deposition film evolution on the nanofiber surface. The noted molecular agglomeration subsequently received further study [90], where the dynamics of the system under ambient and ultrahigh vacuum (UHV) conditions were compared, and significant reduction of molecular mobility in UHV was observed.

A similar deposition method was later used to excite and detect PTCDA fluorescence spectra through a nanofiber [91]. Interestingly, the absolute peak positions were shifted relative to those obtained from solution spectra. The authors associate this with the interaction of the molecules with the fiber surface, and also highlight the non-negligible contribution of self-absorption of fluorescence photons to recorded spectra. This should be minimized, or compensated for, to retrieve the expected mirror symmetry between absorption and fluorescence spectra. Nonlinear experiments have also been conducted with nanofibers, demonstrating two-photon excited fluorescence measurements of adsorbed Rhodamine 6G (Rh6G) molecules. For this experiment, a solvent-dripping technique was developed to extend the applications of surface adsorption spectroscopy to a larger variety of molecules [90]. The aforementioned surface adsorption techniques are highly applicable for modeling systems of organic thin-film growth and—as they are entirely fiber-based—may be used for remote spectroscopic studies. Crucially, they facilitate recording of both absorption and fluorescence spectra for a given molecular surface coverage, and pave the way for nanofiber self-absorption free fluorescence spectroscopy on individual surface-adsorbed molecules.

Optical nanofibers have also been used in saturation absorption spectroscopy studies of acetylene ($^{12}C_2H_2$) molecules in a chamber at 200 Pa pressure [92]. Passing an infrared (IR) pump beam through the nanofiber and retroreflecting it as a probe beam, the spectra of the P9 transition were obtained with a narrow saturated signal. The dependence of the saturation parameter on nanofiber diameter was also calculated and optimized. Due to the fact that lowering the gas pressure can reduce the pressure broadened width, longer ONF lengths are desirable for such studies. Wiedemann *et al.* [93] recently presented a novel application for nanofibers where organic photochromic molecules show a reversible light-induced change of their absorption spectra and are thus ideal candidates for optical switching studies using nanofibers. Low concentrations of SpiroOH molecules which photoswitch between transparent and colored when exposed to UV and white light were drip-coated onto the nanofibers State-switching was then induced by simultaneously coupling light from a UV LED through the fiber. Absorbance spectra confirmed the switching mechanism; this effect can be seen as a time progression in Figure 13a,b. Photobeaching, photodestruction, and cyclability of the molecules were also investigated using the optical nanofibre and the authors indicate that switching speeds (0.025–1 Hz) could be increased by orders of magnitude by propagating tailored laser pulses through the fiber.

Figure 13. Absorbance spectra of spiroOH on a nanofiber, with white light and additional UV-light exposure. All molecules are initially in the transparent state; (**a**) UV illumination increases the absorbance up to a stable point in the photostationary state; (**b**) The absorbance decreases after the UV exposure has stopped. Reprinted with permission from [93]. Copyright 2012 Optical Society of America.



As with neutral atoms, bringing single particles into contact with the evanescent field of a nanofiber has obvious potential for both sensing and spectroscopic studies. Such a technique was demonstrated by Gregor *et al.* [94], who introduced individual charged particles to the surface of a nanofiber via a segmented linear Paul trap. The individual fluorescent dye-doped polystyrene beads were excited with the aid of a microscope objective and preselected before being brought to the fiber surface with a success probability close to 100%. The authors compared the fluorescence spectra achieved using the microscope objective to that obtained through the fiber and calculated a seven-fold overall increase in detected fluorescence using the nanofiber. They also used FDTD simulations to relate the dip observed in fiber transmission following particle introduction to the system to the number of particles in an incident cluster. This noncontact electrospray injection method can facilitate the study of any type of charged particle which can be brought into suspension.

3.2. Quantum Dots and Nanodiamonds

Optical nanofibers were first used for single quantum dot photoluminescence spectroscopy by Srinivasan *et al.* [95]. A single layer of InAs quantum dots (QD) was embedded in an $In_{0.15}Ga_{0.85}As$ quantum well, grown at the center of a GaAs waveguide. To increase accessibility to the QDs and reduce the overall QD number, microdisk cavities of diameter d = 2 μm were fabricated from the material and cryogenically cooled to 14 K. The authors compared the QD emission spectra obtained from objective lens pumping to those obtained by pumping and collecting via nanofiber coupling to the disk. This showed a 25 fold increase in the collected power through the fiber, without coupling to whispering gallery modes in the disk. Spatial mapping and single QD photon collection was demonstrated by scanning the nanofiber over the surface of the disk. Focusing on photon collection efficiency, Davanco *et al.* [96] subsequently modeled optical nanofiber coupling to single emitters embedded in thin dielectric membranes. FDTD simulations were run for the fiber and membrane as a composite system with associated supermodes, and the modified spontaneous emission rate of an embedded quantum dot was modeled as a two-level atom. The fiber collection efficiencies calculated

for both vertically and horizontally oriented dipoles amount to up to 30%, which exceed those obtainable with a high NA objective by an order of magnitude. To further increase the efficiency of such a system, they modeled the optical nanofiber coupling to a quantum dot embedded in a suspended semiconductor channel waveguide [97], predicting that up to 70% of the dipole's emission can be collected by the nanofiber in this system. The authors subsequently theoretically investigated nanofiber coupling to individual emitters bound to the surface of thin dielectric membranes via polymer, sol-gel, or crystalline hosts [98], again yielding high collection efficiencies.

Simplifying the aforementioned systems to quantum dots attached directly to nanofibers, Garcia-Fernandez *et al.* [90] dripped CdSe QDs dissolved in heptane onto a nanofiber waist. Adsorbed dots were calculated to number 3×10^5, and absorption and fluorescence spectra were recorded through the fiber. In a similar theme to above, an observed shift in the fluorescence maximum was attributed to surface interactions with the nanofiber. Yalla *et al.* [99] subsequently progressed this line of inquiry to observe fluorescence and emission properties of single quantum dots. To achieve this, they deposited CdSeTe (ZnS) QDs at 20 μm intervals along a nanofiber using a sub-picoliter needle dispenser, with a positioning accuracy of 5 μm. Deposition sites were individually excited using an inverted microscope, as illustrated in Figure 14(left). Photon correlations were measured from one fiber pigtail, clearly showing anti-bunching behavior, and QD blinking was also observed. Single-step and double-step blinking corresponded to one and two QDs on site, respectively, where the probability of depositing a single QD using this method was estimated at 60% and fluorescence photon coupling rates into fiber guided modes were calculated. The saturation behavior of the QDs relative to excitation intensity was also addressed (see Figure 14(right)). The channeling of fluorescence photons into the nanofiber modes was studied, highlighting that the total channeled efficiency should take into account the efficiency of the QD itself [100]. To accurately measure this, the authors simultaneously recorded the photon count rates through both the guided and radiation modes of a nanofiber. QD sites were individually excited through an objective lens and the guided fluorescent photons were detected through the fiber pigtails. To factor in radiation mode guidance, fluorescent photons were also collected by the objective. Photon emission rates into both guided and radiation modes were calculated by analyzing photon-count rate histograms. By factoring in the light transmission parameters for both mode paths, the maximum channeling efficiency of $(22.0 \pm 4.8)\%$ agreed with the theoretical predictions [32,64]. It is expected that a photon channeling efficiency of higher than 90% could theoretically be obtained by incorporating a cavity structure on a nanofiber [99].

Other work related to photon coupling from nanoemitters into optical nanofibers is contained in Fujiwara *et al.* [101]. Here, the authors coupled $(7.4 \pm 1.2\%)$ of the photons emitted from single CdSe/ZnS quantum dots into an ONF of diameter 300 nm. A schematic of the experimental setup is given in Figure 15(left). The authors were able to obtain scanning images of the QD on the fiber down to single quantum dot resolution and made second order photon correlation measurements. Clear anti-bunching was observed with a $g^{(2)}(0)$ value of 0.96 obtained. Their results are presented in Figure 15(right), including the dependence of the photon counts on the excitation laser intensity.

Figure 14. (**Left**) Fluorescence counts depicted through a nanofiber as each QD deposition site is individually excited through a microscope objective; (**Right**) Observed fluorescence count-rate for increasing intensities at positions 3, 4, 5 and 7 in (a), showing QD saturation. Reprinted with permission from [99]. Copyright 2012 Optical Society of America.

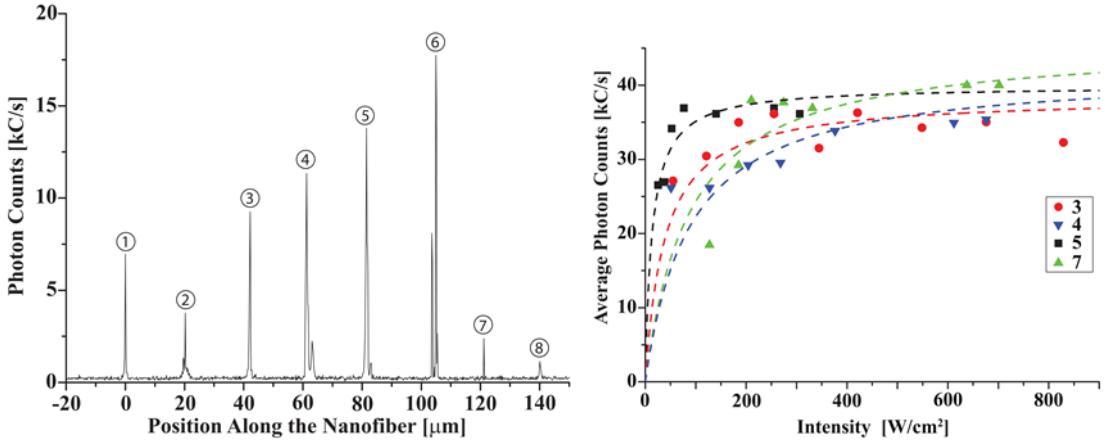
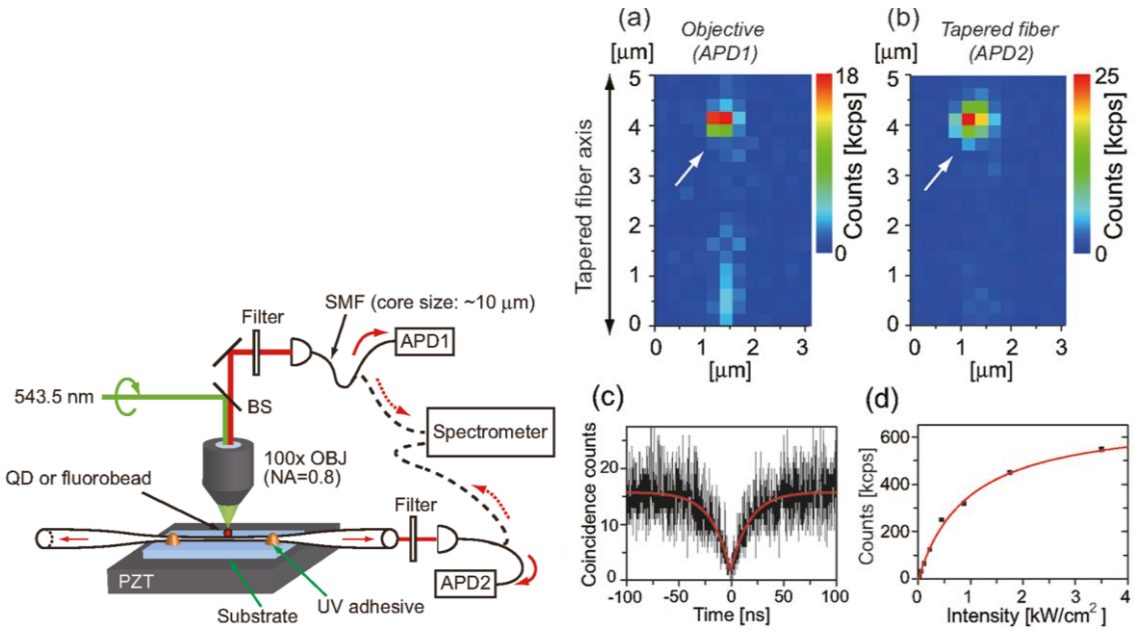


Figure 15. (**Left**) Schematic illustration of the setup. Note that the detection method was changed from APDs to a spectrometer, depending on the experiment. (**Right**) Scanning images of quantum dots on the ONF using (**a**) an objective and (**b**) an ONF. The quantum dot is next to the white arrow. (**c**) Second order photon correlation measurements. (**d**) Photon count from the quantum dot as a function of excitation laser intensity. Reprinted with permission from [101] . Copyright 2011 American Chemical Society.



As QDs typically suffer from blinking and photobleaching, their potential as stable single photon sources is questionable. Nanodiamonds with nitrogen-vacancy-centers which are free from these difficulties have been deposited onto optical nanofibers by a dip-coating and translation technique. This scheme facilitates real-time estimation of the attached diamond numbers through fiber transmission monitoring [102]. Individual diamonds were illuminated through a microscope objective.

Red-shifted fluorescence spectra of these nanodiamonds were obtained through the fiber, and auto- and cross-correlation measurements showed anti-bunching of photons, again indicating that the light came from a single photon emitter. Combining nanofibers with unblinking color centers, such as nanodiamonds, could lead to fiber-coupled, on-demand single photon generation [103,104]. The techniques described above also offer exciting possibilities for nanofiber detection and spectroscopy of biomolecules [105].

4. Alternative Techniques

The development of optical cavities has been of great interest in research for many years due to the significant enhancement effects and detection sensitivity offered by these devices [106]. With improved fabrication techniques various types of optical microcavities have been investigated [107–112]. Such microcavities have proven to be a productive platform for experiments with such effects as strong coupling [113] and the Purcell effect [114] being demonstrated. For detection purposes, microcavities are extremely sensitive devices, arising from the low optical mode volume and long interaction times available due to the high-Q factors [106,115], thereby enabling the detection of single atoms [113] and single molecules [116].

Typically, for optical microcavities, the trend has been to use optical nanofibers to achieve coupling of light into and out of the cavity modes [113,117–121]. Due to the advantages offered by cavities for detection, a movement from these two components to a simpler system where the cavity is directly incorporated within the tapered optical fiber itself is underway. An example of this comes in the form of bottle resonators [18,122–124], where the taper region itself is deformed to create a resonator, which generally still requires an external taper to couple light into the cavity. This shows how the tapered fiber can itself be used as a cavity. More direct examples of cavities within the fiber come in the form of fiber Bragg gratings (FBGs), for which much theoretical work has already been done on the interaction of a few/single atoms close to the nanofiber cavity [103,125–129].

The fabrication of such FBGs has been developing in recent years, from micron scale fibers down to nanometer scale fibers. For this, three fabrication techniques are used most frequently: (i) ultraviolet irradiation [130–133], (ii) focused ion beam (FIB) milling [104,134–137], and (iii) femtosecond laser irradiation [138–141]. Each technique has advantages and disadvantages with quite possibly the most work to date concentrating on the FIB technique, see Figure 16 for an example [104]. More recently, however, there has been success using femtosecond laser ablation to create highly ordered photonic crystal structures on a nanofiber, see Figure 17 [141]. Such nanofiber cavities offer to be promising devices for the detection of very low numbers of atoms.

One problem with fixed cavities in the nanofiber region is that of tuning the cavity to useful wavelengths for detection purposes. This can be achieved, for example, by straining the fiber [142]. Other resonators which can be fabricated directly from tapered optical fibers and may avoid this problem are those where the fiber is looped upon itself. Examples of this are microcoils [143–145], microfiber knots [146,147], and microfiber loops [148,149]. With these cavities, different tuning opportunities may be available [150–154]. For future possibilities using optical nanofibers, it has already been shown that polarization maintaining fiber can be tapered to micron sizes, whilst still maintaining the polarization of the coupled light [155]. Such control and maintenance of polarization

within the fiber may be of use when probing polarization sensitive states of atoms, or utilizing polarized confined modes within an optical cavity.

Figure 16. Scanning ion microscope (SIM) image of a nanofiber Bragg grating fabricated using the FIB milling technique. The fiber diameter is ~560 nm. The grating period is ~360 nm, with each groove having a depth of ~100 nm and width of ~150 nm. The scale bar represents 1.0 μm. The image was taken at 60,000× magnification used in the SIM, but the scale bar gives the correct scaling for this image. Reprinted with permission from [104]. Copyright 2011 Optical Society of America.

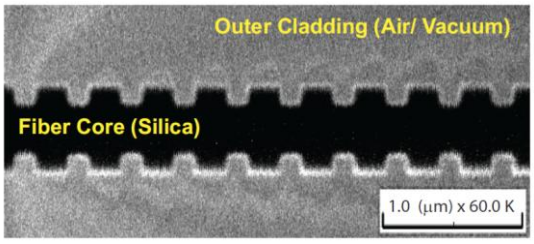
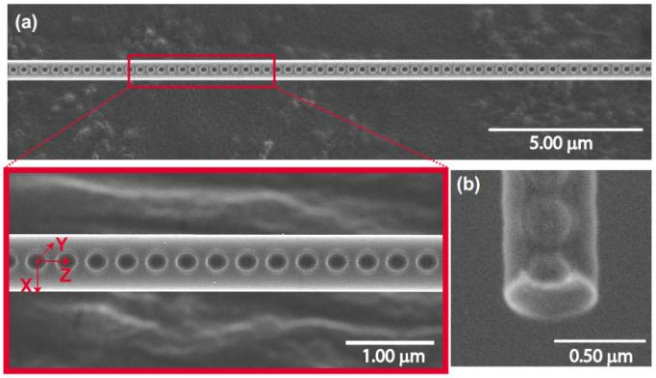


Figure 17. (**a**) Scanning electron microscope image of a structured nanofiber fabricated using single-shot irradiation of the ONF by a femtosecond laser beam. Inset: Enlarged view. Periodic nanocrater structures are observed on the shadow side of the nanofiber. (**b**) Cross-sectional image of a nanocrater measured by tilting the nanofiber. Reprinted with permission from [141]. Copyright 2013 Optical Society of America.



5. Conclusions/Outlook

The systematic fabrication of ONFs has now become readily available, with several techniques already developed to achieve a smooth surface profile with low transmission losses and high mechanical strength, making them ideal for the researcher to utilize in the development of quantum optical devices. In this article, we have reviewed the state-of-the-art schemes that utilize ONFs for ultra-sensitive detection, trapping, and manipulation of atoms and molecules. Due to the high coupling efficiency of atoms into the guided modes of the fiber, as well as the significant fraction of photons that can be absorbed from the evanescent field, ONFs provide an interface whereby the spectral properties of the atoms close to the surface of the fiber can be investigated. The ONF has the inherent ability to suppress ambient scattering of light, while maintaining the high coupling efficiencies of atoms. This allows the ONF to operate as a nondestructive detector to determine characteristics of

atom clouds such as temperature, size and shape, as well as dynamic properties such as loading and decay times. Such techniques can have many future applications for nondestructive characterization of atomic ensembles. Based on the same principal, the ONF also acts as a sensor device for the detection of few atoms, as well as single atoms, with a high signal-to-noise ratio. These techniques have shown that ONFs have promise for numerous applications in quantum technologies, where detection of small numbers of atoms will be essential.

Due to the fact that atoms are detected close to the surface of the fiber, the detection schemes can facilitate fundamental research into physical phenomena, such as the van der Waal and Casimir-Polder forces, which are otherwise more difficult to observe. These surface effects become important when considering the long-term performance or the degradation of the ONF in cold atom systems, whereby atoms become bound to the surface decreasing the performance of the ONF over time. This destructive effect can be reversed with the aid of a specific laser frequency passing through the fiber, thereby extending the lifetime of the ONF.

The unique properties of the ONF and its evanescent field allow various trapping schemes to be implemented. The configurations that have already been realized rely on two separate frequencies of light, with specific powers and polarizations, to create local optical lattice sites close to the surface of the ONF. The traps provide strong confinement of single atoms in each lattice site. The atoms trapped in the sites can be translated by controlling the relative detuning of the standing waves, giving the ONF the ability to simultaneously, trap, probe, and manipulate single atoms. This demonstrates the versatility and functionality of the ONF and paves the way for future ONF experiments, such as entanglement via photon exchange.

Although the focus of this review has been on the utilization of ONFs with cold atoms, the methods and techniques can be easily extended to systems other than atoms. Molecules can be detected by performing surface absorption spectroscopy via the ONF. This has proven to be a more sensitive method when compared to free space techniques. In addition, for the use of an ONF as an interface with cold atoms, the structure of the ONF itself can be modified to incorporate devices such as grating and cavities. This micro/nanostructuring of the ONF opens the path for multiple possibilities regarding the future of optical nanofibers as tools in the field of atom optics.

Conflicts of Interest

The authors declare no conflict of interest.

References

1. Vetsch, E.; Reitz, D.; Sagué, G.; Schmidt, R.; Dawkins, S.T.; Rauschenbeutel, A. Optical interface created by laser-cooled atoms trapped in the evanescent field surrounding an optical nanofiber. *Phys. Rev. Lett.* **2010**, *104*, 203603.
2. Das, M.; Shirasaki, A.; Nayak, K.P.; Morinaga, M.; Le Kien, F.; Hakuta, K. Measurement of fluorescence emission spectrum of few strongly driven atoms using an optical nanofiber. *Opt. Express* **2010**, *18*, 17154–17164.
3. Russell, L.; Deasy, K.; Daly, M.J.; Morrissey, M.J.; Nic Chormaic, S. Sub-doppler temperature measurements of laser-cooled atoms using optical nanofibres. *Meas. Sci. Tech.* **2012**, *23*, 015201.

4. Goban, A.; Choi, K.S.; Alton, D.J.; Ding, D.; Lacroute, C.; Pototschnig, M.; Thiele, T.; Stern, N.P.; Kimble, H.J. Demonstration of a state-insensitive, compensated nanofiber trap. *Phys. Rev. Lett.* **2012**, *109*, 033603.
5. Brownnutt, M. Private Communication, Innsbruck, Austria, March 2013.
6. Brownnutt, M. Ions and Fibres: A Target Rich Environment. In Proceedings of Optical Nanofiber Applications (ONNA2013), Okinawa, Japan, 1–7 June 2013.
7. Andre, A.; Demille, D.; Doyle, J.M.; Lukin, M.D.; Maxwell, S.E.; Rabl, P.; Schoelkopf, R.J.; Zoller, P. A coherent all-electrical interface between polar molecules and mesoscopic superconducting resonators. *Nat. Phys.* **2006**, *2*, 636–642.
8. Aoki, T.; Dayan, B.; Wilcut, E.; Bowen, W.P.; Parkins, A.S.; Kippenberg, T.J.; Vahala, K.J.; Kimble, H.J. Observation of strong coupling between one atom and a monolithic microresonator. *Nature* **2006**, *443*, 671–674.
9. Reichel, J. Microchip traps and Bose-Einstein condensation. *Appl. Phys. B Las. Opt.* **2002**, *74*, 469–487.
10. Tong, L.M.; Gattass, R.R.; Ashcom, J.B.; He, S.L.; Lou, J.Y.; Shen, M.Y.; Maxwell, I.; Mazur, E. Subwavelength-diameter silica wires for low-loss optical wave guiding. *Nature* **2003**, *426*, 816–819.
11. Tong, L.; Lou, J.; Mazur, E. Single-mode guiding properties of subwavelength-diameter silica and silicon wire waveguides. *Opt. Express* **2004**, *12*, 1025–1035.
12. Tong, L. Brief introduction to optical microfibers and nanofibers. *Front. Optoelectron. China* **2010**, *3*, 54–60.
13. Tong, L.M.; Zi, F.; Guo, X.; Lou, J.Y. Optical microfibers and nanofibers: A tutorial. *Opt. Commun.* **2012**, *285*, 4641–4647.
14. Lee, B. Review of the present status of optical fiber sensors. *Opt. Fiber Tech.* **2003**, *9*, 57–79.
15. Moar, P.; Huntington, S.; Katsifolis, J.; Cahill, L.; Roberts, A.; Nugent, K. Fabrication, modeling, and direct evanescent field measurement of tapered optical fiber sensors. *J. Appl. Phys.* **1999**, *85*, 3395.
16. Brambilla, G.; Finazzi, V.; Richardson, D.J. Ultra-low-loss optical fiber nanotapers. *Opt. Express* **2004**, *12*, 2258–2263.
17. Brambilla, G.; Jung, Y.; Renna, F. Optical fiber microwires and nanowires manufactured by modified flame brushing technique: Properties and applications. *Front. Optoelectron. China* **2010**, *3*, 61–66.
18. Ward, J.; O'Shea, D.; Shortt, B.; Morrissey, M.; Deasy, K.; Nic Chormaic, S. Heat-and-pull rig for fiber taper fabrication. *Rev. Sci. Instrum.* **2006**, *77*, 083105.
19. Ding, L.; Belacel, C.; Ducci, S.; Leo, G.; Favero, I. Ultralow loss single-mode silica tapers manufactured by a microheater. *Appl. Opt.* **2010**, *49*, 2441–2445.
20. Shi, L.; Chen, X.; Liu, H.; Chen, Y.; Ye, Z.; Liao, W.; Xia, Y. Fabrication of submicron-diameter silica fibers using electric strip heater. *Opt. Express* **2006**, *14*, 5055–5060.
21. Kenny, R.; Birks, T.; Oakley, K. Control of optical fibre taper shape. *Elec. Lett.* **1991**, *27*, 1654–1656.
22. Birks, T.A.; Li, Y.W. The shape of fiber tapers. *J. Lightwave Tech.* **1992**, *10*, 432–438.
23. Love, J.; Henry, W.; Stewart, W.; Black, R.; Lacroix, S.; Gonthier, F. Tapered single-mode fibres and devices. I. Adiabaticity criteria. *IEE Proc. J. Optoelectron.* **1991**, *138*, 343–354.

24. Snyder, A.W.; Love, J.D. *Optical Waveguide Theory*; Chapman and Hall: London, UK, 1980.
25. Sagué, G.; Baade, A.; Rauschenbeutel, A. Blue-detuned evanescent field surface traps for neutral atoms based on mode interference in ultra-thin optical fibres. *New J. Phys.* **2008**, *10*, 113008.
26. Petcu-Colan, A.; Frawley, M.; Nic Chormaic, S. Tapered few-mode tapered fibers: Mode evolution during fabrication and adiabaticity. *J. Nonlin. Opt. Phys. Mater.* **2011**, *20*, 293–307.
27. Frawley, M.C.; Petcu-Colan, A.; Viet Giang, T.; Nic Chormaic, S. Higher order mode propagation in an optical nanofiber. *Opt. Commun.* **2012**, *285*, 4648–4654.
28. Bures, J.; Ghosh, R. Power density of the evanescent field in the vicinity of a tapered fiber. *J. Opt. Soc. Am. A* **1999**, *16*, 1992–1996.
29. Franson, J.D.; Jacobs, B.C.; Pittman, T.B. Quantum computing using single photons and the zeno effect. *Phys. Rev. A* **2004**, *70*, 062302.
30. Ghosh, S.; Bhagwat, A.R.; Renshaw, C.K.; Goh, S.; Gaeta, A.L.; Kirby, B.J. Low-light-level optical interactions with rubidium vapor in a photonic band-gap fiber. *Phys. Rev. Lett.* **2006**, *97*, 023603.
31. Tanji-Suzuki, H.; Chen, W.; Landig, R.; Simon, J.; Vuletić, V. Vacuum-induced transparency. *Science* **2011**, *333*, 1266–1269.
32. Le Kien, F.; Gupta, S.D.; Balykin, V.I.; Hakuta, K. Spontaneous emission of a cesium atom near a nanofiber: Efficient coupling of light to guided modes. *Phys. Rev. A* **2005**, *72*, 032509.
33. Ebbesen, T.W.; Lezec, H.J.; Ghaemi, H.F.; Thio, T.; Wolff, P.A. Extraordinary optical transmission through sub-wavelength hole arrays. *Nature* **1998**, *391*, 667–669.
34. Choi, K.Y.; Yoon, J.; Song, S.H.; Oh, C.H.; Kim, P.S. Surface-plasmon coupling in subwavelength periodic structures. *Proc. SPIE* **2005**, *5636*, 22–26.
35. Russell, L.; Gleeson, D.A.; Minogin, V.G.; Nic Chormaic, S. Spectral distribution of atomic fluorescence coupled into an optical nanofibre. *J. Phys. B Atomic Mol. Opt. Phys.* **2009**, *42*, 185006.
36. Minogin, V.G.; Nic Chormaic, S. Manifestation of the van der Waals surface interaction in the spontaneous emission of atoms into an optical nanofiber. *Laser Phys.* **2010**, *20*, 32–37.
37. Frawley, M.C.; Nic Chormaic, S.; Minogin, V.G. The van der Waals interaction of an atom with the convex surface of a nanocylinder. *Phys. Scr.* **2012**, *85*, 058103.
38. Nayak, K.P.; Melentiev, P.N.; Morinaga, M.; Kien, F.L.; Balykin, V.I.; Hakuta, K. Optical nanofiber as an efficient tool for manipulating and probing atomic fluorescence. *Opt. Express* **2007**, *15*, 5431–5438.
39. Watkins, A.; Tiwari, V.B.; Ward, J.M.; Nic Chormaic, S. Observation of Zeeman shift in the rubidium D2 line using an optical nanofiber in vapor. **2012**, arXiv:1208.4708.
40. Esslinger, T.; Bloch, I.; Hänsch, T.W. Bose-Einstein condensation in a quadrupole-Ioffe-configuration trap. *Phys. Rev. A* **1998**, *58*, R2664–R2667.
41. Schlosser, N.; Reymond, G.; Protsenko, I.; Grangier, P. Sub-Poissonian loading of single atoms in a microscopic dipole trap. *Nature* **2001**, *411*, 1024–1027.
42. Paredes, B.; Widera, A.; Murg, V.; Mandel, O.; Folling, S.; Cirac, I.; Shlyapnikov, G.V.; Hansch, T.W.; Bloch, I. Tonks-Girardeau gas of ultracold atoms in an optical lattice. *Nature* **2004**, *429*, 277–281.
43. Bolpasi, V.; Grucker, J.; Morrissey, M.J.; von Klitzing, W. A gradient and offset compensated ioffe-pritchard trap for Bose-Einstein condensation experiments. *J. Phys. B Atomic Mol. Opt. Phys.* **2012**, *45*, 235301.

44. Richmond, J.A.; Nic Chormaic, S.; Cantwell, B.P.; Opat, G.I. A magnetic guide for cold atoms. *Acta Phys. Slovaca* **1998**, *48*, 481–488.
45. Opat, G.I.; Nic Chormaic, S.; Cantwell, B.P.; Richmond, J.A. Optical elements for slowly moving neutral atoms based on magnetic fields. *J. Opt. B Quant. Semiclass. Opt.* **1999**, *1*, 415–419.
46. Denschlag, J.; Cassettari, D.; Schmiedmayer, J. Guiding neutral atoms with a wire. *Phys. Rev. Lett.* **1999**, *82*, 2014–2017.
47. Reichel, J.; Hansell, W.; Hänsch, T.W. Atomic micromanipulation with magnetic surface traps. *Phys. Rev. Lett.* **1999**, *83*, 3398–3401.
48. Kuhr, S.; Alt, W.; Schrader, D.; Muller, M.; Gomer, V.; Meschede, D. Deterministic delivery of a single atom. *Science* **2001**, *293*, 278–280.
49. Gustavson, T.L.; Chikkatur, A.P.; Leanhardt, A.E.; Gorlitz, A.; Gupta, S.; Pritchard, D.E.; Ketterle, W. Transport of Bose-Einstein condensates with optical tweezers. *Phys. Rev. Lett.* **2002**, *88*, 020401.
50. Richmond, J.A.; Cantwell, B.P.; Chormaic, S.N.; Lau, D.C.; Akulshin, A.M.; Opat, G.I. Magnetic guide for neutral atoms. *Phys. Rev. A* **2002**, *65*, 033422.
51. Kadlecek, S.; Sebby, J.; Newell, R.; Walker, T.G. Nondestructive spatial heterodyne imaging of cold atoms. *Opt. Lett.* **2001**, *26*, 137–139.
52. Turner, L.D.; Domen, K.; Scholten, R.E. Diffraction-contrast imaging of cold atoms. *Phys. Rev. A* **2005**, *72*, 031403.
53. Pappa, M.; Condylis, P.C.; Konstantinidis, G.O.; Bolpasi, V.; Lazoudis, A.; Morizot, O.; Sahagun, D.; Baker, M.; von Klitzing, W. Ultra-sensitive atom imaging for matter-wave optics. *New J. Phys.* **2011**, *13*, 115012.
54. Le Kien, F.; Balykin, V.I.; Hakuta, K. Scattering of an evanescent light field by a single cesium atom near a nanofiber. *Phys. Rev. A* **2006**, *73*, 013819.
55. Hennessy, T.; Busch, T. Creating atom-number states around tapered optical fibers by loading from an optical lattice. *Phys. Rev. A* **2012**, *85*, 053418.
56. Masalov, A.V.; Minogin, V.G. Pumping of higher-order modes of an optical nanofiber by laser excited atoms. *Las. Phys. Lett.* **2013**, *10*, 075203.
57. Sagué, G.; Vetsch, E.; Alt, W.; Meschede, D.; Rauschenbeutel, A. Cold-atom physics using ultrathin optical fibers: Light-induced dipole forces and surface interactions. *Phys. Rev. Lett.* **2007**, *99*, 163602.
58. Nayak, K.; Hakuta, K. Single atoms on an optical nanofibre. *New J. Phys.* **2008**, *10*, 053003.
59. Hughes, S. Modified spontaneous emission and qubit entanglement from dipole-coupled quantum dots in a photonic crystal nanocavity. *Phys. Rev. Lett.* **2005**, *94*, 227402.
60. Chang, D.E.; Sorensen, A.S.; Hemmer, P.R.; Lukin, M.D. Quantum optics with surface plasmons. *Phys. Rev. Lett.* **2006**, *97*, 053002.
61. Berman, P. *Cavity Quantum Electrodynamics (Advances in Atomic, Molecular and Optical Physics)*; Academic Press: New York, NY, USA, 1994.
62. Nha, H.; Jhe, W. Cavity quantum electrodynamics for a cylinder: Inside a hollow dielectric and near a solid dielectric cylinder. *Phys. Rev. A* **1997**, *56*, 2213–2220.
63. Sondergaard, T.; Tromborg, B. General theory for spontaneous emission in active dielectric microstructures: Example of a fiber amplifier. *Phys. Rev. A* **2001**, *64*, 033812.

64. Klimov, V.; Ducloy, M. Spontaneous emission rate of an excited atom placed near a nanofiber. *Phys. Rev. A* **2004**, doi:10.1016/S0030-4018(02)01802-3.
65. Nayak, K.; Le Kien, F.; Morinaga, M.; Hakuta, K. Antibunching and bunching of photons in resonance fluorescence from a few atoms into guided modes of an optical nanofiber. *Nat. (Lond.) Phys. Rev. A* **2009**, *79*, 021801.
66. Landragin, A.; Courtois, J.Y.; Labeyrie, G.; Vansteenkiste, N.; Westbrook, C.I.; Aspect, A. Measurement of the van der Waals force in an atomic mirror. *Phys. Rev. Lett.* **1996**, *77*, 1464–1467.
67. Harber, D.M.; Obrecht, J.M.; McGuirk, J.M.; Cornell, E.A. Measurement of the Casimir-Polder force through center-of-mass oscillations of a Bose-Einstein condensate. *Phys. Rev. A* **2005**, *72*, 033610.
68. Le Kien, F.; Gupta, S.D.; Hakuta, K. Optical excitation spectrum of an atom in a surface-induced potential. *Phys. Rev. A* **2007**, *75*, 032508.
69. Le Kien, F.; Hakuta, K. Spontaneous radiative decay of translational levels of an atom near a dielectric surface. *Phys. Rev. A* **2007**, *75*, 013423.
70. Nayak, K.P.; Das, M.; Kien, F.L.; Hakuta, K. Spectroscopy of near-surface atoms using an optical nanofiber. *Opt. Commun.* **2012**, *285*, 4698–4704.
71. Deasy, K.; Watkins, A.; Morrissey, M.; Schmidt, R.; Nic Chormaic, S. Few Atom Detection and Manipulation using Optical Nanofibres. In *Quantum Communication and Quantum Networking*; Sergienko, A., Pascazio, S., Villoresi, P., Eds.; Springer: Berlin Heidelberg, Germany, 2010; Volume 36, pp. 200–209.
72. Morrissey, M.J.; Deasy, K.; Wu, Y.; Chakrabarti, S.; Nic Chormaic, S. Tapered optical fibers as tools for probing magneto-optical trap characteristics. *Rev. Sci. Instrum.* **2009**, *80*, 053102.
73. Russell, L.; Kumar, R.; Tiwari, V.; Nic Chormaic, S. Measurements on release-recapture of cold Rb-85 atoms using an optical nanofibre in a magneto-optical trap. *Opt. Commun.* **2013**, doi:10.1016/j.optcom.2013.07.080.
74. Kien, F.L.; Balykin, V.I.; Hakuta, K. Light-induced force and torque on an atom outside a nanofiber. *Phys. Rev. A* **2006**, *74*, 033412.
75. Hakuta, K. Single atoms on an optical nanofiber: A novel work system for slow light. *Proc. SPIE* **2008**, *6904*, 690406.
76. Letokhov, V. Nonlinear high resolution laser spectroscopy. *Science* **1975**, *190*, 344–351.
77. Spillane, S.M.; Pati, G.S.; Salit, K.; Hall, M.; Kumar, P.; Beausoleil, R.G.; Shahriar, M.S. Observation of nonlinear optical interactions of ultralow levels of light in a tapered optical nanofiber embedded in a hot rubidium vapor. *Phys. Rev. Lett.* **2008**, *100*, 233602.
78. Hendrickson, S.M.; Pittman, T.B.; Franson, J.D. Nonlinear transmission through a tapered fiber in rubidium vapor. *J. Opt. Soc. Am. B* **2009**, *26*, 267–271.
79. Hendrickson, S.M.; Lai, M.M.; Pittman, T.B.; Franson, J.D. Observation of two-photon absorption at low power levels using tapered optical fibers in rubidium vapor. *Phys. Rev. Lett.* **2010**, *105*, 173602.
80. Russell, L.; Daly, M.; Nic Chormaic, S. 1- and 2-photon absorption by laser-cooled ^{85}Rb using an optical nanofiber. *AIP Conf. Proc.* **2012**, *1469*, 82–90.

81. Lai, M.; Franson, J.D.; Pittman, T.B. Transmission degradation and preservation for tapered optical fibers in rubidium vapor. *Appl. Opt.* **2013**, *52*, 2595–2601.
82. Balykin, V.I.; Hakuta, K.; Le Kien, F.; Liang, J.Q.; Morinaga, M. Atom trapping and guiding with a subwavelength-diameter optical fiber. *Phys. Rev. A* **2004**, *70*, 011401.
83. Le Kien, F.; Balykin, V.I.; Hakuta, K. Atom trap and waveguide using a two-color evanescent light field around a subwavelength-diameter optical fiber. *Phys. Rev. A* **2004**, *70*, 063403.
84. Dawkins, S.T.; Mitsch, R.; Reitz, D.; Vetsch, E.; Rauschenbeutel, A. Dispersive optical interface based on nanofiber-trapped atoms. *Phys. Rev. Lett.* **2011**, *107*, 243601.
85. Schneeweiss, P.; Dawkins, S.; Mitsch, R.; Reitz, D.; Vetsch, E.; Rauschenbeutel, A. A nanofiber-based optical conveyor belt for cold atoms. *Appl. Phys. B* **2013**, *110*, 279–283.
86. Reitz, D.; Rauschenbeutel, A. Nanofiber-based double-helix dipole trap for cold neutral atoms. *Opt. Commun.* **2012**, *285*, 4705–4708.
87. Le Kien, F.; Liang, J.Q.; Hakuta, K.; Balykin, V.I. Field intensity distributions and polarization orientations in a vacuum-clad subwavelength-diameter optical fiber. *Opt. Commun.* **2004**, *242*, 445–455.
88. Fatemi, F.K.; Ravets, S.; Hoffman, J.E.; Beadie, G.; Rolston, S.L.; Orozco, L.A. Higher order mode propagation in ultrathin optical fibers for atom traps. *Proc. SPIE* **2013**, *8637*, 86370X.
89. Warken, F.; Vetsch, E.; Meschede, D.; Sokolowski, M.; Rauschenbeutel, A. Ultra-sensitive surface absorption spectroscopy using sub-wavelength diameter optical fibers. *Opt. Express* **2007**, *15*, 11952–11958.
90. Garcia-Fernandez, R.; Alt, W.; Bruse, F.; Dan, C.; Karapetyan, K.; Rehband, O.; Stiebeiner, A.; Wiedemann, U.; Meschede, D.; Rauschenbeutel, A. Optical nanofibers and spectroscopy. *Appl. Phys. B Las. Opt.* **2011**, *105*, 3–15.
91. Stiebeiner, A.; Rehband, O.; Garcia-Fernandez, R.; Rauschenbeutel, A. Ultra-sensitive fluorescence spectroscopy of isolated surface-adsorbed molecules using an optical nanofiber. *Opt. Express* **2009**, *17*, 21704–21711.
92. Takiguchi, M.; Yoshikawa, Y.; Yamamoto, T.; Nakayama, K.; Kuga, T. Saturated absorption spectroscopy of acetylene molecules with an optical nanofiber. *Opt. Lett.* **2011**, *36*, 1254–1256.
93. Wiedemann, U.; Alt, W.; Meschede, D. Switching photochromic molecules adsorbed on optical microfibres. *Opt. Express* **2012**, *20*, 12710–12720.
94. Gregor, M.; Kuhlicke, A.; Benson, O. Soft-landing and optical characterization of a preselected single fluorescent particle on a tapered optical fiber. *Opt. Express* **2009**, *17*, 24234–24243.
95. Srinivasan, K.; Painter, O.; Stintz, A.; Krishna, S. Single quantum dot spectroscopy using a fiber taper waveguide near-field optic. *Appl. Phys. Lett.* **2007**, *91*, 091102.
96. Davanco, M.; Srinivasan, K. Efficient spectroscopy of single embedded emitters using optical fiber taper waveguides. *Opt. Express* **2009**, *17*, 10542–10563.
97. Davanco, M.; Srinivasan, K. Fiber-coupled semiconductor waveguides as an efficient optical interface to a single quantum dipole. *Opt. Lett.* **2009**, *34*, 2542–2544.
98. Davanco, M.; Srinivasan, K. Hybrid gap modes induced by fiber taper waveguides: Application in spectroscopy of single solid-state emitters deposited on thin films. *Opt. Express* **2010**, *18*, 10995–11007.

99. Yalla, R.; Nayak, K.P.; Hakuta, K. Fluorescence photon measurements from single quantum dots on an optical nanofiber. *Opt. Express* **2012**, *20*, 2932–2941.
100. Yalla, R.; Le Kien, F.; Morinaga, M.; Hakuta, K. Efficient channeling of fluorescence photons from single quantum dots into guided modes of optical nanofiber. *Phys. Rev. Lett.* **2012**, *109*, 063602.
101. Fujiwara, M.; Toubaru, K.; Noda, T.; Zhao, H.-Q.; Takeuchi, S. Highly efficient coupling of photons from nanoemitters into single-mode optical fibers. *Nano Lett.* **2011**, *11*, 4362–4365.
102. Schröder, T.; Fujiwara, M.; Noda, T.; Zhao, H.-Q.; Benson, O.; Takeuchi, S. A nanodiamond-tapered fiber system with high single-mode coupling efficiency. *Opt. Express* **2012**, *20*, 10490–10497.
103. Le Kien, F.; Hakuta, K. Cavity-enhanced channeling of emission from an atom into a nanofiber. *Phys. Rev. A* **2009**, *80*, 053826.
104. Nayak, K.P.; Le Kien, F.; Kawai, Y.; Hakuta, K.; Nakajima, K.; Miyazaki, H.T.; Sugimoto, Y. Cavity formation on an optical nanofiber using focused ion beam milling technique. *Opt. Express* **2011**, *19*, 14040–14050.
105. Tian, Y.; Wang, W.; Wu, N.; Zou, X.; Wang, X. Tapered optical fiber sensor for label-free detection of biomolecules. *Sensors* **2011**, *11*, 3780–3790.
106. Yoshie, T.; Tang, L.; Su, S.-Y. Optical microcavity: Sensing down to single molecules and atoms. *Sensors* **2011**, *11*, 1972–1991.
107. Vahala, K.J. Optical microcavities. *Nature* **2003**, *424*, 839–846.
108. Ward, J.M.; O'Shea, D.G.; Shortt, B.J.; Nic Chormaic, S. Optical bistability in Er-Yb codoped phosphate glass microspheres at room temperature. *J. Appl. Phys.* **2007**, *102*, 023104.
109. Wu, Y.; Ward, J.M.; Nic Chormaic, S. Ultralow threshold green lasing and optical bistability in ZBNA microspheres. *J. Appl. Phys.* **2010**, *107*, 033103–033106.
110. Ward, J.M.; Wu, Y.; Khalfi, K.; Nic Chormaic, S. Short vertical tube furnace for the fabrication of doped glass microsphere lasers. *Rev. Sci. Instrum.* **2010**, *81*, 073106.
111. Nic Chormaic, S.; Wu, Y.; Ward, J.; Watkins, A. Fano Resonances and Electromagnetically Induced Absorption and Transparency-like Effects in Single Silica Microspheres. In Proceedings of the Frontiers in Optics 2010/Laser Science XXVI, OSA Technical Digest (CD), Rochester, NY, USA, 24–28 October 2010.
112. Watkins, A.; Ward, J.; Wu, Y.; Nic Chormaic, S. Single-input spherical microbubble resonator. *Opt. Lett.* **2011**, *36*, 2113–2115.
113. Alton, D.J.; Stern, N.P.; Aoki, T.; Lee, H.; Ostby, E.; Vahala, K.J.; Kimble, H.J. Strong interactions of single atoms and photons near a dielectric boundary. *Nat. Phys.* **2011**, *7*, 159–165.
114. Purcell, E.M. Spontaneous emission probabilities at radio frequencies. *Phys. Rev.* **1946**, *69*, 681–681.
115. Vollmer, F.; Yang, L. Label-free detection with high-q microcavities: A review of biosensing mechanisms for integrated devices. *Nanophotonics* **2012**, *1*, 267–291.
116. Armani, A.M.; Kulkarni, R.P.; Fraser, S.E.; Flagan, R.C.; Vahala, K.J. Label-free, single-molecule detection with optical microcavities. *Science* **2007**, *317*, 783–787.
117. Knight, J.C.; Cheung, G.; Jacques, F.; Birks, T.A. Phase-matched excitation of whispering-gallery-mode resonances by a fiber taper. *Opt. Lett.* **1997**, *22*, 1129–1131.
118. Cai, M.; Painter, O.; Vahala, K.J. Observation of critical coupling in a fiber taper to a silica-microsphere whispering-gallery mode system. *Phys. Rev. Lett.* **2000**, *85*, 74–77.

119. Spillane, S.M.; Kippenberg, T.J.; Painter, O.J.; Vahala, K.J. Ideality in a fiber-taper-coupled microresonator system for application to cavity quantum electrodynamics. *Phys. Rev. Lett.* **2003**, *91*, 043902.
120. Srinivasan, K.; Painter, O. Optical fiber taper coupling and high-resolution wavelength tuning of microdisk resonators at cryogenic temperatures. *Appl. Phys. Lett.* **2007**, *90*, 031114.
121. Watkins, A.; Ward, J.; Nic Chormaic, S. Thermo-optical tuning of whispering gallery modes in Erbium: Ytterbium doped glass microspheres to arbitrary probe wavelengths. *Jpn. J. Appl. Phys.* **2012**, *51*, 052501.
122. Kakarantzas, G.; Dimmick, T.E.; Birks, T.A.; Le Roux, R.; Russell, P.S.J. Miniature all-fiber devices based on CO_2 laser microstructuring of tapered fibers. *Opt. Lett.* **2001**, *26*, 1137–1139.
123. Pöllinger, M.; O'Shea, D.; Warken, F.; Rauschenbeutel, A. Ultrahigh-Q tunable whispering-gallery-mode microresonator. *Phys. Rev. Lett.* **2009**, *103*, 053901.
124. Junge, C.; O'Shea, D.; Volz, J.; Rauschenbeutel, A. Strong coupling between single atoms and nontransversal photons. *Phys. Rev. Lett.* **2013**, *110*, 213604.
125. Fam Le, K.; Hakuta, K. Intracavity electromagnetically induced transparency in atoms around a nanofiber with a pair of Bragg grating mirrors. *Phys. Rev. A* **2009**, *79*, 043813.
126. Fam Le, K.; Hakuta, K. Triggered generation of single guided photons from a single atom in a nanofiber cavity. *Phys. Rev. A* **2011**, *83*, 043801.
127. Le Kien, F.; Hakuta, K. Deterministic generation of a pair of entangled guided photons from a single atom in a nanofiber cavity. *Phys. Rev. A* **2011**, *84*, 053801.
128. Kien, F.L.; Nayak, K.P.; Hakuta, K. Nanofibers with Bragg gratings from equidistant holes. *J. Mod. Opt.* **2012**, *59*, 274–286.
129. Fam Le, K.; Hakuta, K. Translational motion of an atom in a weakly driven fiber-Bragg-grating cavity. *Adv. Nat. Sci. Nanosci. Nanotechnol.* **2012**, *3*, 025009.
130. Lindner, E.; Chojetzki, C.; Brückner, S.; Becker, M.; Rothhardt, M.; Bartelt, H. Thermal regeneration of fiber Bragg gratings in photosensitive fibers. *Opt. Express* **2009**, *17*, 12523–12531.
131. Zhang, Y.; Lin, B.; Tjin, S.C.; Zhang, H.; Wang, G.; Shum, P.; Zhang, X. Refractive index sensing based on higher-order mode reflection of a microfiber Bragg grating. *Opt. Express* **2010**, *18*, 26345–26350.
132. Wieduwilt, T.; Brueckner, S.; Bartelt, H. High force measurement sensitivity with fiber Bragg gratings fabricated in uniform-waist fiber tapers. *Meas. Sci. Tech.* **2011**, *22*, 075201.
133. Yang, R.; Long, J.; Yan-Nan, T.; Li-Peng, S.; Jie, L.; Bai-Ou, G. High-efficiency ultraviolet inscription of Bragg gratings in microfibers. *IEEE Photon. J.* **2012**, *4*, 181–186.
134. Ding, M.; Zervas, M.N.; Brambilla, G. A compact broadband microfiber Bragg grating. *Opt. Express* **2011**, *19*, 15621–15626.
135. Liu, Y.; Meng, C.; Zhang, A.P.; Xiao, Y.; Yu, H.; Tong, L. Compact microfiber Bragg gratings with high-index contrast. *Opt. Lett.* **2011**, *36*, 3115–3117.
136. Ding, M.; Wang, P.; Lee, T.; Brambilla, G. A microfiber cavity with minimal-volume confinement. *Appl. Phys. Lett.* **2011**, *99*, 051105.
137. Feng, J.; Ding, M.; Kou, J.-L.; Xu, F.; Lu, Y.-Q. An optical fiber tip micrograting thermometer. *IEEE Photon. J.* **2011**, *3*, 810–814.

138. Dragomir, A.; Nikogosyan, D.N.; Zagorulko, K.A.; Kryukov, P.G.; Dianov, E.M. Inscription of fiber Bragg gratings by ultraviolet femtosecond radiation. *Opt. Lett.* **2003**, *28*, 2171–2173.
139. Grobnic, D.; Mihailov, S.J.; Ding, H.M.; Smelser, C.W. Bragg grating evanescent field sensor made in biconical tapered fiber with femtosecond ir radiation. *IEEE Photon. Tech. Lett.* **2006**, *18*, 160–162.
140. Zhao, P.; Li, Y.; Zhang, J.; Shi, L.; Zhang, X. Nanohole induced microfiber Bragg gratings. *Opt. Express* **2012**, *20*, 28625–28630.
141. Nayak, K.P.; Hakuta, K. Photonic crystal formation on optical nanofibers using femtosecond laser ablation technique. *Opt. Express* **2013**, *21*, 2480–2490.
142. Wuttke, C.; Becker, M.; Brückner, S.; Rothhardt, M.; Rauschenbeutel, A. Nanofiber Fabry-Perot microresonator for nonlinear optics and cavity quantum electrodynamics. *Opt. Lett.* **2012**, *37*, 1949–1951.
143. Sumetsky, M. Optical fiber microcoil resonator. *Opt. Express* **2004**, *12*, 2303–2316.
144. Fei, X.; Horak, P.; Brambilla, G. Optimized design of microcoil resonators. *J. Lightwave Tech.* **2007**, *25*, 1561–1567.
145. Fei, X.; Brambilla, G. Manufacture of 3-D microfiber coil resonators. *IEEE Photon. Tech. Lett.* **2007**, *19*, 1481–1483.
146. Jiang, X.; Yang, Q.; Vienne, G.; Li, Y.; Tong, L.; Zhang, J.; Hu, L. Demonstration of microfiber knot laser. *Appl. Phys. Lett.* **2006**, *89*, 143513.
147. Xiao, L.; Birks, T.A. High finesse microfiber knot resonators made from double-ended tapered fibers. *Opt. Lett.* **2011**, *36*, 1098–1100.
148. Sumetsky, M.; Dulashko, Y.; Fini, J.M.; Hale, A. Optical microfiber loop resonator. *Appl. Phys. Lett.* **2005**, *86*, 161108.
149. Sumetsky, M.; Dulashko, Y.; Fini, J.M.; Hale, A.; DiGiovanni, D.J. The microfiber loop resonator: Theory, experiment, and application. *J. Lightwave Tech.* **2006**, *24*, 242–250.
150. Yu, W.; Xu, Z.; Changlun, H.; Jian, B.; Guoguang, Y. A tunable all-fiber filter based on microfiber loop resonator. *Appl. Phys. Lett.* **2008**, *92*, 191112.
151. Chen, Z.; Hsiao, V.K.S.; Li, X.; Li, Z.; Yu, J.; Zhang, J. Optically tunable microfiber-knot resonator. *Opt. Express* **2011**, *19*, 14217–14222.
152. Chen, G.Y.; Lee, T.; Zhang, X.L.; Brambilla, G.; Newson, T.P. Temperature compensation techniques for resonantly enhanced sensors and devices based on optical microcoil resonators. *Opt. Commun.* **2012**, *285*, 4677–4683.
153. Sulaiman, A.; Harun, S.W.; Ahmad, F.; Norizan, S.F.; Ahmad, H. Electrically tunable microfiber knot resonator based erbium-doped fiber laser. *IEEE J. Quantum Electron.* **2012**, *48*, 443–446.
154. Sulaiman, A.; Harun, S.W.; Ahmad, H. Thermally tunable microfiber knot resonator based erbium-doped fiber laser. *Opt. Commun.* **2012**, *285*, 4684–4687.
155. Jung, Y.M.; Brambilla, G.; Richardson, D.J. Polarization-maintaining optical microfiber. *Opt. Lett.* **2010**, *35*, 2034–2036.

© 2013 by the authors; licensee MDPI, Basel, Switzerland. This article is an open access article distributed under the terms and conditions of the Creative Commons Attribution license (http://creativecommons.org/licenses/by/3.0/).

References

[1] H. Walther, "Quantum optics of single atoms," *Fortschritte der Physik*, vol. 52, no. 11-12, pp. 1154–1164, 2004.

[2] M. K. Tey, Z. Chen, S. A. Aljunid, B. Chng, F. Huber, G. Maslennikov, and C. Kurtsiefer, "Strong interaction between light and a single trapped atom without the need for a cavity," *Nature Physics*, vol. 4, no. 12, pp. 924–927, 2008.

[3] P. Pinkse, T. Fischer, P. Maunz, T. Puppe, and G. Rempe, "How to catch an atom with single photons," *Journal of Modern Optics*, vol. 47, no. 14-15, pp. 2769–2787, 2000.

[4] P. Pinkse, T. Fischer, P. Maunz, and G. Rempe, "Trapping an atom with single photons," *Nature*, vol. 404, no. 6776, pp. 365–368, 2000.

[5] M. Mücke, E. Figueroa, J. Bochmann, C. Hahn, K. Murr, S. Ritter, C. J. Villas-Boas, and G. Rempe, "Electromagnetically induced transparency with single atoms in a cavity," *Nature*, vol. 465, no. 7299, pp. 755–758, 2010.

[6] D. van Oosten and L. Kuipers, "Trapping a single atom with a fraction of a photon using a photonic crystal nanocavity," *Physical Review A*, vol. 84, no. 1, p. 011802, 2011.

[7] J. I. Cirac, P. Zoller, H. J. Kimble, and H. Mabuchi, "Quantum state transfer and entanglement distribution among distant nodes in a quantum network," *Physical Review Letters*, vol. 78, no. 16, p. 3221, 1997.

[8] A. D. Boozer, A. Boca, R. Miller, T. E. Northup, and H. J. Kimble, "Reversible state transfer between light and a single trapped atom," *Physical Review Letters*, vol. 98, no. 19, p. 193601, 2007.

[9] S. Gleyzes, S. Kuhr, C. Guerlin, J. Bernu, S. Deleglise, U. B. Hoff, M. Brune, J.-M. Raimond, and S. Haroche, "Quantum jumps of light recording the birth

and death of a photon in a cavity," *Nature*, vol. 446, no. 7133, pp. 297–300, 2007.

[10] S. Ritter, C. Nölleke, C. Hahn, A. Reiserer, A. Neuzner, M. Uphoff, M. Mücke, E. Figueroa, J. Bochmann, and G. Rempe, "An elementary quantum network of single atoms in optical cavities," *Nature*, vol. 484, no. 7393, pp. 195–200, 2012.

[11] L. Tong, R. R. Gattass, J. B. Ashcom, S. He, J. Lou, M. Shen, I. Maxwell, and E. Mazur, "Subwavelength-diameter silica wires for low-loss optical wave guiding," *Nature*, vol. 426, no. 6968, pp. 816–819, 2003.

[12] T. Birks, Y. W. Li, *et al.*, "The shape of fiber tapers," *Journal of Lightwave Technology*, vol. 10, no. 4, pp. 432–438, 1992.

[13] K. P. Nayak and K. Hakuta, "Single atoms on an optical nanofibre," *New Journal of Physics*, vol. 10, no. 5, p. 053003, 2008.

[14] L. Tong, J. Lou, and E. Mazur, "Single-mode guiding properties of subwavelength-diameter silica and silicon wire waveguides," *Optics Express*, vol. 12, no. 6, pp. 1025–1035, 2004.

[15] F. Le Kien, J. Liang, K. Hakuta, and V. Balykin, "Field intensity distributions and polarization orientations in a vacuum-clad subwavelength-diameter optical fiber," *Optics Communications*, vol. 242, no. 4, pp. 445–455, 2004.

[16] Z. Tian, S. S.-H. Yam, J. Barnes, W. Bock, P. Greig, J. M. Fraser, H.-P. Loock, and R. D. Oleschuk, "Refractive index sensing with mach–zehnder interferometer based on concatenating two single-mode fiber tapers," *Photonics Technology Letters, IEEE*, vol. 20, no. 8, pp. 626–628, 2008.

[17] M. Belal, Z. Song, Y. Jung, G. Brambilla, and T. Newson, "Optical fiber microwire current sensor," *Optics Letters*, vol. 35, no. 18, pp. 3045–3047, 2010.

[18] F.-J. Bueno, O. Esteban, N. Díaz-Herrera, M.-C. Navarrete, and A. González-Cano, "Sensing properties of asymmetric double-layer-covered tapered fibers," *Applied Optics*, vol. 43, no. 8, pp. 1615–1620, 2004.

[19] M. Sumetsky, "Optical fiber microcoil resonators," *Optics Express*, vol. 12, no. 10, pp. 2303–2316, 2004.

[20] A. K. Patnaik, J. Liang, and K. Hakuta, "Slow light propagation in a thin optical fiber via electromagnetically induced transparency," *Physical Review A*, vol. 66, no. 6, p. 063808, 2002.

[21] V. Balykin, K. Hakuta, F. Le Kien, J. Liang, and M. Morinaga, "Atom trapping and guiding with a subwavelength-diameter optical fiber," *Physical Review A*, vol. 70, no. 1, p. 011401, 2004.

[22] F. Le Kien, V. Balykin, and K. Hakuta, "Atom trap and waveguide using a two-color evanescent light field around a subwavelength-diameter optical fiber," *Physical Review A*, vol. 70, no. 6, p. 063403, 2004.

[23] F. Le Kien, S. D. Gupta, V. Balykin, and K. Hakuta, "Spontaneous emission of a cesium atom near a nanofiber: Efficient coupling of light to guided modes," *Physical Review A*, vol. 72, no. 3, p. 032509, 2005.

[24] F. Le Kien, V. Balykin, and K. Hakuta, "Scattering of an evanescent light field by a single cesium atom near a nanofiber," *Physical Review A*, vol. 73, no. 1, p. 013819, 2006.

[25] F. Le Kien, V. Balykin, and K. Hakuta, "Angular momentum of light in an optical nanofiber," *Physical Review A*, vol. 73, no. 5, p. 053823, 2006.

[26] F. Le Kien, V. Balykin, and K. Hakuta, "Light-induced force and torque on an atom outside a nanofiber," *Physical Review A*, vol. 74, no. 3, p. 033412, 2006.

[27] F. Le Kien and K. Hakuta, "Correlations between photons emitted by multiatom fluorescence into a nanofiber," *Physical Review A*, vol. 77, no. 3, p. 033826, 2008.

[28] J. Fu, X. Yin, N. Li, and L. Tong, "Atom waveguide and 1d optical lattice using a two-color evanescent light field around an optical micro/nano-fiber," *Chinese Optics Letters*, vol. 6, no. 2, pp. 112–115, 2008.

[29] G. Sagué, A. Baade, and A. Rauschenbeutel, "Blue-detuned evanescent field surface traps for neutral atoms based on mode interference in ultrathin optical fibres," *New Journal of Physics*, vol. 10, no. 11, p. 113008, 2008.

[30] F. Le Kien and K. Hakuta, "Slowing down of a guided light field along a nanofiber in a cold atomic gas," *Physical Review A*, vol. 79, no. 1, p. 013818, 2009.

[31] V. G. Minogin and S. Nic Chormaic, "Manifestation of the van der waals surface interaction in the spontaneous emission of atoms into an optical nanofiber," *Laser Physics*, vol. 20, no. 1, pp. 32–37, 2010.

[32] L. Russell, D. A. Gleeson, V. G. Minogin, and S. Nic Chormaic, "Spectral distribution of atomic fluorescence coupled into an optical nanofibre," *Journal of Physics B: Atomic, Molecular and Optical Physics*, vol. 42, no. 18, p. 185006, 2009.

[33] R. Schmidt, S. N. Chormaic, and V. G. Minogin, "van der waals interaction of a neutral atom with the surface of a metal or dielectric nanosphere," *Journal of Physics B: Atomic, Molecular and Optical Physics*, vol. 44, no. 1, p. 015004, 2011.

[34] M. C. Frawley, S. Nic Chormaic, and V. G. Minogin, "The van der waals interaction of an atom with the convex surface of a nanocylinder," *Physica Scripta*, vol. 85, no. 5, p. 058103, 2012.

[35] F. Le Kien and K. Hakuta, "Motion of an atom in a weakly driven fiber-bragg-grating cavity: force, friction, and diffusion," *Physical Review A*, vol. 81, no. 6, p. 063808, 2010.

[36] F. Le Kien and K. Hakuta, "Deterministic generation of a pair of entangled guided photons from a single atom in a nanofiber cavity," *Physical Review A*, vol. 84, no. 5, p. 053801, 2011.

[37] F. Le Kien, K. Hakuta, D. Reitz, P. Schneeweiss, and A. Rauschenbeutel, "Quantum dynamics of an atom orbiting around an optical nanofiber," *Physical Review A*, vol. 87, no. 6, p. 063607, 2013.

[38] A. Masalov and V. Minogin, "Pumping of higher-order modes of an optical nanofiber by laser excited atoms," *Laser Physics Letters*, vol. 10, no. 7, p. 075203, 2013.

[39] F. Le Kien and A. Rauschenbeutel, "Anisotropy in scattering of light from an atom into the guided modes of a nanofiber," *Physical Review A*, vol. 90, no. 2, p. 023805, 2014.

[40] P. Schneeweiss, F. Le Kien, and A. Rauschenbeutel, "Nanofiber-based atom trap created by combining fictitious and real magnetic fields," *New Journal of Physics*, vol. 16, no. 1, p. 013014, 2014.

[41] K. Nayak, P. Melentiev, M. Morinaga, F. L. Kien, V. Balykin, and K. Hakuta, "Optical nanofiber as an efficient tool for manipulating and probing atomic fluorescence," *Optics Express*, vol. 15, no. 9, pp. 5431–5438, 2007.

[42] G. Sagué, E. Vetsch, W. Alt, D. Meschede, and A. Rauschenbeutel, "Cold-atom physics using ultrathin optical fibers: Light-induced dipole forces and surface interactions," *Physical Review Letters*, vol. 99, no. 16, p. 163602, 2007.

[43] M. J. Morrissey, K. Deasy, Y. Wu, S. Chakrabarti, and S. Nic Chormaic, "Tapered optical fibers as tools for probing magneto-optical trap characteristics," *Review of scientific instruments*, vol. 80, no. 5, p. 053102, 2009.

[44] M. Das, A. Shirasaki, K. Nayak, M. Morinaga, F. Le Kien, and K. Hakuta, "Measurement of fluorescence emission spectrum of few strongly driven atoms using an optical nanofiber," *Optics Express*, vol. 18, no. 16, pp. 17154–17164, 2010.

[45] E. Vetsch, D. Reitz, G. Sagué, R. Schmidt, S. Dawkins, and A. Rauschenbeutel, "Optical interface created by laser-cooled atoms trapped in the evanescent field surrounding an optical nanofiber," *Physical Review Letters*, vol. 104, no. 20, p. 203603, 2010.

[46] L. Russell, K. Deasy, M. J. Daly, M. J. Morrissey, and S. Nic Chormaic, "Sub-Doppler temperature measurements of laser-cooled atoms using optical nanofibres," *Measurement Science and Technology*, vol. 23, no. 1, p. 015201, 2012.

[47] L. Russell, R. Kumar, V. Tiwari, and S. Nic Chormaic, "Measurements on release–recapture of cold ^{85}Rb atoms using an optical nanofibre in a magneto-optical trap," *Optics Communications*, vol. 309, pp. 313–317, 2013.

[48] D. Reitz, C. Sayrin, B. Albrecht, I. Mazets, R. Mitsch, P. Schneeweiss, and A. Rauschenbeutel, "Backscattering properties of a waveguide-coupled array of atoms in the strongly nonparaxial regime," *Physical Review A*, vol. 89, no. 3, p. 031804, 2014.

[49] R. Kumar, V. Gokhroo, K. Deasy, A. Maimaiti, M. C. Frawley, C. Phelan, and S. Nic Chormaic, "Interaction of laser-cooled ^{87}Rb atoms with higher order modes of an optical nanofibre," *New Journal of Physics*, vol. 17, no. 1, p. 013026, 2015.

[50] R. Kumar, V. Gokhroo, K. Deasy, and S. Nic Chormaic, "Autler-townes splitting via frequency up-conversion at ultralow-power levels in cold rb 87

atoms using an optical nanofiber," *Physical Review A*, vol. 91, no. 5, p. 053842, 2015.

[51] C. Sayrin, C. Clausen, B. Albrecht, P. Schneeweiss, and A. Rauschenbeutel, "Storage of fiber-guided light in a nanofiber-trapped ensemble of cold atoms," *Optica*, vol. 2, no. 4, pp. 353–356, 2015.

[52] B. Gouraud, D. Maxein, A. Nicolas, O. Morin, and J. Laurat, "Demonstration of a memory for tightly guided light in an optical nanofiber," *Physical Review Letters*, vol. 114, no. 18, p. 180503, 2015.

[53] S. Spillane, G. Pati, K. Salit, M. Hall, P. Kumar, R. Beausoleil, and M. Shahriar, "Observation of nonlinear optical interactions of ultralow levels of light in a tapered optical nanofiber embedded in a hot rubidium vapor," *Physical Review Letters*, vol. 100, no. 23, p. 233602, 2008.

[54] H. You, S. Hendrickson, and J. Franson, "Analysis of enhanced two-photon absorption in tapered optical fibers," *Physical Review A*, vol. 78, no. 5, p. 053803, 2008.

[55] S. Hendrickson, T. Pittman, and J. Franson, "Nonlinear transmission through a tapered fiber in rubidium vapor," *Journal of the Optical Society of America B*, vol. 26, no. 2, pp. 267–271, 2009.

[56] S. Hendrickson, M. Lai, T. Pittman, and J. Franson, "Observation of two-photon absorption at low power levels using tapered ptical fibers in rubidium vapor," *Physical Review Letters*, vol. 105, no. 17, p. 173602, 2010.

[57] K. Salit, M. Salit, S. Krishnamurthy, Y. Wang, P. Kumar, and M. Shahriar, "Ultra-low power, zeno effect based optical modulation in a degenerate v-system with a tapered nano fiber in atomic vapor," *Optics Express*, vol. 19, no. 23, pp. 22874–22881, 2011.

[58] T. Pittman, D. Jones, and J. Franson, "Ultralow-power nonlinear optics using tapered optical fibers in metastable xenon," *Physical Review A*, vol. 88, no. 5, p. 053804, 2013.

[59] D. Jones, J. Franson, and T. Pittman, "Saturation of atomic transitions using subwavelength diameter tapered optical fibers in rubidium vapor," *Journal of the Optical Society of America B*, vol. 31, no. 8, pp. 1997–2001, 2014.

[60] D. Jones, J. Franson, and T. Pittman, "Ladder-type electromagnetically induced transparency using nanofiber-guided light in a warm atomic vapor," *Physical Review A*, vol. 92, no. 4, p. 043806, 2015.

[61] S. H. Autler and C. H. Townes, "Stark effect in rapidly varying fields," *Physical Review*, vol. 100, no. 2, p. 703, 1955.

[62] K.-J. Boller, A. Imamoğlu, and S. E. Harris, "Observation of electromagnetically induced transparency," *Physical Review Letters*, vol. 66, no. 20, p. 2593, 1991.

[63] D. Marcuse, *Light Transmission Optics*. Van Nostrand Reinhold New York, 1972.

[64] A. Yariv and P. Yeh, *Photonics: Optical Electronics in Modern Communications*. Oxford University Press, New York, 2006.

[65] C. C. Davis, "Optical fibers and waveguides," in *Lasers and Electro-optics*, pp. 481–538, Cambridge University Press, 2014.

[66] M. J. Adams, *An Introduction to Optical Waveguides*. John Wiley & Sons, Inc., New York, 1981.

[67] D. Gloge, "Weakly guiding fibers," *Applied Optics*, vol. 10, no. 10, pp. 2252–2258, 1971.

[68] L. Tong and M. Sumetsky, *Subwavelength and nanometer diameter optical fibers*. Zhejiang University Press, Hangzhou and Springer-Verlag Berlin Heidelberg, 2010.

[69] P. Z. Dashti, F. Alhassen, and H. P. Lee, "Observation of orbital angular momentum transfer between acoustic and optical vortices in optical fiber," *Physical Review Letters*, vol. 96, no. 4, p. 043604, 2006.

[70] J. M. Ward, D. G. O'Shea, B. J. Shortt, M. J. Morrissey, K. Deasy, and S. Nic Chormaic, "Heat-and-pull rig for fiber taper fabrication," *Review of Scientific Instruments*, vol. 77, no. 8, p. 083105, 2006.

[71] E. J. Zhang, W. D. Sacher, and J. K. Poon, "Hydrofluoric acid flow etching of low-loss subwavelength-diameter biconical fiber tapers," *Optics Express*, vol. 18, no. 21, pp. 22593–22598, 2010.

[72] S. Harun, K. Lim, C. Tio, K. Dimyati, and H. Ahmad, "Theoretical analysis and fabrication of tapered fiber," *Optik-International Journal for Light and Electron Optics*, vol. 124, no. 6, pp. 538–543, 2013.

[73] L. Tong, L. Hu, J. Zhang, J. Qiu, Q. Yang, J. Lou, Y. Shen, J. He, and Z. Ye, "Photonic nanowires directly drawn from bulk glasses," *Optics Express*, vol. 14, no. 1, pp. 82–87, 2006.

[74] L. Tong, J. Lou, Z. Ye, G. T. Svacha, and E. Mazur, "Self-modulated taper drawing of silica nanowires," *Nanotechnology*, vol. 16, no. 9, p. 1445, 2005.

[75] H. Liu, J. B. Edel, L. M. Bellan, and H. Craighead, "Electrospun polymer nanofibers as subwavelength optical waveguides incorporating quantum dots," *Small*, vol. 2, no. 4, pp. 495–499, 2006.

[76] J. Ward, A. Maimaiti, V. H. Le, and S. Nic Chormaic, "Contributed review: Optical micro-and nanofiber pulling rig," *Review of Scientific Instruments*, vol. 85, no. 11, p. 111501, 2014.

[77] J. Love, W. Henry, W. Stewart, R. Black, S. Lacroix, and F. Gonthier, "Tapered single-mode fibres and devices. part 1: Adiabaticity criteria," *IEE Proceedings-J (Optoelectronics)*, vol. 138, no. 5, pp. 343–354, 1991.

[78] Y. Jung, G. Brambilla, and D. J. Richardson, "Broadband single-mode operation of standard optical fibers by using a sub-wavelength optical wire filter," *Optics Express*, vol. 16, no. 19, pp. 14661–14667, 2008.

[79] M. C. Frawley, A. Petcu-Colan, V. G. Truong, and S. Nic Chormaic, "Higher order mode propagation in an optical nanofiber," *Optics Communications*, vol. 285, no. 23, pp. 4648–4654, 2012.

[80] R. P. Kenny, T. A. Birks, and K. P. Oakley, "Control of optical fibre taper shape," *Electronics letters*, vol. 27, no. 18, pp. 1654–1656, 1991.

[81] S. Ravets, J. Hoffman, L. Orozco, S. Rolston, G. Beadie, and F. Fatemi, "A low-loss photonic silica nanofiber for higher-order modes," *Optics Express*, vol. 21, no. 15, pp. 18325–18335, 2013.

[82] N. Matsumoto, T. Ando, T. Inoue, Y. Ohtake, N. Fukuchi, and T. Hara, "Generation of high-quality higher-order Laguerre-Gaussian beams using liquid-crystal-on-silicon spatial light modulators," *Journal Optical Society of America A*, vol. 25, no. 7, pp. 1642–1651, 2008.

[83] A. Petcu-Colan, M. Frawley, and S. Nic Chormaic, "Tapered few-mode fibers: mode evolution during fabrication and adiabaticity," *Journal of Nonlinear Optical Physics & Materials*, vol. 20, no. 03, pp. 293–307, 2011.

[84] P. Lambropoulos and D. Petrosyan, *Fundamentals of Quantum Optics and Quantum Information*. Springer-Verlag Berlin Heidelberg New York, 2007.

[85] B. Shore, *The theory of Coherent Atomic Excitation*. John Wiley & Sons, Inc., New York, 1990.

[86] R. Loudon, *The Quantum Theory of Light*. Oxford University Press, New York, 2000.

[87] M. Fox, *Quantum Optics: An Introduction*. Oxford University Press, New York, 2006.

[88] C. J. Foot, *Atomic Physics*. Oxford University Press, New York, 2004.

[89] H. J. Metcalf and P. Van der Straten, *Laser Cooling and Trapping*. Springer-Verlag Berlin Heidelberg New York, 2012.

[90] S. Stenholm, *Foundations of Laser Spectroscopy*. Dover Publications, Inc., New York, 2012.

[91] U. Raitzsch, R. Heidemann, H. Weimer, B. Butscher, P. Kollmann, R. Löw, H. Büchler, and T. Pfau, "Investigation of dephasing rates in an interacting Rydberg gas," *New Journal of Physics*, vol. 11, no. 5, p. 055014, 2009.

[92] P. Berman, E. Arimondo, and C. Lin, *Advances in Atomic, Molecular, and Optical Physics*. No. v. 61 in Advances In Atomic, Molecular, and Optical Physics, Elsevier Science, 2012.

[93] T. Y. Abi-Salloum, "Interference between competing pathways in the interaction of three-level ladder atoms and radiation," *Journal of Modern Optics*, vol. 57, no. 14-15, pp. 1366–1376, 2010.

[94] G. Vemuri, G. Agarwal, and B. N. Rao, "Sub-Doppler resolution in inhomogeneously broadened media using intense control fields," *Physical Review A*, vol. 53, no. 4, p. 2842, 1996.

[95] S. E. Harris, "Electromagnetically induced transparency," *Physics Today*, vol. 50, no. 7, pp. 36–42, 2008.

[96] A. Ashkin, "Atomic-beam deflection by resonance-radiation pressure," *Physical Review Letters*, vol. 25, no. 19, p. 1321, 1970.

[97] T. W. Hänsch and A. L. Schawlow, "Cooling of gases by laser radiation," *Optics Communications*, vol. 13, no. 1, pp. 68–69, 1975.

[98] S. Chu, L. Hollberg, J. E. Bjorkholm, A. Cable, and A. Ashkin, "Three-dimensional viscous confinement and cooling of atoms by resonance radiation pressure," *Physical Review Letters*, vol. 55, no. 1, p. 48, 1985.

[99] E. Raab, M. Prentiss, A. Cable, S. Chu, and D. E. Pritchard, "Trapping of neutral sodium atoms with radiation pressure," *Physical Review Letters*, vol. 59, no. 23, p. 2631, 1987.

[100] D. A. Steck, "Rubidium 87 D line data," 2001.

[101] H. Youk, "Numerical study of quadrupole magnetic traps for neutral atoms: anti-Helmholtz coils and a U-chip," vol. 3, pp. 13–18, 2005.

[102] E. R. Abraham and E. A. Cornell, "Teflon feedthrough for coupling optical fibers into ultrahigh vacuum systems," *Applied Optics*, vol. 37, no. 10, pp. 1762–1763, 1998.

[103] C. Monroe, W. Swann, H. Robinson, and C. Wieman, "Very cold trapped atoms in a vapor cell," *Physical Review Letters*, vol. 65, no. 13, p. 1571, 1990.

[104] G. S. Cassany, *Cold atom physics using ultra-thin optical fibres*. PhD thesis, Dissertation, Rheinischen Freidrich-Wilhelms-Universität Bonn, Bonn, 2008.

[105] P. v. d. Straten and H. Metcalf, *The Quest for BEC*. Wiley-VCH GmbH & Co., Weinheim, 2005.

[106] R. Silva, K. M. F. Magalhães, E. A. d. L. Henn, L. G. Marcassa, and V. S. Bagnato, "Temperature determination for magneto optical trapped atoms using a single parameter transient absorption," *Optics Communications*, vol. 265, no. 2, pp. 526–531, 2006.

[107] A. Goban, K. Choi, D. Alton, D. Ding, C. Lacroûte, M. Pototschnig, T. Thiele, N. Stern, and H. Kimble, "Demonstration of a state-insensitive, compensated nanofiber trap," *Physical Review Letters*, vol. 109, no. 3, p. 033603, 2012.

[108] J. E. Hoffman, J. A. Grover, Z. Kim, A. K. Wood, J. R. Anderson, A. J. Dragt, M. Hafezi, C. J. Lobb, L. A. Orozco, S. L. Rolston, J. M. Taylor, C. P. Vlahacos, and F. C. Wellstood, "Atoms talking to squids," *arXiv preprint arXiv:1108.4153*, 2011.

[109] J.-B. Béguin, E. Bookjans, S. Christensen, H. Sørensen, J. Müller, E. Polzik, and J. Appel, "Generation and detection of a sub-poissonian atom number distribution in a one-dimensional optical lattice," *Physical Review Letters*, vol. 113, no. 26, p. 263603, 2014.

[110] M. Fleischhauer, A. Imamoglu, and J. P. Marangos, "Electromagnetically induced transparency: Optics in coherent media," *Reviews of modern physics*, vol. 77, no. 2, p. 633, 2005.

[111] L. Russell, M. Daly, and S. Nic Chormaic, "1-and 2-photon absorption by laser-cooled ^{85}Rb using an optical nanofiber," in *Quantum Africa 2010: Theoretical and Experimental Foundations of Recent Quantum Technology*, vol. 1469, pp. 82–90, AIP Publishing, 2012.

[112] R. Ryan, L. Westling, and H. J. Metcalf, "Two-photon spectroscopy in rubidium with a diode laser," *Journal of the Optical Society of America B*, vol. 10, no. 9, pp. 1643–1648, 1993.

[113] R. Fox, H. Robinson, S. Gilbert, L. Hollberg, and J. Marquardt, "Optical probing of cold trapped atoms," *Optics Letters*, vol. 18, no. 17, pp. 1456–1458, 1993.

[114] M. Piotrowicz, C. MacCormick, A. Kowalczyk, S. Bergamini, I. Beterov, and E. Yakshina, "Measurement of the electric dipole moments for transitions to rubidium Rydberg states via autler–townes splitting," *New Journal of Physics*, vol. 13, no. 9, p. 093012, 2011.

[115] H. Zhang, L. Wang, J. Chen, S. Bao, L. Zhang, J. Zhao, and S. Jia, "Autler–townes splitting of a cascade system in ultracold cesium Rydberg atoms," *Phys. Rev. A*, vol. 87, p. 033835, 2013.

[116] J. Bjorkholm and P. Liao, "Line shape and strength of two-photon absorption in an atomic vapor with a resonant or nearly resonant intermediate state," *Physical Review A*, vol. 14, no. 2, p. 751, 1976.

[117] M. B. Kienlen, N. T. Holte, H. A. Dassonville, A. M. Dawes, K. D. Iversen, R. M. McLaughlin, and S. K. Mayer, "Collimated blue light generation in rubidium vapor," *American Journal of Physics*, vol. 81, no. 6, pp. 442–449, 2013.

[118] O. Heavens, "Radiative transition probabilities of the lower excited states of the alkali metals," *Journal of the Optical Society of America*, vol. 51, no. 10, pp. 1058–1061, 1961.

[119] A. M. Akulshin, R. J. McLean, A. I. Sidorov, and P. Hannaford, "Coherent and collimated blue light generated by four-wave mixing in Rb vapour," *Optics Express*, vol. 17, no. 25, pp. 22861–22870, 2009.

[120] F. Le Kien and K. Hakuta, "Spontaneous radiative decay of translational levels of an atom near a dielectric surface," *Physical Review A*, vol. 75, no. 1, p. 013423, 2007.

[121] J. Lee, J. Grover, J. Hoffman, L. Orozco, and S. Rolston, "Inhomogeneous broadening of optical transitions of ^{87}Rb atoms in an optical nanofiber trap," *arXiv preprint arXiv:1412.6754*, 2014.

[122] S. Stenholm, *Foundations of Laser Spectroscopy*. Wiley, New York, 1984.

[123] S. Hendrickson, C. Weiler, R. Camacho, P. Rakich, A. Young, M. Shaw, T. Pittman, J. Franson, and B. Jacobs, "All-optical-switching demonstration using two-photon absorption and the zeno effect," *Physical Review A*, vol. 87, no. 2, p. 023808, 2013.

[124] S. Krishnamurthy, Y. Wang, Y. Tu, S. Tseng, and M. Shahriar, "Optically controlled polarizer using a ladder transition for high speed stokesmetric imaging and quantum zeno effect based optical logic," *Optics Express*, vol. 21, no. 21, pp. 24514–24531, 2013.

[125] A. Vernier, S. Franke-Arnold, E. Riis, and A. Arnold, "Enhanced frequency up-conversion in rb vapor," *Optics Express*, vol. 18, no. 16, pp. 17020–17026, 2010.

[126] S. Ravets, J. Hoffman, P. Kordell, J. Wong-Campos, S. Rolston, and L. Orozco, "Intermodal energy transfer in a tapered optical fiber: optimizing transmission," *Journal of the Optical Society of America A*, vol. 30, no. 11, pp. 2361–2371, 2013.

[127] R. Mitsch, C. Sayrin, B. Albrecht, P. Schneeweiss, and A. Rauschenbeutel, "Exploiting the local polarization of strongly confined light for sub-micrometer-resolution internal state preparation and manipulation of cold atoms," *Physical Review A*, vol. 89, no. 6, p. 063829, 2014.

[128] H. J. Kimble, "The quantum internet," *Nature*, vol. 453, no. 7198, pp. 1023–1030, 2008.

[129] R. Miller, T. Northup, K. Birnbaum, A. Boca, A. Boozer, and H. Kimble, "Trapped atoms in cavity QED: coupling quantized light and matter,"

Journal of Physics B: Atomic, Molecular and Optical Physics, vol. 38, no. 9, p. S551, 2005.

[130] S. Van Enk, J. Cirac, and P. Zoller, "Photonic channels for quantum communication," *Science*, vol. 279, no. 5348, pp. 205–208, 1998.

[131] T. Wilk, S. C. Webster, A. Kuhn, and G. Rempe, "Single-atom single-photon quantum interface," *Science*, vol. 317, no. 5837, pp. 488–490, 2007.

[132] J. Volz, R. Gehr, G. Dubois, J. Estève, and J. Reichel, "Measurement of the internal state of a single atom without energy exchange," *Nature*, vol. 475, no. 7355, pp. 210–213, 2011.

[133] H. Zoubi and H. Ritsch, "Hybrid quantum system of a nanofiber mode coupled to two chains of optically trapped atoms," *New Journal of Physics*, vol. 12, no. 10, p. 103014, 2010.

[134] V. Klimov and M. Ducloy, "Spontaneous emission rate of an excited atom placed near a nanofiber," *Physical Review A*, vol. 69, no. 1, p. 013812, 2004.

[135] R. Yalla, F. Le Kien, M. Morinaga, and K. Hakuta, "Efficient channeling of fluorescence photons from single quantum dots into guided modes of optical nanofiber," *Physical Review Letters*, vol. 109, no. 6, p. 063602, 2012.

[136] L. Liebermeister, F. Petersen, A. v. Münchow, D. Burchardt, J. Hermelbracht, T. Tashima, A. W. Schell, O. Benson, T. Meinhardt, A. Krueger, *et al.*, "Tapered fiber coupling of single photons emitted by a deterministically positioned single nitrogen vacancy center," *Applied Physics Letters*, vol. 104, no. 3, p. 031101, 2014.

[137] M. Lukin and A. Imamoğlu, "Nonlinear optics and quantum entanglement of ultraslow single photons," *Physical Review Letters*, vol. 84, no. 7, p. 1419, 2000.

[138] R.-Y. Chang, W.-C. Fang, B.-C. Ke, Z.-S. He, M.-D. Tsai, Y.-C. Lee, and C.-C. Tsai, "Suppression and recovery of the trapping of atoms using a ladder-type electromagnetically induced transparency," *Physical Review A*, vol. 76, no. 5, p. 055404, 2007.

[139] Z.-P. Wang and S.-X. Zhang, "High-efficiency four-wave mixing in a five-level atomic system based on two-electromagnetically induced transparency in the ultraslow propagation regime," *Physica Scripta*, vol. 81, no. 3, p. 035401, 2010.

[140] J. Gea-Banacloche, Y.-q. Li, S.-z. Jin, and M. Xiao, "Electromagnetically induced transparency in ladder-type inhomogeneously broadened media: Theory and experiment," *Physical Review A*, vol. 51, no. 1, p. 576, 1995.

[141] M. A. Kumar and S. Singh, "Electromagnetically induced transparency and slow light in three-level ladder systems: Effect of velocity-changing and dephasing collisions," *Physical Review A*, vol. 79, no. 6, p. 063821, 2009.

[142] L. Van Doai, P. Van Trong, D. X. Khoa, and N. H. Bang, "Electromagnetically induced transparency in five-level cascade scheme of ^{85}Rb atoms: An analytical approach," *Optik-International Journal for Light and Electron Optics*, vol. 125, no. 14, pp. 3666–3669, 2014.

[143] H. S. Moon, L. Lee, and J. B. Kim, "Coupling-intensity effects in ladder-type electromagnetically induced transparency of rubidium atoms," *Journal of the Optical Society of America B*, vol. 22, no. 12, pp. 2529–2533, 2005.

[144] H. S. Moon, L. Lee, and J. B. Kim, "Double-resonance optical pumping of Rb atoms," *Journal of the Optical Society of America B*, vol. 24, no. 9, pp. 2157–2164, 2007.

[145] M. S. Ali, A. Ray, and A. Chakrabarti, "Control of coherence in a ladder type system with double resonance optical pumping and electromagnetically induced transparency," *The European Physical Journal D*, vol. 69, no. 2, pp. 1–10, 2015.

[146] A. Masalov and V. Minogin, "Spontaneous decay rates of the hyperfine structure atomic states into an optical nanofiber," *Journal of Experimental and Theoretical Physics*, vol. 118, no. 5, pp. 714–722, 2014.

[147] K. Hakuta and K. P. Nayak, "Manipulating single atoms and photons using optical nanofibers," *Advances in Natural Sciences: Nanoscience and Nanotechnology*, vol. 3, no. 1, p. 015005, 2012.

[148] M. Daly, V. G. Truong, C. Phelan, K. Deasy, and S. Nic Chormaic, "Nanostructured optical nanofibres for atom trapping," *New Journal of Physics*, vol. 16, no. 5, p. 053052, 2014.

[149] G. Brambilla, G. S. Murugan, J. Wilkinson, and D. Richardson, "Optical manipulation of microspheres along a subwavelength optical wire," *Optics Letters*, vol. 32, no. 20, pp. 3041–3043, 2007.

[150] H. Lei, Y. Zhang, X. Li, and B. Li, "Photophoretic assembly and migration of dielectric particles and escherichia coli in liquids using a subwavelength diameter optical fiber," *Lab on a Chip*, vol. 11, no. 13, pp. 2241–2246, 2011.

[151] M. C. Frawley, I. Gusachenko, V. G. Truong, M. Sergides, and S. Nic Chormaic, "Selective particle trapping and optical binding in the evanescent field of an optical nanofiber," *Optics Express*, vol. 22, no. 13, pp. 16322–16334, 2014.

[152] L. Zhang, J. Lou, and L. Tong, "Micro/nanofiber optical sensors," *Photonic Sensors*, vol. 1, no. 1, pp. 31–42, 2011.

[153] P. Wang, G. Brambilla, M. Ding, Y. Semenova, Q. Wu, and G. Farrell, "High-sensitivity, evanescent field refractometric sensor based on a tapered, multimode fiber interference," *Optics Letters*, vol. 36, no. 12, pp. 2233–2235, 2011.

[154] M. J. Morrissey, K. Deasy, M. Frawley, R. Kumar, E. Prel, L. Russell, V. G. Truong, and S. Nic Chormaic, "Spectroscopy, manipulation and trapping of neutral atoms, molecules, and other particles using optical nanofibers: A review," *Sensors*, vol. 13, no. 8, pp. 10449–10481, 2013.

[155] C. Phelan, T. Hennessy, and T. Busch, "Shaping the evanescent field of optical nanofibers for cold atom trapping," *Optics Express*, vol. 21, no. 22, pp. 27093–27101, 2013.

[156] A. Yariv, "Introduction to optical electronics," 1976.

[157] G. Volpe and D. Petrov, "Generation of cylindrical vector beams with few-mode fibers excited by Laguerre-Gaussian beams," *Optics Communications*, vol. 237, no. 1, pp. 89–95, 2004.

[158] L. Allen, M. W. Beijersbergen, R. Spreeuw, and J. Woerdman, "Orbital angular momentum of light and the transformation of Laguerre-Gaussian laser modes," *Physical Review A*, vol. 45, no. 11, p. 8185, 1992.

[159] W. Power, L. Allen, M. Babiker, and V. Lembessis, "Atomic motion in light beams possessing orbital angular momentum," *Physical Review A*, vol. 52, no. 1, p. 479, 1995.

[160] J. Tabosa and D. Petrov, "Optical pumping of orbital angular momentum of light in cold cesium atoms," *Physical Review Letters*, vol. 83, no. 24, p. 4967, 1999.

[161] A. Mair, A. Vaziri, G. Weihs, and A. Zeilinger, "Entanglement of the orbital angular momentum states of photons," *Nature*, vol. 412, no. 6844, pp. 313–316, 2001.

[162] Q.-F. Chen, B.-S. Shi, Y.-S. Zhang, and G.-C. Guo, "Entanglement of the orbital angular momentum states of the photon pairs generated in a hot atomic ensemble," *Physical Review A*, vol. 78, no. 5, p. 053810, 2008.

[163] J. Wang, J.-Y. Yang, I. M. Fazal, N. Ahmed, Y. Yan, H. Huang, Y. Ren, Y. Yue, S. Dolinar, M. Tur, and A. E. Willner, "Terabit free-space data transmission employing orbital angular momentum multiplexing," *Nature Photonics*, vol. 6, no. 7, pp. 488–496, 2012.

[164] N. Bozinovic, Y. Yue, Y. Ren, M. Tur, P. Kristensen, H. Huang, A. E. Willner, and S. Ramachandran, "Terabit-scale orbital angular momentum mode division multiplexing in fibers," *Science*, vol. 340, no. 6140, pp. 1545–1548, 2013.

[165] A. Nicolas, L. Veissier, L. Giner, E. Giacobino, D. Maxein, and J. Laurat, "A quantum memory for orbital angular momentum photonic qubits," *Nature Photonics*, vol. 8, no. 3, pp. 234–238, 2014.